

**PREPARATION AND CHARACTERIZATION OF MANGANESE DOPED IRON  
OXIDE MAGNETIC NANOPARTICLES COATED PINE CONE POWDER AND ITS  
APPLICATIONS IN WATER TREATMENT**

Thesis submitted in fulfilment of the requirements for the degree

Doctor of Philosophy in Chemistry

In the Faculty of Applied and Computer Sciences



Vaal University of Technology

Immaculate Linda Achieng' Ouma  
BSc Chemistry (University of Nairobi)  
MSc Chemical Science (University of the Western Cape)

Promoter: Prof. A. E. Ofomaja  
Co-promoter: Prof. E. B. Naidoo

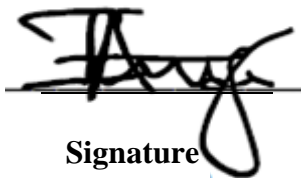
March 2019

## DECLARATION

---

I declare that the dissertation titled “**Preparation and characterisation of manganese doped iron oxide magnetic nanoparticles coated pine cone powder and its applications in water treatment**” is my own work, that it has not been submitted for any degree or examination in any other university, and that all the sources I have used or quoted have been indicated and acknowledged by complete references.

**Immaculate Linda Achieng' Ouma**



Signature

March 2019

Date

## DEDICATION

---

*For Angela and Eden*

## ACKNOWLEDGEMENTS

---

I wish to express my sincere gratitude to everyone whose contribution made this Thesis a success. First, I thank the Almighty God for His grace and providence which has been abundant in my life thus far.

I greatly appreciate the expert guidance of my supervisors Prof Ofomaja and Prof Naidoo who provided much needed direction and support throughout the course of this work and oversaw its successful completion.

My sincere gratitude goes to my colleagues in the adsorption-catalysis lab who together we navigated the waters of post-graduate research, the encouragement as we shared our joys and frustrations kept me going and am ever so grateful.

I wish to thank Mr. Ngoy for his humility and patience during training in the use of analytical instruments and much appreciation also goes to the technicians at Metallurgy department for access to instruments in their lab.

I am grateful to the Vaal University of Technology for the opportunity and facilities to carry out this work.

I appreciate the financial support from the National Research Foundation and Vaal University of Technology that enabled me to successfully complete my studies.

Finally, my deepest gratitude goes to my husband Seth and my children Angela and Eden whose love, support and encouragement make each day brighter.

## TABLE OF CONTENTS

---

<b>DECLARATION.....</b>	<b>I</b>
<b>DEDICATION.....</b>	<b>II</b>
<b>ACKNOWLEDGEMENTS .....</b>	<b>III</b>
<b>LIST OF TABLES .....</b>	<b>X</b>
<b>LIST OF FIGURES .....</b>	<b>XI</b>
<b>LIST OF ABBREVIATIONS AND SYMBOLS .....</b>	<b>XV</b>
<b>RESEARCH OUTPUT.....</b>	<b>XVII</b>
<b>CONFERENCE CONTRIBUTIONS .....</b>	<b>XVII</b>
<b>PEER REVIEWED ARTICLES .....</b>	<b>XVII</b>
<b>ABSTRACT.....</b>	<b>XVIII</b>
<b>CHAPTER 1 .....</b>	<b>1</b>
<b>1 INTRODUCTION.....</b>	<b>1</b>
<b>1.1 BACKGROUND.....</b>	<b>1</b>
<b>1.2 PROBLEM STATEMENT .....</b>	<b>2</b>
<b>1.3 AIM .....</b>	<b>3</b>
1.3.1 Specific Objectives .....	3
<b>1.4 THESIS LAYOUT.....</b>	<b>4</b>
<b>1.5 REFERENCES.....</b>	<b>6</b>
<b>CHAPTER 2 .....</b>	<b>9</b>
<b>2 LITERATURE REVIEW .....</b>	<b>9</b>
<b>2.1 WATER POLLUTION .....</b>	<b>9</b>
2.1.1 Heavy Metal Pollution .....	9
2.1.2 Arsenic .....	11
2.1.3 Chromium .....	11

<b>2.2</b>	<b>REMEDIATION OF HEAVY METAL CONTAMINATED WATER.....</b>	<b>12</b>
2.2.1	Oxidation.....	12
2.2.2	Coagulation-flocculation.....	12
2.2.3	Ion Exchange .....	13
2.2.4	Adsorption.....	13
2.2.4.1	<i>Physisorption</i> .....	13
2.2.4.2	<i>Chemisorption</i> .....	14
<b>2.3</b>	<b>DESORPTION .....</b>	<b>14</b>
<b>2.4</b>	<b>TYPES OF ADSORBENTS.....</b>	<b>14</b>
2.4.1	Biosorbents .....	14
2.4.2	Nanosized Adsorbents .....	16
2.4.2.1	<i>Nanoparticle Doping</i> .....	17
2.4.3	Composite Adsorbents .....	17
<b>2.5</b>	<b>FACTORS AFFECTING ADSORPTION .....</b>	<b>18</b>
2.5.1	Solution pH .....	18
2.5.2	Adsorbent Mass .....	18
2.5.3	Adsorbate Concentration .....	18
<b>2.6</b>	<b>ADSORPTION MODELLING .....</b>	<b>18</b>
2.6.1	Thermodynamic Modelling .....	18
2.6.1.1	<i>Langmuir</i> .....	19
2.6.1.2	<i>Freundlich</i> .....	19
2.6.1.3	<i>Redlich-Peterson</i> .....	19
2.6.1.4	<i>Sips</i> .....	20
2.6.1.5	<i>Dubinin-Raduschkevich</i> .....	20
2.6.1.6	<i>Flory-Huggins</i> .....	21
2.6.2	Kinetic Modelling .....	21
2.6.2.1	<i>Pseudo-First Order Model</i> .....	22
2.6.2.2	<i>Pseudo-Second Order Model</i> .....	22
2.6.2.3	<i>Elovich Model</i> .....	22
2.6.2.4	<i>Intraparticle Diffusion</i> .....	23
<b>2.7</b>	<b>CONCLUSION .....</b>	<b>23</b>

<b>2.8</b>	<b>REFERENCES.....</b>	<b>24</b>
<b>CHAPTER 3 .....</b>	<b>35</b>	
<b>3</b>	<b>PREPARATION AND CHARACTERIZATION OF PINE CONE AND MAGNETITE BASED ADSORBENTS .....</b>	<b>35</b>
<b>3.1</b>	<b>INTRODUCTION .....</b>	<b>35</b>
<b>3.2</b>	<b>EXPERIMENTAL .....</b>	<b>36</b>
3.2.1	Materials .....	36
3.2.2	Methods.....	36
3.1.1.1	<i>Preparation of Fenton’s Treated Pine Cone Powder .....</i>	<i>36</i>
3.1.1.2	<i>Synthesis of Magnetite Nanoparticles.....</i>	<i>37</i>
3.1.1.3	<i>Synthesis of Manganese Doped Magnetite Nanoparticles.....</i>	<i>37</i>
3.1.1.4	<i>Preparation of Pine Cone-Magnetite Composite .....</i>	<i>37</i>
3.1.1.5	<i>Synthesis of Manganese Doped Pine Cone-Magnetite Composite .....</i>	<i>37</i>
3.2.3	Characterization .....	37
<b>3.3</b>	<b>RESULTS AND DISCUSSIONS .....</b>	<b>38</b>
3.3.1	X-ray Diffraction .....	38
3.3.2	Thermal Analysis .....	42
3.3.3	Infrared Analysis.....	46
3.3.4	Surface Properties .....	50
3.3.5	Electron Microscopy .....	51
3.3.6	Magnetic Measurements .....	53
3.3.7	X-ray Photoelectron Spectroscopic Analysis.....	55
<b>3.4</b>	<b>CONCLUSION .....</b>	<b>58</b>
<b>3.5</b>	<b>REFERENCES.....</b>	<b>59</b>
<b>CHAPTER 4 .....</b>	<b>64</b>	
<b>4</b>	<b>OPTIMIZATION OF ADSORPTION PARAMETERS FOR AS(III) AND CR(VI) ADSORPTION ONTO THE PREPARED ADSORBENTS .....</b>	<b>64</b>
<b>4.1</b>	<b>INTRODUCTION .....</b>	<b>64</b>
<b>4.2</b>	<b>EXPERIMENTAL .....</b>	<b>64</b>

4.2.1	Materials .....	64
4.2.2	Methods.....	65
<b>4.3</b>	<b>RESULTS AND DISCUSSIONS .....</b>	<b>65</b>
4.3.1	Effect of pH.....	66
4.3.2	Effect of Adsorbent Dose.....	70
4.3.3	Effect of Initial Adsorbate Concentration.....	76
<b>4.4</b>	<b>CONCLUSION .....</b>	<b>78</b>
<b>4.5</b>	<b>REFERENCES.....</b>	<b>80</b>
<b>CHAPTER 5 .....</b>	<b>83</b>	
<b>5</b>	<b>THERMODYNAMICS STUDIES OF AS(III) AND CR(VI) ADSORPTION ONTO THE PREPARED ADSORBENTS .....</b>	<b>83</b>
<b>5.1</b>	<b>INTRODUCTION.....</b>	<b>83</b>
5.1.1	Isotherm Models .....	83
5.1.1.1	<i>Langmuir</i> .....	83
5.1.1.2	<i>Freundlich</i> .....	84
5.1.1.3	<i>Redlich-Peterson</i> .....	84
5.1.1.4	<i>Sips</i> .....	85
5.1.1.5	<i>Dubinin-Radushkevich</i> .....	85
5.1.1.6	<i>Flory-Huggins Isotherm and Thermodynamic Parameters</i> .....	86
<b>5.2</b>	<b>EXPERIMENTAL .....</b>	<b>87</b>
5.2.1	Materials .....	87
5.2.2	Methods.....	87
5.2.2.1	<i>Thermodynamic Studies</i> .....	87
<b>5.3</b>	<b>RESULTS AND DISCUSSIONS .....</b>	<b>87</b>
5.3.1	Arsenic Adsorption .....	88
5.3.1.1	<i>Isotherm Analyses</i> .....	88
5.3.1.2	<i>Thermodynamic Analyses</i> .....	89
5.3.2	Chromium Adsorption.....	91
5.3.2.1	<i>Isotherm Analyses</i> .....	91
5.3.2.2	<i>Thermodynamic Analyses</i> .....	91



<b>5.4</b>	<b>CONCLUSION .....</b>	<b>94</b>
<b>5.5</b>	<b>REFERENCES.....</b>	<b>95</b>
<b>CHAPTER 6.....</b>		<b>99</b>
<b>6</b>	<b>KINETICS STUDIES OF AS(III) AND CR(VI) ADSORPTION ONTO THE PREPARED ADSORBENTS.....</b>	<b>99</b>
<b>6.1</b>	<b>INTRODUCTION.....</b>	<b>99</b>
6.1.1	Kinetic Models.....	99
6.1.1.1	<i>Pseudo-first and Pseudo-second Order Models .....</i>	<i>99</i>
6.1.1.2	<i>Elovich Model .....</i>	<i>100</i>
6.1.1.3	<i>Intraparticle Diffusion Model.....</i>	<i>100</i>
<b>6.2</b>	<b>EXPERIMENTAL .....</b>	<b>101</b>
6.2.1	Materials .....	101
6.2.2	Methods.....	101
<b>6.3</b>	<b>RESULTS AND DISCUSSIONS .....</b>	<b>101</b>
6.3.1	Arsenic Adsorption .....	101
6.3.2	Chromium Adsorption .....	108
<b>6.4</b>	<b>CONCLUSION .....</b>	<b>115</b>
<b>6.5</b>	<b>REFERENCES.....</b>	<b>116</b>
<b>CHAPTER 7.....</b>		<b>119</b>
<b>7</b>	<b>ADSORBENT REGENERATION STUDIES AND THE DETERMINATION OF THE MECHANISM OF AS(III) AND CR(VI) ADSORPTION ONTO FTP-MNP AS A MODEL ADSORBENT.....</b>	<b>119</b>
<b>7.1</b>	<b>INTRODUCTION.....</b>	<b>119</b>
<b>7.2</b>	<b>EXPERIMENTAL .....</b>	<b>120</b>
7.2.1	Materials .....	120
7.2.2	Methods.....	120
7.2.2.1	<i>Adsorbent Regeneration.....</i>	<i>120</i>
7.2.2.2	<i>Adsorption mechanism studies.....</i>	<i>120</i>
<b>7.3</b>	<b>RESULTS AND DISCUSSIONS .....</b>	<b>121</b>

7.3.1	Adsorbent Regeneration.....	121
7.3.2	Mechanism studies.....	124
7.3.2.1	<i>Arsenic Adsorption Mechanism</i> .....	124
7.3.2.1.1	<i>Ionic Strength</i> .....	124
7.3.2.1.2	<i>Ion Exchange Mechanism</i> .....	125
7.3.2.1.3	<i>Infrared Analysis</i> .....	126
7.3.2.1.4	<i>X-ray Photoelectron Spectroscopic Analysis</i> .....	127
7.3.2.2	<i>Chromium Adsorption Mechanism</i> .....	131
7.3.2.2.1	<i>Change in H<sup>+</sup> Concentration</i> .....	132
7.3.2.2.2	<i>Cr(III) Concentration After Adsorption</i> .....	133
7.3.2.2.3	<i>Change in Redox Potential</i> .....	135
7.3.2.2.4	<i>X-ray Photoelectron Spectroscopic Analysis</i> .....	135
7.3.2.2.5	<i>Ion-exchange mechanism</i> .....	138
7.3.3	Effects of competing anions.....	139
<b>7.4</b>	<b>CONCLUSION</b> .....	<b>141</b>
<b>7.5</b>	<b>REFERENCES</b> .....	<b>142</b>
<b>CHAPTER 8</b>	<b>.....</b>	<b>147</b>
<b>8</b>	<b>CONCLUSIONS AND RECOMMENDATIONS</b> .....	<b>147</b>
<b>8.1</b>	<b>CONCLUSIONS</b> .....	<b>147</b>
<b>8.2</b>	<b>RECOMMENDATIONS</b> .....	<b>149</b>
<b>APPENDICES</b>	<b>.....</b>	<b>150</b>
<b>APPENDIX A: ISOTHERM MODELLING DATA</b>	<b>.....</b>	<b>151</b>
<b>APPENDIX B: KINETICS MODELLING DATA</b>	<b>.....</b>	<b>161</b>

## LIST OF TABLES

---

Table 2.1: Common sources of heavy metals and the associated health risks.....	10
Table 3.1: BET Surface area and pore characteristics for as-synthesized materials .....	50
Table 3.2: Point of zero charge results for as-synthesized materials .....	51
Table 3.3: Magnetic properties of the as-synthesized adsorbents.....	55
Table 5.1: Flory-Huggins model parameters and thermodynamic parameters for As(III) adsorption onto the prepared adsorbents. ....	90
Table 5.2: Flory-Huggins model parameters and thermodynamic parameters for Cr(VI) adsorption onto the prepared adsorbents. ....	93
Table A-1: Isotherm modelling parameters for the adsorption of As(III) onto FTP .....	151
Table A-2: Isotherm modelling parameters for the adsorption of As(III) onto MNP .....	152
Table A-3: Isotherm modelling parameters for the adsorption of As(III) onto FTP-MNP .....	153
Table A-4: Isotherm modelling parameters for the adsorption of As(III) onto Mn MNP .....	154
Table A-5: Isotherm modelling parameters for the adsorption of As(III) onto Mn FTP-MNP..	155
Table A-6: Isotherm modelling parameters for the adsorption of Cr(VI) onto FTP .....	156
Table A-7: Isotherm modelling parameters for the adsorption of Cr(VI) onto MNP.....	157
Table A-8: Isotherm modelling parameters for the adsorption of Cr(VI) onto FTP-MNP .....	158
Table A-9: Isotherm modelling parameters for the adsorption of Cr(VI) onto Mn MNP .....	159
Table A-10: Isotherm modelling parameters for the adsorption of Cr(VI) onto Mn FTP-MNP	160
Table B-11: Kinetic modelling parameters for the adsorption of As(III) onto FTP.....	161
Table B-12: Kinetic modelling parameters for the adsorption of As(III) onto MNP .....	162
Table B-13: Kinetic modelling parameters for the adsorption of As(III) onto FTP-MNP .....	163
Table B-14: Kinetic modelling parameters for the adsorption of As(III) onto Mn MNP.....	164
Table B-15: Kinetic modelling parameters for the adsorption of As(III) onto Mn FTP-MNP ..	165
Table B-16: Kinetic modelling parameters for the adsorption of Cr(VI) onto FTP .....	166
Table B-17: Kinetic modelling parameters for the adsorption of Cr(VI) onto MNP .....	167
Table B-18: Kinetic modelling parameters for the adsorption of Cr(VI) onto FTP-MNP .....	168
Table B-19: Kinetic modelling parameters for the adsorption of Cr(VI) onto Mn MNP.....	169
Table B-20: Kinetic modelling parameters for the adsorption of Cr(VI) onto Mn FTP-MNP...	170

## LIST OF FIGURES

Fig. 3.1: XRD Diffractograms of FTP, FTP-MNP and MNP .....	40
Fig. 3.2: XRD diffractograms of magnetite with different levels of manganese doping.....	41
Fig. 3.3: Thermogravimetric and differential thermal analysis curves for FTP .....	44
Fig. 3.4: Thermogravimetric and differential thermal analysis curves for MNP.....	44
Fig. 3.5: Thermogravimetric and differential thermal analysis curves for FTP-MNP .....	45
Fig. 3.6: Thermogravimetric and differential thermal analysis curves for Mn MNP .....	45
Fig. 3.7: Thermogravimetric and differential thermal analysis curves for Mn FTP-MNP .....	46
Fig. 3.8: FT-IR spectra of (a) Raw pine cone powder, (b) Fenton's treated pine cone powder (FTP) .....	47
Fig. 3.9: Infrared spectra of magnetite nanoparticles (MNP) and Fenton's treated pine-magnetite composite (FTP-MNP).....	49
Fig. 3.10: Infrared spectra of magnetite nanoparticles (MNP) and manganese doped magnetite nanoparticles (Mn MNP) .....	49
Fig. 3.11: SEM image of pine cone powder (a), iron oxide nanoparticles(b) and pine cone -iron oxide nanocomposite (c) and (d).....	52
Fig. 3.12: TEM micrographs of (a) MNP, (b) FTP-MNP and (c) Physical mixture of FTP and MNP .....	53
Fig. 3.13: Pine cone powder (PCP), Nanocomposite (NC) and Nanoparticles (NP) dispersed in water and magnetic separation of Nanocomposite (NC) and Nanoparticles (NP) .....	54
Fig. 3.14: Magnetizations curves of as-synthesized adsorbents .....	55
Fig. 3.15: XPS Survey spectrum of FTP-MNP.....	56
Fig. 3.16: Fe2p spectrum of FTP-MNP .....	57
Fig. 3.17: O1s spectrum of FTP-MNP .....	57
Fig. 3.18: C1s spectrum of FTP-MNP .....	58
Fig. 4.1: Effect of solution pH on arsenite adsorption onto prepared adsorbents.....	67
Fig. 4.2: Effect of solution pH on hexavalent chromium adsorption onto prepared adsorbents ..	68
Fig. 4.3: Formation of As(V) at different solution pH.....	69
Fig. 4.4: Formation of Cr(III) at different solution pH .....	70
Fig. 4.5: Effect of adsorbent dosage on As(III) and Cr(VI) adsorption on to FTP.....	71

Fig. 4.6: Effect of adsorbent dosage on As(III) and Cr(VI) adsorption on to MNP .....	72
Fig. 4.7: Effect of adsorbent dosage on As(III) and Cr(VI) adsorption on to FTP-MNP .....	72
Fig. 4.8: Effect of adsorbent dosage on As(III) and Cr(VI) adsorption on to Mn MNP .....	73
Fig. 4.9: Effect of adsorbent dosage on As(III) and Cr(VI) adsorption on to Mn FTP-MNP .....	73
Fig. 4.10: The effect of adsorbent dose on As(III) distribution coefficient for different adsorbents .....	75
Fig. 4.11: The effect of adsorbent dose on Cr(VI) distribution coefficient for different adsorbents .....	75
Fig. 4.12: Effect of initial solution concentration on As(III) adsorption capacity .....	77
Fig. 4.13: Effect of initial solution concentration on As(III) adsorption efficiency .....	77
Fig. 4.14: Effect of initial solution concentration on Cr(VI) adsorption capacity .....	78
Fig. 4.15: Effect of initial solution concentration on Cr(VI) adsorption efficiency .....	78
Fig. 6.1: Kinetic model fitting for As(III) adsorption onto FTP. Dose: 5g/L, pH: 8, stirring speed: 200 rpm, temperature: 298 K. ....	103
Fig. 6.2: Kinetic model fitting for As(III) adsorption onto MNP. Dose: 5g/L, pH: 8, stirring speed: 200 rpm, temperature: 298 K. ....	103
Fig. 6.3: Kinetic model fitting for As(III) adsorption onto FTP-MNP. Dose: 5g/L, pH: 8, stirring speed: 200 rpm, temperature: 298 K. ....	104
Fig. 6.4: Kinetic model fitting for As(III) adsorption onto Mn MNP. Dose: 5g/L, pH: 8, stirring speed: 200 rpm, temperature: 298 K. ....	104
Fig. 6.5: Kinetic model fitting for As(III) adsorption onto Mn FTP-MNP. Dose: 5g/L, pH: 8, stirring speed: 200 rpm, temperature: 298 K. ....	105
Fig. 6.6: Intraparticle diffusion modelling of As(III) adsorption onto FTP .....	106
Fig. 6.7: Intraparticle diffusion modelling of As(III) adsorption onto MNP .....	106
Fig. 6.8: Intraparticle diffusion modelling of As(III) adsorption onto FTP-MNP .....	107
Fig. 6.9: Intraparticle diffusion modelling of As(III) adsorption onto Mn MNP .....	107
Fig. 6.10: Intraparticle diffusion modelling of As(III) adsorption onto Mn FTP-MNP .....	108
Fig. 6.11: Kinetic model fitting for Cr(VI) adsorption onto FTP. Dose: 5g/L, pH: 2, stirring speed: 200 rpm, temperature: 298 K. ....	109
Fig. 6.12: Kinetic model fitting for Cr(VI) adsorption onto MNP. Dose: 5g/L, pH: 2, stirring speed: 200 rpm, temperature: 298 K. ....	109

Fig. 6.13: Kinetic model fitting for Cr(VI) adsorption onto FTP-MNP. Dose: 5g/L, pH: 2, stirring speed: 200 rpm, temperature: 298 K.....	110
Fig. 6.14: Kinetic model fitting for Cr(VI) adsorption onto Mn MNP. Dose: 5g/L, pH: 2, stirring speed: 200 rpm, temperature: 298 K.....	110
Fig. 6.15: Kinetic model fitting for Cr(VI) adsorption onto Mn FTP-MNP. Dose: 5g/L, pH: 2, stirring speed: 200 rpm, temperature: 298 K. ....	111
Fig. 6.16: Intraparticle diffusion modelling of Cr(VI) adsorption onto FTP.....	112
Fig. 6.17: Intraparticle diffusion modelling of Cr(VI) adsorption onto MNP.....	113
Fig. 6.18: Intraparticle diffusion modelling of Cr(VI) adsorption onto FTP-MNP.....	113
Fig. 6.19: Intraparticle diffusion modelling of Cr(VI) adsorption onto Mn MNP.....	114
Fig. 6.20: Intraparticle diffusion modelling of Cr(VI) adsorption onto Mn FTP-MNP.....	114
Fig. 7.1: Desorption efficiency using different solvents for As(III) desorption.....	122
Fig. 7.2: Desorption efficiency using different solvents for Cr(VI) desorption.....	123
Fig. 7.3: Reusability of prepared adsorbents for As(III) adsorption.....	123
Fig. 7.4: Reusability of prepared adsorbents for Cr(VI) adsorption.....	124
Fig. 7.5: Ionic strength effects on As(III) adsorption onto FTP-MNP.....	125
Fig. 7.6: As(III)/Nitrate exchange coefficient at various initial As(III) solution concentrations	126
Fig. 7.7: FTIR spectrum of FTP-MNP and Arsenic loaded FTP-MNP.....	127
Fig. 7.8: XPS survey scan of FTP-MNP and Arsenic loaded FTP-MNP (Inset: As3d peak) ...	128
Fig. 7.9: O1s spectra of FTP-MNP before and after As(III) adsorption.....	129
Fig. 7.10: O1s deconvoluted spectrum of FTP-MNP after As(III) adsorption.....	129
Fig. 7.11: Fe2p spectrum of FTP-MNP after As(III) adsorption.....	130
Fig. 7.12: As3d spectrum of As loaded FTP-MNP.....	131
Fig. 7.13: Effect of solution pH on Cr(VI) removal and change in H <sup>+</sup> concentration.....	133
Fig. 7.14: Cr(VI) and Cr(III) concentration in solution after adsorption.....	134
Fig. 7.15: Change on redox potential with solution pH.....	135
Fig. 7.16: XPS full spectra before and after Cr(VI) adsorption (Inset: Cr2p peak).....	136
Fig. 7.17: O1s spectrum of FTP-MNP before and after Cr(VI) adsorption.....	137
Fig. 7.18: Cr2p deconvoluted spectrum of FTP-MNP after Cr(VI) adsorption.....	137
Fig. 7.19: Fe2p spectra of FTP-MNP before and after Cr(VI) adsorption.....	138
Fig. 7.20: Ratio of Cr <sup>6+</sup> adsorbed to NO <sub>3</sub> released during adsorption.....	139

Fig. 7.21: Effect of competing anions on As(III) adsorption onto FTP-MNP.....	140
Fig. 7.22: Effect of competing anions on Cr(VI) adsorption onto FTP-MNP .....	141

## LIST OF ABBREVIATIONS AND SYMBOLS

---

AAS	Atomic absorption spectroscopy
As(III)	Arsenite
BET	Brunauer Emmet Teller
Cr(III)	Trivalent chromium
Cr(VI)	Hexavalent chromium
DTA	Differential thermal analysis
EDX	Electron dispersive spectroscopy
FTIR	Fourier-transform infrared spectroscopy
FTP	Fenton's treated pine cone powder
FTP-MNP	Fenton's treated pine cone-magnetite composite
ICP-OES	Inductively coupled plasma optical emission spectroscopy
Mn FTP-MNP	Manganese doped pine cone-magnetite composite
Mn MNP	Manganese doped magnetite nanoparticles
MNP	Magnetite nanoparticles
SEM	Scanning electron microscopy
TGA	Thermogravimetric analysis
UV-vis	Ultra-violet-visible spectroscopy
XPS	X-ray photoelectron spectroscopy
XRD	X-ray diffraction
$C_e$	Equilibrium concentration
$C_o$	Initial concentration



$h$	Initial sorption rate
$k_1$	Pseudo-first order rate constant
$k_2$	Pseudo-second order rate constant
$m$	Mass in grams
$q_e$	Equilibrium capacity
$q_{e,m}$	Equilibrium capacity obtained by calculating from model
$q_t$	Equilibrium capacity at time t
$r^2$	Coefficient of determination
$t^{0.5}$	square root of time in min

## RESEARCH OUTPUT

---

### Conference Contributions

**Immaculate L. A. Ouma**, Augustine E. Ofomaja, Eliazer B. Naidoo. Optimization of magnetite nanoparticle and pine cone-based nanocomposite synthesis for water treatment. *9<sup>th</sup> International conference of the Africa Materials Research Society*, Gaborone, Botswana. 11<sup>th</sup>- 14<sup>th</sup> Dec 2017.

**Immaculate L. A. Ouma**, Augustine E. Ofomaja, Eliazer B. Naidoo. Manganese doping of iron oxide magnetic nanoparticles for arsenic adsorption: A response surface methodology optimization. *International Conference on Pure and Applied Chemistry*, Flic en Flac, Mauritius. 18<sup>th</sup> -22<sup>nd</sup> July 2016.

**Immaculate L. A. Ouma**, Augustine E. Ofomaja, Eliazer B. Naidoo. Magnetic nanoparticles stabilized by lignocellulosic waste as green adsorbent for Cr(VI) removal from wastewater. *Nanomaterials for the Energy and Environment International Conference and Exhibition*, Paris, France. 1<sup>st</sup>-3<sup>rd</sup> June 2016.

**Immaculate L. A. Ouma**, Augustine E. Ofomaja, Eliazer B. Naidoo. Biosorption of Cr(VI) from waste water using pine cone powder and iron oxide-pine cone powder nanocomposite. *The 42<sup>nd</sup> National Convention of the South African Chemical Institute*, Durban, South Africa. 29<sup>th</sup> Nov – 2<sup>nd</sup> Dec 2015.

### Peer Reviewed Articles

**Immaculate L. A. Ouma**, Augustine E. Ofomaja, Eliazer B. Naidoo. Magnetic nanoparticles stabilized by lignocellulosic waste as green adsorbent for Cr(VI) removal from wastewater. *European Physical Journal: Applied Physics* (2017) 79:30401.

**Immaculate L. A. Ouma**, Eliazer B. Naidoo, Augustine E. Ofomaja. Thermodynamic, Kinetic and Spectroscopic Investigation of Arsenite Adsorption Mechanism on Pine Cone-Magnetite Composite. *Journal of Environmental Chemical Engineering* (2018) 6:5409

## ABSTRACT

---

Trivalent arsenic (As(III)) and hexavalent chromium (Cr(VI)) toxicity have necessitated a great deal of research into the remediation of contaminated water. The techniques applied including oxidation, coagulation-flocculation and ion exchange have suffered drawbacks due to the high cost of materials and equipment, complex operations and secondary pollution among others. Adsorption, however, remains a cost-effective solution in the remediation of contaminated water. The use of biosorbent materials further lowers the cost of the adsorption process and improves its eco-friendliness. These biomaterials, however, suffer some drawbacks as poor porosity, low adsorption capacities and mechanical strength thus require modifications to improve their applicability as biosorbents. In this work pine cone powder, a waste from pine trees, was used as a biosorbent for the removal of As(III) and Cr(VI) from water. The powder was pre-treated with Fenton's reagent to oxidize some of the functional groups and provide more binding sites. Iron oxide magnetic nanoparticles (magnetite) were incorporated into the pine cone matrix to form a magnetic composite with higher heavy metal affinity. The magnetite nanoparticles were also doped with manganese to improve their redox capacities and aid in the oxidation of the toxic As(III) to the less toxic As(V) and allow for improved binding. The adsorbents used in the study were therefore named as Fenton's treated pine cone powder (FTP), pine cone -magnetite composite (FTP-MNP), magnetite nanoparticles (MNP), manganese doped magnetite nanoparticles (Mn MNP) and manganese doped pine cone-magnetite composite (Mn FTP-MNP).

The prepared materials were fully characterized, and the adsorption process was optimized for both As(III) and Cr(VI) removal from aqueous solution. After modification the surface area of the particles increased in the order Mn MNP>MNP>Mn FTP-MNP>FTP-MNP>FTP. Surface and X-ray analysis confirmed the formation of magnetite by the presence of both ferric and ferrous ion states on the surface and characteristic diffraction peaks for magnetite. The adsorption data was fitted into isotherm and kinetic models and the nature of adsorption was determined from the thermodynamic and kinetic parameters. Equilibrium studies indicated that the adsorption followed Langmuir isotherm for all adsorbents and was thus monolayer in nature, further analysis indicated that chemisorption was the predominant type of adsorption with ion exchange being the predominant mechanism of adsorption. Spent adsorbents were tested for reusability and displayed excellent adsorption capacities when used for up to three times. Adsorption mechanism was

evaluated using characterization techniques and the ion-exchange mechanism inferred from thermodynamic data was confirmed spectroscopically with redox reactions aiding in the removal of the pollutants from water. The introduction of competing anions in solution, lowered the adsorption efficiency of both arsenic and chromium on the adsorbent indicating that there was competition for adsorption sites.

### 1 Introduction

#### 1.1 Background

The ever-increasing human population has led to a continuous strain on the available natural resources forcing humans to engage in industrial activities to sustain their livelihood. These activities, however, have an adverse effect on the environment and on human health. Industrial and mining activities have led to the accumulation of heavy metals in the ecosystem. These heavy metals are non-biodegradable and hence circulate in the ecosystem for long periods of time if not removed. Water is essential for the sustainability of all forms of life. The problem of water contamination due to industrial and mining activities is therefore a major concern.

Trivalent arsenic and hexavalent chromium are some of the most toxic heavy metal pollutants present in water systems. Their uses in electroplating, leather tanning, mining, paint manufacturing, glass manufacturing, metal processing and ceramics industries have led to their accumulation in water systems (Ge & Ma, 2015; Agrawal & Singh, 2016; Zhang *et al.*, 2016). Their adverse health effects including neurological disorders, infant mortality, liver damage and several carcinogenic effects have prompted investigations into their removal from water systems (Uddin & Huda, 2011; Zhou *et al.*, 2014). Several techniques have been applied in the remediation of arsenic and chromium contaminated water including ion exchange (Szlachta *et al.*, 2012; Lee *et al.*, 2017), electro-chemical precipitation (Guo *et al.*, 2017; Yang *et al.*, 2018), electrocoagulation (Wan *et al.*, 2011; Nidheesh & Singh, 2017), membrane separation (Chatterjee & De, 2017), electrodeposition (Survilienė *et al.*, 2006; Wu *et al.*, 2010) and adsorption (Chowdhury & Yanful, 2010; Cantu *et al.*, 2014; Babalola *et al.*, 2016; Han *et al.*, 2016; Rathore & Mondal, 2017; Xiong *et al.*, 2017; Rashid *et al.*, 2018). Most of these methods suffer drawbacks due to the cost of materials, instrumentation, high energy requirements and the complexity of their designs. Adsorption is favored since it is simple in design and does not require expensive equipment, it is also versatile and makes use of low cost adsorbent materials (Elangovan *et al.*, 2008).

Locally available and environmentally friendly agricultural waste materials have been used as biosorbents thereby significantly lowering the cost of the treatment process (Demirbas, 2008; Agrafioti *et al.*, 2014). They do, however, still pose the challenge of low sorption capacities,

therefore balancing the efficiency of adsorbents with their cost effectiveness, thus the impact on the environment still remains a challenge. In a bid to improve the sorption capacities of biosorbent materials, modifications have been proposed to increase their surface areas and adsorption affinity. Some of the modifications include the incorporation of nanomaterials into the biosorbent matrix to form composite materials. Nanoparticles possess high surface area to volume ratios and high affinities for heavy metal pollutants including arsenic and chromium.

## **1.2 Problem Statement**

Arsenic and chromium contamination have caused severe health effects in large populations in previous years. In order to remove the more toxic trivalent arsenic and hexavalent chromium, treatment techniques capable of both sequestration and redox reactions are required. Adsorption is an effective sequestration technique capable of removing contaminants including heavy metals from water. Application of biomaterials in adsorption, commonly referred to as biosorption, has significantly reduced the cost of adsorption processes. These materials however, suffer some drawbacks including (i) leaching of some extractives which results in the colouration and contamination of treated water (ii) poor selectivity for desired pollutants (iii) low biosorption capacities for heavy metal pollutants (iv) low mechanical strength making them unsuitable for column applications (v) inability to carry out redox reactions required for the removal of heavy metal pollutants with multiple oxidation states. Researchers have attempted different methods to overcome the challenges posed by biosorbent materials to improve their adsorption capacities including pre-treatment, cross-linking, composite formation, among others (Ebrahimian Pirbazari et al., 2014; Pholosi et al., 2013).

This research was aimed at applying locally available pine cones in the remediation of trivalent arsenic and hexavalent chromium contaminated water. In a bid to improve some of the drawbacks of biosorbents listed above, pine cone powder was pre-treated with Fenton's reagent and a composite was formed with iron oxide magnetic nanoparticles (magnetite). To further improve the redox potential of the adsorbent material, manganese doping on the magnetite nanoparticles was carried out.

### 1.3 Aim

The aim of this study was to prepare adsorbents based on pine cone powder and magnetite nanoparticles for the removal of arsenite (As(III)) and hexavalent chromium (Cr(VI)) from water.

#### 1.3.1 *Specific Objectives*

1. To prepare Fenton's treated pine cone powder (FTP), magnetite nanoparticles (MNP) and a magnetic composite consisting of Fenton's treated pine cone powder and magnetite nanoparticles (FTP-MNP) and compare their properties.
2. To carry out manganese doping on magnetite nanoparticles (Mn MNP) and nanoparticles on the composite (Mn FTP-MNP) and characterise the doped materials.
3. To determine the optimum adsorption parameters for As(III) and Cr(VI) adsorption onto the prepared materials.
4. To carry out thermodynamic and kinetic studies of As(III) and Cr(VI) adsorption onto the prepared materials in order to determine the nature of adsorption.
5. To investigate the reusability of the prepared adsorbents and determine the adsorption mechanism of As(III) and Cr(VI) onto FTP-MNP as a model adsorbent.
6. To determine the effects of competing anions on the adsorption of As(III) and Cr(VI) onto FTP-MNP as a model adsorbent.

## **1.4 Thesis Layout**

This thesis is divided into eight chapters with two introductory chapters followed by five chapters each including a brief introduction, methodology, results and discussions and a conclusion covering specific sets of results. The last chapter contains overall conclusions and recommendations for future work.

### **Chapter 1**

This chapter includes a general introduction into the study, the problem statement, aim and objectives of the research. It also gives a general insight into the thesis.

### **Chapter 2**

This chapter covers the review of relevant literature that served as a guide into the research.

### **Chapter 3**

The preparation procedures for all the adsorbents used in the study are discussed in this chapter with the characterization results presented and discussed.

### **Chapter 4**

This chapter discusses the optimization of the adsorption process for As(III) and Cr(VI) adsorption onto the prepared adsorbents. It presents an introduction into factors affecting adsorption, the optimization process following one factor at a time (OFAT) methodology, and finally all the results for the optimization process are discussed.

### **Chapter 5**

In this chapter the effect of temperature on the adsorption process are investigated. Adsorption data is fitted into isotherm models and the thermodynamic parameters of the adsorption processes are calculated and presented and an inference is made into the mechanism of adsorption from the presented results.

### **Chapter 6**

In this chapter the effect of time on the adsorption process is discussed. Data is fitted into kinetic models and model parameters for As(III) and Cr(VI) are tabulated. All the results are presented and discussed followed by a brief conclusion.



## **Chapter 7**

This chapter is divided into two parts. In part one: desorption studies and reusability of the spent adsorbents are presented. In part two the adsorption mechanistic studies of As(III) and Cr(VI) are presented with relevant results presented and discussed.

## **Chapter 8**

The final chapter presents the overall conclusions of the study and presents recommendations for future work based on the research findings.

## 1.5 References

- AGRAFIOTI, E., KALDERIS, D., & DIAMADOPOULOS, E. (2014). Arsenic and chromium removal from water using biochars derived from rice husk, organic solid wastes and sewage sludge. *J. Environ. Manage.* 133. p.309–314.
- AGRAWAL, S., & SINGH, N.B. (2016). Removal of arsenic from aqueous solution by an adsorbent nickel ferrite-polyaniline nanocomposite. *Indian J. Chem. Technol.* 23. p.374–383.
- BABALOLA, J.O., BAMIDELE, T.M., ADENIJI, E.A., ODOZI, N.W., OLATUNDE, A.M., & OMOROGIE, M.O. (2016). Adsorptive modelling of toxic cations and ionic dyes onto cellulosic extract. *Model. Earth Syst. Environ.* 2. p.190.
- CANTU, Y., REMES, A., REYNA, A., MARTINEZ, D., VILLARREAL, J., RAMOS, H., TREVINO, S., TAMEZ, C., MARTINEZ, A., EUBANKS, T., & PARSONS, J.G. (2014). Thermodynamics, kinetics, and activation energy studies of the sorption of chromium(III) and chromium(VI) to a Mn<sub>3</sub>O<sub>4</sub> nanomaterial. *Chem. Eng. J.* 254. p.374–383.
- CHATTERJEE, S., & DE, S. (2017). Adsorptive removal of arsenic from groundwater using chemically treated iron ore slime incorporated mixed matrix hollow fiber membrane. *Sep. Purif. Technol.* 179. p.357–368.
- CHOWDHURY, S.R., & YANFUL, E.K. (2010). Arsenic and chromium removal by mixed magnetite-maghemite nanoparticles and the effect of phosphate on removal. *J. Environ. Manage.* 91. p.2238–47.
- DEMIRBAS, A. (2008). Heavy metal adsorption onto agro-based waste materials: a review. *J. Hazard. Mater.* 157. p.220–9.
- EBRAHIMIAN PIRBAZARI, A., SABERIKHAH, E., & HABIBZADEH KOZANI, S.S.S. (2014). Fe<sub>3</sub>O<sub>4</sub>-wheat straw: Preparation, characterization and its application for methylene blue adsorption. *Water Resour. Ind.* 7–8. p.23–37.
- ELANGO VAN, R., PHILIP, L., & CHANDRARAJ, K. (2008). Biosorption of hexavalent and trivalent chromium by palm flower (*Borassus aethiopum*). *Chem. Eng. J.* 141. p.99–111.
- GE, H., & MA, Z. (2015). Microwave preparation of triethylenetetramine modified graphene oxide/chitosan composite for adsorption of Cr(VI). *Carbohydr. Polym.* 131. p.280–287.

GUO, Z., YANG, M., & HUANG, X.-J. (2017). Recent developments in electrochemical determination of arsenic. *Curr. Opin. Electrochem.* 3. p.130–136.

HAN, Y., CAO, X., OUYANG, X., SOHI, S.P., & CHEN, J. (2016). Adsorption kinetics of magnetic biochar derived from peanut hull on removal of Cr (VI) from aqueous solution: Effects of production conditions and particle size. *Chemosphere*. 145. p.336–341.

LEE, C., ALVAREZ, P.J.J., NAM, A., PARK, S., DO, T., CHOI, U., & LEE, S. (2017). Arsenic ( V ) removal using an amine-doped acrylic ion exchange fiber : Kinetic , equilibrium , and regeneration studies. *J. Hazard. Mater.* 325. p.223–229.

NIDHEESH, P. V., & SINGH, T.S.A. (2017). Arsenic removal by electrocoagulation process: Recent trends and removal mechanism. *Chemosphere*. 181. p.418–432.

PHOLOSİ, A., OFOMAJA, A.E., & NAIDOO, E.B. (2013). Effect of chemical extractants on the biosorptive properties of pine cone powder: Influence on lead(II) removal mechanism. *J. Saudi Chem. Soc.* 17. p.77–86.

RASHID, M., STERBINSKY, G.E., PINILLA, M.Á.G., CAI, Y., & O'SHEA, K.E. (2018). Kinetic and Mechanistic Evaluation of Inorganic Arsenic Species Adsorption onto Humic Acid Grafted Magnetite Nanoparticles. *J. Phys. Chem. C*. 122. p.13540–13547.

RATHORE, V.K., & MONDAL, P. (2017). Competitive Adsorption of Arsenic and Fluoride onto Economically Prepared Aluminum Oxide/Hydroxide Nanoparticles: Multicomponent Isotherms and Spent Adsorbent Management. *Ind. Eng. Chem. Res.* 56. p.8081–8094.

SURVILIENĖ, S., NIVINSKIENĖ, O., ČEŠUNIENĖ, A., & SELSKIS, A. (2006). Effect of Cr(III) solution chemistry on electrodeposition of chromium. *J. Appl. Electrochem.* 36. p.649–654.

SZLACHTA, M., GERDA, V., & CHUBAR, N. (2012). Adsorption of arsenite and selenite using an inorganic ion exchanger based on Fe-Mn hydrous oxide. *J. Colloid Interface Sci.* 365. p.213–221.

UDDIN, R., & HUDA, N.H. (2011). Arsenic poisoning in Bangladesh. *Oman Med. J.* 26. p.207.

WAN, W., PEPPING, T.J., BANERJI, T., CHAUDHARI, S., & GIAMMAR, D.E. (2011). Effects of water chemistry on arsenic removal from drinking water by electrocoagulation. *Water Res.* 45.

p.384–392.

WU, M.-S., GUO, Z.-S., & JOW, J.-J. (2010). Highly Regulated Electrodeposition of Needle-Like Manganese Oxide Nanofibers on Carbon Fiber Fabric for Electrochemical Capacitors. *J. Phys. Chem. C*. 114. p.21861–21867.

XIONG, Y., TONG, Q., SHAN, W., XING, Z., WANG, Y., WEN, S., & LOU, Z. (2017). Arsenic transformation and adsorption by iron hydroxide/manganese dioxide doped straw activated carbon. *Appl. Surf. Sci.* 416. p.618–627.

YANG, M., LI, P.H., XU, W.H., WEI, Y., LI, L.N., HUANG, Y.Y., SUN, Y.F., CHEN, X., LIU, J.H., & HUANG, X.J. (2018). Reliable electrochemical sensing arsenic(III) in nearly groundwater pH based on efficient adsorption and excellent electrocatalytic ability of AuNPs/CeO<sub>2</sub>-ZrO<sub>2</sub>nanocomposite. *Sensors Actuators, B Chem.* 255. p.226–234.

ZHANG, L., LUO, H., LIU, P., FANG, W., & GENG, J. (2016). A novel modified graphene oxide/chitosan composite used as an adsorbent for Cr(VI) in aqueous solutions. *Int. J. Biol. Macromol.* 87. p.586–596.

ZHOU, S., LI, Y., CHEN, J., LIU, Z., WANG, Z., & NA, P. (2014). Enhanced Cr(VI) removal from aqueous solutions using Ni/Fe bimetallic nanoparticles: characterization, kinetics and mechanism. *RSC Adv.* 4. p.50699–50707.

## 2 Literature Review

### 2.1 Water Pollution

Clean water is essential in order to sustain all forms of life yet less than 0.3 % of the water on the earth's surface is available as fresh water out of over 70 % water cover (Abdulgader *et al.*, 2013). Although water abundant countries have been estimated to have more than 20,000 liters of water per person per year the world still faces an acute clean water shortage due to contamination of water sources caused by the accumulation of heavy metals and other contaminants (Thompson, 2012; Lytle *et al.*, 2014).

#### 2.1.1 Heavy Metal Pollution

Among the pollutants found in water, heavy metals are of particular concern because they are non-biodegradable and hence lead to accumulation in the environment (Agrafioti *et al.*, 2014; Obike *et al.*, 2018). Table 2.1 lists the common sources of heavy metal pollutants found in wastewater and their associated health risks. Even at low concentrations these metals may interfere with normal biological processes hence becoming toxic and resulting in either heavy metal poisoning or genetic disorders (Inoue, 2011). The removal of these metal species from water is therefore critical to the general availability of clean water for human and animal consumption. This study focuses on the remediation of arsenic and chromium contaminated water due to their toxicity and adverse health effects even at low concentrations.

Table 2.1: Common sources of heavy metals and the associated health risks.

<b>Metal</b>	<b>Sources</b>	<b>Health risks</b>	<b>Ref</b>
Arsenic	Glass industry, pesticide manufacturing, wood preservatives and semiconductor production.	Cardiovascular diseases, neurological disorders, infant mortality, cancers of the skin, lungs, liver and kidney.	(Agrafioti <i>et al.</i> , 2014; Ouma <i>et al.</i> , 2018)
Chromium	Chrome plating, electroplating, leather tanning, photography, metal cleaning, oxidative dying and steel production.	Oxidative stress, DNA damage, skin cancer.	(Vilar <i>et al.</i> , 2012; Agrafioti <i>et al.</i> , 2014; Shraim, 2017)
Nickel	Electroplating, batteries, porcelain enamelling, pigments, steel manufacturing.	Cancer of the lungs, nose and bones, cyanosis, nausea, rapid respiration.	(Panneerselvam <i>et al.</i> , 2011)
Lead	Lead-acid batteries, bullets, solder, pewter and alloys.	Kidney damage, memory disorders, mental disorders.	(Cheng & Hu, 2010; Shraim, 2017)
Copper	Metal cleaning, copper plating, wood pulp production, fertilizer industry and paper board mills.	Necrotic changes in liver and kidneys, severe mucosal and central nervous system irritation.	(Larous <i>et al.</i> , 2005; Ofomaja <i>et al.</i> , 2010b)
Cadmium	Electroplating, smelting, alloy manufacturing, refining processes, pigments, plastics, phosphate industry and battery mining.	Hypertension, anaemia, hypertension, emphysema and renal damage.	(Ho & Ofomaja, 2006; Igberase & Osifo, 2015)
Mercury	Oil refinery, battery production, pharmaceuticals, paint production, mining industry, paper and pulp.	Muscle weakness, neuronal disorders, ataxia, numbness and damage to the cardiovascular system.	(Say <i>et al.</i> , 2008; Pan <i>et al.</i> , 2012)

### 2.1.2 Arsenic

Arsenic is abundant in the earth ranking as the 20<sup>th</sup> most abundant element in the earth's crust, 14<sup>th</sup> and 12<sup>th</sup> in sea water and the human body respectively (Mandal & Suzuki, 2002). It was first isolated in 1250 AD and has since been used in various fields including medicine, agriculture, livestock and electronics among others (Sharma & Sohn, 2009). Arsenic enters the ecosystem following weathering of rocks which converts arsenic sulphides to arsenic trioxide which is in turn released as dust or dissolves in rain, rivers or ground water (Mandal & Suzuki, 2002). It exists in inorganic and organic forms both of which can be found in water. Inorganic arsenic is however more toxic compared to the organic form. It occurs naturally in over 200 different mineral forms, with approximately 60% arsenates, 20% sulfides and sulfosalts and 20% arsenides, arsenites, oxides, silicates and elemental arsenic (Mandal & Suzuki, 2002) and exists in four oxidation states namely,  $\text{As}^{5+}$  (arsenate),  $\text{As}^{3+}$  (arsenite),  $\text{As}^0$  (arsenic), and  $\text{As}^{3-}$  (arsine) (Shafique *et al.*, 2012). Of these states arsenate and arsenite are the predominant forms of arsenic in water with arsenite being more toxic, more soluble and more mobile than arsenate (Mandal & Suzuki, 2002; Katsoyiannis *et al.*, 2004).

Arsenic is highly toxic and carcinogenic even at low quantities therefore its presence in water is of great concern. Arsenic contamination of ground water in Bangladesh resulted in nearly eighty million people being poisoned and a ten percent probability of developing cancer in the affected population (Singh *et al.*, 2015). Cardiovascular diseases, neurological disorders, infant mortality and cancers of the skin, lungs, liver and kidney have all been linked to arsenic poisoning from drinking contaminated water (Mandal & Suzuki, 2002; Choong *et al.*, 2007; Uddin & Huda, 2011). The maximum contaminant level (MCL) of arsenic in drinking water was revised from  $50 \mu\text{g L}^{-1}$  to  $10 \mu\text{g L}^{-1}$  in 1998 by the European Commission (EC) this standard has since been adopted by the United States Environmental Protection Agency (USEPA) and the World Health Organization (WHO) (Lunge *et al.*, 2014). This has therefore prompted an urgent need for water treatment strategies to reduce arsenic concentration in water.

### 2.1.3 Chromium

Chromium was discovered in 1797 and ranks as the 21<sup>st</sup> most abundant element in the earth and 6<sup>th</sup> most abundant transition metal. The principal ore for chromium is ferric chromite,  $\text{FeCr}_2\text{O}_4$ , with 96 % of the world's reserves in South Africa (Mohan & Pittman, 2006). It has several uses

including metal plating, leather processing, surface treatments and in refractories (Cheung & Gu, 2007; Yuan *et al.*, 2010). Chromium is a highly soluble metal pollutant with strong oxidizing properties which can cause irritation in plant and animal tissues (Das & Mishra, 2008; López-Yuan *et al.*, 2010; Téllez *et al.*, 2011). It exists in six oxidation states with Cr(III) and Cr(VI) being the most prevalent in water (Miretzky & Cirelli, 2010). Trivalent chromium is an essential nutrient while the hexavalent form is toxic, carcinogenic, teratogenic and mutagenic to living organisms (Garg *et al.*, 2007; Das & Mishra, 2008). The maximum levels permitted for chromium in water are 5 mg L<sup>-1</sup> and 0.05 mg L<sup>-1</sup> for trivalent and hexavalent chromium respectively (Garg *et al.*, 2007; Miretzky & Cirelli, 2010).

## **2.2 Remediation of Heavy Metal Contaminated Water**

The removal of heavy metals from contaminated water has been investigated over the years with different methods being reported for water treatment. All these methods are aimed at reducing the level of pollutants to produce water suitable for human consumption or agricultural use. Some of the methods for remediation of arsenic and chromium contaminated water include oxidation, coagulation-flocculation, ion exchange, membrane separation and adsorption among others (Baskan & Pala, 2011; Mondal *et al.*, 2013).

### **2.2.1 Oxidation**

In oxidation processes, the toxic As(III) ions are oxidized to the less toxic As(V) form and later precipitated from solution (Ding *et al.*, 2015; Bora *et al.*, 2016; Ociński *et al.*, 2016). This process faces challenges due to the toxic by-products formed from the oxidizing agents including ozone which may be difficult to remove from the treated water (Kim & Nriagu, 2000).

### **2.2.2 Coagulation-flocculation**

Coagulation processes involve the introduction of a chemical coagulant causing colloids to flocculate followed by the precipitation of ions on the flocculated mater. Iron based coagulants have been reported to be more favorable over aluminum based coagulants due to their stability over a wide pH range (Hering *et al.*, 1997). The challenge with this method however is that it produces contaminated sludge which may be difficult to manage resulting in environmental pollution (Mondal *et al.*, 2013).



### **2.2.3 Ion Exchange**

Ion exchange involves transferring or exchanging ions with the same charge between a medium and an electrolyte solution (Abdulgader *et al.*, 2013). This technique involves the stoichiometric exchange of weak electrostatically attracted ions on the resin with ions in solution (Indarawis & Boyer, 2013). Ion exchange resins have functional groups which create a fixed charge. Anion exchange, cation exchange or a combined anion and cation exchange have been used for the purification of drinking water as well as water softening and in the production of ultrapure water (Abdulgader *et al.*, 2013; Indarawis & Boyer, 2013). Ion exchange however has several limitations including the high cost of resins and lack of economically viable methods for regeneration of resins after use resulting in incineration or disposal in landfills which may have adverse effects on the environment (Ebrahimi & Roberts, 2013).

### **2.2.4 Adsorption**

Adsorption is the binding or enrichment of molecules, atoms or ions in the vicinity of an interface usually a solid surface. It is a convenient technique for heavy metal removal as compared to the above-mentioned techniques because of its low cost and simplicity (Shafique *et al.*, 2012). It can be carried out using locally available materials including waste materials therefore lowering the overall treatment cost. Crop residues, plant waste products, geological deposits and waste from industrial processes are some of the materials which have been reported as adsorbents (Yadanaparthi *et al.*, 2009). Nanosized particles have also been used due to their large surface area to volume ratios and their size tunable properties making them suitable for the adsorption of numerous pollutants. Adsorption generally proceeds through either a physical process (physisorption) or a chemical process (chemisorption).

#### **2.2.4.1 Physisorption**

Physisorption occurs when intermolecular forces are responsible for binding the pollutant to the adsorbent surface. These forces usually occur as a result of particular geometric and electronic properties of the adsorbent and adsorbate (Thommes *et al.*, 2015). It is characterised by low adsorption activation energies ( $< 20 \text{ kJ mol}^{-1}$ ) and ease of desorption hence it is a reversible process (Eigenmann *et al.*, 2006; Yang *et al.*, 2011; Monárrez-Cordero *et al.*, 2016).

#### **2.2.4.2 Chemisorption**

Chemisorption is a chemical process involving the exchange of electrons between the adsorbent surface and the adsorbate resulting in the formation of chemical bonds (Sharma *et al.*, 2016). It is mostly characterised by the enthalpy of the system being endothermic as energy is used up during the formation of new chemical bonds. It requires more energy than physisorption and is characterised by high adsorption activation energies ( $40 \text{ kJ mol}^{-1}$ -  $800 \text{ kJ mol}^{-1}$ ) (Cantu *et al.*, 2014).

Ion-exchange may also be responsible for some chemical adsorption process whereby the ions present on the adsorbent surface are replaced by ions from the adsorbate. This process is characterised by intermediate adsorption energies ( $20 \text{ kJ mol}^{-1}$ -  $40 \text{ kJ mol}^{-1}$ ) (Cantu *et al.*, 2014). Adsorption free energy (E) is another distinguishing factor for the type of adsorption and is classified as  $E < 8 \text{ kJ mol}^{-1}$  (physisorption),  $8 \text{ kJ mol}^{-1} > E < 20 \text{ kJ mol}^{-1}$  (chemical ion exchange) and  $E > 20 \text{ kJ mol}^{-1}$  (chemisorption).

### **2.3 Desorption**

Desorption refers to the reversal of the adsorption process and involves detachment of adsorbate species from an adsorbent surface. It is important for concentration and proper disposal of the adsorbate and reusability of the adsorbent (Igberase *et al.*, 2014). Desorption experiments are important in determining the type of interactions between the adsorbate and the adsorbent. Physical interactions can typically be reversed by water while ion-exchange interactions require strong acids/alkali with chemical interactions being reversed by weak acids. For a desorption experiment to be considered successful, a low volume of desorbing agent should remove the adsorbed molecules without altering the adsorption properties of the adsorbent.

### **2.4 Types of Adsorbents**

#### **2.4.1 Biosorbents**

Biosorption refers to an adsorption process using naturally occurring materials. The use of biomaterials in adsorption is preferred because they are biodegradable and do not pose a significant threat to the environment (Pholosi *et al.*, 2013). Agricultural waste materials are favourable for use as biosorbents because they are readily available and do not require expensive pre-treatment

procedures. They are stable under ambient conditions allowing adsorption to be carried out without the need for expensive equipment to provide special operating conditions.

Biosorption of heavy metals has previously been shown to occur in two phases, a fast surface reaction attributed to surface adsorption followed by a slower metal uptake into cell structures (Volesky & Holan, 1995). Materials of cellulosic nature including plant products and crop residues have been suggested as potential biosorbents for heavy metals (Volesky & Holan, 1995; Shafique *et al.*, 2012). Shafique *et al.*, (2012) reported on the use of pine leaves in the removal of arsenic from water. The application of these biosorbents in the removal of toxic metals from water however faces some limitations mainly due to the low surface area of these materials. In this study pine cones were used as biosorbents for the adsorption of arsenic and chromium from water. Pine cones are a waste product from pine trees which is a major tree species in South Africa's plantations (Le Maitre *et al.*, 2002). It has been reported that a single pine tree can produce up to 28 healthy cones per year and while the trees are grown for paper and pulp, the cones are of little economic value (Calama *et al.*, 2011). The composition of a pine cone is approximately 46.5 % hemicellulose, 37.4 % lignin, 18.8 % cellulose and 15.4 % extractives (Pholosi *et al.*, 2013). The functional groups present on pine cone powder are responsible for the sequestration of pollutants and binding nanoparticles during the formation of composites. Pine cone powder has been used for the removal of heavy metal pollutants including lead, cesium, copper and nickel (Argun *et al.*, 2005; Momčilović *et al.*, 2011; Ofomaja & Naidoo, 2011; Ofomaja *et al.*, 2010a, 2014). It has also been used for the remediation of textile waste water in the removal of dyes (Dawood & Sen, 2012; Mahmoodi *et al.*, 2011). These materials however have disadvantages due to their low porosity hence low surface area to volume ratios (Ofomaja *et al.*, 2009) and they contain soluble organic matter which may contaminate the treated water (Ofomaja *et al.*, 2009; Ofomaja & Naidoo, 2011). To curb these disadvantages, the pine cone powder is subjected to pre-treatment procedures which improve its porosity and removes the soluble organic contaminants it contains before it is applied in adsorption studies (Argun *et al.*, 2005, 2008; Pholosi *et al.*, 2013). To improve porosity, dissolve resin acids and other extractives which may be detrimental to the water treatment process, pre-treatment of the pine cone powder is often carried out.

### 2.4.2 Nanosized Adsorbents

Nanotechnology has been used over the past decades to improve the quality of human livelihood in various aspects. Nanotechnology also provides great benefits in the remediation of contaminated water. In adsorption applications, surface area is a major factor that influences the efficiency of the adsorption process. Nanoparticles offer great solutions to the challenge of low surface area to volume ratios that are posed by organic materials especially those of a lignocellulosic nature. They possess very large surface areas to volume ratios and high activities as a result of size quantization effects (Hua *et al.*, 2012). They have been shown to be favorable for the removal of heavy metals due to their high capacity and selectivity, allowing them to considerably lower heavy metal concentrations (Liu *et al.*, 2008; Hua *et al.*, 2012). The nanomaterials commonly applied in adsorption include carbon nanotubes, manganese oxides, titanium oxide and ferric oxides (Anjum *et al.*, 2016).

Iron containing nanoparticles have been used preferentially because they are considered non-toxic and would not result in secondary environmental contamination (Hua *et al.*, 2012). Iron nanoparticles have in the past two decades been applied in water remediation (Yan *et al.*, 2013) with nano zero valent iron being the mostly studied among the iron based nanoparticles (Zuhairi *et al.*, 2012; Khatoon *et al.*, 2013; Yan *et al.*, 2013). Nano sized oxides have also been applied for the removal of different pollutants. These oxides differ in their composition mainly by the iron species present in them. The most common iron oxides also present in nature are magnetite ( $\text{Fe}_3\text{O}_4$ ), maghemite ( $\gamma\text{-Fe}_2\text{O}_3$ ) and hematite ( $\alpha\text{-Fe}_2\text{O}_3$ ), and they have been applied in the removal of heavy metals from water (Teja & Koh, 2009; Mahdavian & Mirrahimi, 2010; Monárrez-Cordero *et al.*, 2014; Kumari *et al.*, 2015). Nanomaterials are not favorable in water treatment strategies because of the difficulty in recovery after the treatment process. Magnetic iron oxides are favorable in this regard since they are ferromagnetic with size-dependent magnetic susceptibilities allowing them to become super paramagnetic making them easy to separate from water by applying a magnetic field (Lai *et al.*, 2004; Mahdavian & Mirrahimi, 2010).

Superparamagnetic iron oxides are therefore preferentially applied mainly because of the ease of separation by use of an external magnetic field (Wang *et al.*, 2014). These nanoparticles do not possess residual magnetization and are easily magnetized upon the application of an external magnetic field and demagnetized on its removal. They are however not stable due to high surface

energies and are prone to agglomeration (Teja & Koh, 2009; Zhang & Gao, 2013; Peng *et al.*, 2014). Adsorption on pristine iron oxide nanoparticles however offers little success owing to agglomeration which lowers the effective surface areas (Luther *et al.*, 2012). Composite formation has been proposed to improve the adsorptive properties of both biosorbents and nanoparticles (Pan *et al.*, 2009).

#### **2.4.2.1 Nanoparticle Doping**

Doping is the process of intentional insertion of impurity atoms into a material, it is usually aimed at improving the properties of the original material while simultaneously retaining its original characteristics which are beneficial for the intended application. To improve the affinity of iron oxide nanoparticles for heavy metal adsorption, doping with other elements is sometimes carried out. For the doping to be efficient, the dopant should be incorporated in the unit cell of the material. Doping of iron oxide nanoparticles helps to improve their adsorptive and redox capabilities which are desirable in the treatment of wastewater.

Manganese is one of the most common elements applied in the doping of iron containing materials due to their similarities in atomic sizes and binding characteristics with iron atoms. It also has a high affinity for metal cations which are the major pollutants of water from industrial activity and leaching from minerals. Manganese has good redox capabilities allowing for efficiency in surface redox reactions which take place during the adsorption of heavy metal species with multiple oxidation states. Manganese dioxide has been reported to be a promising oxidizing agent since it not only oxidizes the toxic As(III) to the less toxic As(V) but also adsorbs the formed As(V) ions. When iron is present with manganese dioxide it enhances the separation process by oxidation followed by adsorption (Lai *et al.*, 2004; Mondal *et al.*, 2013). Manganese doping is regulated to ensure the nanoparticles retain their magnetism since an increase in manganese concentration to more than 10 % results in the nanoparticles becoming non-ferrimagnetic (Pool *et al.*, 2010).

#### **2.4.3 Composite Adsorbents**

To further improve the surface area for adsorption, nanomaterials can be incorporated into biomass materials to form composite materials. These composites would therefore have the advantages of both the nanoparticles and the biosorbent. The nanoparticles improve the surface area of the material with functional groups of the biomass stabilizing the nanomaterials. The combination of biosorption and nanotechnology provides a unique platform for the removal of pollutants from

wastewater (Ebrahimian Pirbazari *et al.*, 2014). The bulk organic material acts as a support for the nanoparticles aiding in their separation from water after treatment by simple filtration and allowing for the regeneration of the adsorbent.

## **2.5 Factors Affecting Adsorption**

### **2.5.1 Solution pH**

Solution pH is an important parameter affecting adsorption especially in ionic based systems since adsorption efficiency is highly dependent on solution pH (Pan *et al.*, 2012). Metal oxidation states as well as adsorbent surface functional group ionization are pH dependent and therefore affect the adsorption of heavy metals. Surface groups are either protonated or deprotonated depending on the solution pH (Agrawal & Singh, 2016).

### **2.5.2 Adsorbent Mass**

The mass of adsorbent used plays an important role in affecting the amount of pollutant ion taken up. As more adsorbent active sites are supplied, the overall surface area increases thereby increasing the adsorption efficiency (Adeli *et al.*, 2012).

### **2.5.3 Adsorbate Concentration**

Increasing the adsorbate concentration generally increases the competition for available adsorption sites. This increases the concentration gradient between the adsorbent surface and the adsorbate solution resulting in increased adsorption capacities (Ucun *et al.*, 2002; Dawood & Sen, 2012).

## **2.6 Adsorption Modelling**

Adsorption data is modelled to determine the optimum parameters for adsorption and determine the nature of binding between the adsorbent and the adsorbate.

### **2.6.1 Thermodynamic Modelling**

Thermodynamic modelling of adsorption data provides information about the type and mechanism of adsorption (Milonjić, 2007). To calculate adsorption parameters, isotherm models are applied and used to evaluate the adsorption data. The most common isotherms are the Langmuir and Freundlich which indicate whether the adsorption is monolayer or multilayer in nature and can be used to calculate the maximum adsorption capacity of the adsorbent. Redlich-Peterson and Sips isotherms are three parameter models which are more versatile and are often used to confirm

homogeneity or heterogeneity of the adsorption system. Dubinin-Raduschkevich and Flory-Huggins models are used to determine the mean adsorption energy, change in Gibbs free energy, enthalpy and entropy of the system which provide information on the adsorption mechanism.

#### 2.6.1.1 Langmuir

Langmuir isotherm model assumes monolayer coverage over homogenous adsorbent sites. The non-linear expression is given by Equation 2.1 where  $C_e$  (mg L<sup>-1</sup>) is the solution concentration at equilibrium,  $q_e$  (mg g<sup>-1</sup>) is the adsorption capacity at equilibrium,  $q_m$  (mg g<sup>-1</sup>) and  $K_L$  (L mg<sup>-1</sup>) are the Langmuir constants representing monolayer capacity and equilibrium constant respectively (Almasri *et al.*, 2018).

$$q_e = \frac{q_m K_L C_e}{1 + K_L C_e} \quad (2.1)$$

#### 2.6.1.2 Freundlich

Freundlich isotherm model is based on a reversible adsorption process on a heterogeneous surface not restricted to monolayer coverage and assumes increasing adsorption with an increase in solution concentration. It is given by Equation 2.2 where  $q_e$  (mg g<sup>-1</sup>) is the equilibrium adsorption capacity,  $C_e$  (mg L<sup>-1</sup>) the concentration of solution at equilibrium,  $K_F$  and  $n$  (L g<sup>-1</sup>) are constants related to adsorption capacity and intensity respectively (Pan *et al.*, 2012; Almasri *et al.*, 2018).

$$q_e = K_F C_e^{1/n} \quad (2.2)$$

#### 2.6.1.3 Redlich-Peterson

Redlich-Peterson (R-P) isotherm model incorporates three parameters into an empirical equation. This model is versatile and can be applied to either homogenous or heterogeneous systems. It has a high concentration dependence with a linear relation in the numerator and exponential dependence in the denominator. It is described by Equation 2.3 where  $K_R$  (L mg<sup>-1</sup>) is a constant related to adsorption capacity,  $\alpha_R$  (L mg<sup>-1</sup>) is a constant related to binding site affinity and  $\beta$  is an exponent related to the adsorption intensity (Lee *et al.*, 2017; Kupeta *et al.*, 2018). When the exponent  $\beta = 1$  the equation reduces to Langmuir isotherm and it approaches Freundlich equation at high concentrations (Gautam *et al.*, 2014; Hadi *et al.*, 2014; Kupeta *et al.*, 2018).

$$q_e = \frac{K_R C_e}{1 + \alpha_R C_e^\beta} \quad (2.3)$$

#### 2.6.1.4 Sips

The Sips isotherm sometimes referred to as Langmuir-Freundlich isotherm, is derived from both isotherm models (Rostamian & Behnejad, 2016). The heterogeneity factor in this model is used to distinguish between the two isotherm models. Heterogeneity values close to 1 indicate a homogenous system while lower values indicate a heterogenous system. Sips isotherm is described by Equation 2.4 where  $q_e$  (mg g<sup>-1</sup>),  $q_{\max}$  (mg g<sup>-1</sup>) and  $C_e$  (mg L<sup>-1</sup>) are the adsorption capacity at equilibrium, maximum adsorption capacity and solution concentration at equilibrium respectively.  $K_s$  (L mg<sup>-1</sup>) is the Sips isotherm constant related to the affinity of binding sites and  $1/n$  is the heterogeneity index (Pérez Marín *et al.*, 2009; Albadarin *et al.*, 2013; Cao *et al.*, 2014; Ebrahimian Pirbazari *et al.*, 2014; Pakade *et al.*, 2017).

$$q_e = \frac{q_{\max} K_s C_e^{1/n}}{1 + K_s C_e^{1/n}} \quad (2.4)$$

#### 2.6.1.5 Dubinin-Radushkevich

Fitting experimental data using the Dubinin-Radushkevich (D-R) model allows for the calculation of the mean adsorption energy (eq 2.7) from which the determination of either physical or chemical adsorption can be made (Argun *et al.*, 2007). The linear relation is given by Equation 2.5 where  $q_e$  (mg g<sup>-1</sup>) is the adsorption capacity at equilibrium,  $q_m$  (mg g<sup>-1</sup>) is the maximum adsorption capacity,  $\beta$  (mol<sup>2</sup> kJ<sup>-2</sup>) is a constant related to adsorption energy and  $\varepsilon$  (eq 2.6) is the Polanyi potential of the surface (Igberase *et al.*, 2017).  $R$  is the gas constant (8.314 J K<sup>-1</sup> Mol<sup>-1</sup>) and  $T$  (K) is the absolute temperature of the system (Almasri *et al.*, 2018).

$$\ln q_e = \ln q_m - \beta \varepsilon^2 \quad (2.5)$$

$$\varepsilon = RT \ln \left( 1 + \frac{1}{C_e} \right) \quad (2.6)$$

$$E = \frac{1}{\sqrt{2\beta}} \quad (2.7)$$



### 2.6.1.6 Flory-Huggins

The Flory-Huggins model was used to calculate the parameters necessary for the thermodynamic evaluation of the adsorption process. The model is described by Equation 2.8 where  $\theta$  is the degree of surface coverage (eq 2.9),  $C_0$  (mg L<sup>-1</sup>) and  $C_e$  (mg L<sup>-1</sup>) are the initial and equilibrium solution concentrations respectively,  $K_{FH}$  (L g<sup>-1</sup>) is the model equilibrium constant and  $n_{FH}$  is the model exponent representing the number of ions occupying adsorption sites (Nechifor *et al.*, 2015). The change in Gibbs free energy ( $\Delta G$  (kJ mol<sup>-1</sup>)) can be determined using the F-H equilibrium constant ( $K_{FH}$  (L g<sup>-1</sup>)) (eq 2.10) where  $R$  is the gas constant (8.314 Jmol<sup>-1</sup>K<sup>-1</sup>) and  $T$  (K) is the absolute temperature and can in turn be applied in the calculation of the change in enthalpy ( $\Delta H$  (kJ mol<sup>-1</sup>)) and change in entropy ( $\Delta S$  (Jmol<sup>-1</sup>K<sup>-1</sup>)) (eq 2.11)).

$$\log \frac{\theta}{C_0} = \log K_{FH} + n_{FH} \log(1 - \theta) \quad (2.8)$$

$$\theta = (1 - \frac{C_e}{C_0}) \quad (2.9)$$

$$\Delta G = RT \ln K_{FH} \quad (2.10)$$

$$\Delta G = \Delta H - T\Delta S \quad (2.11)$$

### 2.6.2 Kinetic Modelling

Adsorption kinetics studies are used to show the relationship between the amount of pollutant adsorbed and the duration or time of adsorption. Kinetics studies are generally described by the following stages: (i) External diffusion; defined by diffusion of molecules from the bulk phase to the interface, (ii) Internal diffusion; Diffusion of molecules inside pores, (iii) Surface diffusion; diffusion of molecules on the surface, (iv) Desorption process (Can, 2015). These stages are important in the determination of the rate limiting step in the adsorption process thereby increasing the understanding of the adsorption mechanism. Kinetics studies also aid in the determination of physical or chemical adsorption allowing for the comparison of different adsorbents used in adsorption of similar pollutants (Agrawal & Singh, 2016). To understand adsorption kinetics

models such as pseudo-first order, pseudo-second order, Elovich and intra-particle diffusion are used to fit the data and the model parameters are then used to evaluate the adsorption process.

### **2.6.2.1 Pseudo-First Order Model**

This rate equation describes the kinetics of adsorption preceded by diffusion through a boundary layer (Ofomaja, 2010). It assumes that the adsorption rate depends only on the adsorbate concentration (Gylienè *et al.*, 2014). It is given by Equation 2.12 where  $q_t$  (mg g<sup>-1</sup>) is the adsorption capacity at time  $t$  (min),  $q_e$  (mg g<sup>-1</sup>) is the equilibrium adsorption capacity and  $k_1$  (min<sup>-1</sup>) is the pseudo-first order rate constant.

$$q_t = q_e(1 - e^{-k_1 t}) \quad (2.12)$$

### **2.6.2.2 Pseudo-Second Order Model**

The pseudo-second order relation assumes that (i) the rate of reaction is proportional to the number of active sites on the adsorbent surface, (ii) the adsorption process occurs in two steps where the first is a fast reaction equilibrating quickly followed by a slow step, (iii) the rate limiting step is a chemical process involving the sharing or exchange of electrons between the adsorbate and the adsorbent surface (Albadarin *et al.*, 2011; Agrafioti *et al.*, 2014;). Pseudo-second order kinetics is described by Equation 2.13 where  $q_t$ ,  $t$  and  $q_e$  are as described above,  $k_2$  (g mg<sup>-1</sup> min<sup>-1</sup>) is the pseudo-second order rate constant and  $h$  (mg g<sup>-1</sup> min<sup>-1</sup>) is the initial sorption rate (eq. 2.14). A higher initial sorption rate, indicates a higher affinity of the adsorbent for the adsorbate (Cheng *et al.*, 2016).

$$q_t = \frac{k_2 q_e^2 t}{1 + k_2 q_e t} \quad (2.13)$$

$$h = k_2 q_e^2 \quad (2.14)$$

### **2.6.2.3 Elovich Model**

The Elovich model describes variation in chemical adsorption and is based on the assumption that the adsorbent surface consists of heterogeneous energies and there are no interactions between adsorbed molecules (Han *et al.*, 2016; Chaudhry *et al.*, 2017;). The relation is given by Equation 2.15 where  $\alpha$  (mg g<sup>-1</sup> min<sup>-1</sup>) is the initial rate of chemisorption and  $\beta$  (g mg<sup>-1</sup>) is the desorption constant (Namasivayam & Sureshkumar, 2008). Activation energy for chemisorption and the

extent of surface coverage are also related to the constant  $\beta$ . A higher value for  $\alpha$  than  $\beta$  is desirable as it indicates viability of the adsorption process.

$$q_t = \frac{1}{\beta} \ln(1 + \alpha\beta t) \quad (2.15)$$

#### **2.6.2.4 Intraparticle Diffusion**

According to the intraparticle diffusion relation, a plot of adsorption capacity versus the square root of time yields a straight line if it controls the adsorption process. However, intraparticle diffusion is the only rate limiting step if the line passes through the origin (Sutherland & Venkobachar, 2010; Aryal & Liakopoulou-Kyriakides, 2011;). A high correlation coefficient for the intraparticle diffusion model implies that adsorption occurs in the pores of the adsorbent (Aryal & Liakopoulou-Kyriakides, 2011). The model is described by Equation 2.16 where  $k_{id}$  ( $\text{mg g}^{-1} \text{min}^{-0.5}$ ) is the intraparticle diffusion rate constant and  $C$  is the intercept reflecting the thickness of the boundary layer.

$$q_t = k_{id} t^{0.5} + C \quad (2.16)$$

## **2.7 Conclusion**

Water pollution is a serious concern and as such treatment methods are continuously being investigated to improve the quality of the available water. Adsorption as a technique has attracted a lot of interest due to its simplicity and cost effectiveness, especially on the account that it makes use of locally available materials for the remediation of contaminated water. The types of adsorbents used in this study have been discussed, including the factors affecting adsorption and modelling equations used to evaluate the efficiency and provide some insight into the adsorption process.

## 2.8 References

- ABDULGADER, H. AL, KOCHKODAN, V., & HILAL, N. (2013). Hybrid ion exchange – Pressure driven membrane processes in water treatment: A review. *Sep. Purif. Technol.* 116. p.253–264.
- ADELI, M., YAMINI, Y., & FARAJI, M. (2012). Removal of copper, nickel and zinc by sodium dodecyl sulphate coated magnetite nanoparticles from water and wastewater samples. *Arab. J. Chem.* 10. p.S514–S521.
- AGRAFIOTI, E., KALDERIS, D., & DIAMADOPOULOS, E. (2014). Arsenic and chromium removal from water using biochars derived from rice husk, organic solid wastes and sewage sludge. *J. Environ. Manage.* 133. p.309–314.
- AGRAWAL, S., & SINGH, N.B. (2016). Removal of arsenic from aqueous solution by an adsorbent nickel ferrite-polyaniline nanocomposite. *Indian J. Chem. Technol.* 23. p.374–383.
- ALBADARIN, A.B., AL-MUHTASEB, A.H., AL-LAQTAH, N.A., WALKER, G.M., ALLEN, S.J., & AHMAD, M.N.M. (2011). Biosorption of toxic chromium from aqueous phase by lignin: mechanism, effect of other metal ions and salts. *Chem. Eng. J.* 169. p.20–30.
- ALBADARIN, A.B., MANGWANDI, C., WALKER, G.M., ALLEN, S.J., AHMAD, M.N.M., & KHRAISHEH, M. (2013). Influence of solution chemistry on Cr(VI) reduction and complexation onto date-pits/tea-waste biomaterials. *J. Environ. Manage.* 114. p.190–201.
- ALMASRI, D.A., RHADFI, T., ATIEH, M.A., MCKAY, G., & AHZI, S. (2018). High performance hydroxyiron modified montmorillonite nanoclay adsorbent for arsenite removal. *Chem. Eng. J.* 335. p.1–12.
- ANJUM, M., MIANDAD, R., WAQAS, M., GEHANY, F., & BARAKAT, M.A. (2016). Remediation of wastewater using various nano-materials. *Arab. J. Chem.*
- ARGUN, M.E., DURSUN, S., GUR, K., OZDEMIR, C., KARATAS, M., & DOGAN, S. (2005). Nickel adsorption on the modified pine tree materials. *Environ. Technol.* 26. p.479–87.
- ARGUN, M.E., DURSUN, S., OZDEMIR, C., & KARATAS, M. (2007). Heavy metal adsorption by modified oak sawdust: Thermodynamics and kinetics. *J. Hazard. Mater.* 141. p.77–85.

- ARGUN, M.E., DURSUN, S., KARATAS, M., & GÜRÜ, M. (2008). Activation of pine cone using Fenton oxidation for Cd(II) and Pb(II) removal. *Bioresour. Technol.* 99. p.8691–8.
- ARYAL, M., & LIAKOPOULOU-KYRIAKIDES, M. (2011). Equilibrium, kinetics and thermodynamic studies on phosphate biosorption from aqueous solutions by Fe(III)-treated *Staphylococcus xylosus* biomass: Common ion effect. *Colloids Surfaces A Physicochem. Eng. Asp.* 387. p.43–49.
- BASKAN, M.B., & PALA, A. (2011). Removal of arsenic from drinking water using modified natural zeolite. *Desalination.* 281. p.396–403.
- BORA, A.J., GOGOI, S., BARUAH, G., & DUTTA, R.K. (2016). Utilization of co-existing iron in arsenic removal from groundwater by oxidation-coagulation at optimized pH. *J. Environ. Chem. Eng.* 4. p.2683–2691.
- CALAMA, R., MUTKE, S., TOMÉ, J., GORDO, J., MONTERO, G., & TOMÉ, M. (2011). Modelling spatial and temporal variability in a zero-inflated variable: The case of stone pine (*Pinus pinea* L.) cone production. *Ecol. Modell.* 222. p.606–618.
- CAN, M. (2015). Studies of the Kinetics for Rhodium Adsorption onto Gallic Acid Derived Polymer: the Application of Nonlinear Regression Analysis. *Acta Phys. Pol. A.* 127. p.1308–1310.
- CANTU, Y., REMES, A., REYNA, A., MARTINEZ, D., VILLARREAL, J., RAMOS, H., TREVINO, S., TAMEZ, C., MARTINEZ, A., EUBANKS, T., & PARSONS, J.G. (2014). Thermodynamics, kinetics, and activation energy studies of the sorption of chromium(III) and chromium(VI) to a Mn<sub>3</sub>O<sub>4</sub> nanomaterial. *Chem. Eng. J.* 254. p.374–383.
- CAO, C., XIAO, L., CHEN, C., SHI, X., CAO, Q., & GAO, L. (2014). In situ preparation of magnetic Fe<sub>3</sub>O<sub>4</sub>/chitosan nanoparticles via a novel reduction–precipitation method and their application in adsorption of reactive azo dye. *Powder Technol.* 260. p.90–97.
- CHAUDHRY, S.A., ZAIDI, Z., & SIDDIQUI, S.I. (2017). Isotherm, kinetic and thermodynamics of arsenic adsorption onto Iron-Zirconium Binary Oxide-Coated Sand (IZBOCS): Modelling and process optimization. *J. Mol. Liq.* 229. p.230–240.
- CHENG, H., & HU, Y. (2010). Lead (Pb) isotopic fingerprinting and its applications in lead pollution studies in China: A review. *Environ. Pollut.* 158. p.1134–1146.

CHENG, W., ZHANG, W., HU, L., DING, W., WU, F., & LI, J. (2016). Etching synthesis of iron oxide nanoparticles for adsorption of arsenic from water. *RSC Adv.* 6. p.15900–15910.

CHEUNG, K.H., & GU, J.-D. (2007). Mechanism of hexavalent chromium detoxification by microorganisms and bioremediation application potential: A review. *Int. Biodeterior. Biodegradation.* 59. p.8–15.

CHOONG, T.S.Y., CHUAH, T.G., ROBIAH, Y., GREGORY KOAY, F.L., & AZNI, I. (2007). Arsenic toxicity, health hazards and removal techniques from water: an overview. *Desalination.* 217. p.139–166.

DAS, A.P., & MISHRA, S. (2008). Hexavalent chromium (VI): Environment pollutant and health hazard. *J. Environ. Res. Dev.* 2. p.386–392.

DAWOOD, S., & SEN, T.K. (2012). Removal of anionic dye Congo red from aqueous solution by raw pine and acid-treated pine cone powder as adsorbent: equilibrium, thermodynamic, kinetics, mechanism and process design. *Water Res.* 46. p.1933–46.

DING, W., WANG, Y., YU, Y., ZHANG, X., LI, J., & WU, F. (2015). Photooxidation of arsenic(III) to arsenic(V) on the surface of kaolinite clay. *J. Environ. Sci.* 36. p.29–37.

EBRAHIMI, S., & ROBERTS, D.J. (2013). Sustainable nitrate-contaminated water treatment using multi cycle ion-exchange/bioregeneration of nitrate selective resin. *J. Hazard. Mater.* 262. p.539–44.

EBRAHIMIAN PIRBAZARI, A., SABERIKHAH, E., & HABIBZADEH KOZANI, S.S.S. (2014). Fe<sub>3</sub>O<sub>4</sub>-wheat straw: Preparation, characterization and its application for methylene blue adsorption. *Water Resour. Ind.* 7–8. p.23–37.

EIGENMANN, F., MACIEJEWSKI, M., & BAIKER, A. (2006). Selective reduction of NO by NH<sub>3</sub> over manganese–cerium mixed oxides: Relation between adsorption, redox and catalytic behavior. *Appl. Catal. B Environ.* 62. p.311–318.

GARG, U.K., KAUR, M.P., GARG, V.K., & SUD, D. (2007). Removal of hexavalent chromium from aqueous solution by agricultural waste biomass. *J. Hazard. Mater.* 140. p.60–68.

GAUTAM, R.K., MUDHOO, A., LOFRANO, G., & CHATTOPADHYAYA, M.C. (2014).

Biomass-derived biosorbents for metal ions sequestration: Adsorbent modification and activation methods and adsorbent regeneration. *J. Environ. Chem. Eng.* 2. p.239–259.

GYLIENĖ, O., BINKIENĖ, R., BARANAUSKAS, M., MORDAS, G., PLAUSKAITĖ, K., & ULEVIČIUS, V. (2014). Influence of dissolved oxygen on Fe(II) and Fe(III) sorption onto chitosan. *Colloids Surfaces A Physicochem. Eng. Asp.* 461. p.151–157.

HADI, P., NING, C., OUYANG, W., LIN, C.S.K., HUI, C.W., & MCKAY, G. (2014). Conversion of an aluminosilicate-based waste material to high-value efficient adsorbent. *Chem. Eng. J.* 256. p.415–420.

HAN, Y., CAO, X., OUYANG, X., SOHI, S.P., & CHEN, J. (2016). Adsorption kinetics of magnetic biochar derived from peanut hull on removal of Cr (VI) from aqueous solution: Effects of production conditions and particle size. *Chemosphere.* 145. p.336–341.

HERING, J.G., CHEN, P., WILKIE, J.A., & ELIMELECH, M. (1997). Arsenic removal from drinking water during coagulation. *J. Environ. Eng.* 123. p.800–807.

HO, Y.S., & OFOMAJA, A.E. (2006). Biosorption thermodynamics of cadmium on coconut copra meal as biosorbent. *Biochem. Eng. J.* 30. p.117–123.

HUA, M., ZHANG, S., PAN, B., ZHANG, W., LV, L., & ZHANG, Q. (2012). Heavy metal removal from water/wastewater by nanosized metal oxides: A review. *J. Hazard. Mater.* 211–212. p.317–331.

IGBERASE, E., & OSIFO, P. (2015). Equilibrium, kinetic, thermodynamic and desorption studies of cadmium and lead by polyaniline grafted cross-linked chitosan beads from aqueous solution. *J. Ind. Eng. Chem.* 26. p.340–347.

IGBERASE, E., OSIFO, P., & OFOMAJA, A. (2014). The adsorption of copper (II) ions by polyaniline graft chitosan beads from aqueous solution: Equilibrium, kinetic and desorption studies. *J. Environ. Chem. Eng.* 2. p.362–369.

IGBERASE, E., OSIFO, P., & OFOMAJA, A. (2017). The Adsorption of Pb, Zn, Cu, Ni, and Cd by Modified Ligand in a Single Component Aqueous Solution: Equilibrium, Kinetic, Thermodynamic, and Desorption Studies. *Int. J. Anal. Chem.* 2017.

INDARAWIS, K.A., & BOYER, T.H. (2013). Superposition of anion and cation exchange for removal of natural water ions. *Sep. Purif. Technol.* 118. p.112–119.

INOUE, K. (2011). Heavy Metal Toxicity. *J. Clin. Toxicol.* s3. p.1–2.

KATSOYIANNIS, I.A., ZOUBOULIS, A.I., & JEKEL, M. (2004). Kinetics of Bacterial As(III) oxidation and subsequent As(V) removal by sorption onto biogenic manganese oxides during groundwater treatment. *Ind. Eng. Chem. Res.* 43. p.486–493.

KHATOON, N., KHAN, A.H., PATHAK, V., AGNIHOTRI, N., & REHMAN, M. (2013). Removal of hexavalent chromium from synthetic waste water using synthetic Nano Zero Valent Iron (NZVI) as adsorbent. *Int. J. Innov. Res. Sci. Eng. Technol.* 2. p.6140–6149.

KIM, M.J., & NRIAGU, J. (2000). Oxidation of arsenite in groundwater using ozone and oxygen. *Sci. Total Environ.* 247. p.71–79.

KUMARI, M., PITTMAN, C.U., & MOHAN, D. (2015). Heavy metals [chromium (VI) and lead (II)] removal from water using mesoporous magnetite (Fe<sub>3</sub>O<sub>4</sub>) nanospheres. *J. Colloid Interface Sci.* 442. p.120–32.

KUPETA, A.J.K., NAIDOO, E.B., & OFOMAJA, A.E. (2018). Kinetics and equilibrium study of 2-nitrophenol adsorption onto polyurethane cross-linked pine cone biomass. *J. Clean. Prod.* 179.

LAI, J., SHAFI, K.V.P.M., ULMAN, A., LOOS, K., YANG, N., CUI, M., VOGT, T., ESTOURNE, C., & LOCKE, D.C. (2004). Mixed Iron - Manganese Oxide Nanoparticles. *J. Phys. Chem. B.* 108. p.14876–14883.

LAROUS, S., MENIAI, A.H., & BENCHEIKH LEHOCINE, M. (2005). Experimental study of the removal of copper from aqueous solutions by adsorption using sawdust. *Desalination.* 185. p.483–490.

LE MAITRE, D., VAN WILGEN, B., GELDERBLOM, C., BAILEY, C., CHAPMAN, R., & NEL, J. (2002). Invasive alien trees and water resources in South Africa: case studies of the costs and benefits of management. *For. Ecol. Manage.* 160. p.143–159.

LEE, C., ALVAREZ, P.J.J., NAM, A., PARK, S., DO, T., CHOI, U., & LEE, S. (2017). Arsenic ( V ) removal using an amine-doped acrylic ion exchange fiber : Kinetic , equilibrium , and



regeneration studies. *J. Hazard. Mater.* 325. p.223–229.

LIU, J., ZHAO, Z., & JIANG, G. (2008). Coating Fe<sub>3</sub>O<sub>4</sub> magnetic nanoparticles with humic acid for high efficient removal of heavy metals in water. *Environ. Sci. Technol.* 42. p.6949–54.

LÓPEZ-TÉLLEZ, G., BARRERA-DÍAZ, C.E., BALDERAS-HERNÁNDEZ, P., ROA-MORALES, G., & BILYEU, B. (2011). Removal of hexavalent chromium in aquatic solutions by iron nanoparticles embedded in orange peel pith. *Chem. Eng. J.* 173. p.480–485.

LUNGE, S., SINGH, S., & SINHA, A. (2014). Magnetic iron oxide (Fe<sub>3</sub>O<sub>4</sub>) nanoparticles from tea waste for arsenic removal. *J. Magn. Magn. Mater.* 356. p.21–31.

LUTHER, S., BORGFELD, N., KIM, J., & PARSONS, J.G. (2012). Removal of arsenic from aqueous solution: A study of the effects of pH and interfering ions using iron oxide nanomaterials. *Microchem. J.* 101. p.30–36.

LYTLE, D.A., SORG, T., WANG, L., & CHEN, A. (2014). The accumulation of radioactive contaminants in drinking water distribution systems. *Water Res.* 50. p.396–407.

MAHDAVIAN, A.R., & MIRRAHIMI, M.A.-S. (2010). Efficient separation of heavy metal cations by anchoring polyacrylic acid on superparamagnetic magnetite nanoparticles through surface modification. *Chem. Eng. J.* 159. p.264–271.

MAHMOODI, N.M., HAYATI, B., ARAMI, M., & LAN, C. (2011). Adsorption of textile dyes on Pine Cone from colored wastewater: Kinetic, equilibrium and thermodynamic studies. *Desalination.* 268. p.117–125.

MANDAL, B.K., & SUZUKI, K.T. (2002). Arsenic round the world: a review. *Talanta.* 58. p.201–235.

MILONJIĆ, S.K. (2007). A consideration of the correct calculation of thermodynamic parameters of adsorption. *J. Serbian Chem. Soc.* 72. p.1363–1367.

MIRETZKY, P., & CIRELLI, A.F. (2010). Cr(VI) and Cr(III) removal from aqueous solution by raw and modified lignocellulosic materials: a review. *J. Hazard. Mater.* 180. p.1–19.

MOHAN, D., & PITTMAN, C.U. (2006). Activated carbons and low cost adsorbents for remediation of tri- and hexavalent chromium from water. *J. Hazard. Mater.* 137. p.762–811.

MOMČILOVIĆ, M., PURENOVIĆ, M., BOJIĆ, A., ZARUBICA, A., & RANĐELOVIĆ, M. (2011). Removal of lead(II) ions from aqueous solutions by adsorption onto pine cone activated carbon. *Desalination*. 276. p.53–59.

MONÁRREZ-CORDERO, B., AMÉZAGA-MADRID, P., ANTÚNEZ-FLORES, W., LEYVA-PORRAS, C., PIZÁ-RUIZ, P., & MIKI-YOSHIDA, M. (2014). Highly efficient removal of arsenic metal ions with high superficial area hollow magnetite nanoparticles synthesized by AACVD method. *J. Alloys Compd.* 586. p.S520–S525.

MONÁRREZ-CORDERO, B.E., AMÉZAGA-MADRID, P., LEYVA-PORRAS, C.C., PIZÁ-RUIZ, P., & MIKI-YOSHIDA, M. (2016). Study of the Adsorption of Arsenic (III and V) by Magnetite Nanoparticles Synthesized via AACVD. *Mater. Res.* 19. p.103–112.

MONDAL, P., BHOWMICK, S., CHATTERJEE, D., FIGOLI, A., & VAN DER BRUGGEN, B. (2013). Remediation of inorganic arsenic in groundwater for safe water supply: a critical assessment of technological solutions. *Chemosphere*. 92. p.157–170.

NAMASIVAYAM, C., & SURESHKUMAR, M.V. (2008). Removal of chromium(VI) from water and wastewater using surfactant modified coconut coir pith as a biosorbent. *Bioresour. Technol.* 99. p.2218–2225.

NECHIFOR, G., PASCU, D.E., NEAGU, M.P., TRAISTARU, G.A., & ALBU, P.C. (2015). Comparative study of temkin and floryhuggins isotherms for adsorption of phosphate anion on membranes. *UPB Sci. Bull. Ser. B Chem. Mater. Sci.* 77. p.63–72.

OBIKE, A., IGWE, J., EMERUWA, C., UWAKWE, K., & AGHALIBE, C. (2018). Diffusion-Chemisorption and Pseudo-Second Order Kinetic Models for Heavy Metal Removal from Aqueous Solutions Using Modified and Unmodified Oil Palm Fruit Fibre. *Chem. Sci. Int. J.* 23. p.1–13.

OCIŃSKI, D., JACUKOWICZ-SOBALA, I., MAZUR, P., RACZYK, J., & KOCIOŁEK-BALAWAJDER, E. (2016). Water treatment residuals containing iron and manganese oxides for arsenic removal from water - Characterization of physicochemical properties and adsorption studies. *Chem. Eng. J.* 294. p.210–221.

OFOMAJA, A.E. (2010). Biosorption studies of Cu(II) onto *Mansonia* sawdust: Process design to

minimize biosorbent dose and contact time. *React. Funct. Polym.* 70. p.879–889.

OFOMAJA, A.E., & NAIDOO, E.B. (2011). Biosorption of copper from aqueous solution by chemically activated pine cone: A kinetic study. *Chem. Eng. J.* 175. p.260–270.

OFOMAJA, A.E., NAIDOO, E.B., & MODISE, S.J. (2009). Removal of copper(II) from aqueous solution by pine and base modified pine cone powder as biosorbent. *J. Hazard. Mater.* 168. p.909–917.

OFOMAJA, A.E., NAIDOO, E.B., & MODISE, S.J. (2010a). Biosorption of copper(II) and lead(II) onto potassium hydroxide treated pine cone powder. *J. Environ. Manage.* 91. p.1674–85.

OFOMAJA, A.E., PHOLOS, A., & NAIDOO, E.B. (2014). Kinetics and competitive modeling of cesium biosorption onto iron(III) hexacyanoferrate modified pine cone powder. *Int. Biodeterior. Biodegradation.* 92. p.71–78.

OFOMAJA, A.E., UNUABONAH, E.I., & OLADOJA, N.A. (2010b). Competitive modeling for the biosorptive removal of copper and lead ions from aqueous solution by *Mansonia* wood sawdust. *Bioresour. Technol.* 101. p.3844–3852.

OUMA, I.L.A., NAIDOO, E.B., & OFOMAJA, A.E. (2018). Thermodynamic, kinetic and spectroscopic investigation of arsenite adsorption mechanism on pine cone-magnetite composite. *J. Environ. Chem. Eng.* 6. p.5409–5419.

PAKADE, V.E., NTULI, T.D., & OFOMAJA, A.E. (2017). Biosorption of hexavalent chromium from aqueous solutions by *Macadamia* nutshell powder. *Appl. Water Sci.* 7. p.3015–3030.

PAN, B., PAN, B., ZHANG, W., LV, L., ZHANG, Q., & ZHENG, S. (2009). Development of polymeric and polymer-based hybrid adsorbents for pollutants removal from waters. *Chem. Eng. J.* 151. p.19–29.

PAN, S., SHEN, H., XU, Q., LUO, J., & HU, M. (2012). Surface mercapto engineered magnetic Fe<sub>3</sub>O<sub>4</sub> nanoadsorbent for the removal of mercury from aqueous solutions. *J. Colloid Interface Sci.* 365. p.204–212.

PANNEERSELVAM, P., MORAD, N., & TAN, K.A. (2011). Magnetic nanoparticle (Fe<sub>3</sub>O<sub>4</sub>) impregnated onto tea waste for the removal of nickel(II) from aqueous solution. *J. Hazard. Mater.*

186. p.160–168.

PENG, X., XU, F., ZHANG, W., WANG, J., ZENG, C., NIU, M., & CHMIELEWSKÁ, E. (2014). Magnetic Fe<sub>3</sub>O<sub>4</sub> @ silica–xanthan gum composites for aqueous removal and recovery of Pb<sup>2+</sup>. *Colloids Surfaces A Physicochem. Eng. Asp.* 443. p.27–36.

PÉREZ MARÍN, A.B., AGUILAR, M.I., MESEGUER, V.F., ORTUÑO, J.F., SÁEZ, J., & LLORÉNS, M. (2009). Biosorption of chromium (III) by orange (*Citrus cinensis*) waste: Batch and continuous studies. *Chem. Eng. J.* 155. p.199–206.

PHOLOSİ, A., OFOMAJA, A.E., & NAIDOO, E.B. (2013). Effect of chemical extractants on the biosorptive properties of pine cone powder: Influence on lead(II) removal mechanism. *J. Saudi Chem. Soc.* 17. p.77–86.

POOL, V.L., KLEM, M.T., JOLLEY, C., ARENHOLZ, E.A., DOUGLAS, T., YOUNG, M., IDZERDA, Y.U., HOLROYD, J., HARRIS, T., ARENHOLZ, E.A., YOUNG, M., DOUGLAS, T., & IDZERDA, Y.U. (2010). Site determination and magnetism of Mn doping in protein encapsulated iron oxide nanoparticles. *J. Appl. Phys.* 107. p.1–3.

ROSTAMIAN, R., & BEHNEJAD, H. (2016). A comparative adsorption study of sulfamethoxazole onto graphene and graphene oxide nanosheets through equilibrium, kinetic and thermodynamic modeling. *Process Saf. Environ. Prot.* 102. p.20–29.

SAY, R., BIRLIK, E., ERDEMGİL, Z., DENİZLİ, A., & ERSÖZ, A. (2008). Removal of mercury species with dithiocarbamate-anchored polymer/organosmectite composites. *J. Hazard. Mater.* 150. p.560–564.

SHAFIQUE, U., IJAZ, A., SALMAN, M., ZAMAN, W. UZ, JAMIL, N., REHMAN, R., & JAVAİD, A. (2012). Removal of arsenic from water using pine leaves. *J. Taiwan Inst. Chem. Eng.* 43. p.256–263.

SHARMA, J.K., SRIVASTAVA, P., AMEEN, S., AKHTAR, M.S., SINGH, G., & YADAVA, S. (2016). Azadirachta indica plant-assisted green synthesis of Mn<sub>3</sub>O<sub>4</sub> nanoparticles: Excellent thermal catalytic performance and chemical sensing behavior. *J. Colloid Interface Sci.* 472. p.220–228.

SHARMA, V.K., & SOHN, M. (2009). Aquatic arsenic: toxicity, speciation, transformations, and

remediation. *Environ. Int.* 35. p.743–59.

SHRAIM, A.M. (2017). Rice is a potential dietary source of not only arsenic but also other toxic elements like lead and chromium. *Arab. J. Chem.* 10. p.S3434–S3443.

SINGH, R., SINGH, S., PARIHAR, P., SINGH, V.P., & PRASAD, S.M. (2015). Arsenic contamination, consequences and remediation techniques: A review. *Ecotoxicol. Environ. Saf.* 112. p.247–270.

SUTHERLAND, C., & VENKOBACHAR, C. (2010). A Diffusion-Chemisorption Kinetic Model for Simulating Biosorption Using Forest Macro-Fungus, *Fomes Fasciatus*. *Int. Res. J. Plant Sci.* 1. p.107–117.

TEJA, A.S., & KOH, P.-Y. (2009). Synthesis, properties, and applications of magnetic iron oxide nanoparticles. *Prog. Cryst. Growth Charact. Mater.* 55. p.22–45.

THOMMES, M., KANEKO, K., NEIMARK, A. V., OLIVIER, J.P., RODRIGUEZ-REINOSO, F., ROUQUEROL, J., & SING, K.S.W. (2015). Physisorption of gases, with special reference to the evaluation of surface area and pore size distribution (IUPAC Technical Report). *Pure Appl. Chem.* 87. p.1051–1069.

THOMPSON, A. (2012). Water abundance and an EKC for water pollution. *Econ. Lett.* 117. p.423–425.

UCUN, H., BAYHAN, Y.K., KAYA, Y., CAKICI, A., & FARUK ALGUR, O. (2002). Biosorption of chromium(VI) from aqueous solution by cone biomass of *Pinus sylvestris*. *Bioresour. Technol.* 85. p.155–158.

UDDIN, R., & HUDA, N.H. (2011). Arsenic poisoning in Bangladesh. *Oman Med. J.* 26. p.207.

VILAR, V.J.P., VALLE, J.A.B., BHATNAGAR, A., SANTOS, J.C., GUELLI U. DE SOUZA, S.M.A., DE SOUZA, A.A.U., BOTELHO, C.M.S., & BOAVENTURA, R.A.R. (2012). Insights into trivalent chromium biosorption onto protonated brown algae *Pelvetia canaliculata*: Distribution of chromium ionic species on the binding sites. *Chem. Eng. J.* 200–202. p.140–148.

VOLESKY, B., & HOLAN, Z.R. (1995). Biosorption of Heavy Metals. *Biotechnol. Prog.* 11. p.235–250.

WANG, Y., MORIN, G., ONA-NGUEMA, G., & BROWN, G.E. (2014). Arsenic(III) and Arsenic(V) Speciation during Transformation of Lepidocrocite to Magnetite. *Environ. Sci. Technol.* 48. p.14282–14290.

YADANAPARTHI, S.K.R., GRAYBILL, D., & VON WANDRUSZKA, R. (2009). Adsorbents for the removal of arsenic, cadmium, and lead from contaminated waters. *J. Hazard. Mater.* 171. p.1–15.

YAN, W., LIEN, H.-L., KOEL, B.E., & ZHANG, W. (2013). Iron nanoparticles for environmental clean-up: recent developments and future outlook. *Environ. Sci. Process. Impacts.* 15. p.63.

YANG, Y., TIAN, C., & ZHAO, X. (2011). Adsorption kinetics of methylene blue onto Fe-doped sulfated titania. *Colloids Surfaces A Physicochem. Eng. Asp.* 389. p.12–17.

YUAN, P., LIU, D., FAN, M., YANG, D., ZHU, R., GE, F., ZHU, J.X., & HE, H. (2010). Removal of hexavalent chromium [Cr(VI)] from aqueous solutions by the diatomite-supported/unsupported magnetite nanoparticles. *J. Hazard. Mater.* 173. p.614–621.

ZHANG, M., & GAO, B. (2013). Removal of arsenic, methylene blue, and phosphate by biochar/AlOOH nanocomposite. *Chem. Eng. J.* 226. p.286–292.

ZUHAIRI, W., YAACOB, W., KAMARUZAMAN, N., & RAHIM, A. (2012). Development of Nano-Zero Valent Iron for the Remediation of Contaminated Water. *Chem. Eng. Trans.* 28. p.25–30.

### 3 Preparation and Characterization of Pine Cone and Magnetite Based Adsorbents

#### 3.1 Introduction

Adsorbent preparation is one of the key considerations in the development of a suitable adsorbent material. Preparation methods can influence the adsorbent's physicochemical properties such as particle size, porosity, crystallinity, functionalization and stability. Magnetite nanoparticles are promising materials because of their unique magnetic properties as well as low toxicity, surface modification ability and colloidal stability (Warner *et al.*, 2012). The preparation method applied for these nanomaterials enables one to have control over the size, uniformity, crystallinity and surface properties of the nanomaterials. There are several synthetic routes for the synthesis of magnetite nanoparticles, co-precipitation method is one of the most popular methods and has advantages over other methods including low cost, low temperature requirements, high product purity and good homogeneity (Ahn *et al.*, 2012; Wu *et al.*, 2016). Co-precipitation involves the precipitation of ferric and ferrous ions in alkaline media in accordance to equation 3.1.



Bare magnetite nanoparticles however, tend to agglomerate because of interparticle dipolar forces therefore impeding their performance (Zheng *et al.*, 2018). Surface coating has therefore been proposed to improve biocompatibility, adsorption capacity, regulate particle size, surface charge and surface functionality (Zheng *et al.*, 2018). Composite formation with lignocellulosic materials introduces surface groups desirable for adsorption while preserving the magnetic properties and large surface areas of magnetite particles (Nata *et al.*, 2011). To further improve the affinity of magnetite to heavy metal pollutants present in the environment, doping with other metals has been considered a promising option. The introduction of dopants to metal oxides have been shown to increase affinities for pollutants. Manganese and iron oxides are both natural oxides with high affinities for metal pollutants. In addition to high affinities, manganese doping on magnetite provides higher magnetic susceptibility than pure magnetite due to the presence of five single unpaired electrons of  $Mn^{2+}$  (Yang *et al.*, 2017). A material consisting of both oxides therefore yields magnetic particles with better sorption capacities for heavy metal pollutants (Warner *et al.*, 2012). To achieve the desired properties, dopant amounts must be carefully monitored.

This chapter describes the synthesis and characterization of adsorbent materials used in this study including Fenton's treated pine cone powder (FTP), Fenton's treated pine cone -magnetite composite (FTP-MNP), magnetite nanoparticles (MNP), manganese doped magnetite nanoparticles (Mn MNP) and manganese doped pine cone-magnetite composite (Mn FTP-MNP). The preparation procedures are explained, and their characterization results are described.

## **3.2 Experimental**

### **3.2.1 Materials**

Pine tree cones were collected from Vaal University of Technology in Vanderbijlpark. They were washed and oven dried at 90 °C to remove sand and other impurities. Raw pine cone powder was obtained by crushing dry cones and sieving to obtain particles with sizes of between 45 µm and 90 µm. Hydrogen peroxide solution (30 %) was purchased from Associated Chemical Enterprises (South Africa). Ammonium hydroxide (NH<sub>4</sub>OH, 25 %) was supplied by Labchem (South Africa). Hydrochloric acid (32 %) and Ferrous sulphate (FeSO<sub>4</sub>·7H<sub>2</sub>O >98 %) were supplied by Merck. Ferric chloride (FeCl<sub>3</sub>·6H<sub>2</sub>O >99 %), manganese sulphate (MnSO<sub>4</sub>·H<sub>2</sub>O >99 %) and sodium arsenite (NaAsO<sub>2</sub> >90 %) were purchased from Sigma-Aldrich. All chemicals were used without any further purification. All syntheses were carried out under nitrogen atmosphere with vigorous stirring to ensure uniform dispersions.

### **3.2.2 Methods**

#### **3.1.1.1 Preparation of Fenton's Treated Pine Cone Powder**

Fenton's reagent was prepared by measuring 303 cm<sup>3</sup> of 30% H<sub>2</sub>O<sub>2</sub> and 6.993 g of FeSO<sub>4</sub>·7H<sub>2</sub>O into separate 1000 cm<sup>3</sup> volumetric flasks. The pH of Fe<sup>2+</sup> solution was adjusted to between 3 and 4.5 using 0.1 M H<sub>2</sub>SO<sub>4</sub>. 100 g of pine cone powder was weighed and transferred into a 2000 cm<sup>3</sup> three-necked round bottom flask, fitted with a gas inlet, magnetic stirrer and condenser. The flask and its contents were degassed for 15 minutes followed by passing nitrogen gas for another 15 minutes. Then 250 cm<sup>3</sup> of the prepared Fe<sup>2+</sup> solution was added and heated at 50° C for 30 minutes. This was followed by the addition of 250 cm<sup>3</sup> of the prepared H<sub>2</sub>O<sub>2</sub> solution and heating for a further 30 min. The resulting powder was filtered and washed with deionized water till a clear filtrate was obtained. The washed powder was dried at 80 °C for eight hours.



### ***3.1.1.2 Synthesis of Magnetite Nanoparticles***

100 cm<sup>3</sup> of deionized water was added to a three-necked round bottom flask fitted with a magnetic stirrer and a condenser. The water was degassed for 15 minutes at 80 °C followed by bubbling nitrogen gas for 15 minutes to create an inert atmosphere. To the water 3.1 g of FeCl<sub>3</sub>.6H<sub>2</sub>O and 2.1 g FeSO<sub>4</sub>.7H<sub>2</sub>O salts were added with vigorous stirring. 20 mL of 25 % NH<sub>4</sub>OH was added for co-precipitation and the stirring was continued for a further 45 minutes. The formed black precipitate was washed with deionized water and ethanol several times, each time allowing the precipitate to settle under the influence of a magnet and decanting the supernatant. The washed precipitate was dried in a vacuum oven overnight at 60 °C.

### ***3.1.1.3 Synthesis of Manganese Doped Magnetite Nanoparticles***

Manganese doped nanoparticles and composite were prepared in a one-pot co-precipitation method by adding 0.5 g manganese sulphate to ferrous and ferric salts before precipitating with 25 % NH<sub>4</sub>OH.

### ***3.1.1.4 Preparation of Pine Cone-Magnetite Composite***

The composite material was prepared in a single step co-precipitation method similar to the method described above for magnetite synthesis. 1.5 g of Fenton's treated pine cone powder was added to the degassed water with the addition of ferrous and ferric salts and the precipitation was carried out at 60 °C.

### ***3.1.1.5 Synthesis of Manganese Doped Pine Cone-Magnetite Composite***

Manganese doped composite was prepared in a similar method to the pine cone-magnetite composite with the introduction of 0.5 g MnSO<sub>4</sub>.H<sub>2</sub>O before precipitation.

All the prepared samples were washed with deionised water to remove excess ammonia and dried in a vacuum oven overnight at 60 °C.

## ***3.2.3 Characterization***

The samples were characterized using various analytical techniques to determine their composition, crystallinity, morphology and magnetic properties. The effects of modification and doping on their properties were also monitored using the different analytical tools.

Fourier Transform Infrared Spectroscopy was carried out on a PerkinElmer spectrum 400 FT-IR/NIR spectrometer to determine surface functional groups and the effects of Fenton's treatment and composite formation on surface functionality.

Thermal analyses were carried out on a PerkinElmer TGA 4000 thermogravimetric analyzer to determine the thermal degradation profiles of the as-synthesized materials. X-ray diffraction (XRD) spectra were recorded on a Bruker AXS D8 advanced diffractometer equipped with Cu K $\alpha$  ( $\lambda = 1.5418 \text{ \AA}$ ) X-ray source. XRD was used to determine the crystallinity of the materials and confirm the formation of magnetite nanoparticles by comparing with reference data for synthetic magnetite. Particle sizes were calculated following Debye-Scherrer's equation to confirm the formation of nano-sized particles.

Scanning electron microscopy (SEM) analysis was carried out on a Carl Zeiss, Sigma scanning electron microscope. High Resolution images of the nanoparticles for shape and size measurements were obtained on a FEI Tecnai F20 transmission electron microscope (TEM) at an acceleration voltage of 200kV. Magnetic measurements were carried out on a LakeShore model 735 vibrating sample magnetometer at room temperature. X-ray photoelectron spectroscopy (XPS) studies were performed using XPS microprobe (PHI 5000 Scanning ESCA Microprobe ULVAC-PHI Inc).

### **3.3 Results and Discussions**

#### **3.3.1 X-ray Diffraction**

The X-ray diffraction pattern of Fenton's treated pine cone in Figure 3.1 shows three major peaks at  $22.3^\circ$ ,  $37.82^\circ$  and  $44.06^\circ$ . These peaks are shifted from previously reported values for crystalline cellulose (I) at  $15.3^\circ$ ,  $21.3^\circ$  and  $34.0^\circ$  and amorphous cellulose (II) at  $26.1^\circ$ ,  $36.2^\circ$  and  $40.1^\circ$  (Ofomaja & Naidoo, 2011). Fenton's oxidation generally reduces the amount of cellulose in pine cone which may account for the absence of some cellulose peaks in the diffraction pattern (Argun *et al.*, 2008). Diffraction pattern of the as-synthesized nanoparticles reveals peaks at  $30.75^\circ$ ,  $36.09^\circ$ ,  $43.81^\circ$ ,  $54.03^\circ$ ,  $57.67^\circ$  and  $63.26^\circ$  attributed to crystalline planes with miller indices (220), (311), (400), (422), (511) and (440) respectively. The pattern matches the standard diffraction pattern for synthetic magnetite (JCPDS Card 19-0629) confirming the inverse spinel structure of the as-synthesized nanoparticles (Rajput *et al.*, 2016; Tao *et al.*, 2008). Diffraction peaks for

magnetite and cellulose from pine cone are present in the composite indicating it consists of both pine cone and magnetite, the peaks corresponding to magnetite are broadened and slightly shifted possibly due to a decrease in crystallinity because of the presence of amorphous cellulose in the composite (Ouma *et al.*, 2017). The binding of pine cone on the surface of magnetite nanoparticles may cause strain on bound surface atoms that differs from unbound surface atoms therefore resulting in a shift of the diffraction peaks (Li *et al.*, 2001; Ofomaja & Naidoo, 2011; Ebrahimian Pirbazari *et al.*, 2014). Incorporation of pine cone lowered the crystallinity of magnetite nanoparticles and decreased particle sizes as evident from the reduced intensities and increased full width at half maximum (FWHM) respectively. The particle sizes for magnetite nanoparticles and magnetite particles on the composite were calculated from the diffraction data using Derby-Scherrer's equation (eq. 3.2) where  $D$  is the particle diameter,  $K$  (0.9) is the Scherrer constant which accounts for the particle shape,  $\lambda$  (1.54 Å) is the wavelength of the incident X-ray beam,  $\beta$  is the full-width at half maximum (FWHM) and  $\theta$  is the angle of incidence or angle of scattering of the X-ray beam (Sharma *et al.*, 2012).

$$D = \frac{K\lambda}{\beta \cos \theta} \quad (3.2)$$

Particle sizes for bare magnetite and magnetite particles on the composite were determined to be 8.9 nm and 6.9 nm respectively (Darroudi *et al.*, 2014). The smaller nanocomposite sizes as compared to the nanoparticles suggests that the added biomass was bound to nanoparticle surfaces hence hindering further crystal growth and stabilizing the particles (Ebrahimian Pirbazari *et al.*, 2014; Li *et al.*, 2001).

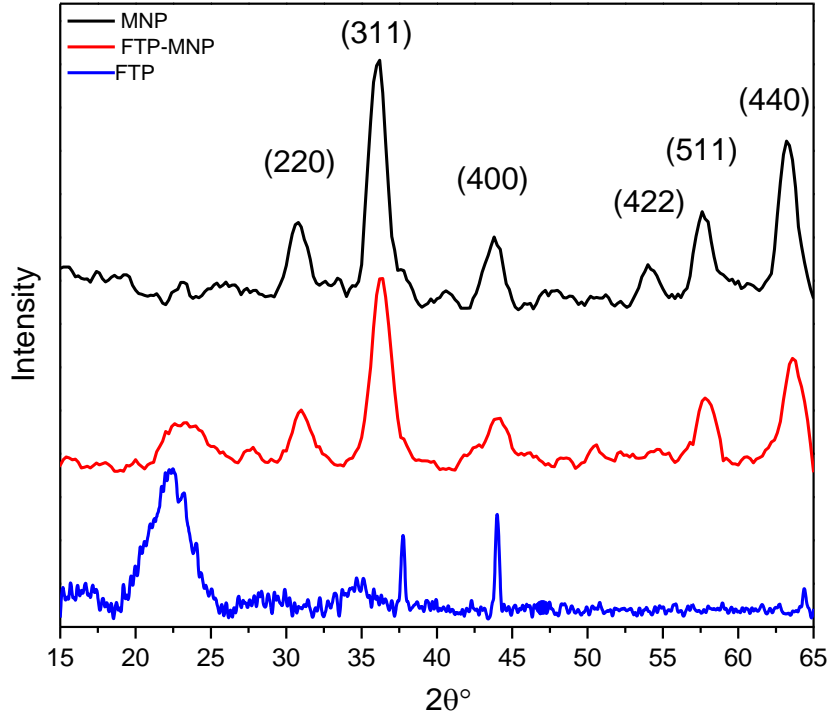


Fig. 3.1: XRD Diffractograms of FTP, FTP-MNP and MNP

Manganese doping was carried out for increased redox properties during adsorption and was considered a suitable dopant due to its size and charge allowing it to suitably replace  $\text{Fe}^{2+}$  cations in magnetite crystal structure (Casula *et al.*, 2016). To determine the effects of doping on magnetite nanoparticles, variable dopant amounts were introduced. With increasing doping amounts the diffraction spectra were recorded to determine the effects of doping on the crystal structure of the particles. The diffraction pattern of magnetite with different dopant amounts indicate similar diffraction patterns for all dopant amounts. The diffraction patterns all matched card data for magnetite (JCPDS 19-0629) with no peaks corresponding to secondary phases or impurities being detected. As doping levels increased, diffraction peaks were shifted to lower  $2\theta$  values since the radius of  $\text{Mn}^{2+}$  at 67 pm is larger than both  $\text{Fe}^{2+}$  (61 pm) and  $\text{Fe}^{3+}$  (55 pm) therefore resulting in increased lattice distance as compared to magnetite. Bragg's law (eq 3.3) where  $n$  is an integer number of wavelengths,  $\lambda$  is the wavelength of the incident X-ray beam,  $d$  is the distance between atomic layers and  $\theta$  is the angle of incidence or angle of scattering of the X-ray beam defines the relation between  $d$  and  $\theta$ .

$$n\lambda = 2d \sin\theta \quad (3.3)$$

Since  $n$  and  $\lambda$  are constant for all the samples therefore as the distance between atomic layers increases, the angle of scattering decreases resulting in shifts to lower  $2\theta$  values as observed in the diffractograms in Figure 3.2.

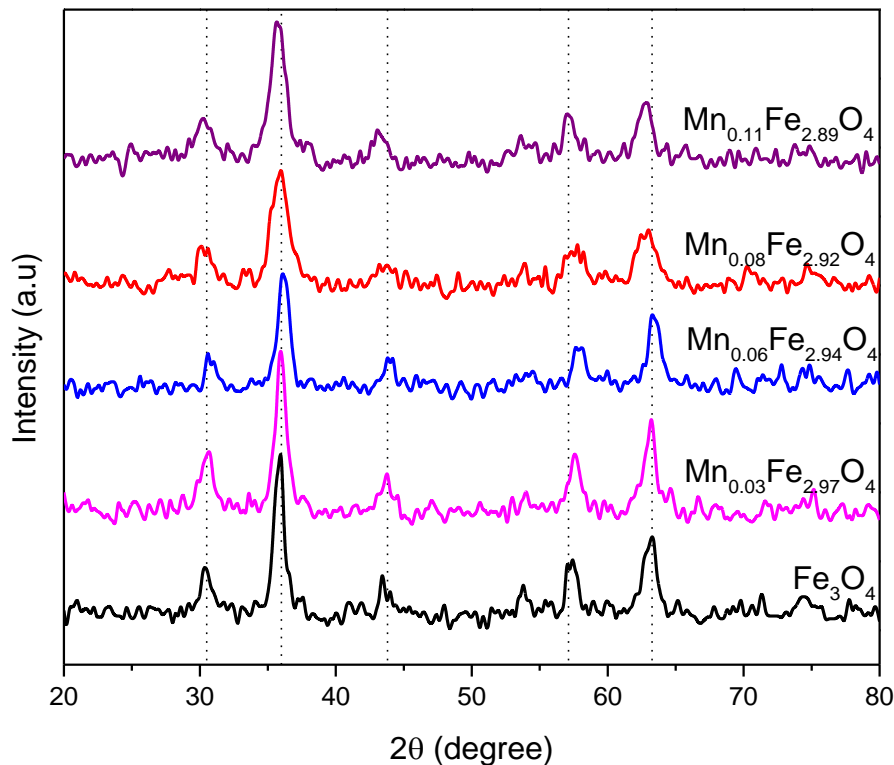


Fig. 3.2: XRD diffractograms of magnetite with different levels of manganese doping

The lattice parameters were calculated to determine the effects of doping on the unit cell of magnetite. Magnetite crystals have a face-centered cubic pattern and the unit cell is characterised by a lattice parameter of 0.8396 nm (8.39 Å) (Cornell & Schwertmann, 2003; Parkinson, 2016). The magnetite crystal is an  $O^{2-}$  face centered cubic lattice with  $Fe^{3+}$  occupying a  $\frac{1}{2}$  of the tetrahedral interstices while  $\frac{1}{8}$  of the octahedral interstices are occupied by a 1:1 mixture of  $Fe^{3+}$  and  $Fe^{2+}$ . The lattice parameter for the as-synthesized magnetite was 8.27 Å which is in good agreement with the value reported for nanosized  $Fe_3O_4$  (Deepak *et al.*, 2015). Manganese doping increased the lattice parameter due to the substitution of larger  $Mn^{2+}$  (0.80 Å) into  $Fe^{3+}$  (0.64 Å) lattices (Varshney & Yogi, 2011). The increase in unit cell was due to cell expansion as indicated by the larger unit cell (8.49-8.51 Å) of  $MnFe_2O_4$ . The cell volume increased with an increase in unit cell sizes and particle composition of  $Fe_{2.94}Mn_{0.06}O_4$  was used in further experiments and labelled as Mn MNP. Nanoparticles on the composite showed lower unit cell values of 8.24 Å due

to the presence of pine cone limiting particle growth. Upon manganese doping, the lattice parameter for the particles on the composite decreased to 8.24 Å with a cell volume of 560 Å.

Table 3.1: Cell Parameter values for synthesized samples

<b>Sample</b>	<b>Lattice Parameter a (Å)</b>	<b>Cell Volume</b>
<b>Fe<sub>3</sub>O<sub>4</sub></b>	8.27	566.33
<b>Fe<sub>2.97</sub>Mn<sub>0.03</sub>O<sub>4</sub></b>	8.31	573.76
<b>Fe<sub>2.94</sub>Mn<sub>0.06</sub>O<sub>4</sub></b>	8.33	577.28
<b>Fe<sub>2.92</sub>Mn<sub>0.08</sub>O<sub>4</sub></b>	8.36	585.28
<b>Fe<sub>2.89</sub>Mn<sub>0.11</sub>O<sub>4</sub></b>	8.81	683.62
<b>FTPMNP</b>	8.24	560.48
<b>Mn FTP- MNP</b>	8.37	585.57

### 3.3.2 Thermal Analysis

Thermogravimetric analysis (TGA) and differential thermal analysis (DTA) were carried out to determine the thermal stability of each sample and investigate their degradation profiles. Thermal degradation profiles for FTP, MNP and FTP-MNP (Fig. 3.3 - 3.5) all showed an initial weight loss step at temperatures below 140 °C accounting for the loss of adsorbed water molecules. In FTP (Fig. 3.3) and FTP-MNP (Fig. 3.5), this step was followed by a slow decomposition step between 140 °C and 240 °C where hemicellulose and cellulose components were lost followed by lignin degradation between 240 °C and 390 °C (Duman *et al.*, 2009). The derivative curve for MNP (Fig. 3.4) showed five decomposition peaks, the first peak was attributed to the loss of adsorbed water from the surface. The peaks at 265 °C and 325 °C were attributed to the loss of pore bound water while the peak at 565 °C was attributed to surface dihydroxylation (Kwon *et al.*, 2014). The last peak at approximately 650 °C was attributed to the reduction of Fe<sub>3</sub>O<sub>4</sub> to FeO and subsequent deoxidation of FeO since the measurement was carried out in a nitrogen atmosphere (Mahdavi *et al.*, 2013). FTP-MNP showed a similar degradation profile to FTP and MNP with a 70 % weight loss compared to 80 % of FTP and 8.3 % for MNP. Magnetite was therefore thermally stable throughout the temperature range and its incorporation into the composite improved the

composites thermal stability. The content of magnetite in the composite was calculated using equation 3.4 where  $L_{total}$  and  $L_{MNP}$  are the total and magnetite weight loss respectively (Xu *et al.*, 2008). The composition of MNP in the composite was determined to be 32.7 wt. % while that of FTP was 67.3 wt. %.

$$MNP_{wt\%} = \frac{1 - L_{total}}{1 - L_{MNP}} * 100\% \quad (3.4)$$

Manganese doping slightly altered the thermal decomposition profile of MNP at temperatures above 500 °C (Fig. 3.6). Upon manganese doping, magnetite reduction and deoxidation took place at 717 °C due to manganese substitution of some iron sites in the crystal structure as indicated by the cell parameters resulting in a change in the composition of magnetite crystals (Puerta & Valerga, 1990). The final derivative peak indicates the deoxidation of manganese oxide present in the doped sample (Puerta & Valerga, 1990). Magnetite doping in the composite (Fig. 3.7) further improves thermal stability with a total weight loss of approximately 40 %. The derivative curves of FTP-MNP (Fig. 3.5) and Mn FTP-MNP (Fig. 3.7) are almost identical except for a reduced intensity of the peak at 355 °C and a reduced intensity and broadening of the peak at 775 °C attributed to the deoxidation of manganese oxide. Thermal analysis results correspond with results obtained from diffraction measurements and confirms the presence of FTP and MNP in the composite. The results also show that manganese incorporation alters the crystal properties in both doped magnetite and magnetite nanoparticles in the composite material.

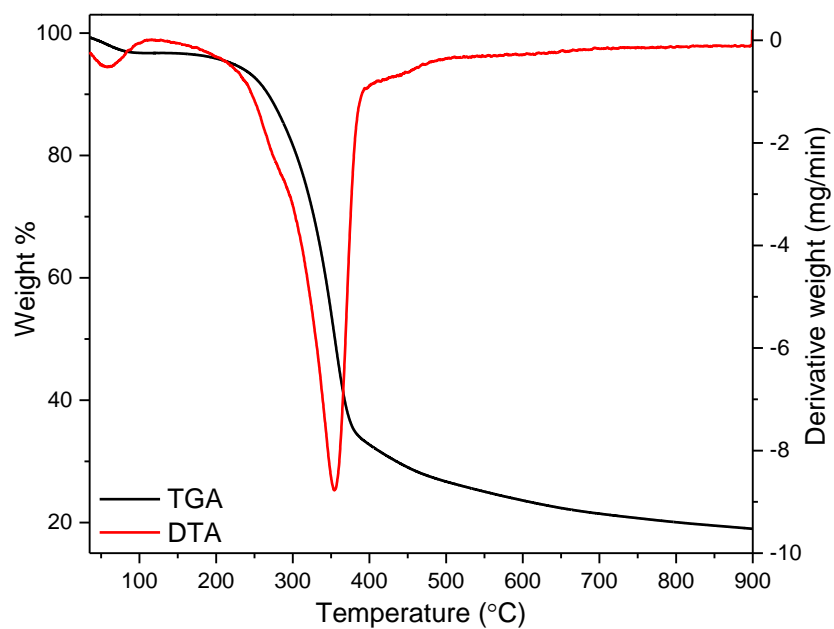


Fig. 3.3: Thermogravimetric and differential thermal analysis curves for FTP

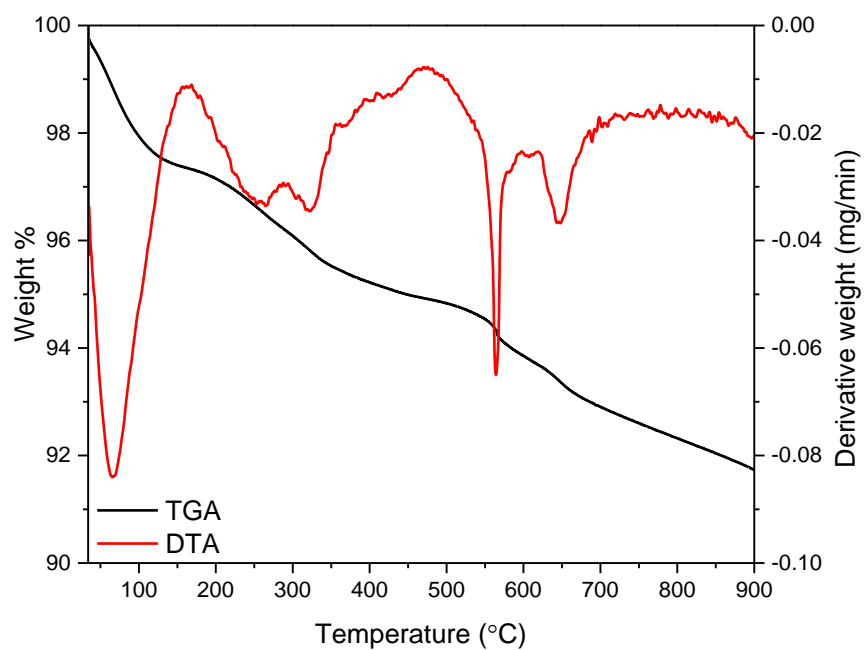


Fig. 3.4: Thermogravimetric and differential thermal analysis curves for MNP



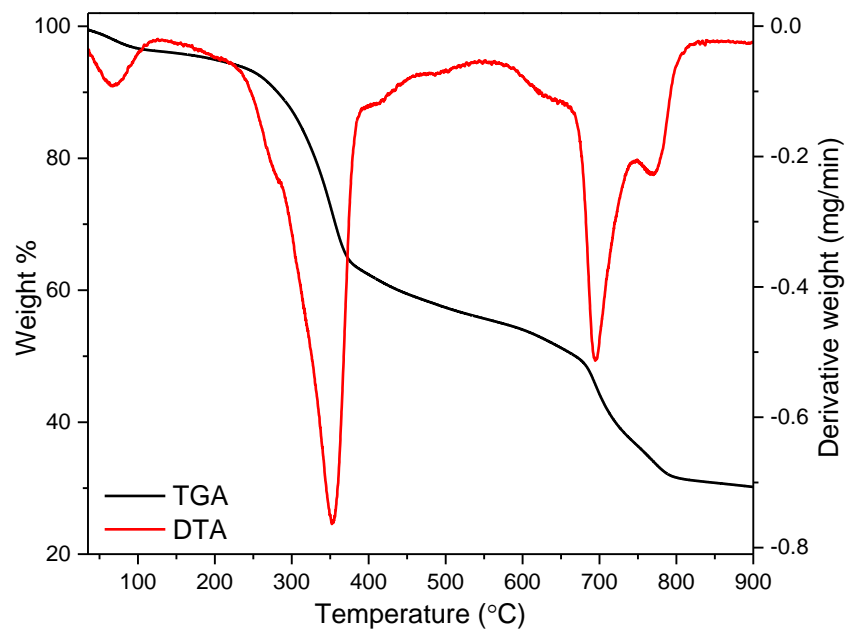


Fig. 3.5: Thermogravimetric and differential thermal analysis curves for FTP-MNP

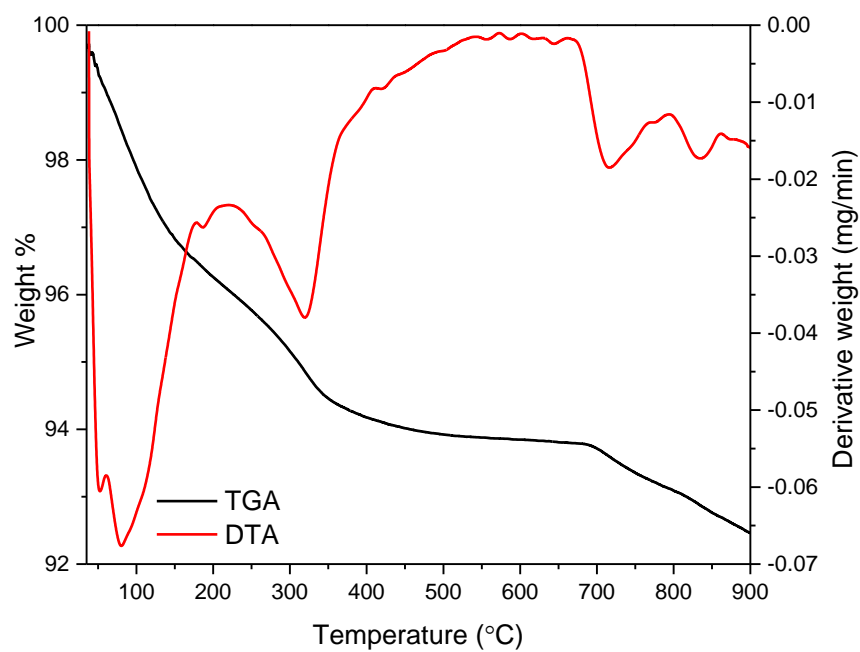


Fig. 3.6: Thermogravimetric and differential thermal analysis curves for Mn MNP

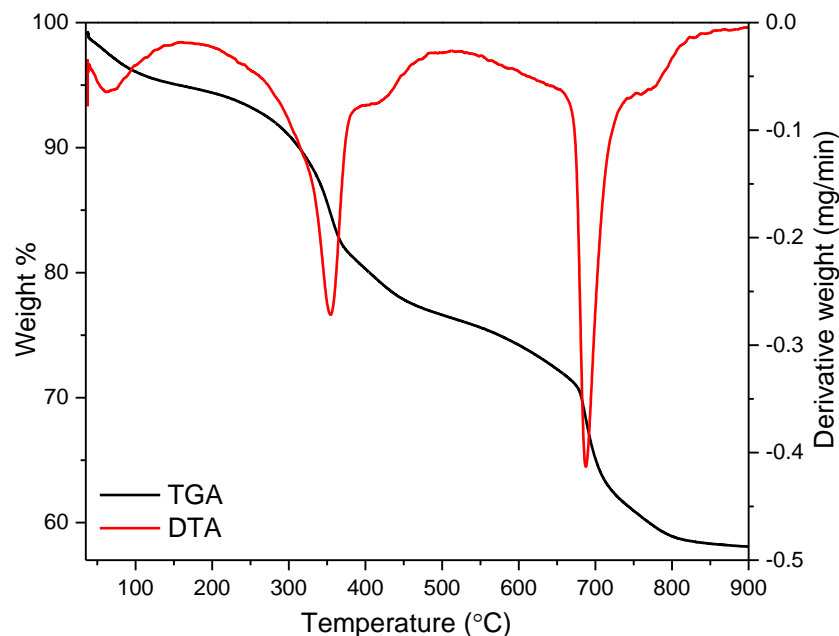


Fig. 3.7: Thermogravimetric and differential thermal analysis curves for Mn FTP-MNP

### 3.3.3 Infrared Analysis

Infrared analysis was carried out to determine the functional groups on the prepared materials. Characteristic peaks of lignocellulosic materials present on the pine cone surface (Fig. 3.8) include stretching vibrations of hydrogen bonds and aliphatic C-H bonds of cellulose at  $3338\text{ cm}^{-1}$  and  $2926\text{ cm}^{-1}$  respectively. Bands at  $1727$  and  $1649\text{ cm}^{-1}$  indicate vibrations of C=O and C-O groups of lignin while stretching vibrations of C-C bonds were observed at  $1509\text{ cm}^{-1}$ . The bands at  $1453$  and  $1424\text{ cm}^{-1}$  were assigned to O-C=O symmetric stretching vibrations and carboxylic acid C=O bond vibration was assigned to the band at  $1370\text{ cm}^{-1}$  with the bands at  $1261\text{ cm}^{-1}$  and  $1226\text{ cm}^{-1}$  representing C-O stretching vibrations. The bending vibrations of ketone, lactone and ether C-O groups were assigned to  $1028\text{ cm}^{-1}$ . Fenton's treatment did not introduce any new bands on the infrared spectrum of pine cone implying that the treatment did not significantly alter the pine cone structure but only resulted in the modification of some functional groups (Kupeta *et al.*, 2018; Ofomaja *et al.*, 2012).

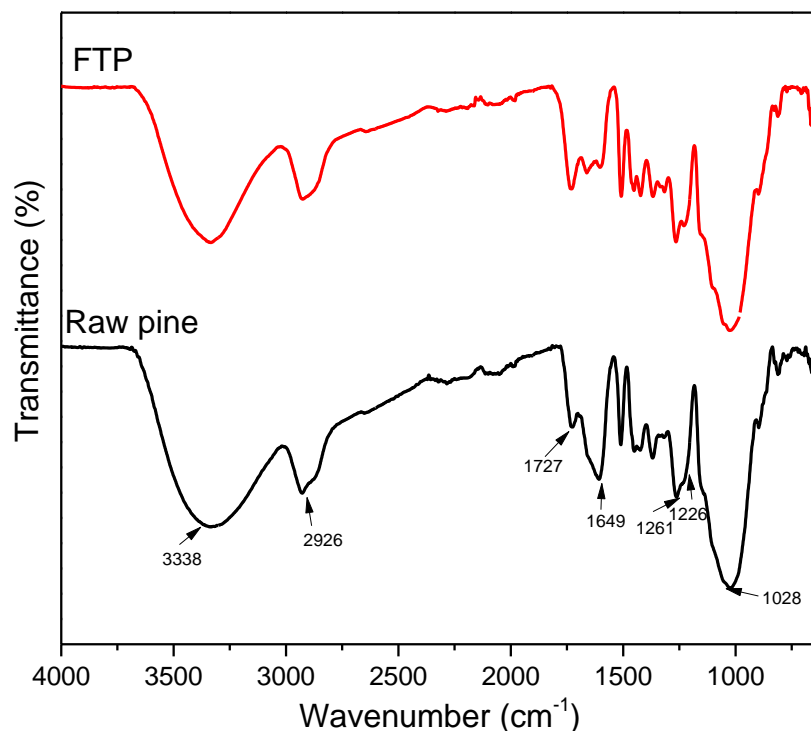


Fig. 3.8: FT-IR spectra of (a) Raw pine cone powder, (b) Fenton's treated pine cone powder (FTP)

The changes in the spectra (Fig. 3.8) included: (i) an increase in intensity and broadening of the peak at  $3338\text{ cm}^{-1}$ , (ii) increasing intensity and shifting of the bands at  $1727$  and  $1649\text{ cm}^{-1}$  to  $1724$  and  $1607\text{ cm}^{-1}$  respectively, and (iii) increasing in intensity of the bands at  $1261$  and  $1226\text{ cm}^{-1}$ . The increase in intensity and broadening of the O-H peak indicates oxidation of surface groups as a result of Fenton's treatment (Ofomaja *et al.*, 2012). An increase in intensity of the C=O and C-O bands is a result of the formation of carboxylic acid and aldehyde groups during peroxide oxidation (Kupeta *et al.*, 2018). Fenton's oxidation therefore increased oxygen containing functional groups which are responsible for binding pollutants. Fenton's treatment also resulted in the oxidation of organic components in carbonaceous materials by hydroxyl radicals generated from the reaction of hydrogen peroxide and ferrous ions as described in equation 3.5 and 3.6 (Ofomaja *et al.*, 2012). The radicals created are transferred to the carbonaceous material (RH) thus breaking down the organic matrix and producing radicals ( $R^{\bullet}$ ) which can be oxidized to breakdown recalcitrant organics that may contaminate the treated water by raising its chemical oxygen demand (Argun *et al.*, 2008).



The Infrared spectrum of magnetite nanoparticles (Fig. 3.9) shows the presence of hydroxyl groups on the surface from adsorbed water (Cornell & Schwertmann, 2003). These hydroxyl groups are chemically reactive in aqueous environments since they provide electron pairs and a dissociative hydrogen atom allowing the oxide to react with both acids and bases (Cornell & Schwertmann, 2003). The surface hydroxyl groups therefore provide binding sites for both pollutants and surface groups from pine cone during composite formation. Pine cone binding resulted in a decrease in intensity and shift of the hydroxyl peak ( $3328\text{ cm}^{-1}$ ) in Figure 3.10 (Cao *et al.*, 2014). A peak at  $437\text{ cm}^{-1}$  in the magnetite spectrum confirmed the formation of iron oxide particles. On the composite spectrum, aliphatic stretching vibrations from pine cone ( $2883\text{ cm}^{-1}$ ) and Fe-O bond vibration at  $555\text{ cm}^{-1}$  (Fig. 3.9) confirms the presence of both pine cone and iron oxide particles in the composite (Cao *et al.*, 2014). Manganese doping of the magnetite particles resulted in a shift of the Fe-O peak from  $435\text{ cm}^{-1}$  to  $466\text{ cm}^{-1}$  (Fig. 3.10). The introduction of a peak at  $552\text{ cm}^{-1}$  attributed to Mn-substituted iron oxyhydroxide confirms the introduction of manganese into the iron oxide structure and its dissolution as a solid solution (Lakshmipathiraj *et al.*, 2006).

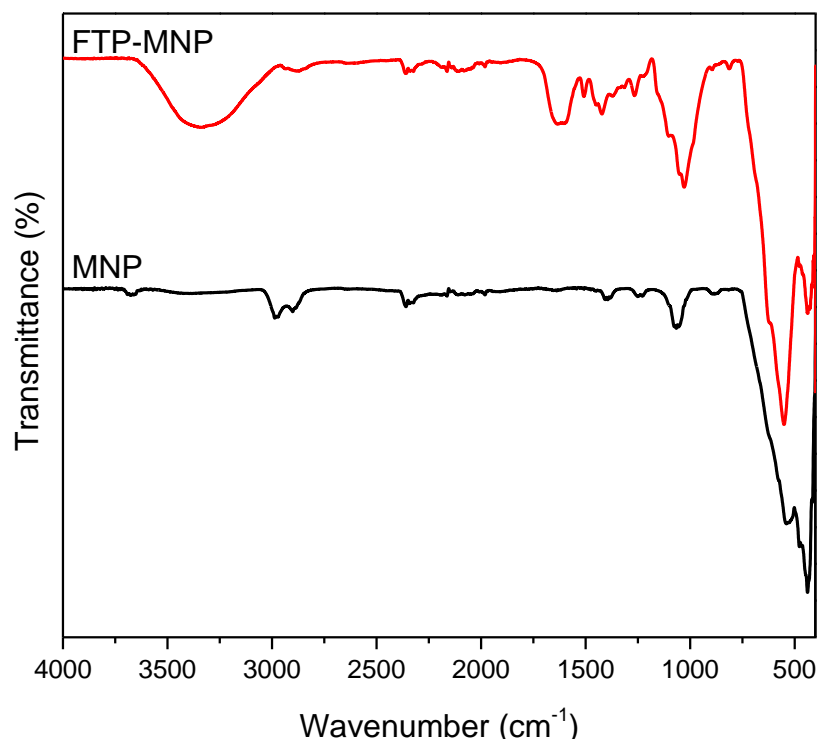


Fig. 3.9: Infrared spectra of magnetite nanoparticles (MNP) and Fenton's treated pine-magnetite composite (FTP-MNP)

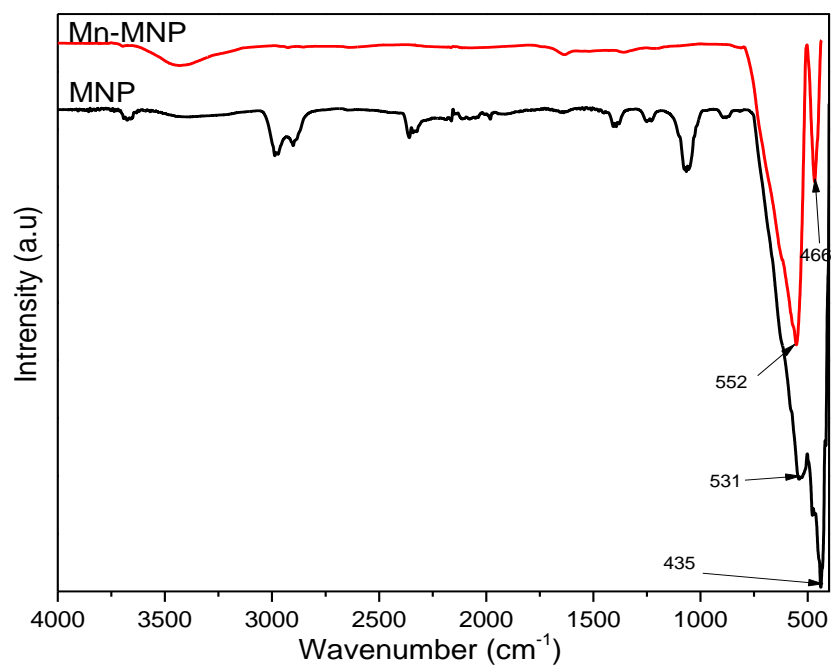


Fig. 3.10: Infrared spectra of magnetite nanoparticles (MNP) and manganese doped magnetite nanoparticles (Mn MNP)

### 3.3.4 Surface Properties

The Brunauer Emmet Teller (BET) surface area of the synthesized materials was determined to effectively study the effect of modification on the surface area of materials. The results in Table 3.1 indicate that magnetite incorporation significantly increases the surface area of the composite and manganese doping further increases the surface area of magnetite particles. The surface area of the particles was in the order Mn MNP>MNP>Mn FTP-MNP>FTP-MNP>FTP. These results indicate that nitrogen adsorption was highest in magnetite containing samples and decreased with the introduction of FTP. The incorporation of magnetite therefore improves not only FTP's thermal stability but significantly improves the surface area which is important in the consideration of a good adsorbent. Pore diameters were however higher in FTP due to the micro-sized powder that was used. In manganese doped particles the pore sizes were reduced due to the formation of MnO<sub>2</sub> blocking pores. The presence of MnO<sub>2</sub> on the surface provides additional binding sites, therefore even with lower pore sizes adsorption capacities could still be increased on the additional functional groups presented by binding manganese as presented by FTIR results (Liu *et al.*, 2015).

Table 3.1: BET Surface area and pore characteristics for as-synthesized materials

	<b>FTP</b>	<b>MNP</b>	<b>FTP-MNP</b>	<b>Mn MNP</b>	<b>Mn FTP-MNP</b>
Surface Area (m <sup>2</sup> g <sup>-1</sup> )	4.1694	113.5977	52.7627	127.2668	103.3091
Pore Volume (cm <sup>3</sup> g <sup>-1</sup> )	0.008828	0.623067	0.151357	0.345529	0.247746
Average Pore Diameter (nm)	152.0006	19.8914	12.1962	10.9262	9.8189

To further investigate the effects of modifications on the suitability of the synthesized materials for adsorption, the iso-electric point or point of zero charge (pH<sub>PZC</sub>) for each material was determined and recorded in Table 3.2. At the isoelectric point, the net surface charge is 0 therefore the material is neither negatively nor positively charged and is effectively neutral. Below the iso-electric point, the surface possesses a positive charge and attracts negatively charged ions through electrostatic attraction. Above the point of zero charge, the surface has a net negative charge hence attracting positively charged ions. The isoelectric point of raw pine cone was reported to be pH 7.49 (Ofomaja *et al.*, 2009, 2015) while the observed iso-electric point for FTP was 2.42 implying that Fenton's oxidation resulted in increased acidity of pine cone surface (Ofomaja *et al.*, 2012).

Oxidation of surface groups resulting in more acidic groups was also observed from infrared spectra.

Table 3.2: Point of zero charge results for as-synthesized materials

	<b>FTP</b>	<b>MNP</b>	<b>FTP-MNP</b>	<b>Mn MNP</b>	<b>Mn FTP-MNP</b>
pH <sub>PZC</sub>	2.4233	7.1216	6.3218	6.7567	6.8024

Iron atoms on MNP surfaces coordinate with H<sub>2</sub>O molecules which readily dissociate resulting in hydroxyl functionalized surfaces. These surface hydroxyl groups are amphoteric reacting with either acids or bases resulting in a near neutral pH<sub>PZC</sub>. MNP surfaces can either be negatively or positively charged depending on the pH of the solution. Below the isoelectric point, the surface is protonated leading to the formation of  $\equiv Fe-OH_2^+$  resulting in a net positive charge. Above the isoelectric point, the surface hydroxyl groups are deprotonated forming  $\equiv Fe-O^-$  surface groups (Dias *et al.*, 2011). The observed isoelectric point of pH 7.1 is in good agreement with reported values for magnetite particles at pH 6.8 (Badrudodoza *et al.*, 2013; Dias *et al.*, 2011), 6.5 (Aredes *et al.*, 2012), 6.78 (Banerjee & Chen, 2007). The attachment of FTP on the magnetite surface was further confirmed by the lowering of the isoelectric point upon composite formation (Table 3.2). Banerjee and Chen (2007) also reported a shift in magnetite isoelectric point after modification with gum arabic (Banerjee & Chen, 2007).

### 3.3.5 Electron Microscopy

In Fig. 3.11a Fenton's treated pine cone powder was observed to have a smooth porous surface which allows for sequestration of ions (Deniz, 2015). Fig. 3.11b shows that the prepared nanoparticles were agglomerated, possibly due to high surface energies resulting from their small sizes (Hua *et al.*, 2012). During the formation of magnetite nanoparticles ferric and ferrous ions are precipitated in the presence of hydroxide ions to form nanoparticles. The nanoparticle surfaces are therefore covered with excess hydroxyl groups from solution and these group interactions as well as magnetic attraction increase agglomeration (Alqadami *et al.*, 2016). In the presence of pine cone powder, magnetite particles are precipitated within the pores (Fig. 3.11c) leading to breakage of the pine cone hence exposing more surfaces while simultaneously stabilizing the nanoparticles (Fig. 3.11d) (Panneerselvam *et al.*, 2011).

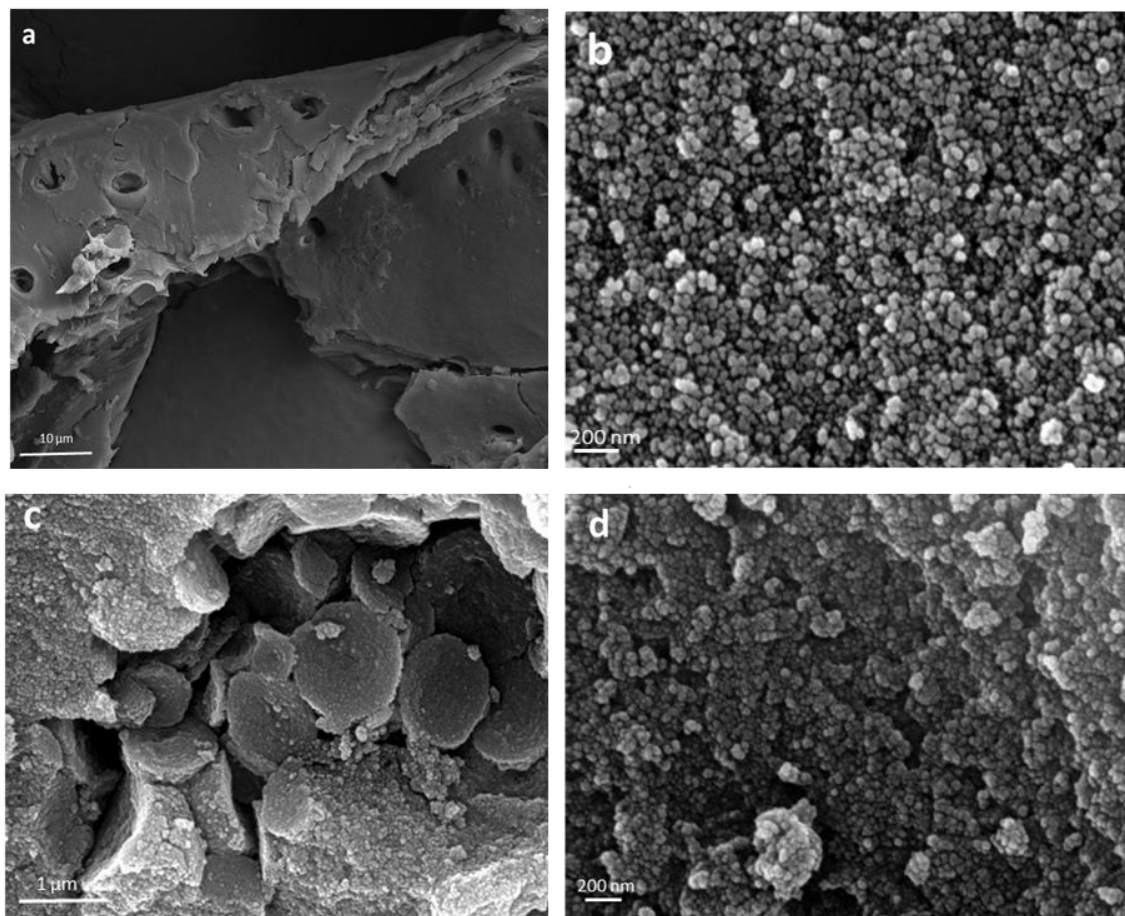


Fig. 3.11: SEM image of pine cone powder (a), iron oxide nanoparticles(b) and pine cone -iron oxide nanocomposite (c) and (d)

TEM micrographs of MNP (Fig. 3.12a) and FTP-MNP (Fig. 3.12b) show that the particles are spherical and nanoparticles forming the composite have better separation than the pristine particles (MNP). This was due to the precipitation of magnetite nanoparticles onto FTP hence an interaction between the surface groups of pine cone and nanoparticle surface thus controlling the particle growth therefore lowering their surface energies leading to less aggregation (Fig. 3.12b). In Figure 3.12a, electron microscopy shows that magnetite nanoparticles are aggregated possibly due to high surface energies and magnetism (Kumari *et al.*, 2015). A physical mixture of MNP and FTP (Fig. 3.12c) showed a significant difference from the synthesized composite. In the mixture, a carbon film from pine cone was distributed over the nanoparticles contrasting the uniform composition in the synthesized composite. Size measurement from TEM micrographs revealed that the bare nanoparticles and nanoparticles on the composite had diameters of  $7.77 \pm 1.17$  nm and  $6.86 \pm 0.93$



nm respectively. The sizes were comparable to those estimated from the diffraction spectra in Figure 3.12 of 7.2 nm and 6.9 nm for nanoparticles and particles on the composite respectively.

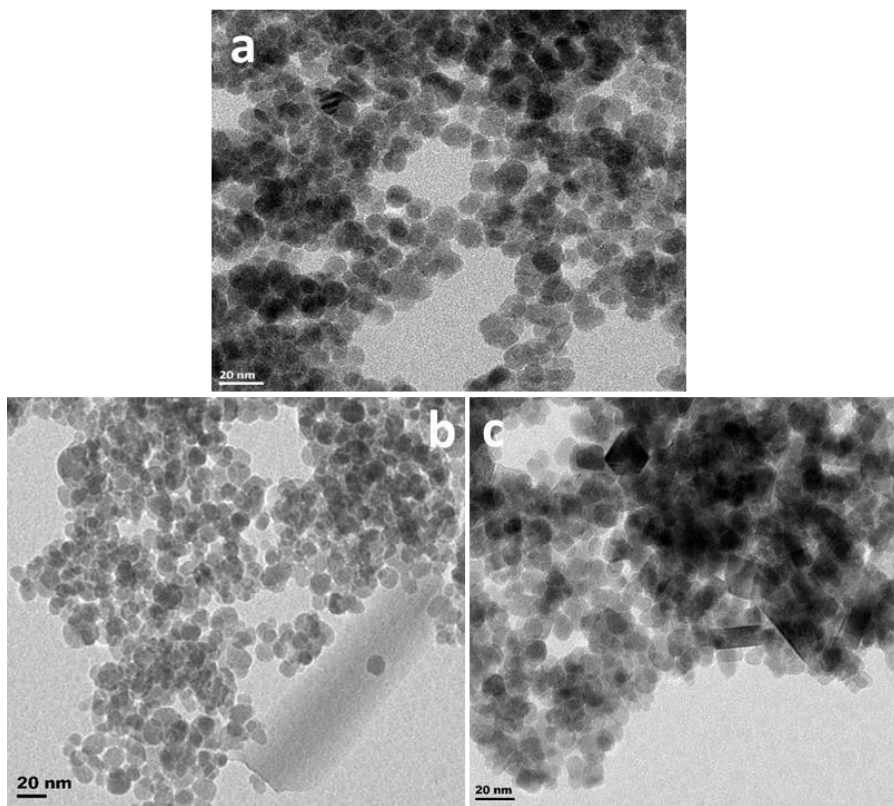


Fig. 3.12: TEM micrographs of (a) MNP, (b) FTP-MNP and (c) Physical mixture of FTP and MNP

### 3.3.6 Magnetic Measurements

The prepared nanoparticles and nanocomposite formed dispersions in water (Fig. 3.13) and were retained allowing the water to be decanted upon the introduction of a permanent magnet. Introduction of pine cone to coat the particles did not alter the magnetic properties of the nanoparticles but instead resulted in the formation of a uniform magnetic nanocomposite.

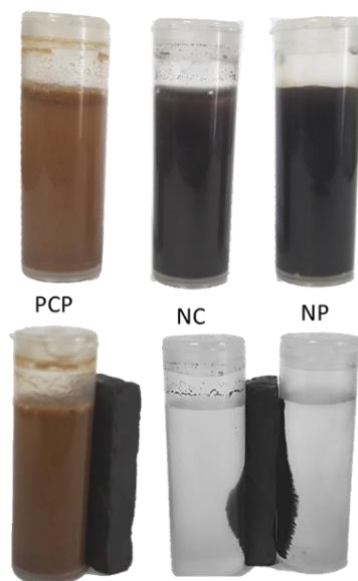


Fig. 3.13: Pine cone powder (PCP), Nanocomposite (NC) and Nanoparticles (NP) dispersed in water and magnetic separation of Nanocomposite (NC) and Nanoparticles (NP)

Magnetization curves of the as-synthesized composite at room temperature (Fig. 3.14) showed no hysteresis and the saturation magnetization ( $M_s$ ) value of 27.2 emu/g (Table 3.3) indicated that the synthesized composite was superparamagnetic (Mahdavi *et al.*, 2013). The saturation magnetization ( $M_s$ ) for synthesized bare magnetite nanoparticles was 64.7 emu/g and was thus lower than that of bulk magnetite (92 emu/g) as a result of the smaller particle size since magnetization is dependent on particle size and composition (Wu *et al.*, 2013; Zaitsev *et al.*, 1999). The incorporation of pine cone to form the composite led to a reduction in remanence magnetization from 2.4 to 0.4 (Table 3.3) indicating that the agglomeration in the samples due to residual magnetism was lower for the particles in the composite as compared to the bare particles. With the formation of the composite, coercivity of the particles was reduced from 24.9 to 9.7 thereby enhancing their superparamagnetism (Mohammadi & Barikani, 2014). Squareness values were 0.04 and 0.01 for the bare nanoparticles and composite indicating that both the nanoparticles and composite were superparamagnetic (Wu *et al.*, 2013). Particle sizes of bare nanoparticles and particles on the composite as determined by TEM analyses confirmed that they were <30nm in size which is the threshold size for superparamagnetism in magnetite particles (O'Brien *et al.*, 1996). Manganese doping of magnetite nanoparticles resulted in a 6% increase of the particles saturation magnetization with the magnetization of particles on the composite also increasing upon

doping. Manganese doping increases the magnetic susceptibility of magnetite particles due to the presence of five single electrons on  $\text{Mn}^{2+}$ .

Table 3.3: Magnetic properties of the as-synthesized adsorbents

Material	Saturation Magnetization ( $\text{emu g}^{-1}$ )	Remanence Magnetization ( $\text{emu g}^{-1}$ )	Coercivity (G)	Squareness ( $M_r M_s^{-1}$ )
FTP	4.6	0.02	60.2	0.004
MNP	64.7	2.48	24.9	0.038
FTP-MNP	27.2	0.40	9.7	0.014
Mn MNP	68.3	1.13	10.9	0.017
Mn FTP-MNP	57.7	0.51	6.8	0.009

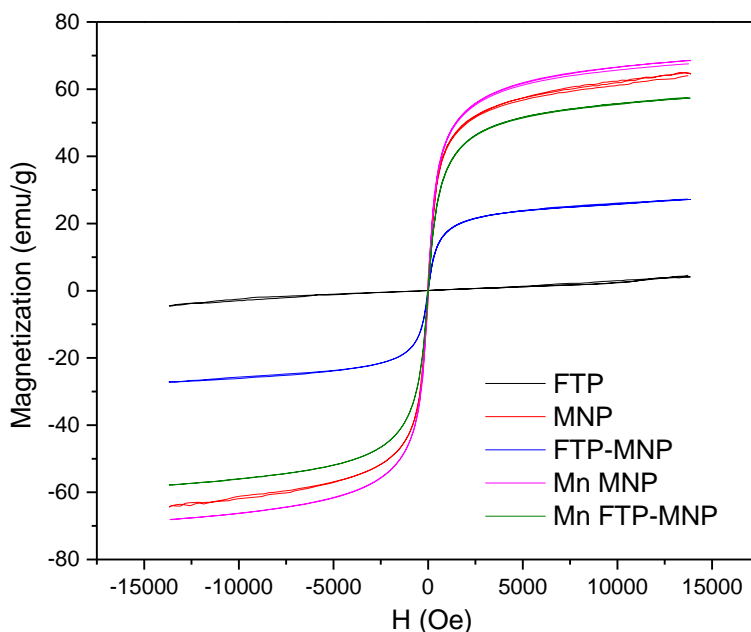


Fig. 3.14: Magnetizations curves of as-synthesized adsorbents

### 3.3.7 X-ray Photoelectron Spectroscopic Analysis

X-ray Photoelectron Spectroscopic analysis (XPS) was used to determine the surface states present in FTP-MNP and confirm the formation of magnetite nanoparticles. The survey spectrum (Fig. 3.17) shows peaks at 709, 529 and 284 eV indicating the presence of Fe, O and C respectively. Photoelectron peaks at 722.6 eV and 709.3 eV (Fig. 3.16) corresponding to  $\text{Fe } 2p_{1/2}$  and  $\text{Fe } 2p_{3/2}$  respectively compared well to literature values for  $\text{Fe}_3\text{O}_4$  (Poulin *et al.*, 2010) and were lower than values reported for  $\gamma\text{-Fe}_2\text{O}_3$  at 725.3 and 711.6 eV for  $\text{Fe } 2p_{1/2}$  and  $\text{Fe } 2p_{3/2}$  (Yamashita & Hayes, 2008; Yu *et al.*, 2013). The ratio of the  $2p_{3/2}/2p_{1/2}$  transition was 1.85 while the ratio of  $\text{Fe}^{2+}/\text{Fe}^{3+}$

in the  $2p_{3/2}$  transition was 0.5, which are in good agreement with reported values for magnetite (Wilson & Langell, 2014). The O1s spectrum (Fig. 3.17) was deconvoluted into three peaks at 529.6, 530.9 and 531.9 eV, the peaks were assigned to Fe-O in  $\text{Fe}_3\text{O}_4$ , and C-O and O-H from FTP. The C1s peak was deconvoluted into three components (Fig. 3.18) corresponding to C-C bonds, C-O bonds and C=O from lignin and cellulose components of pine cone (Dupont & Guillon, 2003).

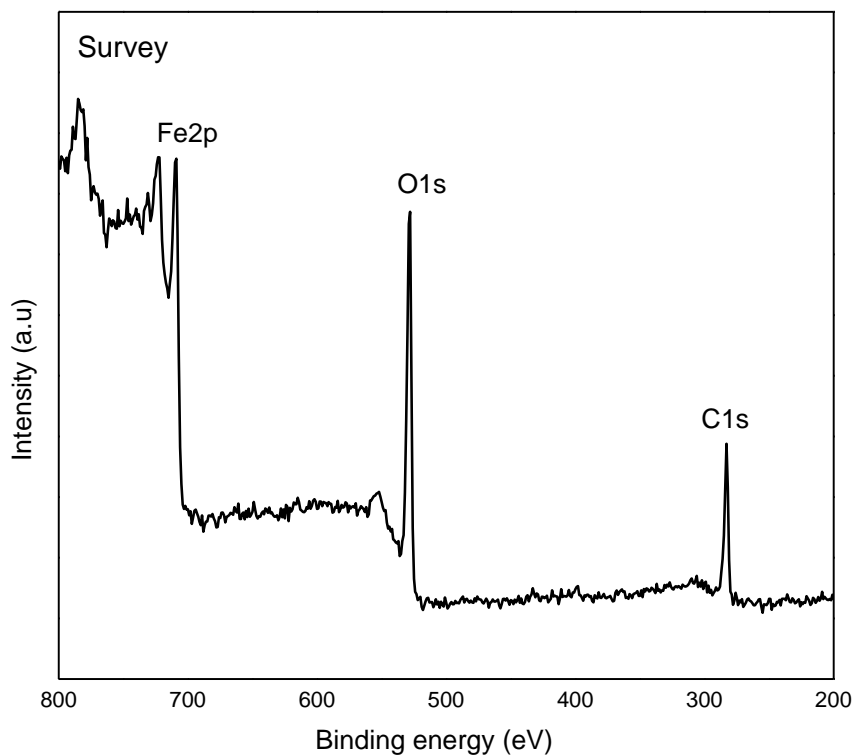


Fig. 3.15: XPS Survey spectrum of FTP-MNP

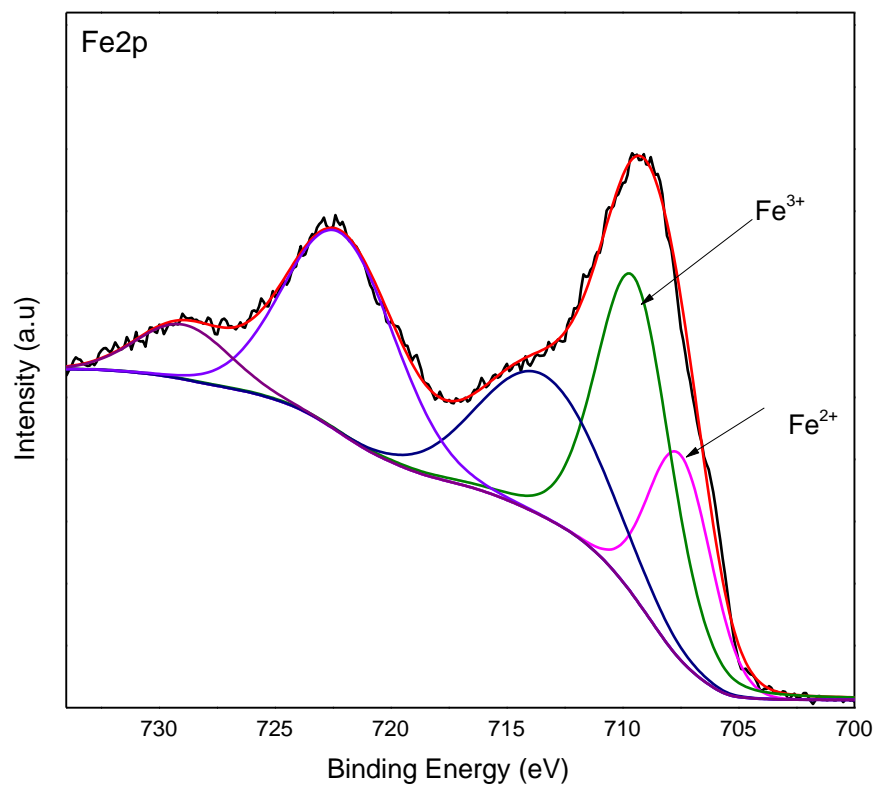


Fig. 3.16: Fe2p spectrum of FTP-MNP

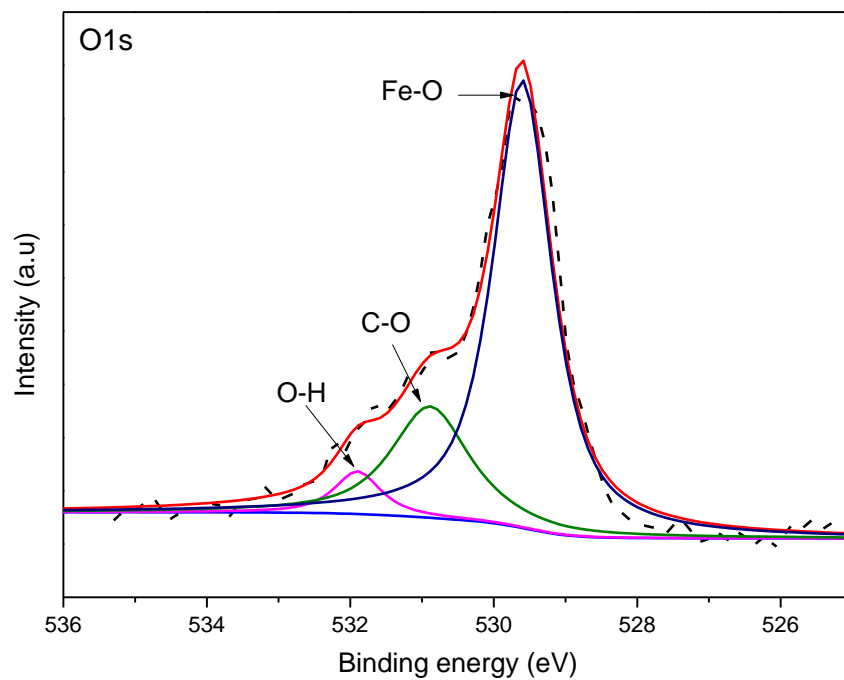


Fig. 3.17: O1s spectrum of FTP-MNP

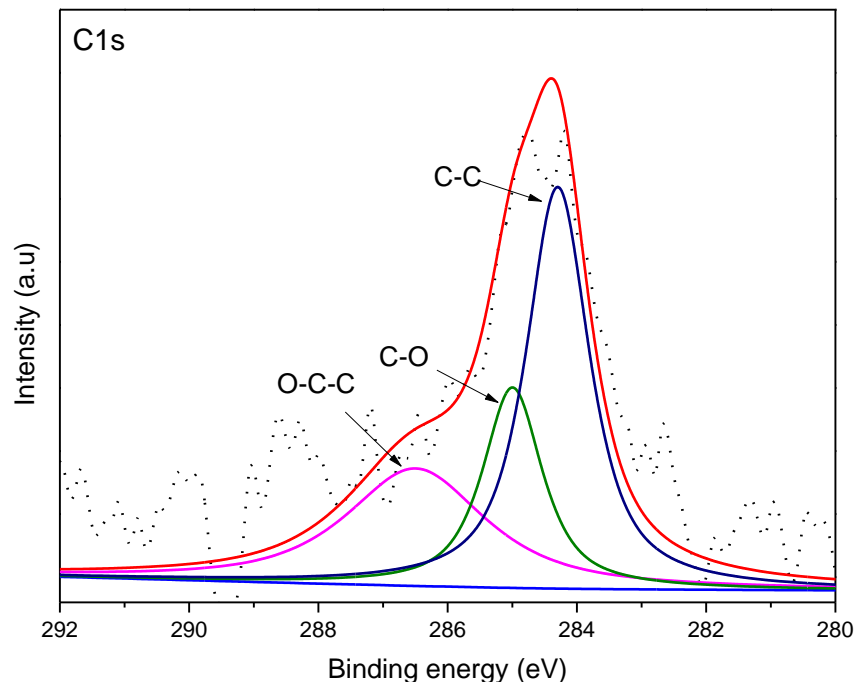


Fig. 3.18: C1s spectrum of FTP-MNP

### 3.4 Conclusion

The adsorbent materials were successfully synthesized and characterized. Diffraction studies revealed that the synthesized magnetite nanoparticles had an inverse cubic spinel structure. Composite formation with FTP did not alter the nanoparticles crystal structure and maintained the crystallinity of the material. The formation of  $\text{Mn}_x\text{Fe}_{(3-x)}\text{O}_4$  was successfully carried out with varying dopant amounts. Doping did not alter the crystal structure of magnetite resulting only in an increase of lattice parameters and cell volume because of the larger manganese ions occupying ferric ion lattices. All the synthesized materials were thermally stable with MNP significantly improving the thermal stability and surface areas of FTP. Electron microscopy revealed that the synthesized particles were spherical in shape and particles on the composite retained their morphology. Manganese doping increased the saturation magnetization of FTP-MNP while slightly lowering the saturation magnetization of MNP. The modifications on MNP therefore improved their properties, hence improving their suitability for heavy metal adsorption.

### 3.5 References

- AHN, T., KIM, J.H., YANG, H.M., LEE, J.W., & KIM, J.D. (2012). Formation pathways of magnetite nanoparticles by coprecipitation method. *J. Phys. Chem. C*. 116. p.6069–6076.
- ALQADAMI, A.A., NAUSHAD, M., ABDALLA, M.A., AHAMAD, T., ALOTHMAN, Z.A., & ALSHEHRI, S.M. (2016). Synthesis and characterization of Fe<sub>3</sub>O<sub>4</sub>@TSC nanocomposite: Highly efficient removal of toxic metal ions from aqueous medium. *RSC Adv.* 6. p.22679–22689.
- AREDES, S., KLEIN, B., & PAWLIK, M. (2012). The removal of arsenic from water using natural iron oxide minerals. *J. Clean. Prod.* 29–30. p.208–213.
- ARGUN, M.E., DURSUN, S., KARATAS, M., & GÜRÜ, M. (2008). Activation of pine cone using Fenton oxidation for Cd(II) and Pb(II) removal. *Bioresour. Technol.* 99. p.8691–8.
- BADRUDDOZA, A.Z.M., SHAWON, Z.B.Z., TAY, W.J.D., HIDAJAT, K., & UDDIN, M.S. (2013). Fe 3O 4/cyclodextrin polymer nanocomposites for selective heavy metals removal from industrial wastewater. *Carbohydr. Polym.* 91. p.322–332.
- BANERJEE, S.S., & CHEN, D.H. (2007). Fast removal of copper ions by gum arabic modified magnetic nano-adsorbent. *J. Hazard. Mater.* 147. p.792–799.
- CAO, C., XIAO, L., CHEN, C., SHI, X., CAO, Q., & GAO, L. (2014). In situ preparation of magnetic Fe<sub>3</sub>O<sub>4</sub>/chitosan nanoparticles via a novel reduction–precipitation method and their application in adsorption of reactive azo dye. *Powder Technol.* 260. p.90–97.
- CASULA, M.F., CONCA, E., BAKAIMI, I., SATHYA, A., MATERIA, M.E., CASU, A., FALQUI, A., SOGNE, E., PELLEGRINO, T., & KANARAS, A.G. (2016). Manganese doped-iron oxide nanoparticle clusters and their potential as agents for magnetic resonance imaging and hyperthermia. *Phys. Chem. Chem. Phys.* 18. p.16848–16855.
- CORNELL, R.M., & SCHWERTMANN, U. The Iron Oxides. 2nd Edition ed. Weinheim, FRG: Wiley-VCH Verlag GmbH & Co. KGaA, 2003.
- DARROUDI, M., HAKIMI, M., GOODARZI, E., & KAZEMI OSKUEE, R. (2014). Superparamagnetic iron oxide nanoparticles (SPIONs): Green preparation, characterization and their cytotoxicity effects. *Ceram. Int.* 40. p.14641–14645.

DEEPAK, F.L., BAÑOBRE-LÓPEZ, M., CARBÓ-ARGIBAY, E., CERQUEIRA, M.F., PIÑEIRO-REDONDO, Y., RIVAS, J., THOMPSON, C.M., KAMALI, S., RODRÍGUEZ-ABREU, C., KOVNIR, K., & KOLEN'KO, Y. V. (2015). A Systematic Study of the Structural and Magnetic Properties of Mn-, Co-, and Ni-Doped Colloidal Magnetite Nanoparticles. *J. Phys. Chem. C*. 119. p.11947–11957.

DENIZ, F. (2015). Dye Biosorption from Water Employing Chemically Modified Calabrian Pine Cone Shell as an Effective Biosorbent. *Environ. Prog. Sustain. Energy*. 34. p.1267–1278.

DIAS, A.M.G.C., HUSSAIN, A., MARCOS, A.S., & ROQUE, A.C.A. (2011). A biotechnological perspective on the application of iron oxide magnetic colloids modified with polysaccharides. *Biotechnol. Adv.* 29. p.142–155.

DUMAN, G., ONAL, Y., OKUTUCU, C., ONENC, S., & YANIK, J. (2009). Production of Activated Carbon from Pine Cone and Evaluation of Its Physical , Chemical , and Adsorption Properties. *Energy & Fuels*. 23. p.2197–2204.

DUPONT, L., & GUILLON, E. (2003). Removal of hexavalent chromium with a lignocellulosic substrate extracted from wheat bran. *Environ. Sci. Technol.* 37. p.4235–4241.

EBRAHIMIAN PIRBAZARI, A., SABERIKHAH, E., & HABIBZADEH KOZANI, S.S.S. (2014). Fe<sub>3</sub>O<sub>4</sub>-wheat straw: Preparation, characterization and its application for methylene blue adsorption. *Water Resour. Ind.* 7–8. p.23–37.

HUA, M., ZHANG, S., PAN, B., ZHANG, W., LV, L., & ZHANG, Q. (2012). Heavy metal removal from water/wastewater by nanosized metal oxides: A review. *J. Hazard. Mater.* 211–212. p.317–331.

KUMARI, M., PITTMAN, C.U., & MOHAN, D. (2015). Heavy metals [chromium (VI) and lead (II)] removal from water using mesoporous magnetite (Fe<sub>3</sub>O<sub>4</sub>) nanospheres. *J. Colloid Interface Sci.* 442. p.120–32.

KUPETA, A.J.K., NAIDOO, E.B., & OFOMAJA, A.E. (2018). Kinetics and equilibrium study of 2-nitrophenol adsorption onto polyurethane cross-linked pine cone biomass. *J. Clean. Prod.* 179.

KWON, J.H., WILSON, L.D., & SAMMYNAIKEN, R. (2014). Synthesis and characterization of magnetite and activated carbon binary composites. *Synth. Met.* 197. p.8–17.



- LAKSHMIPATHIRAJ, P., NARASIMHAN, B.R. V, PRABHAKAR, S., & BHASKAR RAJU, G. (2006). Adsorption studies of arsenic on Mn-substituted iron oxyhydroxide. *J. Colloid Interface Sci.* 304. p.317–22.
- LI, W.S., SHEN, Z.X., LI, H.Y., SHEN, D.Z., & FAN, X.W. (2001). Blue shift of Raman peak from coated TiO<sub>2</sub> nanoparticles. *J. Raman Spectrosc.* 32. p.862–865.
- LIU, Y., LUO, C., CUI, G., & YAN, S. (2015). Synthesis of manganese dioxide/iron oxide/graphene oxide magnetic nanocomposites for hexavalent chromium removal. *RSC Adv.* 5. p.54156–54164.
- MAHDAVI, M., AHMAD, M. BIN, HARON, M.J., NAMVAR, F., NADI, B., AB RAHMAN, M.Z., & AMIN, J. (2013). Synthesis, surface modification and characterisation of biocompatible magnetic iron oxide nanoparticles for biomedical applications. *Molecules.* 18. p.7533–7548.
- MOHAMMADI, A., & BARIKANI, M. (2014). Synthesis and characterization of superparamagnetic Fe<sub>3</sub>O<sub>4</sub> nanoparticles coated with thiodiglycol. *Mater. Charact.* 90. p.88–93.
- NATA, I.F., SURESHKUMAR, M., & LEE, C.-K. (2011). One-pot preparation of amine-rich magnetite/bacterial cellulose nanocomposite and its application for arsenate removal. *RSC Adv.* 1. p.625.
- O'BRIEN, S.M., THOMAS, O.R.T., & DUNNILL, P. (1996). Non-porous magnetic chelator supports for protein recovery by immobilised metal affinity adsorption. *J. Biotechnol.* 50. p.13–25.
- OFOMAJA, A.E., & NAIDOO, E.B. (2011). Biosorption of copper from aqueous solution by chemically activated pine cone: A kinetic study. *Chem. Eng. J.* 175. p.260–270.
- OFOMAJA, A.E., NAIDOO, E.B., & MODISE, S.J. (2009). Removal of copper(II) from aqueous solution by pine and base modified pine cone powder as biosorbent. *J. Hazard. Mater.* 168. p.909–917.
- OFOMAJA, A.E., NGEMA, S.L., & NAIDOO, E.B. (2012). The grafting of acrylic acid onto biosorbents: Effect of plant components and initiator concentration. *Carbohydr. Polym.* 90. p.201–209.

- OFOMAJA, A.E., PHOLOS, A., & NAIDOO, E.B. (2015). Application of raw and modified pine biomass material for cesium removal from aqueous solution. *Ecol. Eng.* 82. p.258–266.
- OUMA, I.L.A., NAIDOO, E.B., & OFOMAJA, A.E. (2017). Iron oxide nanoparticles stabilized by lignocellulosic waste as green adsorbent for Cr(VI) removal from wastewater. *Eur. Phys. J. Appl. Phys.* 79. p.30401.
- PANNEERSELVAM, P., MORAD, N., & TAN, K.A. (2011). Magnetic nanoparticle (Fe<sub>3</sub>O<sub>4</sub>) impregnated onto tea waste for the removal of nickel(II) from aqueous solution. *J. Hazard. Mater.* 186. p.160–168.
- PARKINSON, G.S. (2016). Iron oxide surfaces. *Surf. Sci. Rep.* 71. p.272–365.
- POULIN, S., FRANÇA, R., MOREAU-BÉLANGER, L., & SACHER, E. (2010). Confirmation of X-ray photoelectron spectroscopy peak attributions of nanoparticulate iron oxides, using symmetric peak component line shapes. *J. Phys. Chem. C.* 114. p.10711–10718.
- PUERTA, M.C., & VALERGA, P. (1990). Thermal decomposition of a natural manganese dioxide: A laboratory experiment for undergraduate students. *J. Chem. Educ.* 67. p.344.
- RAJPUT, S., PITTMAN, C.U., & MOHAN, D. (2016). Magnetic magnetite (Fe<sub>3</sub>O<sub>4</sub>) nanoparticle synthesis and applications for lead (Pb<sup>2+</sup>) and chromium (Cr<sup>6+</sup>) removal from water. *J. Colloid Interface Sci.* 468. p.334–346.
- SHARMA, R., BISEN, D.P., SHUKLA, U., & SHARMA, B.G. (2012). X-ray diffraction : a powerful method of characterizing nanomaterials. *Recent Res. Sci. Technol.* 4. p.77–79.
- TAO, K., DOU, H., & SUN, K. (2008). Interfacial coprecipitation to prepare magnetite nanoparticles: Concentration and temperature dependence. *Colloids Surfaces A Physicochem. Eng. Asp.* 320. p.115–122.
- VARSHNEY, D., & YOGI, A. (2011). Structural and transport properties of stoichiometric Mn<sup>2+</sup>-doped magnetite: Fe<sub>3-x</sub>Mn<sub>x</sub>O<sub>4</sub>. *Mater. Chem. Phys.* 128. p.489–494.
- WARNER, C.L., CHOUYYOK, W., MACKIE, K.E., NEINER, D., SARAF, L. V., DROUBAY, T.C., WARNER, M.G., & ADDLEMAN, R.S. (2012). Manganese doping of magnetic iron oxide nanoparticles: Tailoring surface reactivity for a regenerable heavy metal sorbent. *Langmuir.* 28.

p.3931–3937.

WILSON, D., & LANGELL, M.A. (2014). XPS analysis of oleylamine/oleic acid capped Fe<sub>3</sub>O<sub>4</sub> nanoparticles as a function of temperature. *Appl. Surf. Sci.* 303. p.6–13.

WU, S., WANG, Z., HE, C., ZHAO, N., SHI, C., LIU, E., & LI, J. (2013). Synthesis of uniform and superparamagnetic Fe<sub>3</sub>O<sub>4</sub> nanocrystals embedded in a porous carbon matrix for a superior lithium ion battery anode. *J. Mater. Chem. A*. 1. p.11011.

WU, W., JIANG, C.Z., & ROY, V.A.L. (2016). Designed synthesis and surface engineering strategies of magnetic iron oxide nanoparticles for biomedical applications. *Nanoscale*. 8. p.19421–19474.

XU, P., HAN, X., WANG, C., ZHAO, H., WANG, J., WANG, X., & ZHANG, B. (2008). Synthesis of electromagnetic functionalized barium ferrite nanoparticles embedded in polypyrrole. *J. Phys. Chem. B*. 112. p.2775–2781.

YAMASHITA, T., & HAYES, P. (2008). Analysis of XPS spectra of Fe<sup>2+</sup> and Fe<sup>3+</sup> ions in oxide materials. *Appl. Surf. Sci.* 254. p.2441–2449.

YANG, L., MA, L., XIN, J., LI, A., SUN, C., WEI, R., REN, B.W., CHEN, Z., LIN, H., & GAO, J. (2017). Composition Tunable Manganese Ferrite Nanoparticles for Optimized T<sub>2</sub> Contrast Ability. *Chem. Mater.* 29. p.3038–3047.

YU, X., TONG, S., GE, M., ZUO, J., CAO, C., & SONG, W. (2013). One-step synthesis of magnetic composites of cellulose@iron oxide nanoparticles for arsenic removal. *J. Mater. Chem. A*. 1. p.959–965.

ZAITSEV, V.S., FILIMONOV, D.S., PRESNYAKOV, I.A., GAMBINO, R.J., & CHU, B. (1999). Physical and Chemical Properties of Magnetite and Magnetite-Polymer Nanoparticles and Their Colloidal Dispersions. *J. Colloid Interface Sci.* 212. p.49–57.

ZHENG, M., LU, J., & ZHAO, D. (2018). Effects of starch-coating of magnetite nanoparticles on cellular uptake, toxicity and gene expression profiles in adult zebrafish. *Sci. Total Environ.* 622–623. p.930–941.

### 4 Optimization of Adsorption Parameters for As(III) and Cr(VI) Adsorption onto the Prepared Adsorbents

#### 4.1 Introduction

Adsorption has been identified as a promising method for the remediation of heavy metal contaminated water because of its low cost, simplicity and ease of operation (Luo *et al.*, 2018). Though it has been successfully used to treat contaminated water, the adsorption process is influenced by different operational variables which need to be optimized to suit individual adsorbent-adsorbate systems (Santra & Sarkar, 2016). To optimize this process, the capacity of each adsorbent for adsorbate removal was monitored under different conditions to determine the conditions which provided optimum adsorbate removal while maximizing the adsorbent capacity. In this study adsorption of arsenite and hexavalent chromium was carried out separately on the adsorbents described in the previous chapter. The effects of solution pH, adsorbent mass, adsorbate and concentration on the adsorption of the arsenic and chromium on the prepared adsorbents are presented and compared.

This chapter discusses the optimization of adsorption parameters to determine optimum conditions applied during the adsorption of arsenite and chromium onto the previously described materials.

#### 4.2 Experimental

Similar experimental conditions were applied during the adsorption of both arsenic and chromium on the synthesized adsorbents. All experiments were run in batch mode with the optimum conditions established from previous experiments being used for all further experiments.

##### 4.2.1 Materials

All adsorbents used herein, were sourced and synthesized as described in Chapter 3. Hydrochloric acid (32%) was supplied by Merck, sodium arsenite ( $\text{NaAsO}_2$  >90%) was purchased from Sigma-Aldrich. Potassium dichromate ( $\text{K}_2\text{Cr}_2\text{O}_7$  >99 %) and Sodium Hydroxide ( $\text{NaOH}$  >98 %) were purchased from Associated Chemical Enterprises (South Africa). All chemicals were used as supplied without any further purification.

#### 4.2.2 Methods

Arsenite (As(III)) and hexavalent chromium (Cr(VI)) solutions were prepared by dissolving sodium arsenite and potassium dichromate respectively in deionized water.

To determine the effect of solution pH, adsorbent mass and concentration on arsenic and chromium adsorption, batch adsorption experiments were carried out. A Stock solution of  $1000 \text{ mg L}^{-1}$  was prepared and diluted to prepare solutions of desired concentrations. To determine the effect of solution pH, solutions of  $100 \text{ mg L}^{-1}$  were prepared in separate volumetric flasks and the solution pH in each flask was varied between 2 and 12 using 0.01 M HCl and 0.01 M NaOH. 0.5 g of each adsorbent was introduced into a separate sealable flask containing 100 mL solution and shaken in a water bath shaker at 200 rpm for 2 hours.

To study the effect of adsorbent mass on adsorption, solutions of  $100 \text{ mg L}^{-1}$  of each adsorbate were prepared. From each solution, 100 mL of each solution was transferred to a separate sealable flask and adsorbents of masses ranging from 0.1 g to 1.5 g were transferred into the solutions and agitated for 2 hours.

To study the effect of the initial solution concentration, solutions of concentrations ranging from  $25 \text{ mg L}^{-1}$  to  $200 \text{ mg L}^{-1}$  were prepared in separate flasks and adjusted to the previously determined optimum solution pH. 100 mL of each solution was transferred into a sealable flask and agitated with the adsorbents at the previously determined optimum mass.

After adsorption, As(V) and As(III) were separated using arsenic speciation cartridges (Metalsoft Centre, New Jersey, USA) (Meng *et al.*, 2000; Meng & Wang, 1998). The concentration of arsenite and total arsenic in solution were determined on a Thermo Fischer Scientific ICAP 7000 inductively coupled plasma-optical emission spectrometer (ICP-OES). Cr(VI) concentration was determined spectrophotometrically following the diphenyl-carbazide method at a wavelength of 540 nm (Bishop *et al.*, 2014). Total chromium concentration was determined on a Shimadzu AA 7000 Atomic Absorption Spectrophotometer with an air/acetylene flame and wavelength of 357.9 nm.

#### 4.3 Results and Discussions

Arsenic and chromium both occur in several oxidation states which exist simultaneously in nature therefore their adsorption is dependent not only on the adsorbate state but also on redox reactions

occurring during the adsorption process (Mohan & Pittman, 2006; Liu *et al.*, 2015; Monárrez-Cordero *et al.*, 2016; Roy *et al.*, 2017). These redox reactions are greatly affected by the solution properties as well as the surface properties of the adsorbent material. The effects of solution pH, adsorbent dosage and initial solution concentrations on the adsorption efficiency and capacity were investigated following one factor at a time with all the other factors being held constant.

$$E = [(C_0 - C_t) / C_0] \times 100 \quad (4.1)$$

$$q = (C_0 - C_t) / m \quad (4.2)$$

The adsorption efficiency and capacity were calculated following Equations 4.1 and 4.2 respectively, where  $E$  is the percentage adsorption efficiency,  $q$  is the adsorption capacity  $C_0$  is the initial solution concentration,  $C_t$  is the solution concentration after adsorption and  $m$  is the adsorbent dose (Padmavathy *et al.*, 2016).

#### 4.3.1 Effect of pH

Solution pH is a factor that significantly influences the adsorption process due to its effects on both the adsorbent surface and adsorbate ions (Sarı *et al.*, 2011). The effect of pH on arsenite and hexavalent chromium adsorption onto the synthesized materials was studied from pH 2-12. As solution pH was increased, the arsenite adsorption capacity for all adsorbents increased up to pH 8 and decreased as the pH was increased further (Fig. 4.1). At solution pH 2-9 arsenite species are predominantly non-ionic ( $H_3AsO_3$ ) and are anionic ( $H_2AsO_3^-$ ) above pH 9 (Katsoyiannis & Zouboulis, 2002). The isoelectric points for the as-synthesized materials (Section 3.3.4) indicate that at pH above 7 all the surfaces are negatively charged therefore cannot undergo electrostatic attraction with the non-ionic arsenite species. Unprotonated surface groups can however be coordinated with the non-ionic arsenite between pH 7-9 (Sarı *et al.*, 2011). Above pH 9, anionic species compete for adsorption sites with excess hydroxyl ions in solution and further increase in pH results in increased repulsion (Lunge *et al.*, 2014; Sarı *et al.*, 2011).

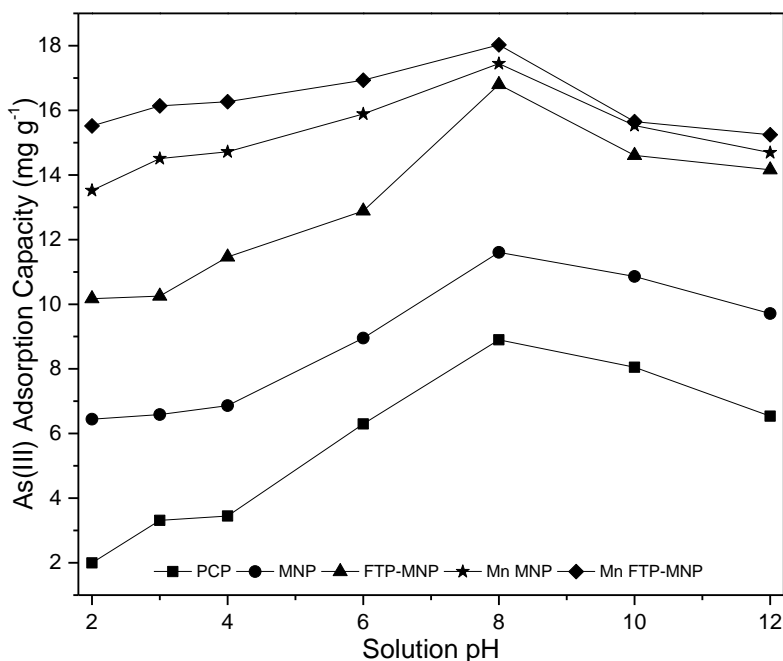


Fig. 4.1: Effect of solution pH on arsenite adsorption onto prepared adsorbents

Figure 4.2 shows that the adsorption capacity for hexavalent chromium is higher at low solution pH and decreased with increasing solution pH for all adsorbents. The stability of different hexavalent chromium species in solution is highly dependent on the solution pH with species occurring as  $\text{H}_2\text{CrO}_4$ ,  $\text{HCrO}_4^-$ ,  $\text{Cr}_2\text{O}_7^{2-}$  and  $\text{CrO}_4^{2-}$  with increasing solution pH from pH <1, pH 2-6 and pH >6 respectively (Ghosh *et al.*, 2015; Saha & Orvig, 2010). At acidic pH there is a high concentration of hydrogen ions in the solution which protonate surface binding sites allowing the negatively charged Cr(VI) to be attracted and bound on the adsorbent surface by electrostatic forces. This in turn leads to the removal of chromium ions from the solution. This removal can either be followed by reduction on the surface of the adsorbent or the ions may remain bound through electrostatic forces. As solution pH increases, the adsorbent surface becomes more negatively charged therefore leading to repulsion with the Cr(VI) molecules (Padmavathy *et al.*, 2016). At the lowest solution pH of 1, most of the Cr(VI) in solution is reduced to Cr(III) therefore pH 2 was taken as the optimum solution pH.

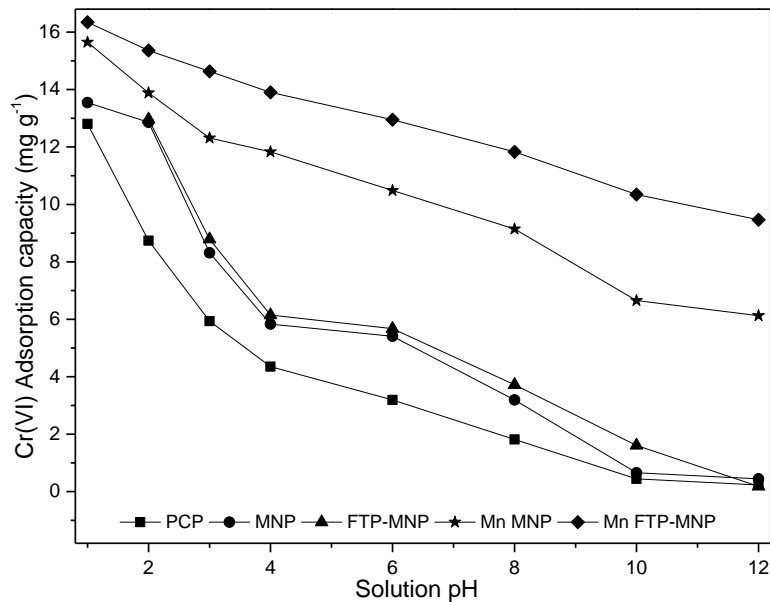


Fig. 4.2: Effect of solution pH on hexavalent chromium adsorption onto prepared adsorbents

The adsorption capacities of arsenic and chromium on both materials increased in the order FTP<MNP<FTP-MNP<Mn MNP<Mn FTP-MNP. The increased adsorption capacity for both adsorbates was due to increased functional groups on the adsorbent surfaces as  $\text{Fe}_3\text{O}_4$  and  $\text{MnO}_2$  were introduced. The surface groups of both  $\text{Fe}_3\text{O}_4$  and  $\text{MnO}_2$  are amphoteric functioning as acids or bases depending on solution pH (Liu *et al.*, 2015). Arsenite adsorption, proceeds through surface complexation of non-ionic arsenite species with the adsorbent surfaces. At lower solution pH, arsenite species are oxidised to arsenate causing a reduction in the arsenite concentration in the solution. At low solution pH arsenate ions are negatively charged and therefore adsorbed as they are formed. All adsorbents show an almost constant rate of arsenite formation throughout the pH range (Fig. 4.3) indicating that both arsenate and arsenite ions are bound to the adsorbent surfaces. As solution pH increases above the isoelectric point of the materials, and negative arsenite species are predominant, repulsive forces cause reduced interactions.



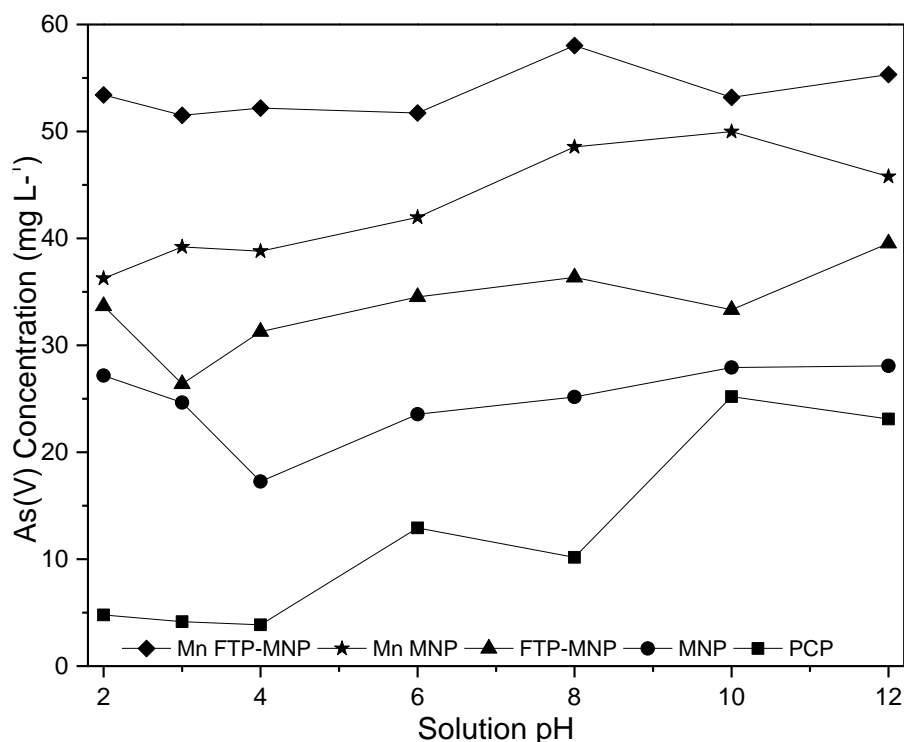


Fig. 4.3: Formation of As(V) at different solution pH

On the other hand, at low solution pH the surfaces are protonated causing negatively charged  $\text{HCrO}_4^-$  to be bound by electrostatic attraction (Fathy *et al.*, 2015). The presence of  $\text{Fe}^{2+}$  in magnetite and FTP, results in the reduction of Cr(VI) to Cr(III) (Wassie & Srivastava, 2016). Cr(III) on the surface is then either complexed by lone pairs of electrons on  $\text{MnO}_2$  surface or released into the solution (Wassie & Srivastava, 2016; Yuan *et al.*, 2010). As solution pH is increased, the concentration of Cr(III) in the solution decreases (Fig. 4.4) due to repulsion between the negatively charged Cr(VI) ions and the adsorbent surface.

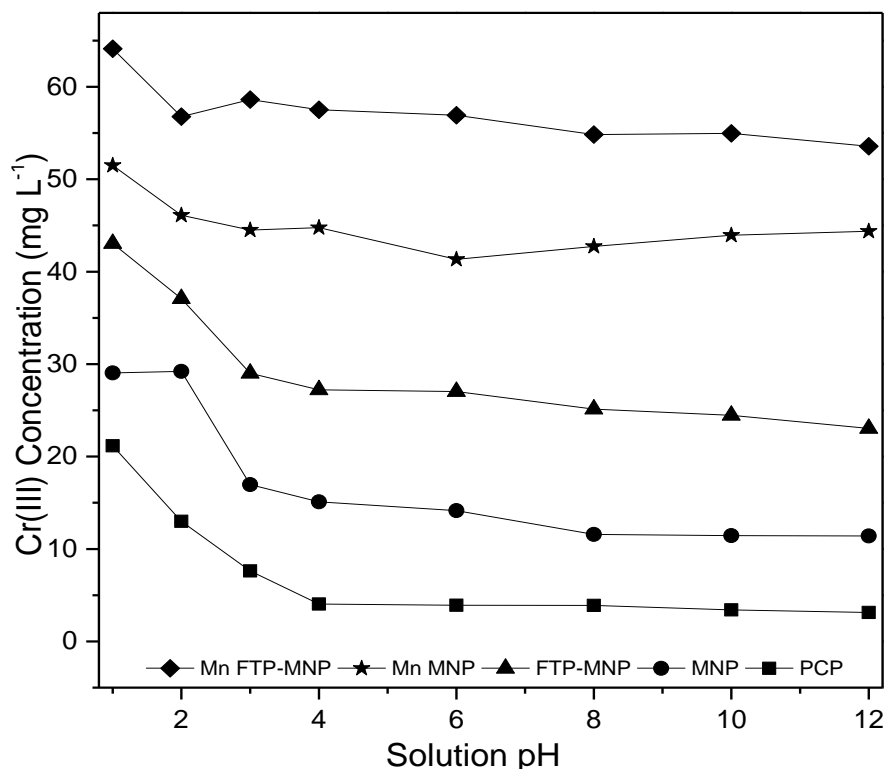


Fig. 4.4: Formation of Cr(III) at different solution pH

#### 4.3.2 Effect of Adsorbent Dose

The amount of adsorbent contacted with the adsorbate influences the uptake and is therefore important in the determination of optimum adsorption conditions. The effect of adsorbent dosage on all adsorbents was determined at an initial pH of 8 and 2 for As(III) and Cr(VI) respectively, adsorbate concentrations of 100 mg L<sup>-1</sup> and an agitation speed of 150 rpm. As the adsorbent dosage is increased, there are increased adsorption sites hence higher adsorption efficiencies (Roy *et al.*, 2017). At low adsorbent doses however, higher adsorption capacities are expected due to competition for binding sites by adsorbate molecules.

For As(III) and Cr(VI) adsorption, there is a marked increase in adsorption efficiency on all applied adsorbents (Fig. 4.5 - 4.9). The adsorption efficiency increased rapidly from 1 g L<sup>-1</sup> to 10 g L<sup>-1</sup> thereafter there was a slower increase while capacity decreased rapidly with an increase in adsorbent dose from 1 to 7.5 g L<sup>-1</sup> thereafter there was a slower rate of decrease. As the adsorbent dose increases, the surface area and adsorption sites are increased with a fixed adsorbate concentration leading to an increasing number of unsaturated sites therefore lowering adsorption amounts per unit mass of adsorbent (Abdulgader *et al.*, 2013; Randhawa *et al.*, 2014; Santra &

Sarkar, 2016; Roy *et al.*, 2017). Further increases in adsorbent dose do not significantly alter the adsorption efficiency and capacity because most adsorbate ions are bound and there is an equilibrium state established between the bound adsorbate ions and the ions in solution (Pérez Marín *et al.*, 2009). In order to optimize the adsorption efficiency and adsorption capacity of the adsorbents, the adsorbent dose of 5 g L<sup>-1</sup> was adopted for all adsorbents as it provided moderate efficiencies without significantly compromising the adsorption capacities. The optimum adsorbent dosage was applied in all further experiments.

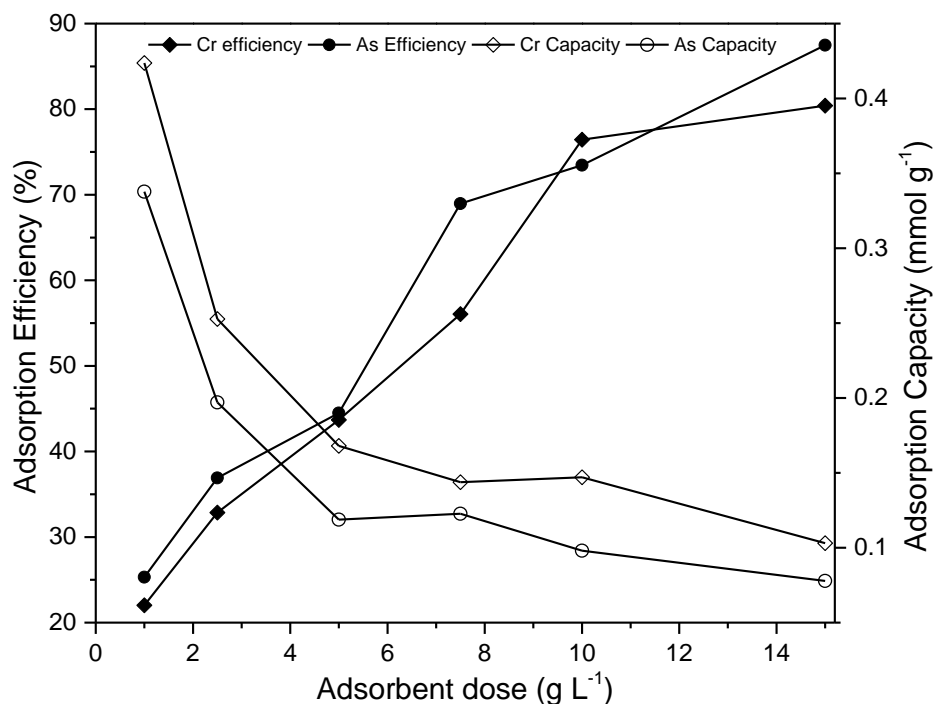


Fig. 4.5: Effect of adsorbent dosage on As(III) and Cr(VI) adsorption on to FTP

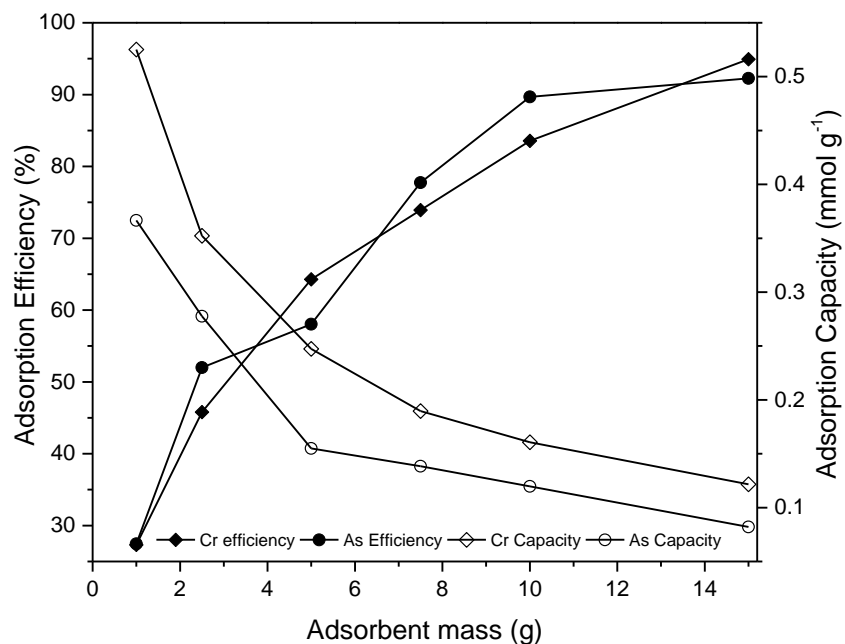


Fig. 4.6: Effect of adsorbent dosage on As(III) and Cr(VI) adsorption on to MNP

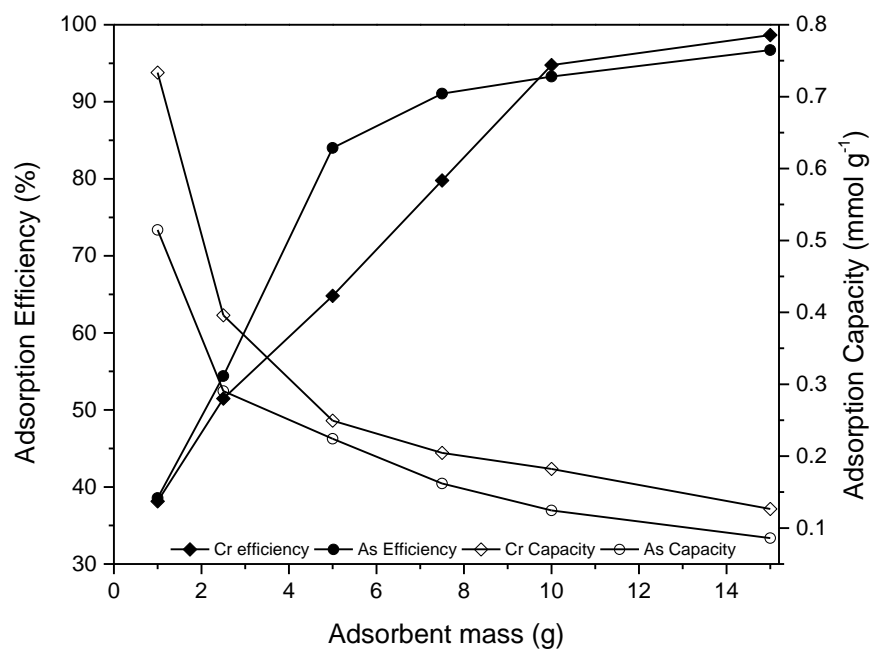


Fig. 4.7: Effect of adsorbent dosage on As(III) and Cr(VI) adsorption on to FTP-MNP

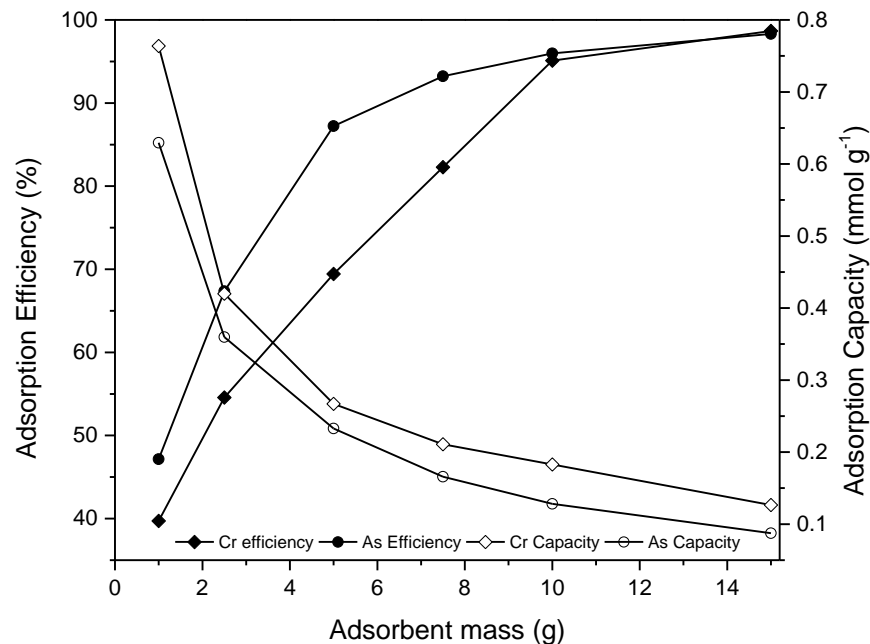


Fig. 4.8: Effect of adsorbent dosage on As(III) and Cr(VI) adsorption on to Mn MNP

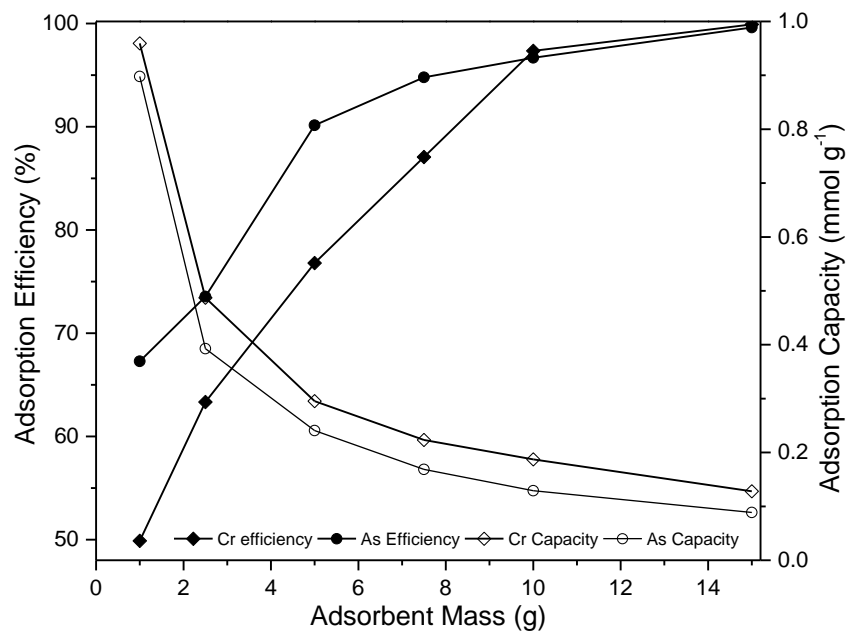


Fig. 4.9: Effect of adsorbent dosage on As(III) and Cr(VI) adsorption on to Mn FTP-MNP

The distribution coefficient is a useful parameter as it describes the ability of the adsorbent surface to bind an adsorbate. This binding ability can be calculated using the following relation (eq 4.3):

$$K_D = C_a / C_s \quad (4.3)$$

Where  $K_D$  (L g<sup>-1</sup>),  $C_a$  (mg g<sup>-1</sup>) and  $C_s$  (mg L<sup>-1</sup>) are the distribution coefficient, concentration on the adsorbent surface and concentration in the solution phase respectively. The value of  $K_D$  can be affected by the adsorbent dose and either remains constant with an increasing adsorbent dose implying that the adsorbent surface is homogenous or changes with the adsorbent dose signifying a heterogenous adsorbent surface (Liu *et al.*, 2011; Tian *et al.*, 2011). Tian *et al.*, (2011) observed an increase in  $K_D$  with an increasing adsorbent dose for the adsorption of arsenic onto magnetic wheat straw and upon further studies it was determined that the adsorption of arsenic onto magnetic wheat straw was via the formation of inner-sphere complexes of arsenic on the {100} surfaces of magnetite loaded on the wheat straw (Tian *et al.*, 2011). Liu *et al.*, (2011) on the other hand, observed a slight decrease of  $K_D$  during the adsorption of cobalt onto magnetite graphene oxide composite attributing the decrease in  $K_D$  to competition among the colloids of the composite (Liu *et al.*, 2011). Both adsorbents were therefore confirmed to consist of heterogenous adsorption sites. The results for adsorption onto the synthesized adsorbents showed that for both As(III) (Fig. 4.10) and Cr(VI) (Fig. 4.11) adsorption, FTP showed a slight increase in distribution coefficients while all the other adsorbents had significant increases in  $K_D$  values with increasing adsorbent doses. All the adsorbents used therefore were determined to have heterogenous surfaces from the effect of adsorbent dose on the distribution coefficients. These results were therefore consistent with the adsorbent characterization results presented in Chapter 3.

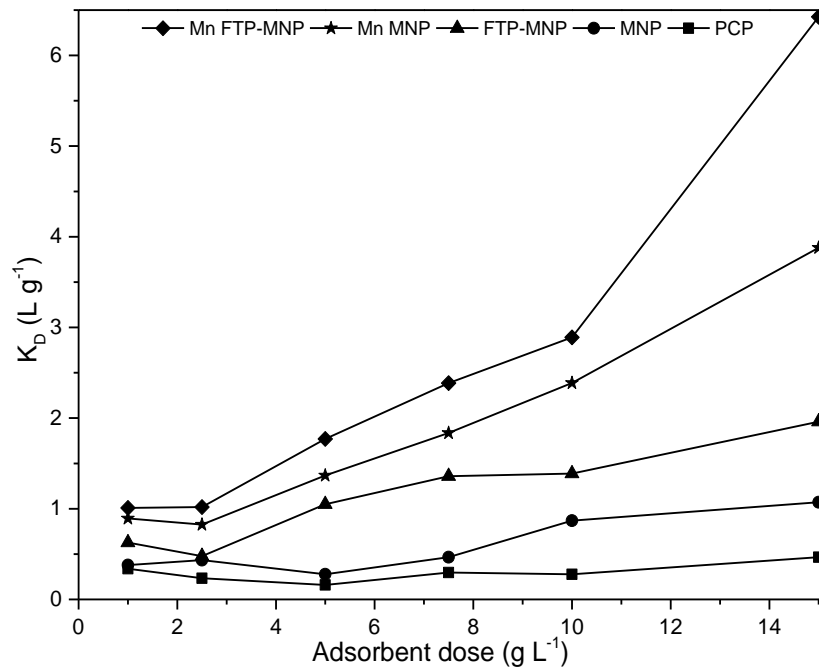


Fig. 4.10: The effect of adsorbent dose on As(III) distribution coefficient for different adsorbents

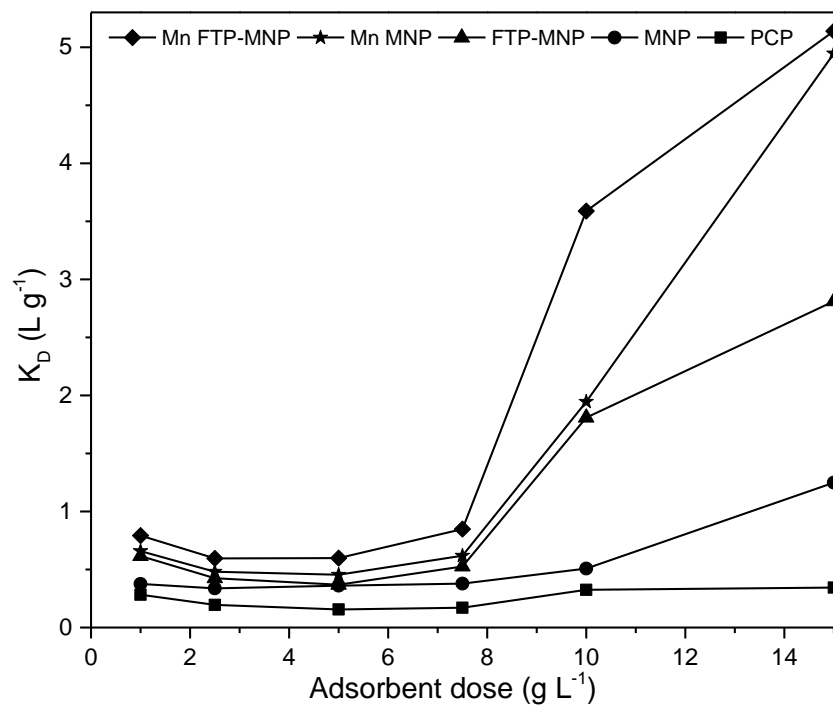


Fig. 4.11: The effect of adsorbent dose on Cr(VI) distribution coefficient for different adsorbents

### 4.3.3 Effect of Initial Adsorbate Concentration

Initial adsorbate concentration is an important factor in the determination of optimum adsorption parameters. To determine the effect of initial solution concentration, all adsorbents were contacted with solutions of concentrations ranging from 25 to 150 mg L<sup>-1</sup> at constant pH of 8 and 2 for As(III) and Cr(VI) respectively, adsorbent dosage of 5 g L<sup>-1</sup> and agitation speed of 150 rpm. At lower initial solution concentrations, low adsorption capacities were observed for all adsorbents with an increase in capacities as concentrations increased (Fig. 4.12 & 4.14). Higher initial solution concentrations provided higher mass transfer of adsorbate from solution to solid phase hence improving the interaction between the adsorbate and adsorbent resulting in increased adsorption capacities (Ucun *et al.*, 2002; Dawood & Sen, 2012). At lower initial solution concentrations, there was higher adsorption capacities for both adsorbates due to the high ratio of adsorption sites to adsorbate molecules (Dhoble *et al.*, 2011). However, a decrease in adsorbent/adsorbate ratios as initial solution concentrations were increased at fixed adsorbent dosage led to a decrease in adsorption efficiency (Fig. 4.13 - 4.15). The decrease in efficiency was due to adsorbent saturation therefore increasing the amount of adsorbate molecules would not increase the amount of adsorbate bound on the adsorbent surface (Khodabakhshi *et al.*, 2011). The suitable solution concentration for hexavalent chromium was identified as 75 mg L<sup>-1</sup> while that of arsenite was 100 mg L<sup>-1</sup> where both efficiency and capacity were optimized.



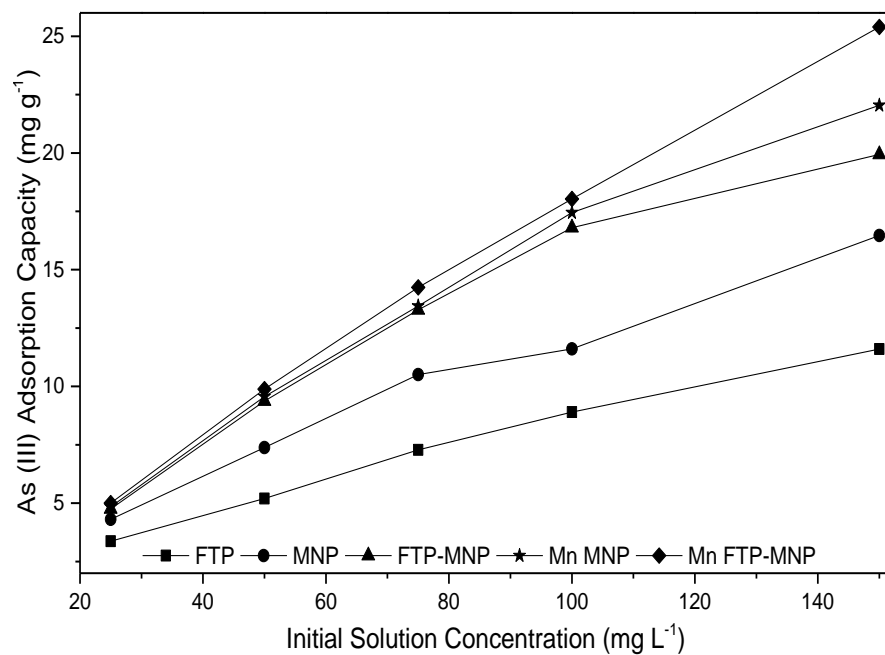


Fig. 4.12: Effect of initial solution concentration on As(III) adsorption capacity

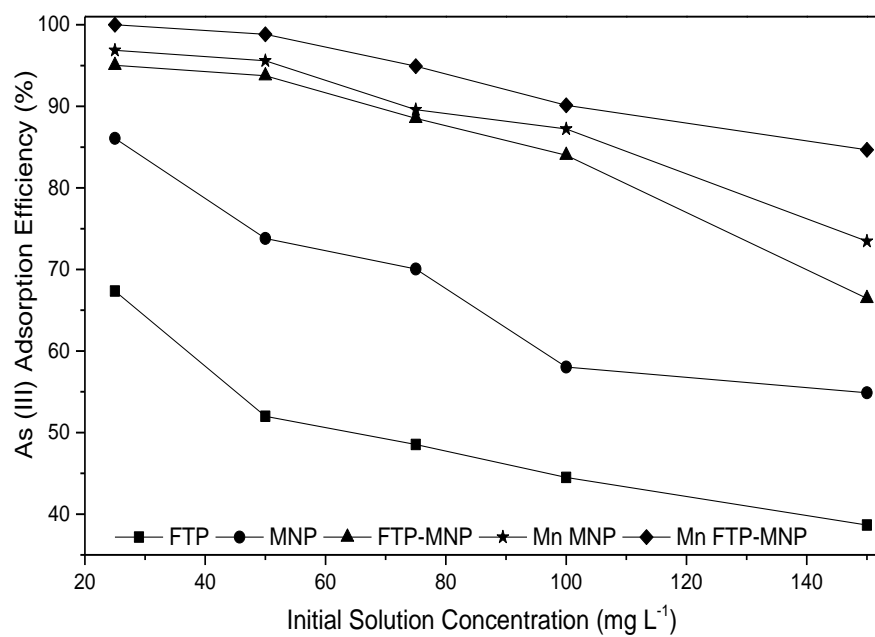


Fig. 4.13: Effect of initial solution concentration on As(III) adsorption efficiency

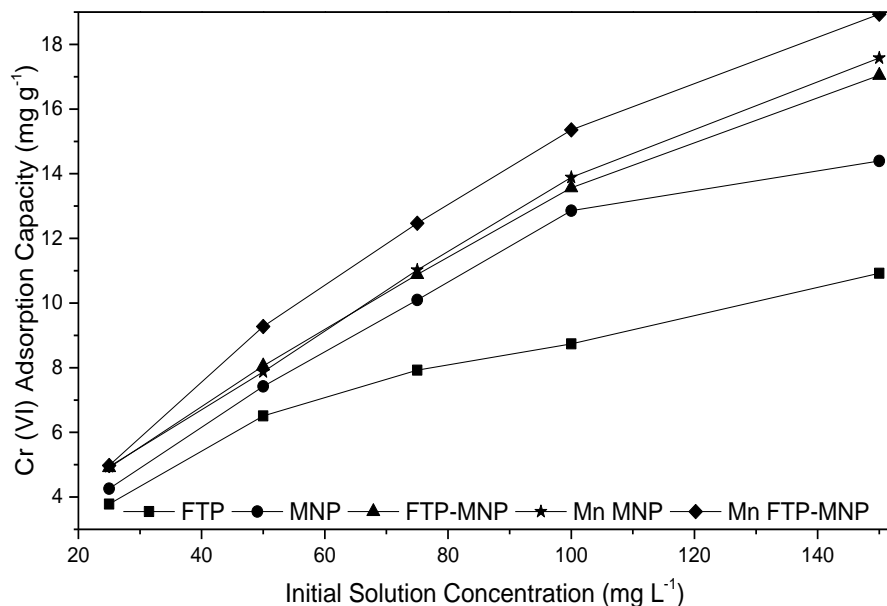


Fig. 4.14: Effect of initial solution concentration on Cr(VI) adsorption capacity

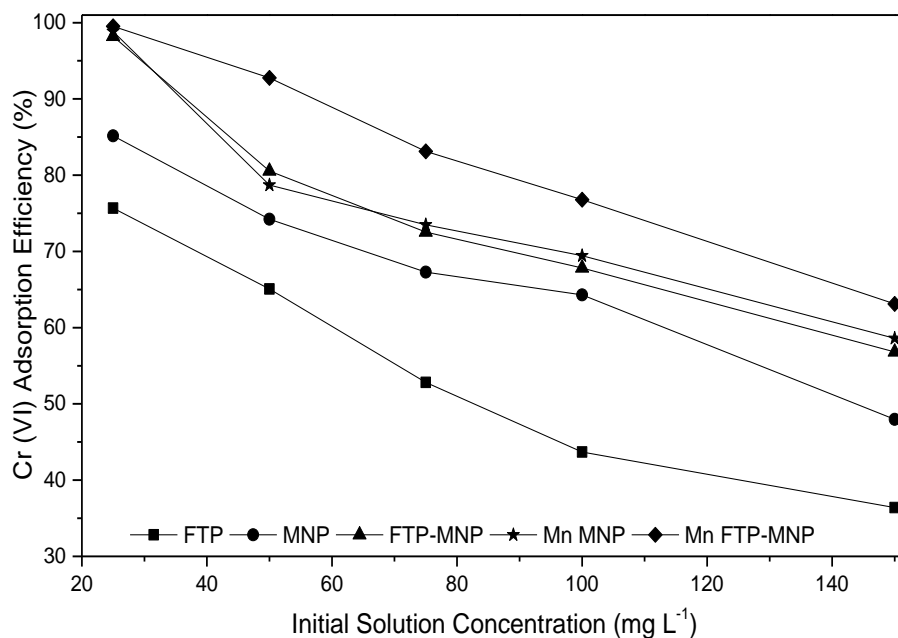


Fig. 4.15: Effect of initial solution concentration on Cr(VI) adsorption efficiency

#### 4.4 Conclusion

The effect of solution pH, adsorbent dosage and initial solution concentration were studied in order to determine the optimum parameters for the adsorption of As(III) and Cr(VI) onto FTP, MNP, FTP-MNP, Mn MNP and Mn FTP-MNP. The optimum conditions were determined to be pH 8,

adsorbent dose of 5 g L<sup>-1</sup> and concentration of 100 mg L<sup>-1</sup> for As(III); adsorption with pH 2, adsorbent dose 5 g L<sup>-1</sup> and concentration of 75 mg L<sup>-1</sup> being identified as the optimum conditions for Cr(VI) adsorption on all adsorbents used. The optimum conditions were therefore used in all further adsorption experiments. All the adsorbents showed similar adsorption profiles indicating that the adsorption on each adsorbent followed a similar mechanistic pathway.

## 4.5 References

- ABDULGADER, H. AL, KOCHKODAN, V., & HILAL, N. (2013). Hybrid ion exchange – Pressure driven membrane processes in water treatment: A review. *Sep. Purif. Technol.* 116. p.253–264.
- BISHOP, M.E., GLASSER, P., DONG, H., AREY, B., & KOVARIK, L. (2014). Reduction and immobilization of hexavalent chromium by microbially reduced Fe-bearing clay minerals. *Geochim. Cosmochim. Acta.* 133. p.186–203.
- DAWOOD, S., & SEN, T.K. (2012). Removal of anionic dye Congo red from aqueous solution by raw pine and acid-treated pine cone powder as adsorbent: equilibrium, thermodynamic, kinetics, mechanism and process design. *Water Res.* 46. p.1933–46.
- DHOBLE, R.M., LUNGE, S., BHOLE, A.G., & RAYALU, S. (2011). Magnetic binary oxide particles (MBOP): A promising adsorbent for removal of As(III) in water. *Water Res.* 45. p.4769–4781.
- FATHY, N.A., EL-WAKEEL, S.T., & ABD EL-LATIF, R.R. (2015). Biosorption and desorption studies on chromium(VI) by novel biosorbents of raw rutin and rutin resin. *J. Environ. Chem. Eng.* 3. p.1137–1145.
- GHOSH, A., PAL, M., BISWAS, K., GHOSH, U.C., & MANNA, B. (2015). Manganese oxide incorporated ferric oxide nanocomposites (MIFN): A novel adsorbent for effective removal of Cr(VI) from contaminated water. *J. Water Process Eng.* 7. p.176–186.
- KATSOYIANNIS, I.A., & ZOUBOULIS, A.I. (2002). Removal of arsenic from contaminated water sources by sorption onto iron-oxide-coated polymeric materials. *Water Res.* 36. p.5141–5155.
- KHODABAKHSHI, A, AMIN, M.M., & MOZAFFARI, M. (2011). Synthesis of Magnetite Nanoparticles and Evaluation of Its Efficiency for Arsenic Removal From Simulated. *J. Environmental Heal. Sci. Eng.*
- LIU, M., CHEN, C., HU, J., WU, X., & WANG, X. (2011). Synthesis of Magnetite/Graphene Oxide Composite and Application for Cobalt(II) Removal. *J. Phys. Chem. C.* 115. p.25234–25240.
- LIU, Y., LUO, C., CUI, G., & YAN, S. (2015). Synthesis of manganese dioxide/iron

oxide/graphene oxide magnetic nanocomposites for hexavalent chromium removal. *RSC Adv.* 5. p.54156–54164.

LUNGE, S., SINGH, S., & SINHA, A. (2014). Magnetic iron oxide (Fe<sub>3</sub>O<sub>4</sub>) nanoparticles from tea waste for arsenic removal. *J. Magn. Magn. Mater.* 356. p.21–31.

LUO, J., MENG, X., CRITTENDEN, J., QU, J., HU, C., LIU, H., & PENG, P. (2018). Arsenic adsorption on  $\alpha$ -MnO<sub>2</sub> nanofibers and the significance of (1 0 0) facet as compared with (1 1 0). *Chem. Eng. J.* 331. p.492–500.

MENG, S.G., BANG, S.B., & KORFIATIS, G.P. (2000). Effects of silicate, sulphate, and carbonate on arsenic removal by ferric chloride. *Water Res.* 34. p.1255–1261.

MENG, X., & WANG, W. Speciation of arsenic by disposable cartridges. Third International Conference on Arsenic Exposure and Health Effects. Anais...Society of Environmental Geochemistry and Health, University of Colorado at Denver., 1998

MOHAN, D., & PITTMAN, C.U. (2006). Activated carbons and low cost adsorbents for remediation of tri- and hexavalent chromium from water. *J. Hazard. Mater.* 137. p.762–811.

MONÁRREZ-CORDERO, B.E., AMÉZAGA-MADRID, P., LEYVA-PORRAS, C.C., PIZÁ-RUIZ, P., & MIKI-YOSHIDA, M. (2016). Study of the Adsorption of Arsenic (III and V) by Magnetite Nanoparticles Synthetized via AACVD. *Mater. Res.* 19. p.103–112.

PADMAVATHY, K.S., MADHU, G., & HASEENA, P.V. (2016). A study on Effects of pH, Adsorbent Dosage, Time, Initial Concentration and Adsorption Isotherm Study for the Removal of Hexavalent Chromium (Cr(VI)) from Wastewater by Magnetite Nanoparticles. *Procedia Technol.* 24. p.585–594.

PÉREZ MARÍN, A.B., AGUILAR, M.I., MESEGUER, V.F., ORTUÑO, J.F., SÁEZ, J., & LLORÉNS, M. (2009). Biosorption of chromium (III) by orange (*Citrus cinensis*) waste: Batch and continuous studies. *Chem. Eng. J.* 155. p.199–206.

RANDHAWA, N.S., DAS, N.N., & JANA, R.K. (2014). Adsorptive remediation of Cu(II) and Cd(II) contaminated water using manganese nodule leaching residue. *Desalin. Water Treat.* 52. p.4197–4211.

- ROY, P., DEY, U., CHATTORAJ, S., & MUKHOPADHYAY, D. (2017). Modeling of the adsorptive removal of arsenic ( III ) using plant biomass : a bioremedial approach. *Appl. Water Sci.* 7. p.1307–1321.
- SAHA, B., & ORVIG, C. (2010). Biosorbents for hexavalent chromium elimination from industrial and municipal effluents. *Coord. Chem. Rev.* 254. p.2959–2972.
- SANTRA, D., & SARKAR, M. (2016). Optimization of process variables and mechanism of arsenic ( V ) adsorption onto cellulose nanocomposite. *J. Mol. Liq.* 224. p.290–302.
- SARI, A., ULUOZLÜ, Ö.D., & TÜZEN, M. (2011). Equilibrium, thermodynamic and kinetic investigations on biosorption of arsenic from aqueous solution by algae (*Maugeotia genuflexa*) biomass. *Chem. Eng. J.* 167. p.155–161.
- TIAN, Y., WU, M., LIN, X., HUANG, P., & HUANG, Y. (2011). Synthesis of magnetic wheat straw for arsenic adsorption. *J. Hazard. Mater.* 193. p.10–16.
- UCUN, H., BAYHAN, Y.K., KAYA, Y., CAKICI, A., & FARUK ALGUR, O. (2002). Biosorption of chromium(VI) from aqueous solution by cone biomass of *Pinus sylvestris*. *Bioresour. Technol.* 85. p.155–158.
- WASSIE, A.B., & SRIVASTAVA, V.C. (2016). Teff straw characterization and utilization for chromium removal from wastewater: Kinetics, isotherm and thermodynamic modelling. *J. Environ. Chem. Eng.* 4. p.1117–1125.
- YUAN, P., LIU, D., FAN, M., YANG, D., ZHU, R., GE, F., ZHU, J.X., & HE, H. (2010). Removal of hexavalent chromium [Cr(VI)] from aqueous solutions by the diatomite-supported/unsupported magnetite nanoparticles. *J. Hazard. Mater.* 173. p.614–621.

### 5 Thermodynamics Studies of As(III) and Cr(VI) Adsorption onto the Prepared Adsorbents

#### 5.1 Introduction

Adsorption thermodynamics involve the study of the effects of temperature on the energy of the adsorption system. The adsorption data is fitted onto isotherm models allowing for the calculation of thermodynamic parameters including Gibbs free energy ( $\Delta G$ ), change in enthalpy ( $\Delta H$ ) and change in entropy ( $\Delta S$ ) which provide information on the nature of the adsorption reaction.

This chapter discusses the effects of temperature on the adsorption of arsenite (As(III)) and hexavalent chromium (Cr(VI)) on all the prepared adsorbents namely Fenton's treated pine cone powder (FTP), magnetite nanoparticles (MNP), Fenton treated pine magnetite nanoparticles composite (FTP-MNP), Manganese doped magnetite nanoparticles (Mn MNP) and Manganese doped Fenton treated pine magnetite nanoparticles (Mn FTP-MNP). The adsorption data were modelled using the Langmuir, Freundlich, Redlich-Peterson (R-P), Sips, Dubinin-Radushkevich (D-R), and Flory-Huggins (F-H) isotherm models. The isotherm modelling results and thermodynamic parameters of the adsorption processes are presented.

##### 5.1.1 Isotherm Models

Several equilibrium isotherm models were applied to the data to determine the nature of adsorption on each adsorbent. Langmuir and Freundlich models were used to provide information on the nature of adsorbate coverage on the adsorbent surface. Redlich-Peterson and Sips models were used to confirm the nature of adsorption and better fit adsorption data. Dubinin-Radushkevich (D-R) model was used to determine the nature of adsorption onto the as-synthesized adsorbents (Chen *et al.*, 2013) and Flory-Huggins (F-H) model was used to calculate the thermodynamic parameters of the adsorption process.

##### 5.1.1.1 Langmuir

Langmuir isotherm described by Equation 5.1 assumes that adsorption occurs on a homogenous surface with adsorption sites of uniform energies hence monolayer coverage with no further adsorption takes place after the sites are occupied (Dada *et al.*, 2012).

$$q_e = \frac{q_m K_L C_e}{1 + K_L C_e} \quad (5.1)$$

$$\frac{C_e}{q_e} = \frac{C_e}{q_m} + \frac{1}{K_L} \quad (5.2)$$

Langmuir isotherm is described in its non-linear and linear forms by Equation 5.1 and 5.2 respectively where  $C_e$  is the solution concentration at equilibrium,  $q_e$  is the adsorption capacity at equilibrium,  $q_m$  is the maximum adsorption capacity and  $K_L$  is the Langmuir constant. The linearized form (eq 5.2) is used to obtain a plot of  $\frac{C_e}{q_e}$  against  $C_e$  from which the constants can be determined.

#### 5.1.1.2 Freundlich

The Freundlich isotherm relates the amount of an adsorbate adsorbed per unit weight of adsorbent to the adsorbate equilibrium concentration. It assumes that the adsorbent surface sites have different binding energies therefore allowing for multilayer coverage by adsorbate molecules (Han *et al.*, 2007).

$$q_e = K_F C_e^{1/n} \quad (5.3)$$

$$\log q_e = \log K_F + \frac{1}{n} \log C_e \quad (5.4)$$

Equations 5.3 and 5.4 describe the non-linear and linear forms of the Freundlich relation respectively with  $q_e$  representing the equilibrium adsorption capacity,  $C_e$  the concentration of solution at equilibrium and  $K_F$  and  $n$  the characteristic constants.

#### 5.1.1.3 Redlich-Peterson

The Redlich-Peterson isotherm model is a three parameter Langmuir-Freundlich hybrid model which reduces to the Freundlich isotherm at high adsorbate concentration when  $\beta > 1$  and to the Langmuir model when  $\beta = 1$  (Ebrahimian Pirbazari *et al.*, 2014a; Han *et al.*, 2007). This model can therefore be applied to either homogenous or heterogenous adsorption systems to describe adsorption over a wide concentration range (Pérez Marín *et al.*, 2009; Ebrahimian Pirbazari *et al.*, 2014b; Pakade *et al.*, 2017).



$$q_e = \frac{K_R C_e}{1 + \alpha_R C_e^\beta} \quad (5.5)$$

Redlich-Peterson model is described by Equation 5.5 where  $K_R$  (L mg<sup>-1</sup>) and  $\alpha_R$  (L mg<sup>-1</sup>) are isotherm constants related to adsorption capacity and binding site affinity respectively, and  $\beta$  is an exponent related to the adsorption intensity (Kupeta *et al.*, 2018; Lee *et al.*, 2017).

#### 5.1.1.4 Sips

Sips isotherm adopts Langmuir and Freundlich parameters and indicates differences in adsorption at high and low adsorbate concentrations (Rostamian & Behnejad, 2016). It is described by Equation 5.6 where  $K_S$  (L mg<sup>-1</sup>) is the Sips isotherm constant related to the affinity of binding sites,  $1/n$  is the heterogeneity index and  $q_e$ ,  $q_{\max}$  and  $C_e$  are the adsorption capacity at equilibrium, maximum adsorption capacity and solution concentration at equilibrium respectively (Albadarin *et al.*, 2013; Cao *et al.*, 2014). The heterogeneity factor  $1/n$  is used to describe the surface binding affinity which ranges between 0 and 1. Values of  $1/n$  close to unity indicate that adsorptions are homogenous while lower  $1/n$  values indicate an increase in heterogeneity (Pérez Marín *et al.*, 2009; Cao *et al.*, 2014; Ebrahimian Pirbazari *et al.*, 2014b; Pakade *et al.*, 2017).

$$q_e = \frac{q_{\max} K_S C_e^{1/n}}{1 + K_S C_e^{1/n}} \quad (5.6)$$

#### 5.1.1.5 Dubinin-Radushkevich

The Dubinin-Radushkevich (D-R) model is used to provide information on the mean free energy of adsorption. The mean free energy values are used to determine the nature of adsorption whether physical or chemical. The linear form of the D-R model is described by Equation 5.7 where  $q_e$  is the adsorption capacity at equilibrium,  $q_m$  is the maximum adsorption capacity,  $\beta$  (mol<sup>2</sup> kJ<sup>-2</sup>) is a constant related to adsorption energy,  $\varepsilon$  is the Polanyi potential of the surface described by Equation 5.8,  $R$  is the gas constant (8.314 J K<sup>-1</sup> Mol<sup>-1</sup>) and  $T$  (K) is the absolute temperature of the system (Almasri *et al.*, 2018; Igberase *et al.*, 2017). The mean adsorption energy can be calculated from D-R isotherm constants following Equation 5.9 and provides information about

the nature of the adsorption process. Values for  $E < 8$  kJ/mol signify physical adsorption while  $8 \leq E \leq 16$  kJ/mol signify chemical adsorption via ion exchange mechanism and  $E > 16$  kJ/mol suggests that particle diffusion is dominant (Argun *et al.*, 2007).

$$\ln q_e = \ln q_m - \beta \varepsilon^2 \quad (5.7)$$

$$\varepsilon = RT \ln \left( 1 + \frac{1}{C_e} \right) \quad (5.8)$$

$$E = \frac{1}{\sqrt{2\beta}} \quad (5.9)$$

#### 5.1.1.6 Flory-Huggins Isotherm and Thermodynamic Parameters

Flory-Huggins model provides information on adsorbate coverage on the adsorbent surface and can be used to calculate thermodynamic parameters (Malana *et al.*, 2011). It is described in its linear form by Equation 5.10 where  $\theta$  is the degree of surface coverage described by Equation 5.11,  $K_{FH}$  (L g<sup>-1</sup>) is the model equilibrium constant,  $n_{FH}$  is the model exponent relating to the number of ions occupying adsorption sites,  $C_0$  and  $C_e$  are the initial and equilibrium solution concentrations respectively (Nechifor *et al.*, 2015). The model equilibrium constant  $K_{FH}$  was used to calculate the change in Gibbs free energy ( $\Delta G$  (kJ mol<sup>-1</sup>)) following Equation 5.12 where  $R$  is the gas constant (8.314 Jmol<sup>-1</sup>K<sup>-1</sup>) and  $T$  (K) is the absolute temperature. Changes in enthalpy ( $\Delta H$  (kJ mol<sup>-1</sup>)) and entropy ( $\Delta S$  (Jmol<sup>-1</sup>K<sup>-1</sup>)) were obtained from a plot of the change in Gibbs free energy against temperature (eq 5.13). The greater negative value for Gibbs free energy as temperature increases indicates a more spontaneous reaction.

$$\log \frac{\theta}{C_0} = \log K_{FH} + n_{FH} \log (1 - \theta) \quad (5.10)$$

$$\theta = \left( 1 - \frac{C_e}{C_0} \right) \quad (5.11)$$

$$\Delta G = RT \ln K_{FH} \quad (5.12)$$

$$\Delta G = \Delta H - T\Delta S \quad (5.13)$$

## 5.2 Experimental

### 5.2.1 Materials

All adsorbents used herein, were sourced and synthesized as described in Chapter 3. Hydrochloric acid (32%) was supplied by Merck, sodium arsenite ( $\text{NaAsO}_2$  >90%) was purchased from Sigma-Aldrich. Potassium dichromate ( $\text{K}_2\text{Cr}_2\text{O}_7$  >99 %) and Sodium Hydroxide ( $\text{NaOH}$  >98 %) were purchased from Associated Chemical Enterprises (South Africa). All chemicals were used as supplied without any further purification.

### 5.2.2 Methods

Stock solutions of As(III) and Cr(VI) were prepared by dissolving the desired amounts of sodium arsenite and potassium dichromate respectively in deionized water to prepare  $1000 \text{ mg L}^{-1}$  solutions. Serial dilution from the stock solutions was used to prepare solutions of concentrations ranging from  $25 \text{ mg L}^{-1}$  to  $150 \text{ mg L}^{-1}$ .

#### 5.2.2.1 Thermodynamic Studies

To study the effect of temperature on adsorption, solutions of different concentration ranging from  $25$  to  $150 \text{ mg L}^{-1}$  were prepared and the pH was adjusted to pH 8 and pH 2 for arsenite and hexavalent chromium adsorption respectively.  $100 \text{ mL}$  of each solution was agitated at  $200 \text{ rpm}$  on a Carousel 6 reaction station fitted with a Tornado overhead stirring system for 15 minutes before contacting it with the adsorbent materials to ensure the solution was at the desired temperature. After 15 minutes  $0.5 \text{ g}$  of the respective adsorbent material was introduced into the flask containing the solution and agitated for a further 2 hours while maintaining the temperature. The temperatures investigated were  $298 \text{ K}$ ,  $304 \text{ K}$ ,  $309 \text{ K}$ ,  $314 \text{ K}$  and  $319 \text{ K}$ .

## 5.3 Results and Discussions

The results in this section are divided into two parts beginning with the isotherm and thermodynamic studies of arsenic, followed by the studies of chromium adsorption onto the prepared adsorbents.

### 5.3.1 Arsenic Adsorption

#### 5.3.1.1 Isotherm Analyses

For all the adsorbents used, the data was a better fit to the non-linear Langmuir isotherm model as compared to the non-linear Freundlich model (Table A-1 – A-5). The Freundlich model was however important in the determination of the favorability of the adsorption process with the values of  $n > 1$  representing a favorable adsorption process (Ebrahimian Pirbazari *et al.*, 2014b). For all adsorbents used, the adsorption of As(III) was favorable at all temperatures as indicated by the magnitude of the Freundlich constant  $n$  which was greater than 1 in all experiments.

The surface of the adsorbents was determined to consist of adsorption sites with equivalent energies and homogenous distribution of active sites as the data was better modelled by the Langmuir relation (Ebrahimian Pirbazari *et al.*, 2014b). With an increase in temperature from 298 K to 319 K, the adsorption capacity increased indicating the adsorption process was favorable at higher temperatures thus an endothermic process. This was reiterated by the increase of  $K_L$  values with temperature indicating increasing heat of adsorption (Ofomaja & Ho, 2008). Composite formation led to increased maximum adsorption capacities for FTP and MNP due to the additional binding sites introduced by the introduction of surface groups from FTP and the increased surface area by magnetite nanoparticles. Doping of the bare nanoparticles and nanoparticles on the composite also resulted in increased adsorption capacities by up to 52% in both MNP and FTP-MNP as a result of manganese presence which aids in the conversion of As(III) to As(V) and subsequent adsorption, and provides additional binding sites (Li *et al.*, 2010; Liu *et al.*, 2015b).

Redlich-Peterson and Sips isotherm models both provided a better fit to the model data when compared to Freundlich isotherm with coefficients of determination  $> 0.99$  for all adsorbents. The adsorption intensity coefficient of Redlich-Peterson isotherm was in the range 0.95 to 1.02 in all adsorbents, it therefore indicated that the adsorption of As(III) on all adsorbents was favorable at all temperatures used and that adsorption sites were of uniform energies therefore resulting in monolayer adsorption (Boddu *et al.*, 2008). Sips isotherm also confirmed the homogeneity of the adsorbent surface with all calculated values of  $\frac{1}{n}$  being close to unity. The maximum adsorption capacities calculated from Sips isotherm were comparable to those obtained from Langmuir model

and was thus considered to be a good representation of the adsorption process (Ebrahimian Pirbazari *et al.*, 2014b).

Dubinin-Raduschkevich isotherm model data allowed for the determination of mean free energy of the adsorption process therefore elucidating whether the adsorption process was physical or chemical in nature. The mean free energy values calculated for all adsorbents were between 12.1 kJ mol<sup>-1</sup> and 15.4 kJ mol<sup>-1</sup> implying that the adsorption of As(III) onto all adsorbents was via chemical adsorption since all values were > 8 kJ mol<sup>-1</sup>. The adsorption was also indicated to proceed predominantly via ion-exchange mechanism as opposed to particle diffusion which would have resulted in mean energies > 16 kJ mol<sup>-1</sup> (Argun *et al.*, 2007).

#### **5.3.1.2 Thermodynamic Analyses**

The Flory-Huggins model was used to determine thermodynamic parameters of the adsorption process. The model parameters were calculated from a linear fit of the experimental data and obtained coefficient values were used to calculate the Gibbs free energy ( $\Delta G$ ), enthalpy ( $\Delta H$ ) and entropy ( $\Delta S$ ) of each adsorbent-adsorbate system. The negative values for  $\Delta G$  (Table 5.1) indicated that the adsorption was spontaneous hence favorable with the degree of spontaneity increasing proportionately with temperature indicating an endothermic process (Liu *et al.*, 2015a). The values of  $\Delta G$  greater than -20 kJ mol<sup>-1</sup> showed that the adsorption of As(III) on all the prepared adsorbents was through chemisorption therefore confirming the inference from the D-R model parameters (Wasim & Khan, 2016).

The positive  $\Delta H$  value indicated that the process was endothermic as implied by an increase in adsorption capacity with increasing temperature. The positive  $\Delta S$  value indicated an increased randomness at the solid-solution interface and the occurrence of ion exchange or ion replacement reactions as alluded to the D-R isotherm model (Goswami *et al.*, 2012). The increased randomness at the solid-solution interface was due to the surface ions being less ordered in the adsorbed state (Argun *et al.*, 2007).

Table 5.1: Flory-Huggins model parameters and thermodynamic parameters for As(III) adsorption onto the prepared adsorbents.

	$T$ (K)	Flory-Huggins model			Thermodynamic parameters		
		$K_{FH}$	$n_{FH}$	$R^2$	$\Delta G$	$\Delta H$	$\Delta S$
		(L g <sup>-1</sup> )			(kJ mol <sup>-1</sup> )	(kJ mol <sup>-1</sup> )	(J mol <sup>-1</sup> K <sup>-1</sup> )
<b>FTP</b>	298	0.060	-1.186	0.980	-20.825		
	304	0.058	-1.308	0.994	-21.171		
	309	0.062	-1.049	0.972	-21.685	11.023	106.58
	314	0.094	-0.904	0.941	-23.128		
	319	0.068	-0.785	0.900	-22.627		
<b>MNP</b>	298	0.058	-1.186	0.994	-20.772		
	304	0.061	-1.060	0.993	-21.302		
	309	0.064	-0.908	0.994	-21.788	5.278	87.466
	314	0.066	-0.834	0.993	-22.203		
	319	0.067	-0.763	0.999	-22.595		
<b>FTP-MNP</b>	298	0.062	-1.040	0.977	-20.905		
	304	0.063	-0.957	0.991	-21.400		
	309	0.065	-0.897	0.994	-21.797	3.648	82.382
	314	0.066	-0.801	0.987	-22.220		
	319	0.068	-0.714	0.990	-22.637		
<b>Mn MNP</b>	298	0.061	-0.953	0.972	-20.870		
	304	0.054	-0.984	0.962	-20.981		
	309	0.057	-0.849	0.898	-21.454	1.230	73.674
	314	0.061	-0.702	0.755	-22.013		
	319	0.059	-0.676	0.782	-22.285		
<b>Mn FTP-MNP</b>	298	0.055	-0.963	0.940	-20.632		
	304	0.053	-0.937	0.931	-20.958		
	309	0.052	-0.886	0.884	-21.231	5.124	52.084
	314	0.050	-0.846	0.852	-21.501		
	319	0.048	-0.800	0.864	-21.714		

### 5.3.2 Chromium Adsorption

#### 5.3.2.1 Isotherm Analyses

The Cr(VI) adsorption results were also modelled by all the isotherms described above to determine the nature of surface coverage, adsorption process whether physical or chemical and the pre-dominant mechanism controlling the adsorption process.

From the coefficients of determination (Table A-6 – A-10) the Langmuir (L), Freundlich (F), Redlich-Peterson (R-P) and Sips (S) isotherm models fitted the Cr(VI) adsorption data in the order  $R-P > S > L > F$  for all adsorbents used. The adsorption of Cr(VI) onto all the adsorbents was therefore determined to be monolayer in nature on homogenous adsorption sites (Ebrahimian Pirbazari *et al.*, 2014b). Redlich-Peterson and Sips coefficients confirmed the favourability of adsorption at all temperatures and the homogeneity of the adsorbent surface (Boddu *et al.*, 2008; Ebrahimian Pirbazari *et al.*, 2014b). Sips maximum adsorption capacities were higher than those obtained from the Langmuir model due to the difference in model fits in the three-parameter and two-parameter models respectively. In both models the maximum adsorption capacity increased with an increase in temperature, and the magnitude of the Langmuir constant ( $K_L$ ) also increased with temperature for all adsorbents indicating an endothermic process (Ofomaja & Ho, 2008). From the maximum adsorption capacities, it was observed that manganese doping increased the adsorption of Cr(VI) onto MNP and FTP-MNP by 14.45 % and 12.52 % respectively. The increase in adsorption capacity with the introduction of manganese was due to binding sites provided by the introduction of manganese (Liu *et al.*, 2015b).

From the Dubinin-Radushkevich isotherm model the mean free energy of adsorption was calculated to be 9.38 kJ mol<sup>-1</sup> <E> 19.46 kJ mol<sup>-1</sup>. These values indicated that adsorption of Cr(VI) on all adsorbents was chemical in nature and predominantly via ion exchange except for adsorption onto manganese doped magnetite at 314 K and 319 K where the free energy values were >16 kJ mol<sup>-1</sup> (Argun *et al.*, 2007).

#### 5.3.2.2 Thermodynamic Analyses

The adsorption data of Cr(VI) on all adsorbents at 298 K, 304 K, 309 K, 314 K and 319 K was modelled by the Flory-Huggins isotherm and used to determine the thermodynamic parameters for the adsorption process (Table 5.2). The Gibbs free energy ( $\Delta G$ ) for all adsorbents was between -

18.76 kJ mol<sup>-1</sup> and -22.43 kJ mol<sup>-1</sup>. For all adsorbents used,  $\Delta G$  values were more negative with temperature indicating an increase in spontaneity with temperature which is characteristic of endothermic processes (Kumar, 2011; Xu *et al.*, 2013; Cantu *et al.*, 2014; Babalola *et al.*, 2016). Positive values for changes in enthalpy  $\Delta H$  and change in entropy  $\Delta S$  were as a result of endothermic process and increased randomness respectively (Goswami *et al.*, 2012).



Table 5.2: Flory-Huggins model parameters and thermodynamic parameters for Cr(VI) adsorption onto the prepared adsorbents.

	$T$ (K)	Flory-Huggins model			Thermodynamic parameters		
		$K_{FH}$	$n_{FH}$	$R^2$	$\Delta G$	$\Delta H$	$\Delta S$
		(L g <sup>-1</sup> )			(kJ mol <sup>-1</sup> )	(kJ mol <sup>-1</sup> )	(J mol <sup>-1</sup> K <sup>-1</sup> )
<b>FTP</b>	298	0.040	-2.874	0.992	-18.918		
	304	0.034	-4.075	0.963	-18.897		
	309	0.046	-2.511	0.944	-19.992	8.081	90.027
	314	0.043	-2.450	0.997	-20.135		
	319	0.046	-2.120	0.997	-20.656		
<b>MNP</b>	298	0.037	-3.386	0.994	-18.759		
	304	0.048	-2.121	0.996	-19.777		
	309	0.055	-1.549	0.995	-20.442	20.845	133.3
	314	0.060	-1.204	0.995	-21.016		
	319	0.066	-0.905	0.986	-21.593		
<b>FTP-MNP</b>	298	0.039	-3.080	0.973	-18.839		
	304	0.058	-1.586	0.982	-20.243		
	309	0.070	-0.984	0.954	-21.053	32.677	173.57
	314	0.090	-0.499	0.838	-22.051		
	319	0.090	-0.453	0.854	-22.426		
<b>Mn MNP</b>	298	0.038	-2.824	0.972	-18.808		
	304	0.043	-2.261	0.961	-19.492		
	309	0.052	-1.531	0.993	-20.299	20.197	130.85
	314	0.060	-1.115	0.973	-20.985		
	319	0.063	-0.937	0.974	-21.465		
<b>Mn FTP-MNP</b>	298	0.045	-2.182	0.982	-19.193		
	304	0.053	-1.498	0.965	-20.036		
	309	0.053	-1.412	0.981	-20.372	7.099	88.705
	314	0.054	-1.357	0.986	-20.727		
	319	0.056	-1.233	0.970	-21.139		

## 5.4 Conclusion

The isotherm and thermodynamic analysis of As(III) and Cr(VI) adsorption onto the as-prepared adsorbents namely FTP, MNP, FTP-MNP, Mn MNP and Mn FTP-MNP all indicated that adsorption was favourable at all temperatures. Adsorption on all adsorbents took place on homogenous sites resulting in monolayer coverage of the adsorbent surface with minimal interaction between adsorbed molecules. Both three-parameter and two-parameter isotherm models accurately predicted the adsorption process, with three-parameter R-P and Sips Isotherm models predicting the adsorption process more accurately. The mean adsorption energy for the adsorption process indicated As(III) and Cr(VI) adsorption on all adsorbents was via chemical adsorption and ion-exchange was the predominant mechanism of adsorption. This was also confirmed by thermodynamic analyses and it was indicated that the adsorption process was endothermic on all adsorbents used and was spontaneous at all temperatures.

The adsorption capacities for all adsorbents were relatively higher for As(III) than for Cr(VI) at all temperatures with 14.92 %, 18.49 %, 14.27 %, 16.64 % and 37.99 % higher capacities on FTP, MNP, FTP-MNP, Mn MNP and Mn FTP-MNP at 298 K respectively. The significantly higher adsorption on magnetite and manganese containing adsorbents was attributed to the higher affinity of magnetite for arsenic and the presence of manganese which enhanced arsenic removal through the oxidation of As(III) to As(V) (Chowdhury & Yanful, 2010; Li *et al.*, 2010).

## 5.5 References

- ALBADARIN, A.B., MANGWANDI, C., WALKER, G.M., ALLEN, S.J., AHMAD, M.N.M., & KHRAISHEH, M. (2013). Influence of solution chemistry on Cr(VI) reduction and complexation onto date-pits/tea-waste biomaterials. *J. Environ. Manage.* 114. p.190–201.
- ALMASRI, D.A., RHADFI, T., ATIEH, M.A., MCKAY, G., & AHZI, S. (2018). High performance hydroxyiron modified montmorillonite nanoclay adsorbent for arsenite removal. *Chem. Eng. J.* 335. p.1–12.
- ARGUN, M.E., DURSUN, S., OZDEMIR, C., & KARATAS, M. (2007). Heavy metal adsorption by modified oak sawdust: Thermodynamics and kinetics. *J. Hazard. Mater.* 141. p.77–85.
- BABALOLA, J.O., KOIKI, B.A., ENIAYEWU, Y., SALIMONU, A., OLOWOYO, J.O., ONINLA, V.O., ALABI, H.A., OFOMAJA, A.E., & OMOROGIE, M.O. (2016). Adsorption efficacy of *Cedrela odorata* seed waste for dyes: Non linear fractal kinetics and non linear equilibrium studies. *J. Environ. Chem. Eng.* 4. p.3527–3536.
- BODDU, V.M., ABBURI, K., TALBOTT, J.L., SMITH, E.D., & HAASCH, R. (2008). Removal of arsenic (III) and arsenic (V) from aqueous medium using chitosan-coated biosorbent. *Water Res.* 42. p.633–642.
- CANTU, Y., REMES, A., REYNA, A., MARTINEZ, D., VILLARREAL, J., RAMOS, H., TREVINO, S., TAMEZ, C., MARTINEZ, A., EUBANKS, T., & PARSONS, J.G. (2014). Thermodynamics, Kinetics, and Activation energy Studies of the sorption of chromium(III) and chromium(VI) to a Mn<sub>3</sub>O<sub>4</sub> nanomaterial. *Chem. Eng. J.* 254. p.374–383.
- CAO, C., XIAO, L., CHEN, C., SHI, X., CAO, Q., & GAO, L. (2014). In situ preparation of magnetic Fe<sub>3</sub>O<sub>4</sub>/chitosan nanoparticles via a novel reduction–precipitation method and their application in adsorption of reactive azo dye. *Powder Technol.* 260. p.90–97.
- CHEN, R., CHAI, L., LI, Q., SHI, Y., WANG, Y., & MOHAMMAD, A. (2013). Preparation and characterization of magnetic Fe<sub>3</sub>O<sub>4</sub>/CNT nanoparticles by RPO method to enhance the efficient removal of Cr(VI). *Environ. Sci. Pollut. Res.* 20. p.7175–7185.
- CHOWDHURY, S.R., & YANFUL, E.K. (2010). Arsenic and chromium removal by mixed magnetite-maghemite nanoparticles and the effect of phosphate on removal. *J. Environ. Manage.*

91. p.2238–47.

DADA, A.O., OLALEKAN, A.P., OLATUNYA, A.M., & DADA, O. (2012). Langmuir , Freundlich , Temkin and Dubinin – Radushkevich Isotherms Studies of Equilibrium Sorption of  $Zn^{2+}$  onto Phosphoric Acid Modified Rice Husk. *IOSR J. Appl. Chem.* 3. p.38–45.

EBRAHIMIAN PIRBAZARI, A., SABERIKHAH, E., BADROUH, M., & EMAMI, M.S. (2014a). Alkali treated Foumanat tea waste as an efficient adsorbent for methylene blue adsorption from aqueous solution. *Water Resour. Ind.* 6. p.64–80.

EBRAHIMIAN PIRBAZARI, A., SABERIKHAH, E., & HABIBZADEH KOZANI, S.S.S. (2014b).  $Fe_3O_4$ -wheat straw: Preparation, characterization and its application for methylene blue adsorption. *Water Resour. Ind.* 7–8. p.23–37.

GOSWAMI, A., RAUL, P.K.K., & PURKAIT, M.K.K. (2012). Arsenic adsorption using copper (II) oxide nanoparticles. *Chem. Eng. Res. Des.* 90. p.1387–1396.

HAN, R., ZOU, W., WANG, Y., & ZHU, L. (2007). Removal of uranium(VI) from aqueous solutions by manganese oxide coated zeolite: discussion of adsorption isotherms and pH effect. *J. Environ. Radioact.* 93. p.127–43.

IGBERASE, E., OSIFO, P., & OFOMAJA, A. (2017). The Adsorption of Pb, Zn, Cu, Ni, and Cd by Modified Ligand in a Single Component Aqueous Solution: Equilibrium, Kinetic, Thermodynamic, and Desorption Studies. *Int. J. Anal. Chem.* 2017. p.1–15.

KUMAR, U. (2011). Thermodynamics of the Adsorption of Cd ( II ) from Aqueous Solution on NCRH. *Int. J. Environ. Sci. Dev.* 2. p.334–336.

KUPETA, A.J.K., NAIDOO, E.B., & OFOMAJA, A.E. (2018). Kinetics and equilibrium study of 2-nitrophenol adsorption onto polyurethane cross-linked pine cone biomass. *J. Clean. Prod.* 179. p.191–209.

LEE, C., ALVAREZ, P.J.J., NAM, A., PARK, S., DO, T., CHOI, U., & LEE, S. (2017). Arsenic ( V ) removal using an amine-doped acrylic ion exchange fiber : Kinetic , equilibrium , and regeneration studies. *J. Hazard. Mater.* 325. p.223–229.

LI, X. JUAN, LIU, C. SHUAI, LI, F. BAI, LI, Y. TAO, ZHANG, L. JIA, LIU, C. PING, & ZHOU,

- Y. ZHANG. (2010). The oxidative transformation of sodium arsenite at the interface of  $\alpha$ -MnO<sub>2</sub> and water. *J. Hazard. Mater.* 173. p.675–681.
- LIU, C.H., CHUANG, Y.H., CHEN, T.Y., TIAN, Y., LI, H., WANG, M.K., & ZHANG, W. (2015a). Mechanism of Arsenic Adsorption on Magnetite Nanoparticles from Water: Thermodynamic and Spectroscopic Studies. *Environ. Sci. Technol.* 49. p.7726–7734.
- LIU, Y., LUO, C., CUI, G., & YAN, S. (2015b). Synthesis of manganese dioxide/iron oxide/graphene oxide magnetic nanocomposites for hexavalent chromium removal. *RSC Adv.* 5. p.54156–54164.
- MALANA, M.A., QURESHI, R.B., & ASHIQ, M.N. (2011). Adsorption studies of arsenic on nano aluminium doped manganese copper ferrite polymer (MA, VA, AA) composite: Kinetics and mechanism. *Chem. Eng. J.* 172. p.721–727.
- NECHIFOR, G., PASCU, D.E., NEAGU, M.P., TRAISTARU, G.A., & ALBU, P.C. (2015). Comparative study of temkin and floryhuggins isotherms for adsorption of phosphate anion on membranes. *UPB Sci. Bull. Ser. B Chem. Mater. Sci.* 77. p.63–72.
- OFOMAJA, A.E., & HO, Y.-S. (2008). Effect of temperatures and pH on methyl violet biosorption by *Mansonia* wood sawdust. *Bioresour. Technol.* 99. p.5411–5417.
- PAKADE, V.E., NTULI, T.D., & OFOMAJA, A.E. (2017). Biosorption of hexavalent chromium from aqueous solutions by *Macadamia* nutshell powder. *Appl. Water Sci.* 7. p.3015–3030.
- PÉREZ MARÍN, A.B., AGUILAR, M.I., MESEGUER, V.F., ORTUÑO, J.F., SÁEZ, J., & LLORÉNS, M. (2009). Biosorption of chromium (III) by orange (*Citrus cinensis*) waste: Batch and continuous studies. *Chem. Eng. J.* 155. p.199–206.
- ROSTAMIAN, R., & BEHNEJAD, H. (2016). A comparative adsorption study of sulfamethoxazole onto graphene and graphene oxide nanosheets through equilibrium, kinetic and thermodynamic modeling. *Process Saf. Environ. Prot.* 102. p.20–29.
- WASIM, A.A., & KHAN, M.N. (2016). Physicochemical Effects of Alkali Treatment on Acid Activated Pine Shell for the Removal of Lead Ions From Aqueous Medium. *J. Dispers. Sci. Technol.* 2691. p.01932691.2016.1225506.

XU, M., WANG, H., LEI, D., QU, D., ZHAI, Y., & WANG, Y. (2013). Removal of Pb(II) from aqueous solution by hydrous manganese dioxide: Adsorption behavior and mechanism. *J. Environ. Sci.* 25. p.479–486.

### 6 Kinetics studies of As(III) and Cr(VI) Adsorption onto the Prepared Adsorbents

#### 6.1 Introduction

Adsorption kinetics involves the study of how rapidly adsorption takes place. The collected data is then fitted into kinetic models which allow for the calculation of parameters which aid in the determination of the nature of adsorption and the rate determining step in the adsorption process.

This chapter describes the effect of time on the adsorption of As(III) and Cr(VI) on the as-synthesized adsorbents. The data was modelled using pseudo-first order, pseudo-second order, Elovich and intraparticle diffusion models to determine the rate controlling processes and to determine the nature of adsorption on the adsorbents.

##### 6.1.1 Kinetic Models

The obtained adsorption data was fitted to kinetic models to determine the adsorption rate constants and identify the rate determining steps in the adsorption of As(III) and Cr(VI) onto the prepared adsorbents. The data was modelled using pseudo-first order, pseudo-second order, Elovich and intraparticle diffusion models.

###### 6.1.1.1 Pseudo-first and Pseudo-second Order Models

These models describe the adsorption process following diffusion through a boundary layer. They assume that (i) adsorption occurs on localised sites with no interaction between adsorbed ions, (ii) the energy of adsorption is not dependent on surface coverage, (iii) saturated monolayer of adsorbates on the adsorbent surface corresponds to maximum adsorption, (iv) adsorbate uptake is governed by a first-order and second order rate equations for pseudo-first and pseudo-order models respectively (Largitte & Pasquier, 2016). Additionally, the pseudo-second order model also assumes that the rate limiting step is chemical adsorption involving the exchange or sharing of electrons between the adsorbate and adsorbent (Albadarin *et al.*, 2011; Qiu *et al.*, 2009). Pseudo-first and pseudo-second order kinetics are described by Equations 6.1 and 6.2 respectively where,  $q_t$  ( $\text{mg g}^{-1}$ ) is the amount of arsenite adsorbed per unit mass of the composite at any time  $t$ ,  $q_e$  ( $\text{mg g}^{-1}$ ) is the amount of arsenite adsorbed per unit mass of composite at equilibrium,  $k_1$  ( $\text{min}^{-1}$ )

and  $k_2$  ( $\text{g mg}^{-1} \text{ min}^{-1}$ ) are the adsorption rate constants for pseudo-first and pseudo-second order models respectively and  $h$  ( $\text{mg g}^{-1} \text{ min}^{-1}$ ) is the initial sorption rate described by Equation 6.3.

$$q_t = q_e (1 - e^{-k_1 t}) \quad (6.1)$$

$$q_t = \frac{k_2 q_e^2 t}{1 + k_2 q_e t} \quad (6.2)$$

$$h = k_2 q_e^2 \quad (6.3)$$

#### 6.1.1.2 Elovich Model

The Elovich model is described by Equation 6.4 where  $\alpha$  ( $\text{mg g}^{-1} \text{ min}^{-1}$ ) is the rate of chemisorption at zero coverage and  $\beta$  ( $\text{g mg}^{-1}$ ) is the desorption constant (Namasivayam & Sureshkumar, 2008).

$$q_t = \frac{1}{\beta} \ln(1 + \alpha \beta t) \quad (6.4)$$

The Elovich model describes the kinetics of chemisorption and assumes that adsorption occurs on localised sites with interaction between adsorbed ions and that the energy of adsorption increases linearly with the surface coverage (Largitte & Pasquier, 2016).

#### 6.1.1.3 Intraparticle Diffusion Model

The intraparticle diffusion model describes ion movements from the bulk solution to the adsorbent surface. This model shows a linear variation of adsorbate uptake ( $q_t$ ) with the square root of contact time ( $t^{0.5}$ ) with a slope of the intraparticle diffusion rate constant ( $k_{id}$ ) (eq 6.5). The plot has a zero intercept ( $C$ ) if intraparticle diffusion is the sole rate limiting step and  $C > 0$  when the rate limiting step is simultaneously controlled by both film and intraparticle diffusion (Qiu *et al.*, 2009). The intercept  $C$  reflects the thickness of the adsorbed species at the boundary layer (Ofomaja *et al.*, 2010).

$$q_t = k_{id} t^{0.5} + C \quad (6.5)$$



## 6.2 Experimental

### 6.2.1 Materials

All adsorbents used herein, were sourced and synthesized as described in Chapter 3. Hydrochloric acid (32%) was supplied by Merck, sodium arsenite ( $\text{NaAsO}_2$  >90%) was purchased from Sigma-Aldrich. Potassium dichromate ( $\text{K}_2\text{Cr}_2\text{O}_7$  >99 %) and Sodium Hydroxide ( $\text{NaOH}$  >98 %) were purchased from Associated Chemical Enterprises (South Africa). All chemicals were used as supplied without any further purification.

### 6.2.2 Methods

Stock solutions of As(III) and Cr(VI) were prepared by dissolving the desired amounts of sodium arsenite and potassium dichromate respectively in deionized water to prepare  $1000 \text{ mg L}^{-1}$  solutions. Serial dilution from the stock solutions was used to prepare solutions of concentrations ranging from  $25 \text{ mg L}^{-1}$  to  $150 \text{ mg L}^{-1}$ .

To study the effect of time on adsorption, solutions with concentrations ranging from 25 to  $150 \text{ mg L}^{-1}$  were prepared and the pH adjusted to pH 8 and pH 2 for arsenite and hexavalent chromium adsorption respectively. 100 mL of each solution was agitated at 200 rpm on a Carousel 6 reaction station fitted with a Tornado overhead stirring system for 15 minutes before contacting with the adsorbent materials to ensure the solution was at the desired temperature of 298 K. After 15 minutes 0.5 g of the respective adsorbent material was introduced into the flask containing the solution and agitated for a further two hours with samples being taken for analysis at specified intervals. After adsorption, the concentration of arsenite in solution was determined on a Thermo Fischer Scientific ICP 7000 inductively coupled plasma-optical emission spectrometer (ICP-OES) and Cr(VI) concentration was determined spectrophotometrically following the diphenyl-carbazide method at a wavelength of 540 nm (Bishop *et al.*, 2014).

## 6.3 Results and Discussions

### 6.3.1 Arsenic Adsorption

The model data (Fig. 6.1 - 6.5) shows that the As(III) adsorption capacity of the adsorbents increased rapidly within the first five minutes and later slowed reaching equilibrium after approximately 60 minutes. During the fast-initial adsorption stage, arsenite ions were rapidly transferred to the adsorbent surface due to a high number of vacant sites and a high concentration

gradient (Kamsonlian *et al.*, 2012). This fast adsorption step may be a result of external surface adsorption (Feng *et al.*, 2012) followed by a slower step in which intraparticle diffusion was dominant (Zhang *et al.*, 2010). As adsorption proceeded the concentration gradient was gradually reduced as adsorbent sites were occupied till an equilibrium state was reached between the concentration of ions in the solution and at the adsorbent surface. During the fast adsorption phase, pseudo-first order, pseudo-second order and Elovich models accurately predicted the experimental results. After the fast phase, pseudo-first order and Elovich models deviated from the experimental data and pseudo-second order model better fitted the experimental data for all adsorbents (Fig. 6.1 - 6.5). The pseudo-second order model assumes the rate limiting step is the sharing or exchange of electrons between arsenic and the adsorbent surface (Kamsonlian *et al.*, 2012). It thus indicates chemical adsorption was the main mechanism of adsorption hence confirming the results obtained from the D-R isotherm model (Randhawa *et al.*, 2014).

The Elovich model described by Equation 6.4 was used to interpret the kinetics of chemisorption on heterogenous adsorbents. It assumes heterogenous active surface sites exhibiting different activation energies (Pérez Marín *et al.*, 2009). Elovich constants were determined from the non-linear fit of the model on the experimental data (Table B-1 – B-5). The initial sorption rate  $\alpha$  was higher than the desorption constant  $\beta$  for all adsorbents indicating that all the adsorbents used were viable for arsenic adsorption (Chaudhry *et al.*, 2017). The coefficients of determination for Elovich model were  $> 0.9$  for all adsorbents confirming that the adsorption of As(III) on all adsorbents was a chemical process.

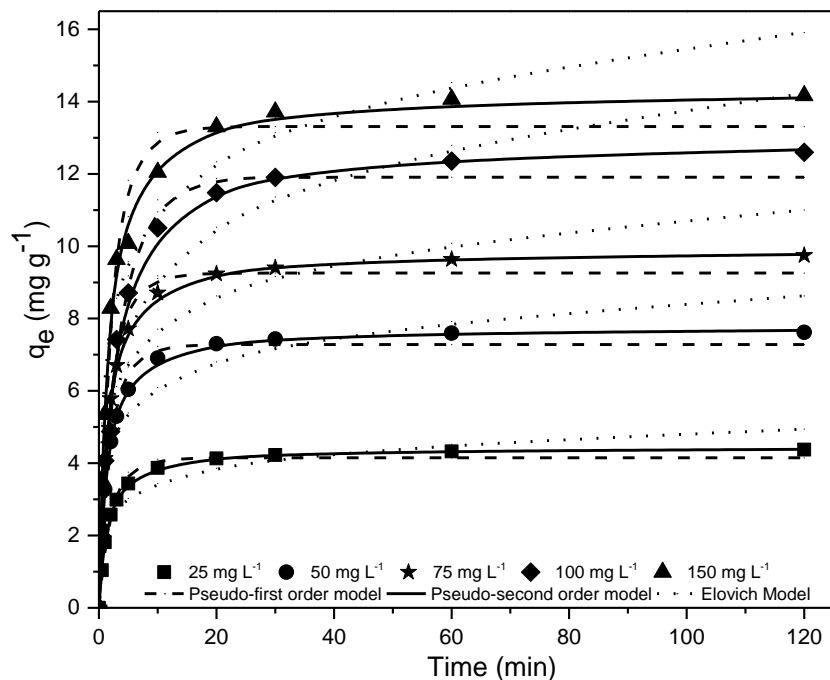


Fig. 6.1: Kinetic model fitting for As(III) adsorption onto FTP. Dose: 5g/L, pH: 8, stirring speed: 200 rpm, temperature: 298 K.

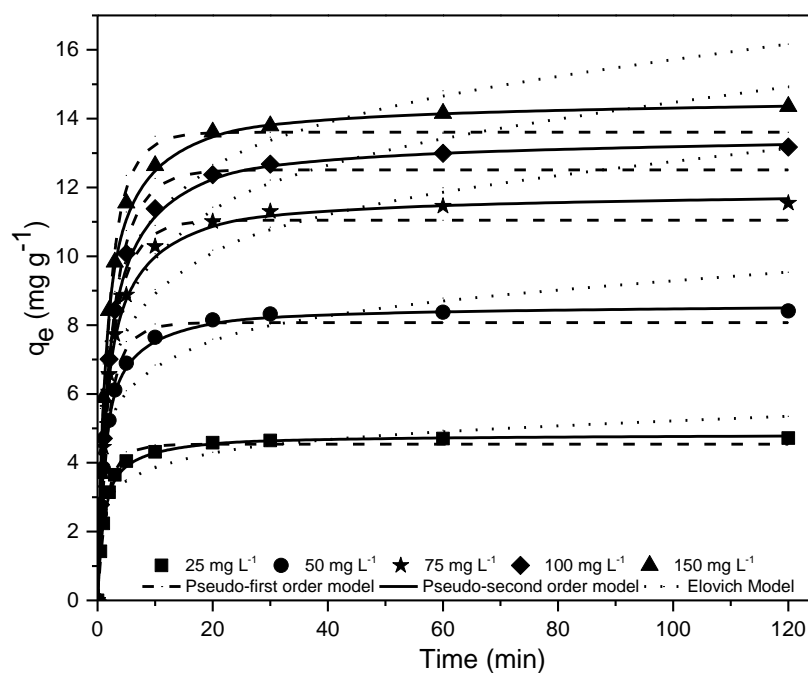


Fig. 6.2: Kinetic model fitting for As(III) adsorption onto MNP. Dose: 5g/L, pH: 8, stirring speed: 200 rpm, temperature: 298 K.

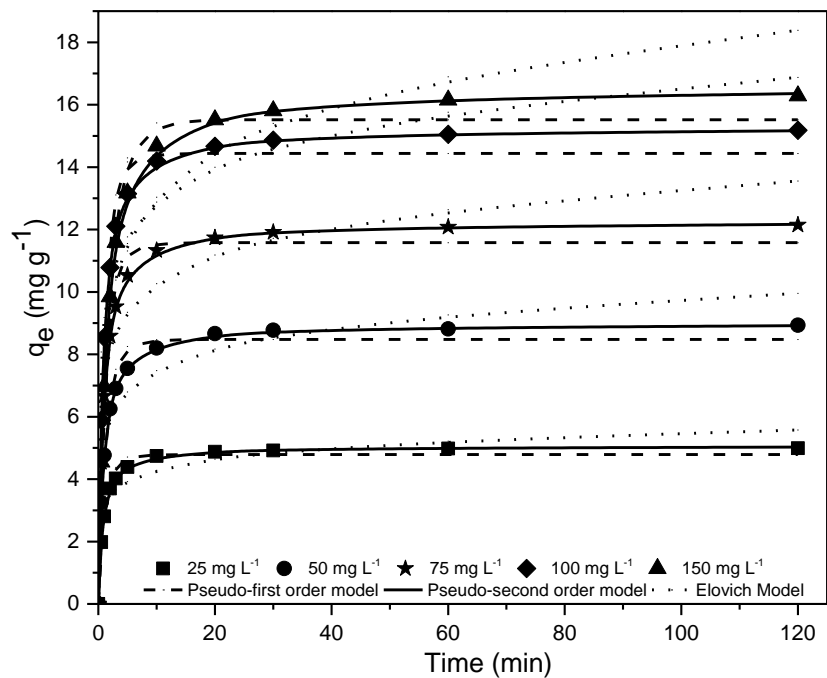


Fig. 6.3: Kinetic model fitting for As(III) adsorption onto FTP-MNP. Dose: 5g/L, pH: 8, stirring speed: 200 rpm, temperature: 298 K.

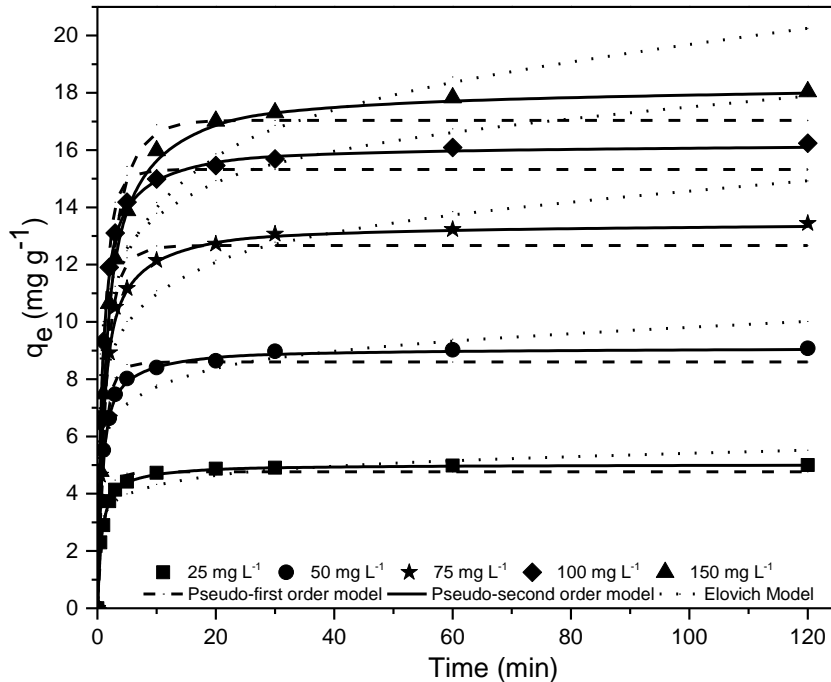


Fig. 6.4: Kinetic model fitting for As(III) adsorption onto Mn MNP. Dose: 5g/L, pH: 8, stirring speed: 200 rpm, temperature: 298 K.

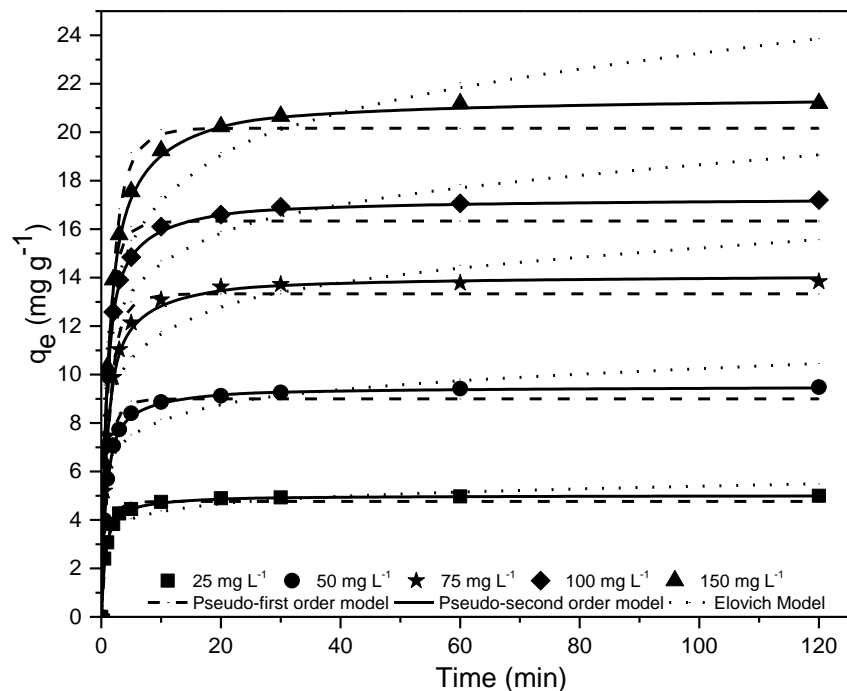


Fig. 6.5: Kinetic model fitting for As(III) adsorption onto Mn FTP-MNP. Dose: 5g/L, pH: 8, stirring speed: 200 rpm, temperature: 298 K.

The data was modelled using the intraparticle diffusion model to determine the role of diffusion on the adsorption process. The intraparticle diffusion model describes ion movements from the bulk solution to the adsorbent surface. The experimental data (Fig. 6.6 - 6.10) showed a curve from the origin to the start of the linear section indicating external mass transfer and/or boundary layer diffusion (Igberase *et al.*, 2018; Kamsonlian *et al.*, 2012). The intercept of the linear section in the plot of  $q_t$  against  $t^{0.5}$  indicated the thickness of the boundary layer and  $C > 0$  for all adsorbents confirmed that intraparticle diffusion was not the sole rate limiting step, therefore surface adsorption also contributed to the rate limiting step (Ranjan *et al.*, 2009). Linear sections of the plots were almost parallel suggesting that the rate of adsorption was comparable at initial solution concentrations for all adsorbents used. An increase in intraparticle diffusion rate constant ( $k_{id}$ ) as the solution concentration increased (Table B-1 – B-5) resulted from greater driving forces for

mass transfer and enhanced diffusion through macro-pores as solution concentration was increased (Kamsonlian *et al.*, 2012).

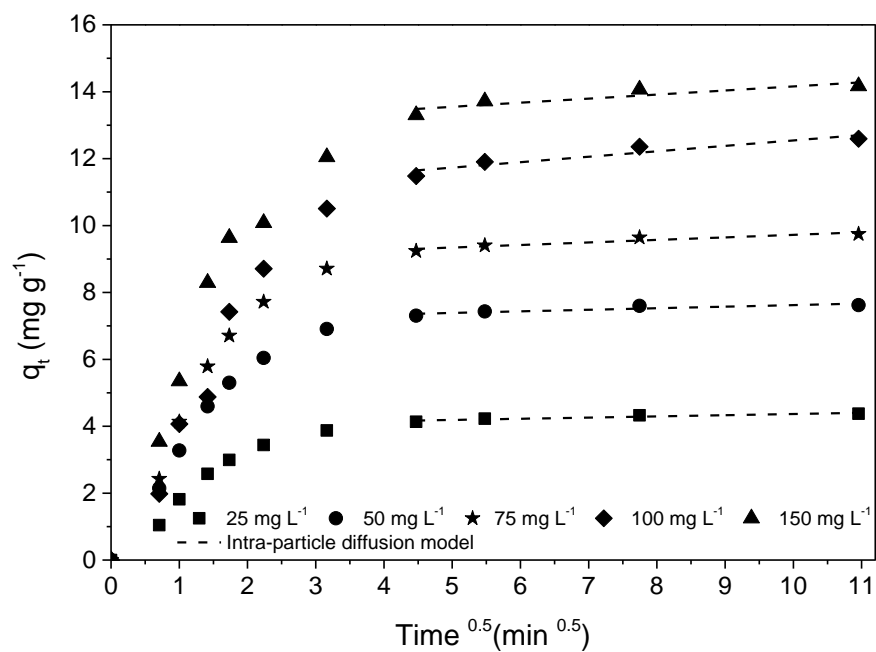


Fig. 6.6: Intraparticle diffusion modelling of As(III) adsorption onto FTP

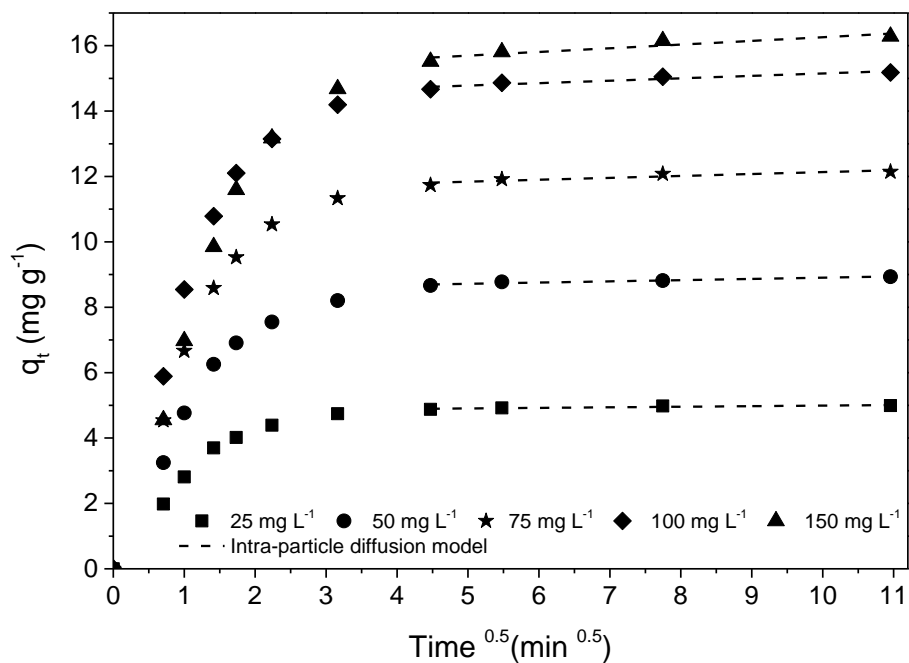


Fig. 6.7: Intraparticle diffusion modelling of As(III) adsorption onto MNP

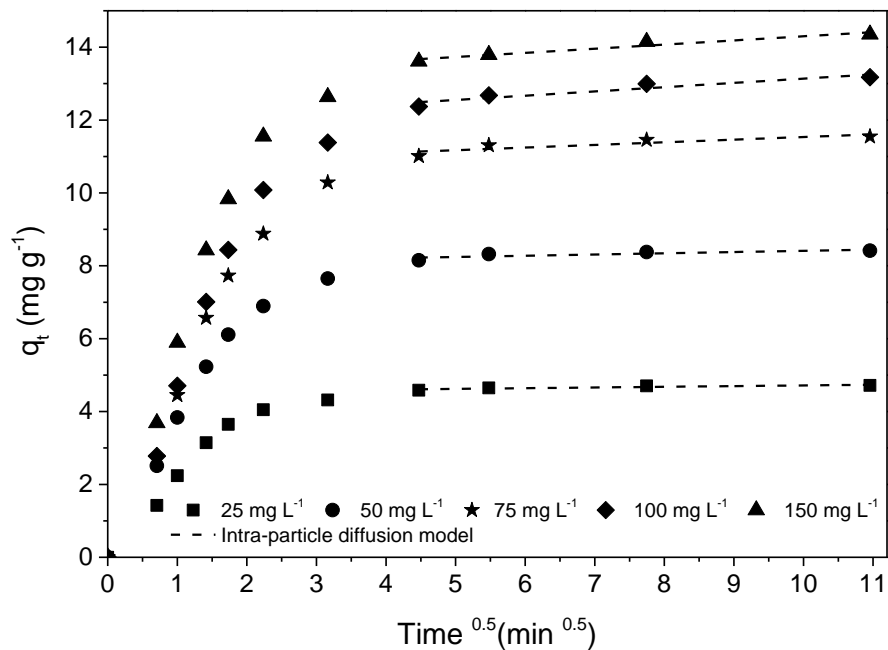


Fig. 6.8: Intraparticle diffusion modelling of As(III) adsorption onto FTP-MNP

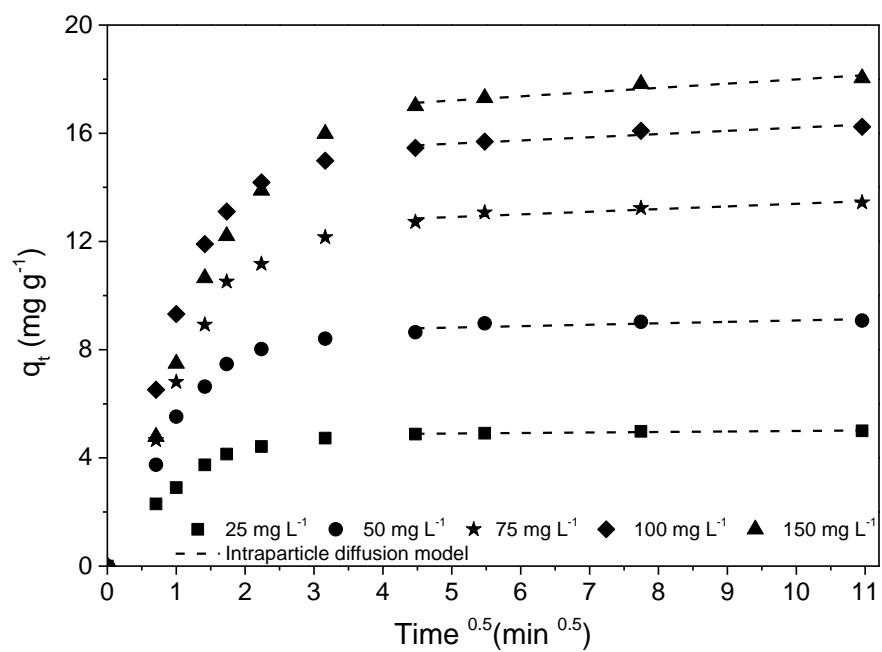


Fig. 6.9: Intraparticle diffusion modelling of As(III) adsorption onto Mn MNP

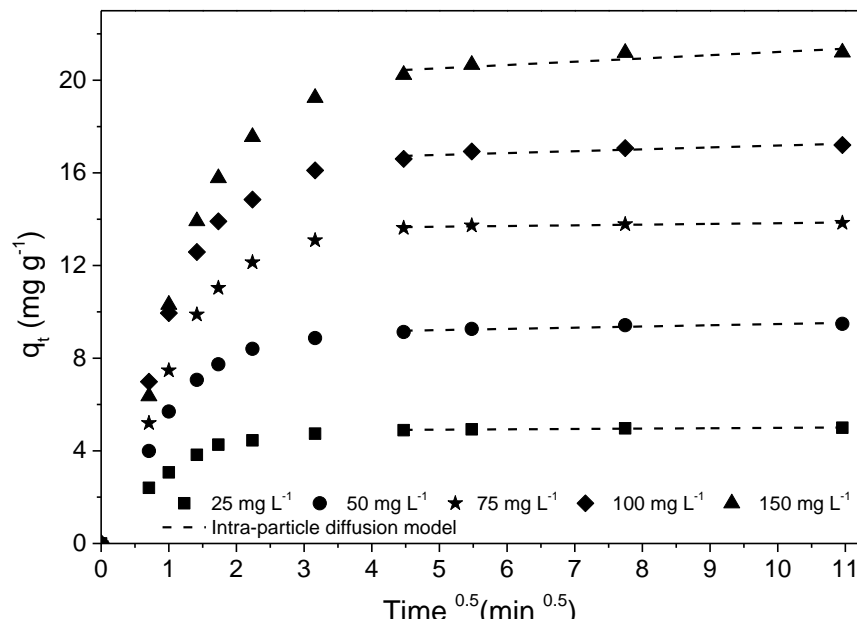


Fig. 6.10: Intraparticle diffusion modelling of As(III) adsorption onto Mn FTP-MNP

### 6.3.2 Chromium Adsorption

Hexavalent chromium (Cr(VI)) adsorption data was modelled using pseudo-first order, pseudo-second order, Elovich and intraparticle diffusion kinetic models to determine the nature of adsorption onto the as-synthesised adsorbent materials. The fitting of experimental data to the pseudo-first order, pseudo-second order and Elovich models was done using non-linear regression and the corresponding coefficients of determination were used to determine the model with the best fit. The non-linear curve fits (Fig. 6.11 - 6.15) were used to calculate model parameters for pseudo-first order, pseudo-second order and Elovich kinetic models.



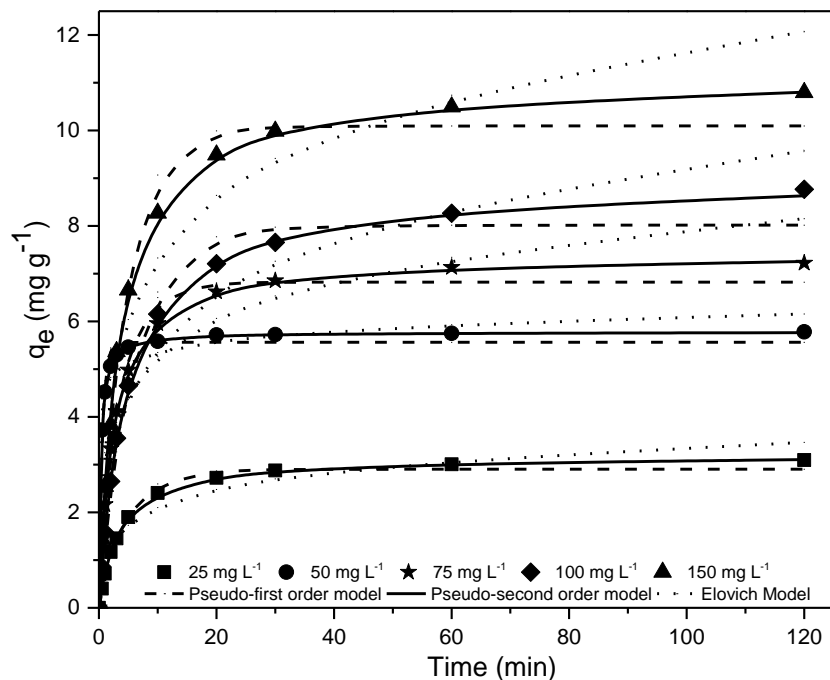


Fig. 6.11: Kinetic model fitting for Cr(VI) adsorption onto FTP. Dose: 5g/L, pH: 2, stirring speed: 200 rpm, temperature: 298 K.

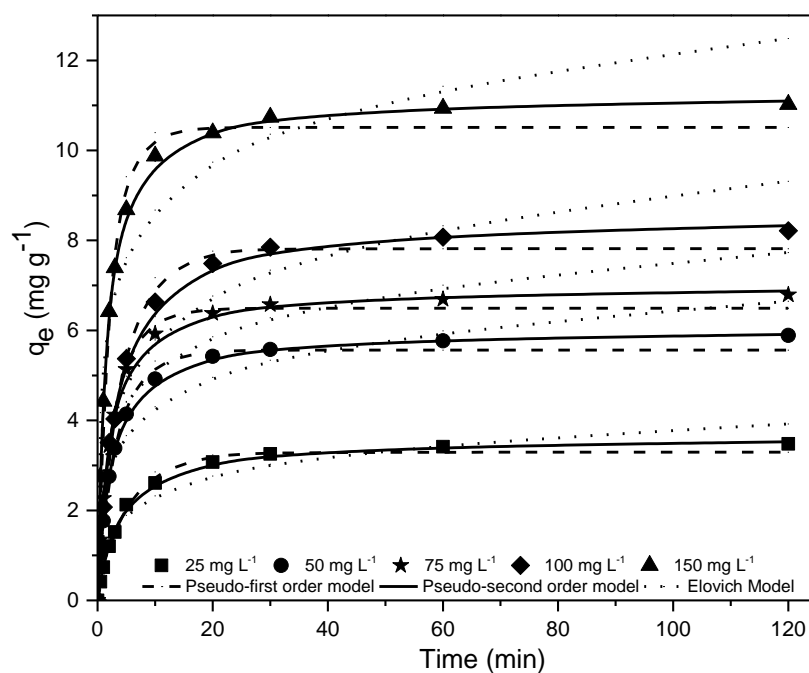


Fig. 6.12: Kinetic model fitting for Cr(VI) adsorption onto MNP. Dose: 5g/L, pH: 2, stirring speed: 200 rpm, temperature: 298 K.

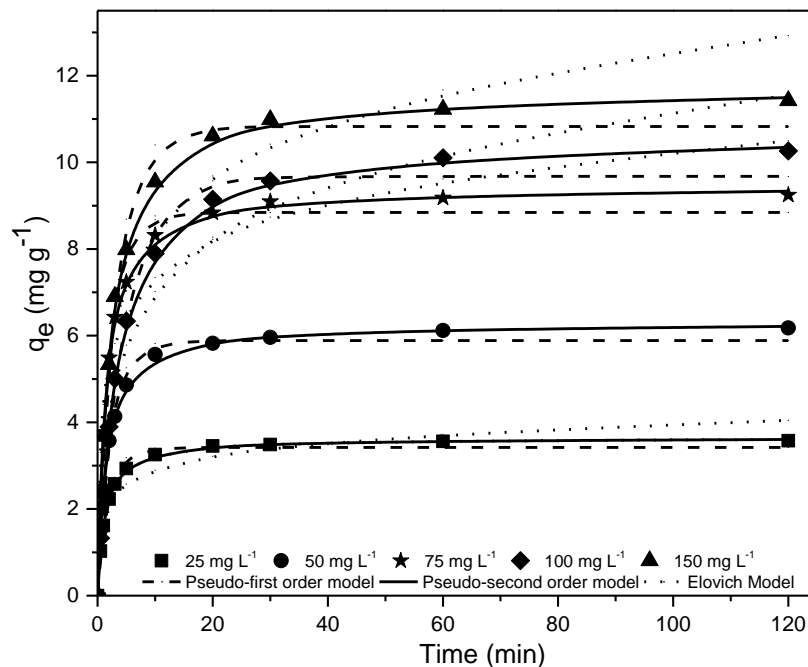


Fig. 6.13: Kinetic model fitting for Cr(VI) adsorption onto FTP-MNP. Dose: 5g/L, pH: 2, stirring speed: 200 rpm, temperature: 298 K.

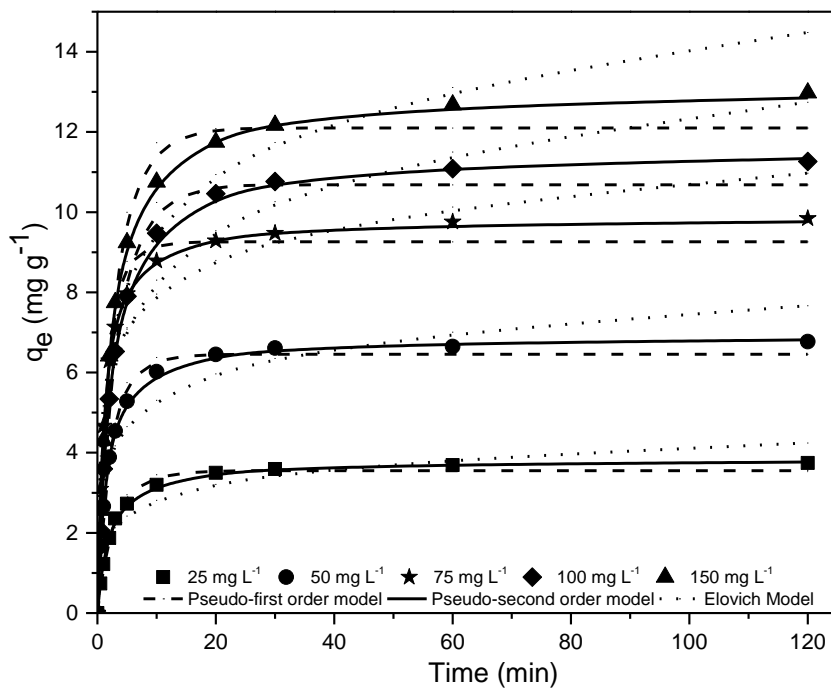


Fig. 6.14: Kinetic model fitting for Cr(VI) adsorption onto Mn MNP. Dose: 5g/L, pH: 2, stirring speed: 200 rpm, temperature: 298 K.

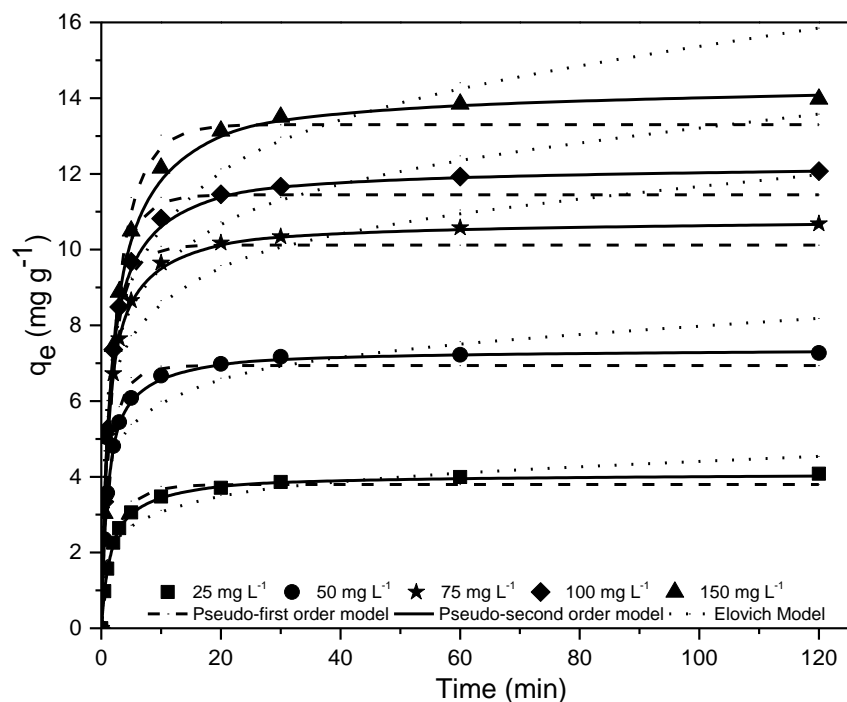


Fig. 6.15: Kinetic model fitting for Cr(VI) adsorption onto Mn FTP-MNP. Dose: 5g/L, pH: 2, stirring speed: 200 rpm, temperature: 298 K.

Model parameters were calculated and presented in Table B-6 – B-10. From the obtained data, the Cr(VI) adsorption coefficient of determination was higher for the pseudo-second order model as compared to the other models. The experimental  $q_e$  values were close to those obtained from the pseudo-second order model indicating that chemisorption was the rate controlling factor, with the adsorption capacity being proportional to the number of sites on the adsorbent (Makrigianni *et al.*, 2017). The adsorption capacity increased with increasing initial Cr(VI) concentration due to the greater driving force resulting in a more efficient utilization of the adsorption capacity (Luo *et al.*, 2013). Cr(VI) adsorption has been reported to be via adsorption and reduction to Cr(III). The rate constants were low for all adsorbents indicating that the adsorption of Cr(VI) onto all the used adsorbents was a slow process implying that Cr(VI) reduction was more via ion exchange resulting in Cr(III) formation than direct adsorption of Cr(VI) ions (Luo *et al.*, 2013; El-Korashy *et al.*, 2016; Makrigianni *et al.*, 2017). The Elovich model was used to confirm the kinetics of chemisorption. The initial sorption rate ( $\alpha$ ) was higher than the desorption constant ( $\beta$ ) at all concentrations indicating that Cr(VI) adsorption was favorable on the used adsorbents (El-Korashy *et al.*, 2016). The correlation coefficients for the Elovich model were close to unity suggesting that

the adsorption of Cr(VI) was via chemical adsorption involving the exchange of electrons between adsorbent and adsorbate (Namasivayam & Sureshkumar, 2008).

To determine the contribution of diffusion to the adsorption process, the intraparticle diffusion model was applied, the plot of  $q_t$  against  $t^{0.5}$  showed an initial curved section followed by a linear section (Fig. 6.16 - 6.20). The curved section indicated boundary layer adsorption and film diffusion while in the linear section intraparticle diffusion was dominant (Bajpai & Armo, 2009; Chen *et al.*, 2011; Zhang *et al.*, 2016). The linear section had a low gradient for all adsorbents indicating a slow kinetic rate controlled by intraparticle diffusion into the macro and meso pores of the adsorbent leading to equilibrium (El-Korashy *et al.*, 2016). The results therefore indicated that both film diffusion and intraparticle diffusion were involved in the adsorption process (Zhang *et al.*, 2016).

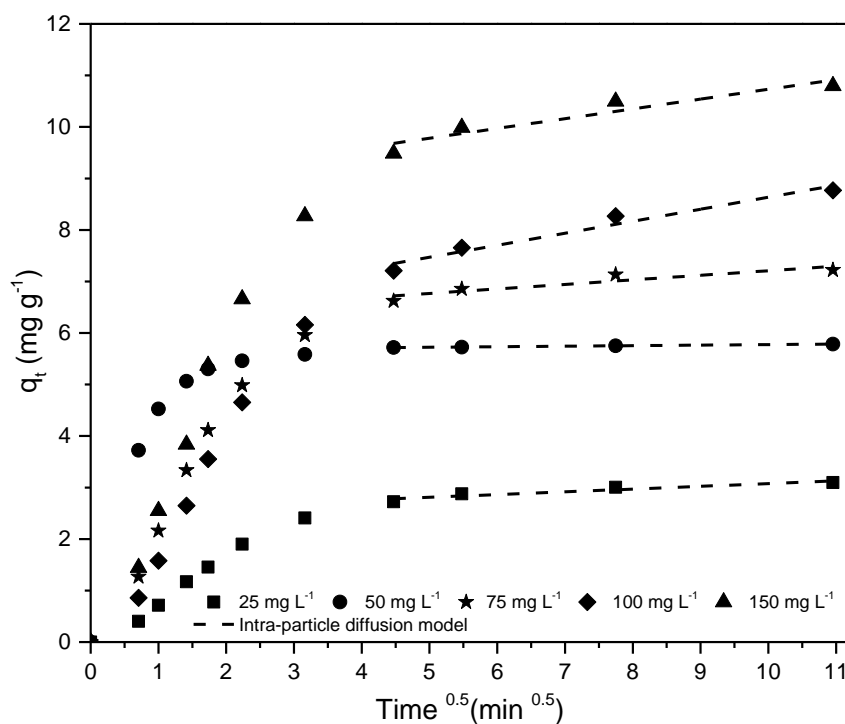


Fig. 6.16: Intraparticle diffusion modelling of Cr(VI) adsorption onto FTP

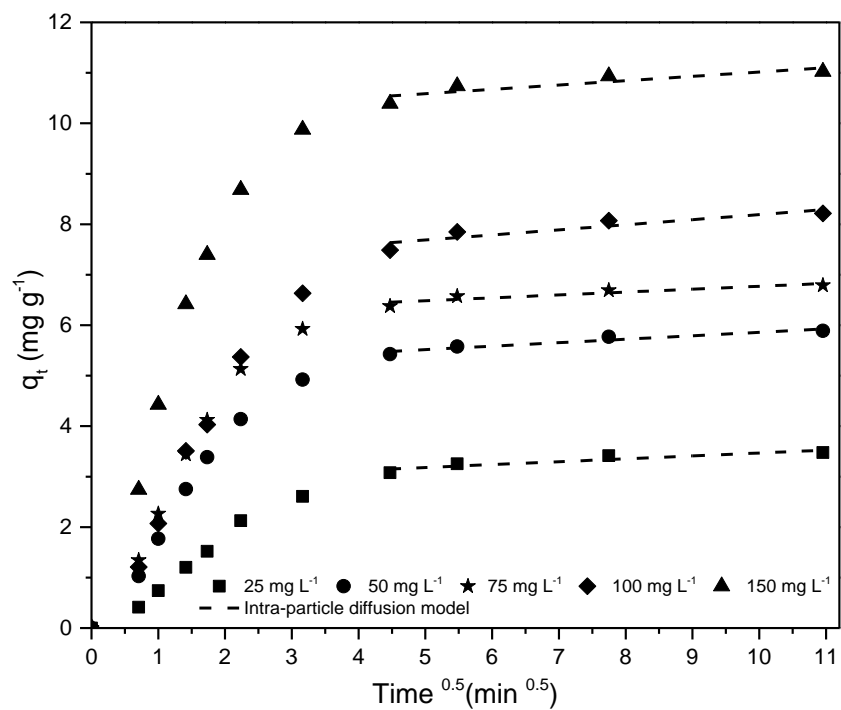


Fig. 6.17: Intraparticle diffusion modelling of Cr(VI) adsorption onto MNP

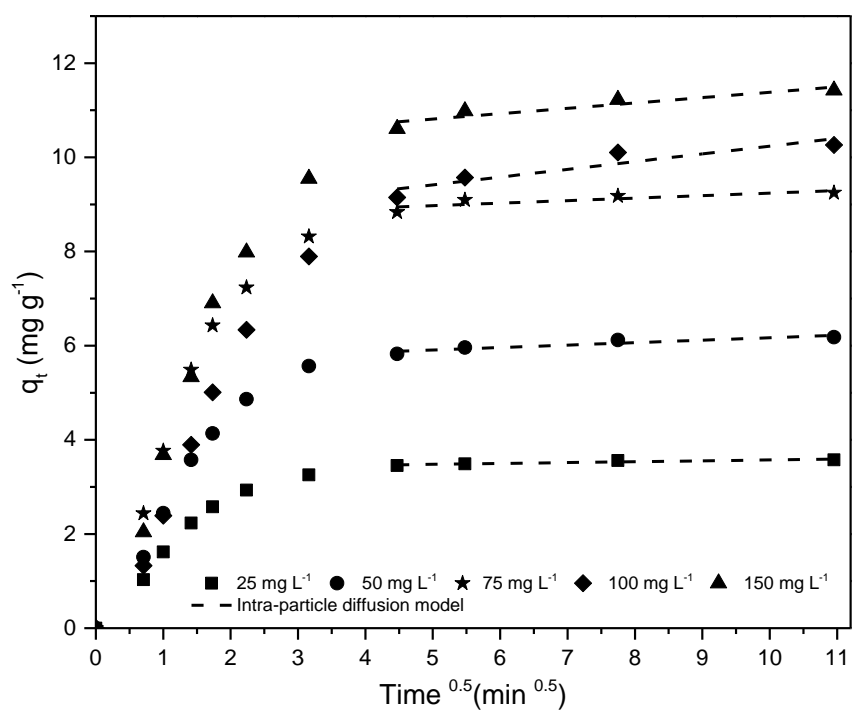


Fig. 6.18: Intraparticle diffusion modelling of Cr(VI) adsorption onto FTP-MNP

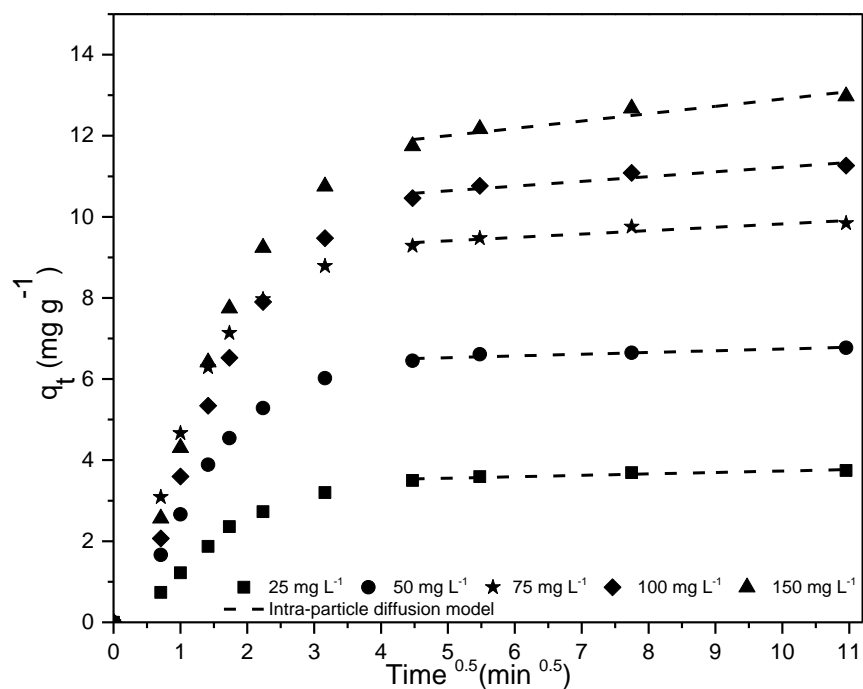


Fig. 6.19: Intraparticle diffusion modelling of Cr(VI) adsorption onto Mn MNP

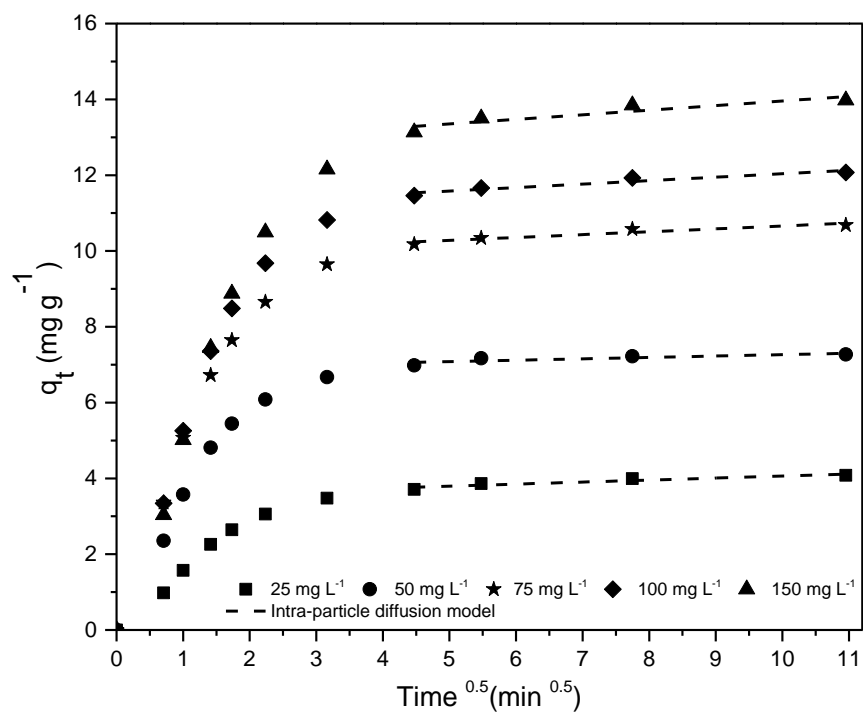


Fig. 6.20: Intraparticle diffusion modelling of Cr(VI) adsorption onto Mn FTP-MNP

## 6.4 Conclusion

Kinetic studies indicated that all the adsorbents used were efficient for binding As(III) and Cr(VI). The mechanism of adsorption on all adsorbents was determined to be via chemisorption with both film diffusion and intraparticle diffusion contributing to the rate limiting steps. The initial sorption rates for As(III) were generally higher than those for Cr(VI) indicating that the adsorbents had better affinity for As(III) than Cr(VI). The Elovich model confirmed that adsorption on all adsorbents was more favourable than desorption and was via the exchange of electrons between adsorbent and adsorbate at all concentrations. The results obtained from kinetic modelling were consistent with deductions made from isotherm fitting and thermodynamic data.

## 6.5 References

- ALBADARIN, A.B., AL-MUHTASEB, A.H., AL-LAQTAH, N.A., WALKER, G.M., ALLEN, S.J., & AHMAD, M.N.M. (2011). Biosorption of toxic chromium from aqueous phase by lignin: mechanism, effect of other metal ions and salts. *Chem. Eng. J.* 169. p.20–30.
- BAJPAI, S.K., & ARMO, M.K. (2009). Equilibrium Sorption of Hexavalent Chromium from Aqueous Solution Using Iron(III)-Loaded Chitosan-Magnetite Nanocomposites As Novel Sorbent. *J. Macromol. Sci. Part A.* 46. p.510–520.
- BISHOP, M.E., GLASSER, P., DONG, H., AREY, B., & KOVARIK, L. (2014). Reduction and immobilization of hexavalent chromium by microbially reduced Fe-bearing clay minerals. *Geochim. Cosmochim. Acta.* 133. p.186–203.
- CHAUDHRY, S.A., ZAIDI, Z., & SIDDIQUI, S.I. (2017). Isotherm, kinetic and thermodynamics of arsenic adsorption onto Iron-Zirconium Binary Oxide-Coated Sand (IZBOCS): Modelling and process optimization. *J. Mol. Liq.* 229. p.230–240.
- CHEN, S., YUE, Q., GAO, B., LI, Q., & XU, X. (2011). Removal of Cr ( VI ) from aqueous solution using modified corn stalks : Characteristic , equilibrium , kinetic and thermodynamic study. *Chem. Eng. J.* 168. p.909–917.
- EL-KORASHY, S.A., ELWAKEEL, K.Z., & EL-HAFEIZ, A.A. (2016). Fabrication of bentonite/thiourea-formaldehyde composite material for Pb(II), Mn(VII) and Cr(VI) sorption: A combined basic study and industrial application. *J. Clean. Prod.* 137. p.40–50.
- FENG, L., CAO, M., MA, X., ZHU, Y., & HU, C. (2012). Superparamagnetic high-surface-area Fe<sub>3</sub>O<sub>4</sub> nanoparticles as adsorbents for arsenic removal. *J. Hazard. Mater.* 217–218. p.439–446.
- IGBERASE, E., OSIFO, P., & OFOMAJA, A. (2018). Adsorption of metal ions by microwave assisted grafting of cross-linked chitosan beads. Equilibrium, isotherm, thermodynamic and desorption studies. *Appl. Organomet. Chem.* 32. p.e4131.
- KAMSONLIAN, S., SURESH, S., RAMANAIAH, V., MAJUMDER, C.B., CHAND, S., & KUMAR, A. (2012). Biosorptive behaviour of mango leaf powder and rice husk for arsenic(III) from aqueous solutions. *Int. J. Environ. Sci. Technol.* 9. p.565–578.
- LARGITTE, L., & PASQUIER, R. (2016). A review of the kinetics adsorption models and their



application to the adsorption of lead by an activated carbon. *Chem. Eng. Res. Des.* 109. p.495–504.

LUO, C., TIAN, Z., YANG, B., ZHANG, L., & YAN, S. (2013). Manganese dioxide/iron oxide/acid oxidized multi-walled carbon nanotube magnetic nanocomposite for enhanced hexavalent chromium removal. *Chem. Eng. J.* 234. p.266–275.

MAKRIGIANNI, V., GIANNAKAS, A., BAIRAMIS, F., PAPADAKI, M., & KONSTANINOU, I. (2017). Adsorption of Cr(VI) from aqueous solutions by HNO<sub>3</sub>-purified and chemically activated pyrolytic tire char. *J. Dispers. Sci. Technol.* 38. p.992–1002.

NAMASIVAYAM, C., & SURESHKUMAR, M.V. (2008). Removal of chromium(VI) from water and wastewater using surfactant modified coconut coir pith as a biosorbent. *Bioresour. Technol.* 99. p.2218–2225.

OFOMAJA, A.E., NAIDOO, E.B., & MODISE, S.J. (2010). Dynamic studies and pseudo-second order modeling of copper(II) biosorption onto pine cone powder. *Desalination*. 251. p.112–122.

PÉREZ MARÍN, A.B., AGUILAR, M.I., MESEGUER, V.F., ORTUÑO, J.F., SÁEZ, J., & LLORÉNS, M. (2009). Biosorption of chromium (III) by orange (*Citrus cinensis*) waste: Batch and continuous studies. *Chem. Eng. J.* 155. p.199–206.

QIU, H., LV, L., PAN, B., ZHANG, Q.Q., ZHANG, W., & ZHANG, Q.Q. (2009). Critical review in adsorption kinetic models. *J. Zhejiang Univ. Sci. A.* 10. p.716–724.

RANDHAWA, N.S., DAS, N.N., & JANA, R.K. (2014). Adsorptive remediation of Cu(II) and Cd(II) contaminated water using manganese nodule leaching residue. *Desalin. Water Treat.* 52. p.4197–4211.

RANJAN, D., TALAT, M., & HASAN, S.H. (2009). Biosorption of arsenic from aqueous solution using agricultural residue “rice polish”. *J. Hazard. Mater.* 166. p.1050–1059.

ZHANG, L., LUO, H., LIU, P., FANG, W., & GENG, J. (2016). A novel modified graphene oxide/chitosan composite used as an adsorbent for Cr(VI) in aqueous solutions. *Int. J. Biol. Macromol.* 87. p.586–596.

ZHANG, S., NIU, H., CAI, Y., ZHAO, X., & SHI, Y. (2010). Arsenite and arsenate adsorption on

coprecipitated bimetal oxide magnetic nanomaterials:  $\text{MnFe}_2\text{O}_4$  and  $\text{CoFe}_2\text{O}_4$ . *Chem. Eng. J.* 158. p.599–607.

### 7 Adsorbent Regeneration Studies and the Determination of the Mechanism of As(III) and Cr(VI) Adsorption onto FTP-MNP as a Model Adsorbent

#### 7.1 Introduction

Regeneration of the spent adsorbent involves the desorption of adsorbed molecules from the adsorbent surface followed by repeated adsorption on the regenerated adsorbent. Desorption is the extraction of molecules from a surface. It is the opposite of adsorption, where adsorbed molecules are released back into solution. The objectives of desorption are to restore the adsorption capacity of an adsorbent and to concentrate and recover metals adsorbed on the surface (Hu *et al.*, 2007; Gautam *et al.*, 2014;). The eluents used in desorption are of importance and should maintain the integrity of the adsorbent surface. Dilute acids and bases are commonly used in the recovery of adsorbed metals because of their ability to initiate ion-exchange reactions (Gautam *et al.*, 2014; Bagbi *et al.*, 2016;). Regeneration is used in order to ensure the reuse of the adsorbent and aid in proper pollutant disposal (Fomina & Gadd, 2014; Ghosh *et al.*, 2015).

To understand the process of pollutant removal, it is important to determine the mechanism of adsorption or binding of pollutants onto the adsorbent surface. From the thermodynamics (Chapter 5) and kinetics (Chapter 6) studies, the adsorption of As(III) and Cr(VI) onto the prepared adsorbents was a chemical process dominated by ion exchange. During the adsorption process, changes took place on the adsorbent surface as well as in the adsorbate solution as determined by the adsorption optimization studies (Chapter 4).

Arsenic and chromium in nature do not however, exist in isolation and the presence of other anions may hinder their removal (Han *et al.*, 2008). Complexation, speciation and non-specific adsorption are some of the factors that have been cited for the reduction of metal biosorption in the presence of other anions. Some of the metal-anion complexes formed are more stable than the metal-adsorbent linkages therefore, considerably reducing adsorption efficiency (Han *et al.*, 2008; Kapoor & Viraraghavan, 1995). To determine the effect of co-existing anions in As(III) and Cr(VI) adsorption, sodium salts of chloride, nitrate, sulphate, carbonate and phosphate were introduced into the adsorbate solution in separate flasks before adsorption.

This chapter is divided into three sections, the first section discusses the desorption of As(III) and Cr(VI) from the adsorbent surfaces and adsorbent reuse, the second section describes the adsorption mechanism of As(III) and Cr(VI) onto FTP-MNP as a model adsorbent in order to determine the mechanistic pathway for the adsorption process and the last section describes the effects of competing anions during As(III) and Cr(VI) adsorption.

## **7.2 Experimental**

Similar experimental conditions were applied during the desorption and adsorption of both arsenic and chromium on the synthesized adsorbents.

### **7.2.1 Materials**

All materials used in this study were sourced as described in previous chapters. Additionally, acetic acid ( $\text{CH}_3\text{COOH}$  >99 %), sodium chloride ( $\text{NaCl}$  >99 %), sodium dihydrogen phosphate ( $\text{NaH}_2\text{PO}_4$  >99 %), sodium carbonate ( $\text{Na}_2\text{CO}_3$  >99 %), sodium sulphate ( $\text{Na}_2\text{SO}_4$  >99 %) and sodium nitrate ( $\text{NaNO}_3$  >99 %) were supplied by Labchem (South Africa).

### **7.2.2 Methods**

Arsenite (As(III)) and hexavalent chromium (Cr(VI)) solutions were prepared by dissolving the desired amounts of sodium arsenite and potassium dichromate respectively in deionized water.

#### **7.2.2.1 Adsorbent Regeneration**

To determine the most appropriate solvent for desorption, 0.1 L of 200 mg L<sup>-1</sup> solutions of As(III) and Cr(VI) were contacted separately with 1 g of adsorbent material for 2 hours. After adsorption the adsorbent was filtered, washed with deionised water and dried overnight. The loaded adsorbent was divided into four parts and each part was then shaken using a water bath shaker in one of the four desorption solvents namely deionised water ( $\text{H}_2\text{O}$ ), 0.1M Acetic acid (AA), 0.1M Hydrochloric acid (HCl) and 0.1M Sodium hydroxide (NaOH) for 2 hours and filtered to obtain the supernatant solution while the spent adsorbent was rinsed using deionised water to and oven dried for reuse. The residual solutions after adsorption and desorption were both analysed for As(III) and Cr(VI) content.

#### **7.2.2.2 Adsorption mechanism studies**

The mechanisms of As(III) and Cr(VI) adsorption on FTP-MNP as a model adsorbent were determined to establish the binding of adsorbates on the adsorbent surface. The adsorption

mechanism was investigated by the determination of electrolyte, ion-exchange, pH effects and characterization of the loaded adsorbent.

The effect of electrolyte on adsorption was determined by dissolving As(III) and Cr(VI) in solutions of 0–150 mM sodium nitrate. Thereafter the solutions were contacted with 0.5 g FTP-MNP for 2 h. To determine the influence of ion exchange on the adsorption process, 1.5 g of FTP-MNP was soaked in 100 mL of 100 mg L<sup>-1</sup> Nitrate solution overnight. The samples were washed and dried. 0.1 g of the washed sample was shaken for 2 h at 200 rpm with different concentrations of As(III) and Cr(VI) (0 mg L<sup>-1</sup>, 5 mg L<sup>-1</sup>, 25 mg L<sup>-1</sup>, 50 mg L<sup>-1</sup> and 100 mg L<sup>-1</sup>). The resulting samples were filtered and the nitrate concentration in the supernatant solution was measured using an Ion selective electrode. The effect of solution pH was determined as described in Section 4.2.2.

To study the effects of competing anions, As(III) and Cr(VI) solutions were prepared in separate flasks containing 0.1 M NaCl, NaNO<sub>3</sub>, Na<sub>2</sub>SO<sub>4</sub>, Na<sub>2</sub>CO<sub>3</sub> and NaH<sub>2</sub>PO<sub>4</sub>. Adsorption was carried out onto FTP-MNP as previously described and the residual As(III) and Cr(VI) concentrations were determined.

Analysis of the supernatant solutions for As(III), total arsenic, Cr(VI) and total chromium was carried out as described in Chapter 4.

## **7.3 Results and Discussions**

### **7.3.1 Adsorbent Regeneration**

Reuse of spent adsorbents is important in making the adsorption process more economical (Argun & Dursun, 2008). In order to determine the reusability of the adsorbent it is important to establish the most suitable eluent solution to desorb the bound adsorbate from the adsorbent surface. Desorption studies are important in the practical considerations of adsorbents for water treatment (Liu *et al.*, 2013). Desorption of As(III) and Cr(VI) was carried out using four solvents namely deionised water (H<sub>2</sub>O), 0.1 M Acetic acid (AA), 0.1 M Hydrochloric acid (HCl) and 0.1 M Sodium hydroxide (NaOH). The adsorption of both As(III) and Cr(VI) are pH dependent therefore their desorption was also affected by the pH of the eluent solution. The percentage efficiency of As(III) and Cr(VI) desorption was calculated following Equation 7.1 and the results are presented (Fig. 7.1 - 7.2) (Aryal & Liakopoulou-Kyriakides, 2011). For all the adsorbents used, the efficiency of the eluents was in the order H<sub>2</sub>O<AA<HCl<NaOH for both adsorbates. NaOH was therefore

considered the best eluent for both As(III) and Cr(VI) desorption and used in the determination of adsorbent reusability. The presence of OH<sup>-</sup> ions from NaOH leads to the formation of soluble sodium arsenite and chromate which are then released into the solution while OH<sup>-</sup> ions replace them on the adsorbent surface (Ghosh *et al.*, 2015; Setyono & Valiyaveetil, 2014). Hydroxyl groups in the solution increase the solution pH therefore, resulting in repulsion between the adsorbent surface and negatively charged Cr(VI) species hence resulting in the release of adsorbed HCrO<sub>4</sub><sup>-</sup> and CrO<sub>4</sub><sup>2-</sup> (Hu *et al.*, 2004).

$$\text{Desorption (\%)} = \frac{\text{amount desorbed}}{\text{amount adsorbed}} \times 100 \quad (7.1)$$

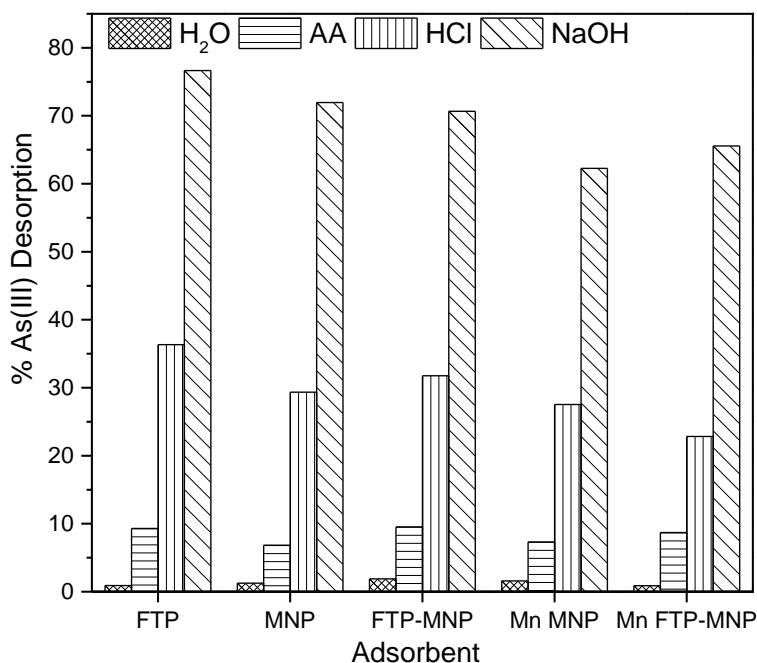


Fig. 7.1: Desorption efficiency using different solvents for As(III) desorption

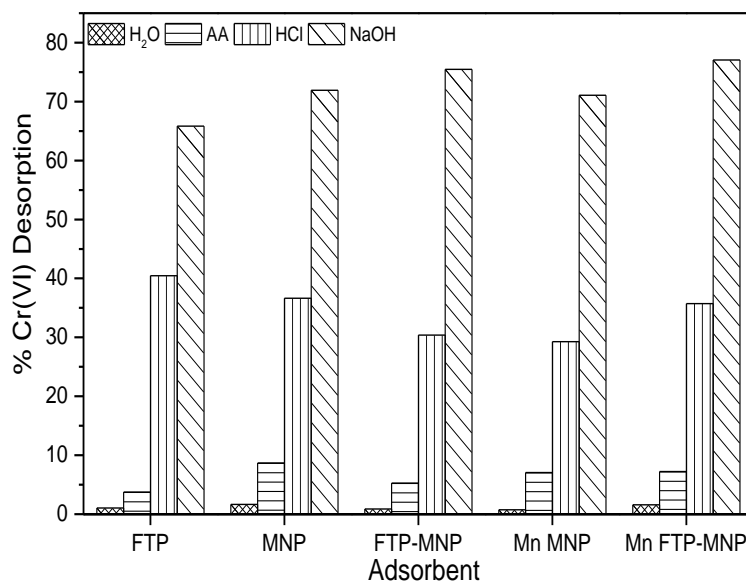


Fig. 7.2: Desorption efficiency using different solvents for Cr(VI) desorption

The reusability of the adsorbents was studied by consecutive adsorption-desorption cycles. After each adsorption, the loaded adsorbent was shaken with the eluent solution then filtered and washed with deionised water and dried before being contacted with the adsorbate solution. After three cycles all adsorbents retained >50 % of their initial adsorption capacities for As(III) (Fig. 7.3) and Cr(VI) (Fig. 7.4). All the prepared adsorbents were therefore favourable for As(III) and Cr(VI) adsorption and can be applied in at least three cycles therefore increasing their cost effectiveness.

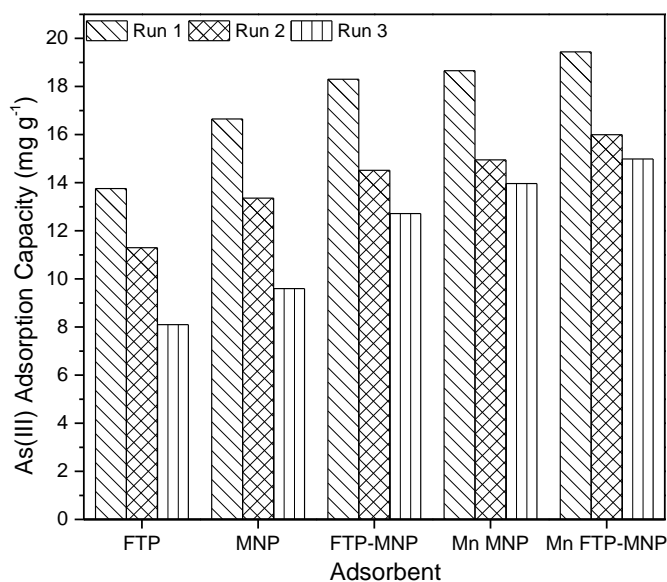


Fig. 7.3: Reusability of prepared adsorbents for As(III) adsorption

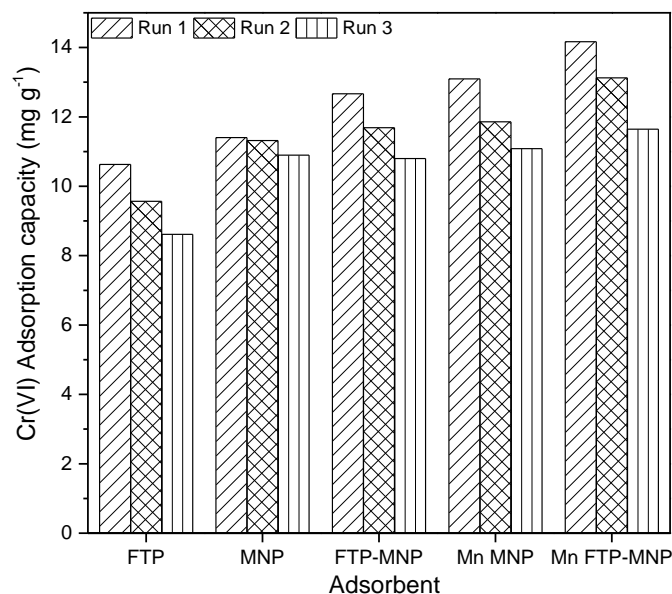


Fig. 7.4: Reusability of prepared adsorbents for Cr(VI) adsorption

### 7.3.2 Mechanism studies

#### 7.3.2.1 Arsenic Adsorption Mechanism

Arsenic adsorption has previously been reported to proceed via the oxidation of As(III) to As(V) followed by adsorption forming inner-sphere complexes with surface iron atoms (Bhowmick *et al.*, 2014). The transformations of functional groups on the adsorbent surface were monitored by infrared analysis while changes in chemical states were investigated by X-ray photoelectron spectroscopy (XPS). The determination of ion exchange mechanism was carried out by pre-loading the adsorbent with an anion whose displacement was monitored after the adsorption process. Electrolyte effects on the adsorption of As(III) aided in the understanding of arsenic complexation with the adsorbent surface.

##### 7.3.2.1.1 Ionic Strength

To investigate the type of surface binding that took place between the composite and arsenite ions, the ionic strength of the solution was increased 150-fold using  $\text{NaNO}_3$ . Figure 7.5 shows that As(III) adsorption on the composite increased with an increase in ionic strength from 0 to 150  $\text{mmol L}^{-1}$ , and was thus indicative of the formation of inner sphere complexes (Setyono & Valiyaveetil, 2014). Inner sphere complex formation is indicated by an increase or constant adsorption with increasing ionic strength while outer sphere complexes are indicated by decreasing



adsorption with increasing ionic strength (Cheng *et al.*, 2009; Goldberg & Johnston, 2001). Arsenite adsorption onto magnetite nanoparticles and colloidal hematite reported by Liu *et al.*, and Brechbühl *et al.*, also proceeded through the formation of inner sphere complexes (Brechbühl *et al.*, 2012; Liu *et al.*, 2015).

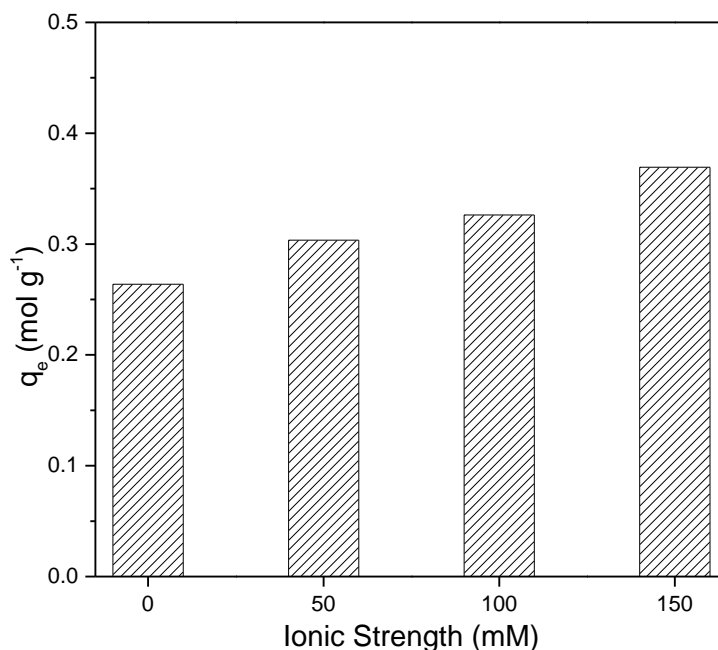


Fig. 7.5: Ionic strength effects on As(III) adsorption onto FTP-MNP

#### 7.3.2.1.2 Ion Exchange Mechanism

To further investigate whether ion exchange was involved during the adsorption, FTP-MNP pre-loaded with nitrate ions was contacted with solutions of different arsenite concentrations. The concentration ratio of adsorbed arsenite to nitrate released from the adsorbent surface described by Wu *et al.*, as the exchange coefficient ( $R_{As/NO_3}$ ) was determined (Wu *et al.*, 2013). The exchange coefficient increased from 0.05 to 0.51 with increasing arsenite concentrations between 5 mg L<sup>-1</sup> and 100 mg L<sup>-1</sup> (Fig. 7.6) indicating that nitrate ions on the surface were exchanged with arsenic ions during adsorption. Wu *et al.* also observed arsenite/sulphate exchange during the adsorption of arsenite onto Fe-based backwashing sludge with exchange coefficients between 0.16 and 0.31 confirming the exchange of surface sulphate ions with arsenic ions (Wu *et al.*, 2013).

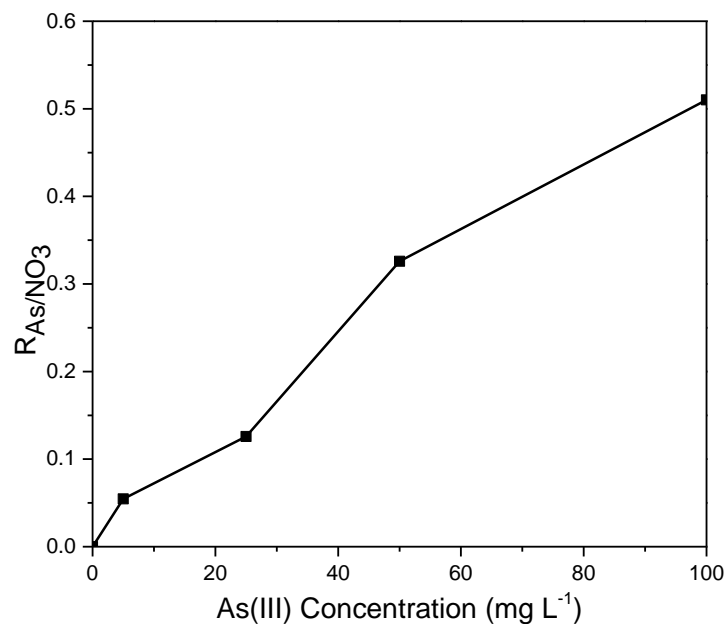


Fig. 7.6: As(III)/Nitrate exchange coefficient at various initial As(III) solution concentrations

#### 7.3.2.1.3 Infrared Analysis

To determine the functional groups involved in the adsorption process the IR spectrum was obtained. Figure 7.7 shows that after As adsorption the (i) hydroxyl band was slightly shifted, (ii) the C-O band and the Fe-O band decreased in intensity, and (iii) there was a new peak at  $854\text{ cm}^{-1}$  attributed to As-O bond vibrations. The spectrum therefore shows that oxygen containing groups were involved in the adsorption process and Fe-O bonds were altered during adsorption. The As-O bond vibration at  $854\text{ cm}^{-1}$  compares well to literature values reported for As-O-Fe bond vibrations in the rare mineral symplectite ( $\text{Fe}(\text{AsO}_4)_2 \cdot 8\text{H}_2\text{O}$ ) (Makreski *et al.*, 2015). The formation of As-O-Fe bond accounts for the Fe-O peak shift and further confirms the formation of inner sphere complexes (Tang *et al.*, 2013).

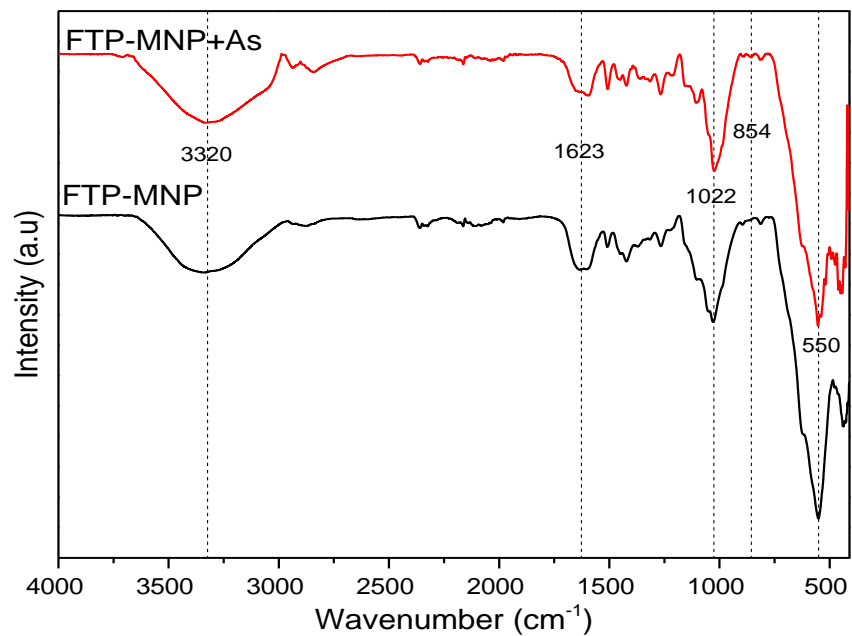


Fig. 7.7: FTIR spectrum of FTP-MNP and Arsenic loaded FTP-MNP

#### 7.3.2.1.4 X-ray Photoelectron Spectroscopic Analysis

X-ray photoelectron spectroscopy (XPS) was used to determine the surface ionic states of FTP-MNP after arsenite adsorption. A comparison of the survey scans of FTP-MNP and As-loaded FTP-MNP (Fig. 7.8) shows that the As loaded adsorbent retained all FTP-MNP peaks with an introduction of As3d peak at 43 eV after adsorption.

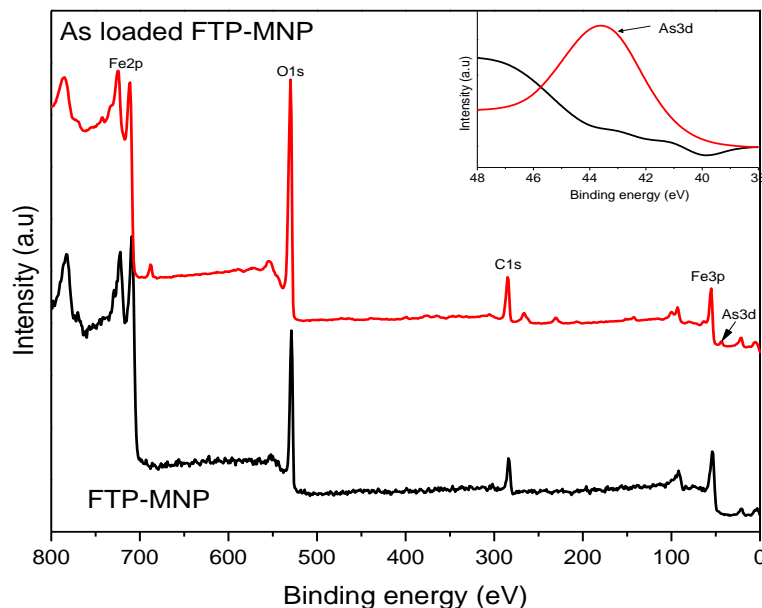


Fig. 7.8: XPS survey scan of FTP-MNP and Arsenic loaded FTP-MNP (Inset: As3d peak)

The O1s peak in Figure 7.9 was shifted from 529.8 eV to 530.1 eV after As(III) adsorption indicating that oxygen containing surface groups were involved in arsenic adsorption. In the O1s deconvoluted spectrum (Fig. 7.10), a peak at 530.2 eV attributed to As-O was introduced after As(III) adsorption indicating that arsenic was bound to the FTP-MNP surface by co-ordination with surface oxygen atoms (Liu *et al.*, 2015; Tang *et al.*, 2013; Zhang *et al.*, 2010). Similar results have previously been reported with Liu *et al.*, 2015 attributing the As-O coordination to 3 oxygen atoms at 1.79 Å corresponding to AsO<sub>3</sub>.

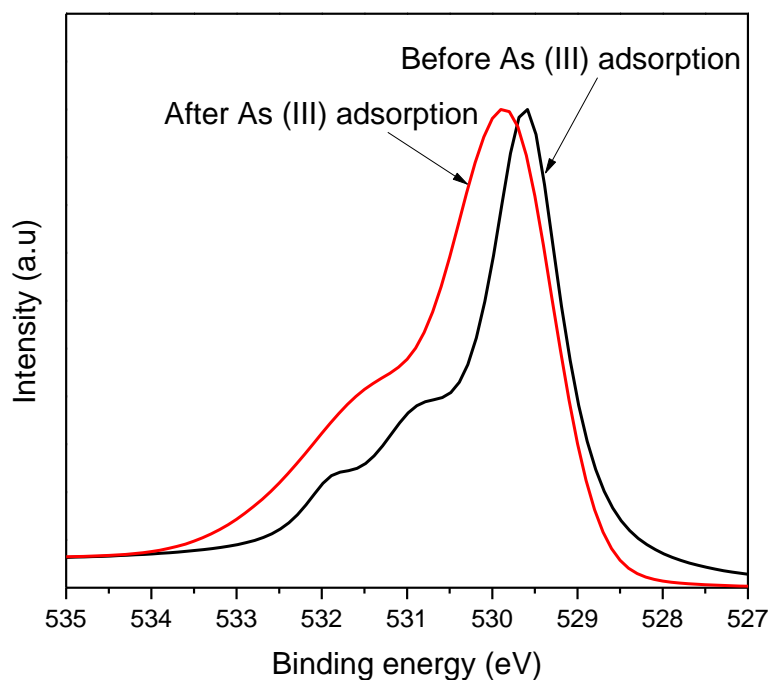


Fig. 7.9: O1s spectra of FTP-MNP before and after As(III) adsorption

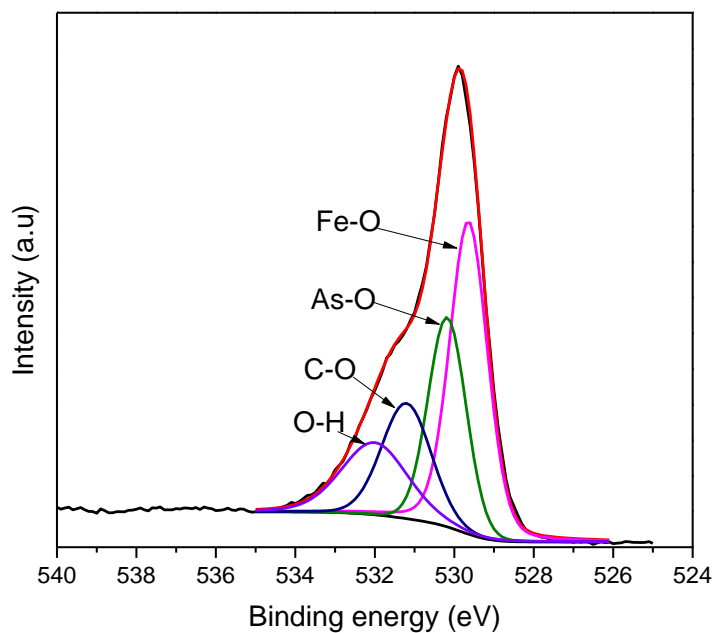


Fig. 7.10: O1s deconvoluted spectrum of FTP-MNP after As(III) adsorption

The  $\text{Fe}^{2+}/\text{Fe}^{3+}$  ratio increased from 0.5 on the as-synthesized composite (Fig. 3.16) to 1.4 on the arsenic loaded composite (Fig. 7.11) with both peaks being shifted to higher binding energies. An increase in the  $\text{Fe}^{2+}/\text{Fe}^{3+}$  ratio indicated a reduction of ferric to ferrous ions as adsorption took place during As(III) adsorption.

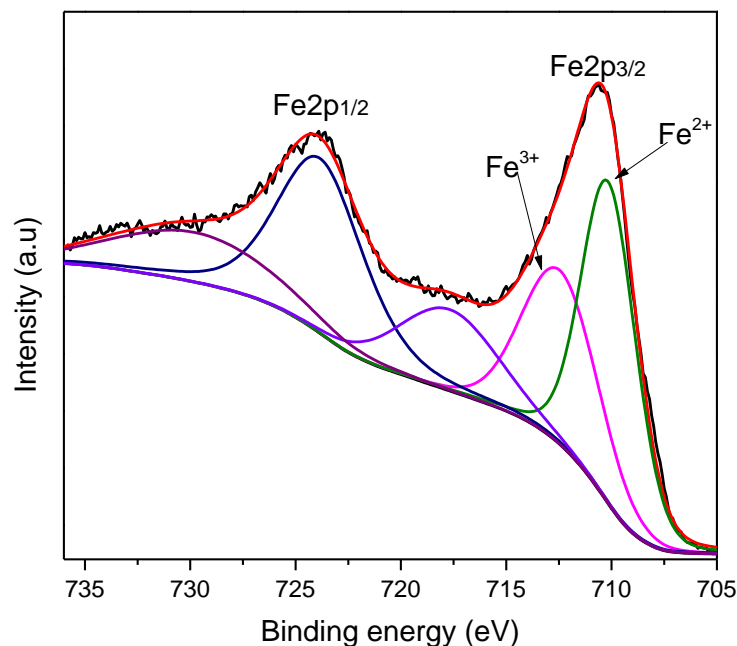


Fig. 7.11: Fe2p spectrum of FTP-MNP after As(III) adsorption

The As3d spectrum showed that the arsenite on FTP-MNP surface consisted of two oxidation states at binding energies of 43.6 eV and 45.0 eV attributed to As<sub>2</sub>O<sub>5</sub> and As<sub>2</sub>O<sub>3</sub> respectively (Fig. 7.12). The lower energy peak at 43.6 eV was slightly lower than the reported values of 44.3-44.7 eV for As<sub>2</sub>O<sub>3</sub> possibly due to differential charging (Du *et al.*, 2013). The peak at 45.0 eV was assigned to As<sub>2</sub>O<sub>5</sub> which occurs at 45.2 - 45.6 eV (Du *et al.*, 2013). The composition of arsenic states was 58.5% As(V) and 41.5% As(III).

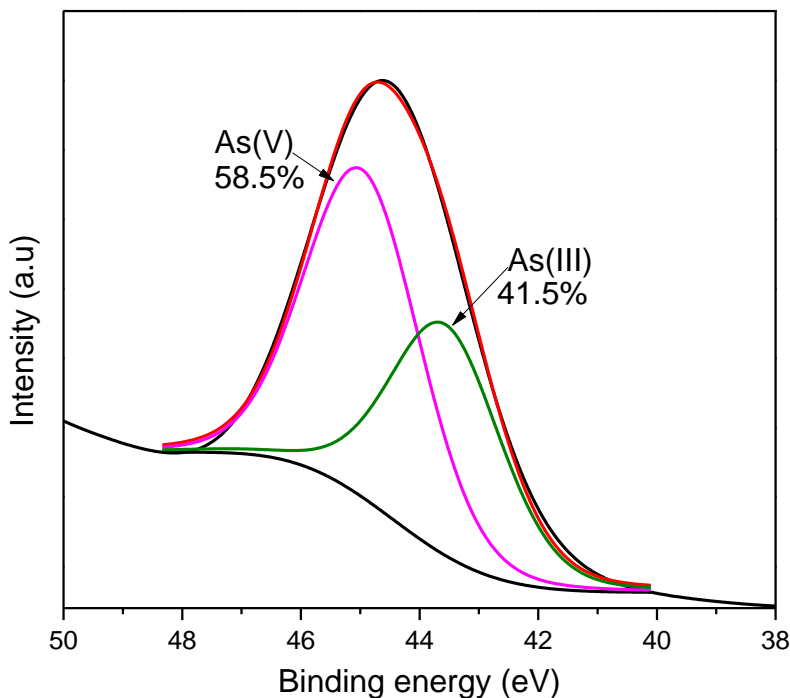


Fig. 7.12: As3d spectrum of As loaded FTP-MNP

The surface composition after arsenic adsorption indicated that arsenite adsorption proceeded by ligand exchange with the surface hydroxyl group (Liu *et al.*, 2015). Some of the adsorbed arsenite was oxidized to arsenate with a simultaneous reduction of surface  $\text{Fe}^{3+}$  suggesting the adsorption of arsenite onto FTP-MNP was through oxidation coupled adsorption. The ligand exchange reaction between arsenite and surface hydroxyl groups at pH 8 can be summarized in Equation 18 (Jaafarzadeh *et al.*, 2012).



### 7.3.2.2 Chromium Adsorption Mechanism

Hexavalent chromium adsorption mechanism has been reported to proceed by a combination of mechanisms involving electrostatic attraction, ion exchange, surface complexation and reduction (Hu *et al.*, 2004; Ramrakhiani *et al.*, 2011; Burks *et al.*, 2013). These mechanisms are based on two principles namely: (i) electrostatic attraction of negatively charged Cr(VI) ions in solutions to the adsorbent surface and (ii) reduction of Cr(VI) ions to Cr(III) ions followed either by adsorption or repulsion by the adsorbent surface. The mechanism for Cr(VI) removal from aqueous solutions by biomaterials has been determined to be by direct and indirect reduction (Park *et al.*, 2008). In the direct reduction mechanism, Cr(VI) is reduced to Cr(III) by the electron donating groups of

the biomaterial. The indirect reduction mechanism is a three step process in which anionic Cr(VI) ions bind to cationic groups on the biomaterial surface, Cr(VI) ions are then reduced to Cr(III) by adjacent electron donating groups followed by either the release of Cr(III) into the solution due to repulsion or complexation with adjacent groups (Park *et al.*, 2008). The proposed mechanisms each lead to the consumption of hydrogen ions therefore raising the solution pH during adsorption.

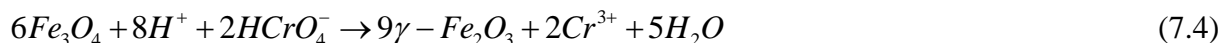
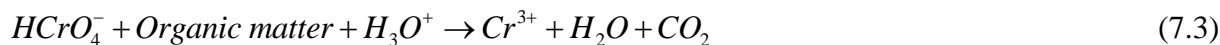
Both mechanisms have been shown to describe the adsorption of Cr(VI) on lignocellulosic bio sorbents and iron oxide nanoparticles (Albadarin *et al.*, 2011; Kumari *et al.*, 2015; Villacís-García *et al.*, 2015). Yu *et al.*, reported that monitoring pH and oxidation-reduction potential (ORP) during Cr(VI) removal presented correlation coefficients of 0.81 and 0.72 respectively indicating that Cr(VI) adsorption is dependent on the solution's hydrogen ion concentration and redox potential (Yu *et al.*, 2014). The high redox potential (+1.3V) of chromium under acidic conditions has also been reported to favor its adsorption on biomaterials (Miretzky & Cirelli, 2010).

To determine which mechanism was responsible for the removal of Cr(VI) from solution by FTP-MNP, the changes in hydrogen ion ( $H^+$ ) concentration, oxidation-reduction potential (ORP) and Cr(III) concentration in solution were studied. X-ray photoelectron spectroscopy (XPS) was used to determine the chromium states on the adsorbent surface. Ion exchange mechanism was also investigated using nitrate pre-loaded adsorbent to confirm the conclusions from thermodynamic and kinetic studies.

#### **7.3.2.2.1 Change in $H^+$ Concentration**

The adsorption of hexavalent chromium is highly dependent on solution pH and has been reported to be favoured by its high redox potential (+1.3V) at acidic pH (Miretzky & Cirelli, 2010). The optimum pH for Cr(VI) adsorption was found to be pH 2 where  $HCrO_4^-$  is predominant as discussed in Chapter 4 (Ouma *et al.*, 2017). This species has low adsorption free energy and is therefore favourably adsorbed at low pH when the adsorbent surface is positively charged allowing for electrostatic attraction with the anionic species (Zhao *et al.*, 2017). Reduction of Cr(VI) to Cr(III) in the presence of organic matter and magnetite results in the consumption of hydrogen ions as shown in Equations 7.3 and 7.4 (Namasivayam & Sureshkumar, 2008; Villacís-García *et al.*, 2015). Cr(VI) can be reduced by electron donor groups on the biomass which have a lower reduction potential than Cr(VI) of 1.3 V (Joutey *et al.*, 2011).





At low solution pH the change in hydrogen concentration was high due to large amounts of Cr(VI) being either bound or reduced by the adsorbent (Fig. 7.13). As the solution pH was raised the change in  $\text{H}^+$  was reduced and the amount of Cr(VI) removed was lowered.

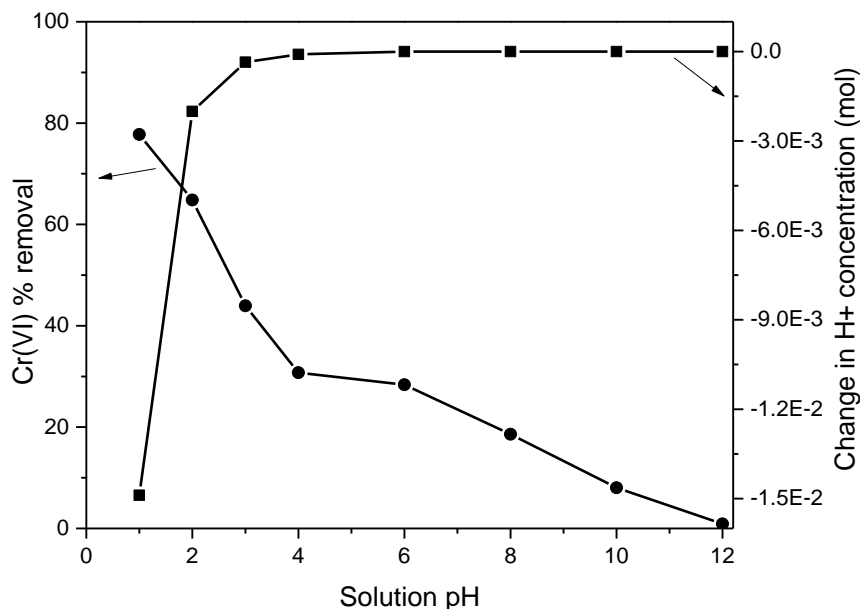


Fig. 7.13: Effect of solution pH on Cr(VI) removal and change in  $\text{H}^+$  concentration

In both the electrostatic attraction and adsorption coupled reduction mechanisms, removal of Cr(VI) is favoured at lower solution pH due to the presence of high concentrations of hydrogen ions. The consumption of hydrogen ions also causes the solution pH to increase during the reduction of Cr(VI) to Cr(III) (Yu *et al.*, 2014). The change in  $\text{H}^+$  concentration was therefore not sufficient in determining whether the adsorption of Cr(VI) onto FTP-MNP proceeded through either electrostatic attraction or reduction to Cr(III).

#### 7.3.2.2.2 Cr(III) Concentration After Adsorption

The amount of Cr(III) ions in solutions was determined to confirm whether Cr(VI) reduction in concentration was via electrostatic attraction or reduction to Cr(III). In the electrostatic attraction mechanism, only Cr(VI) ions are expected to be present in solution since there is no reduction expected to take place. In the reduction coupled adsorption however, Cr(III) ions are present in the

solution. This is a result of the reduction process which may be followed by some of the formed Cr(III) ions being adsorbed while others are repelled back into the solution by positive charges on the adsorbent surface. Therefore, the total amount of chromium in solution is the sum of Cr(VI) and Cr(III) in the solution. In the case of complete reduction from Cr(VI) to Cr(III) as reported by Sanghi *et al.* the chromium ions left in solution only consist of Cr(III) ions (Sanghi *et al.*, 2009).

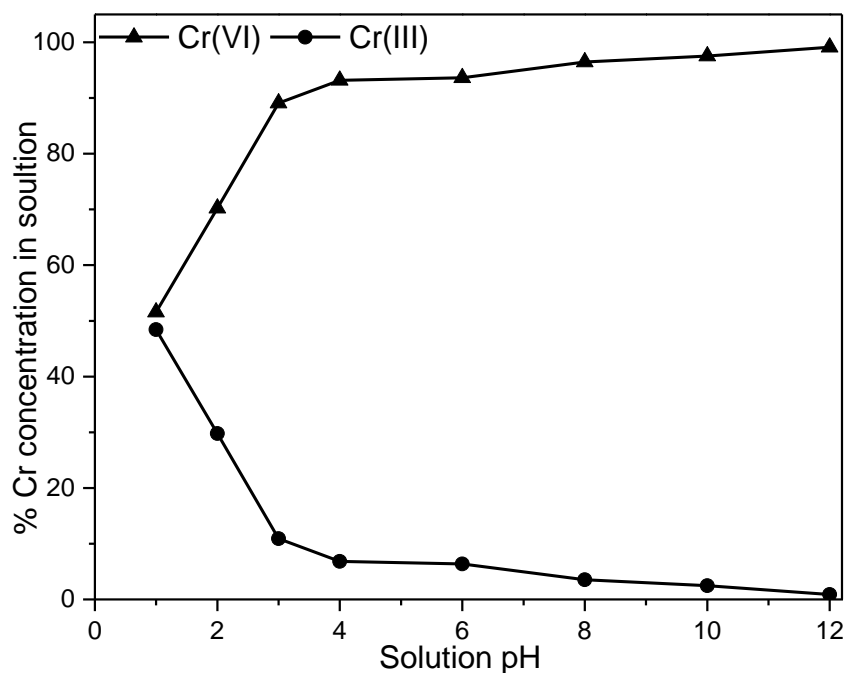


Fig. 7.14: Cr(VI) and Cr(III) concentration in solution after adsorption

Throughout the studied pH range, there was some amount of Cr(III) ions remaining in the solution after adsorption (Fig. 7.14). The highest amount of Cr(III) was observed at lower solution pH due to the presence of high amounts of  $H^+$  ions aiding in the reduction of Cr(VI) to Cr(III). However, at high solution pH the amount of Cr(III) was lower due to repulsion of Cr(VI) anions from the negatively charged adsorbent surface therefore resulting in low reduction. Some of the formed Cr(III) ions were not adsorbed due to repulsion of the cations by the positively charged adsorbent surface, leading to higher amounts of Cr(III) in solution at low solution pH since there was maximum reduction at low pH following higher redox potentials.

#### 7.3.2.2.3 Change in Redox Potential

The difference in oxidation reduction potential (ORP) of the solution before and after adsorption was determined in order to confirm Cr(VI) reduction to Cr(III). A reduction in ORP indicates Cr(VI) reduction as observed by Yu *et al.*, when nanoscale zero-valent iron particles which have a strong reductive capacity were introduced into Cr(VI) wastewater (Yu *et al.*, 2014). During Cr(VI) adsorption onto FTP-MNP the difference between the final and initial ORP of the solution increased with increasing pH (Fig. 7.15). This was because of decreased Cr(VI) reduction as the pH of the solution increased with greater decreases in ORP being observed at lower pH where higher Cr(VI) reduction was expected. Similar trends have been reported for Cr(VI) reduction by magnetite indicating that reduction to Cr(III) decreases in significance as pH increases (He & Traina, 2005; Kendelewicz *et al.*, 2000).

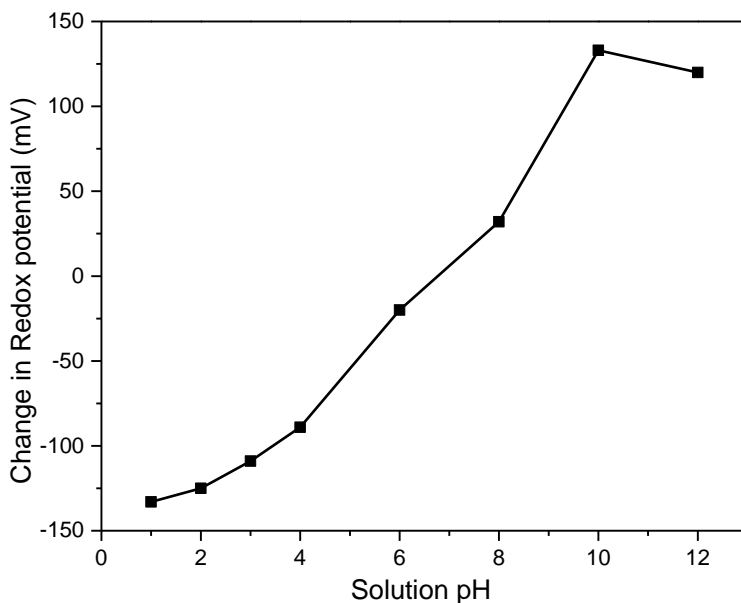


Fig. 7.15: Change on redox potential with solution pH

#### 7.3.2.2.4 X-ray Photoelectron Spectroscopic Analysis

The XPS spectra of FTP-MNP before and after Cr(VI) adsorption was studied to determine the mechanism of adsorption. The survey spectrum of the chromium loaded adsorbent showed a Cr2p peak at approximately 580 eV (Fig. 7.16). All the other peaks in the pristine adsorbent were retained after Cr adsorption.

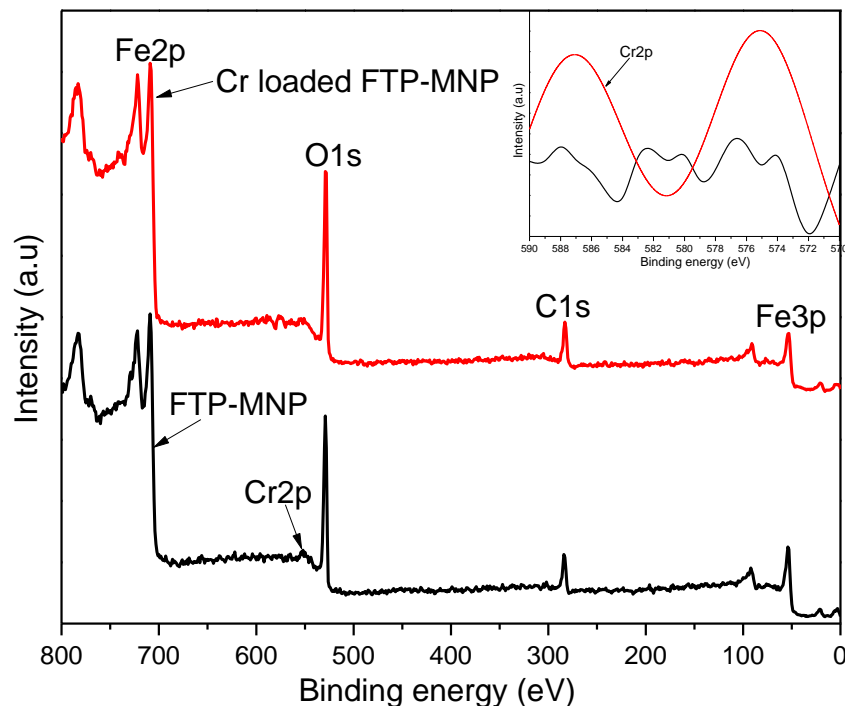


Fig. 7.16: XPS full spectra before and after Cr(VI) adsorption (Inset: Cr2p peak)

The O1s peak in Figure 7.17 was slightly shifted from 529.4 eV to 529.9 eV after Cr(VI) adsorption indicating that oxygen containing groups were involved in the binding of Cr(VI) to the FTP-MNP surface. The Cr2p band (Fig. 7.18) consisted of two peaks at 587 eV and 575 eV which were assigned to Cr2p<sub>1/2</sub> and Cr2p<sub>3/2</sub> representing Cr(VI) and Cr(III) respectively (Zhao *et al.*, 2017). The presence of both peaks suggested that Cr(VI) was adsorbed and later reduced to Cr(III) on the surface (Yuan *et al.*, 2009). The reduction of Cr(VI) to Cr(III) at acidic pH or in the presence of organic matter follows a redox reaction (eq 7.5) (Zhao *et al.*, 2017).



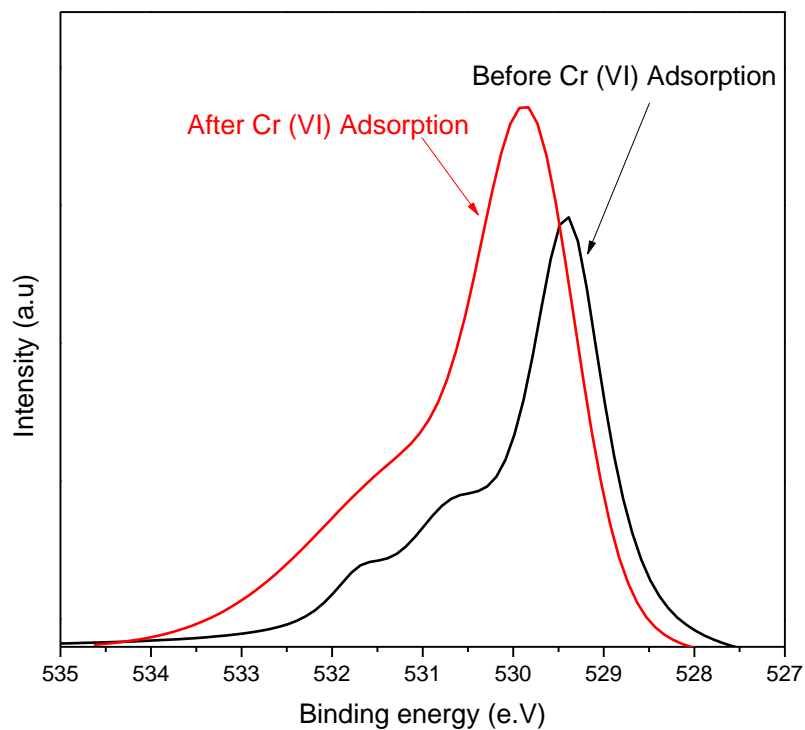


Fig. 7.17: O1s spectrum of FTP-MNP before and after Cr(VI) adsorption

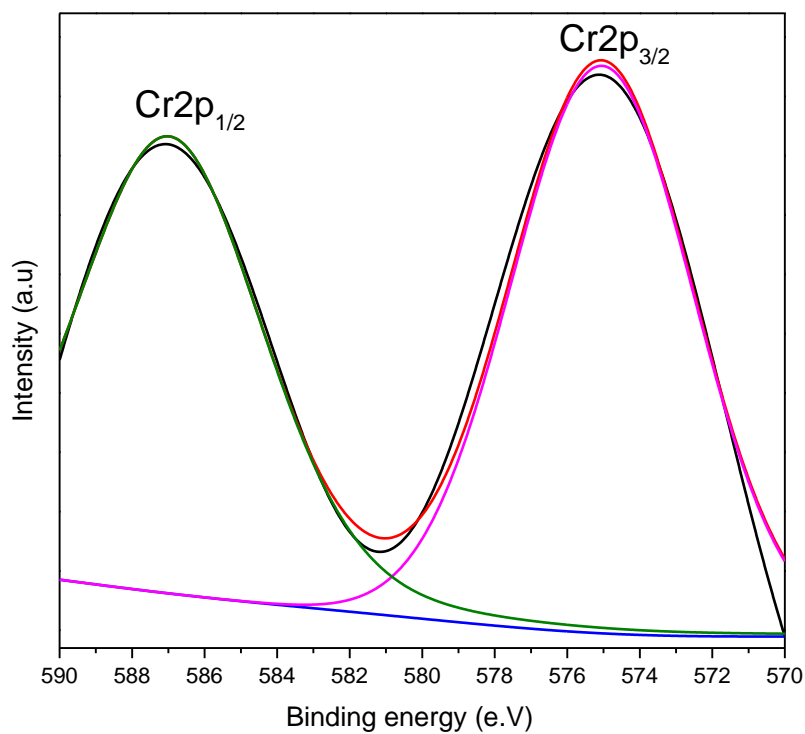


Fig. 7.18: Cr2p deconvoluted spectrum of FTP-MNP after Cr(VI) adsorption

The binding energies for Fe2p<sub>1/2</sub> and Fe2p<sub>3/2</sub> showed no significant shift after chromium adsorption at energies of 722.6 eV and 709.3 eV in the pristine adsorbent and 722.9 eV and 709.6 eV in the chromium loaded adsorbent (Fig. 7.19). The constant binding energies for Fe2p indicates that there was no Cr substitution in the iron phase of the adsorbent and magnetite phase was retained throughout the adsorption process (Poulin *et al.*, 2010; Yuan *et al.*, 2009).

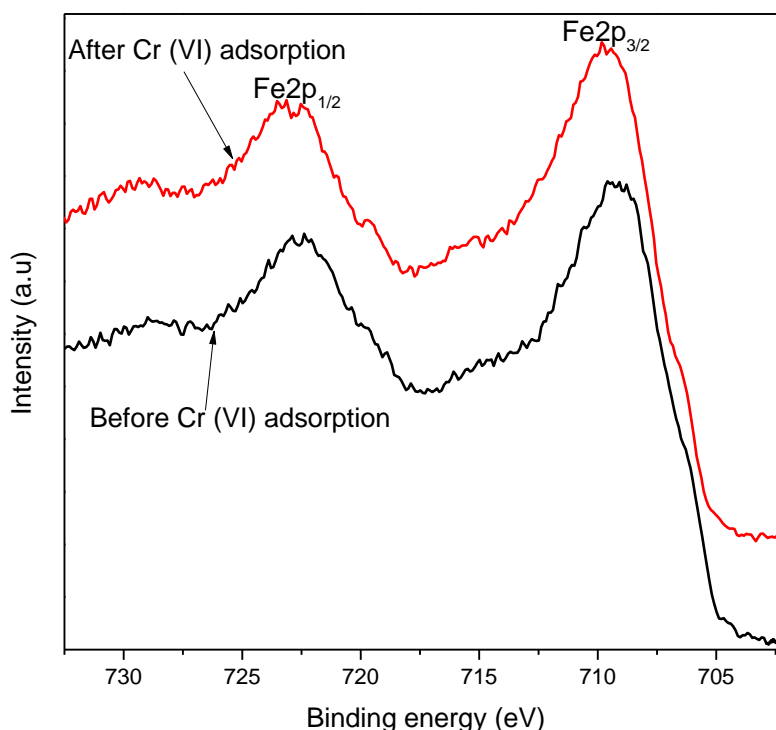


Fig. 7.19: Fe2p spectra of FTP-MNP before and after Cr(VI) adsorption

#### 7.3.2.2.5 Ion-exchange mechanism

To determine the role of ion exchange during chromium adsorption, a sample of FTP-MNP was pre-loaded with nitrate ions prior to contacting with Cr(VI) solutions of varying concentrations. The amount of NO<sup>3-</sup> ions released during Cr(VI) adsorption was monitored for different amounts of adsorbed chromium. The amount of NO<sup>3-</sup> released into the solution increased linearly with the amount of adsorbed Cr<sup>6+</sup> ions (Fig. 7.20) indicating that ion exchange was the mechanism responsible for Cr(VI) binding on the adsorbent surface as Cr<sup>6+</sup> ions displaced NO<sup>3-</sup> ions from the adsorbent surface (Ramrakhiani *et al.*, 2011).

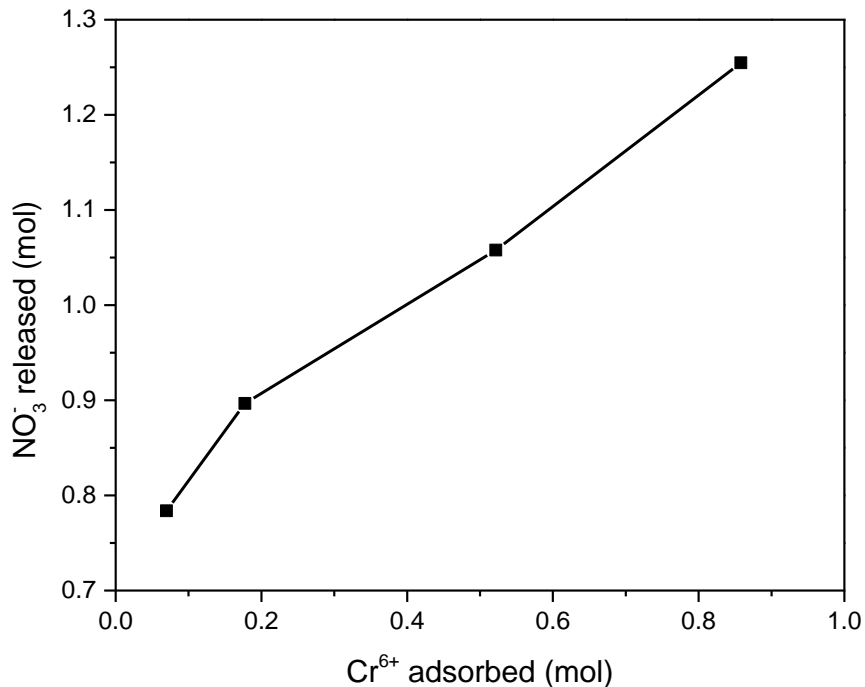


Fig. 7.20: Ratio of Cr<sup>6+</sup> adsorbed to NO<sub>3</sub><sup>-</sup> released during adsorption

### 7.3.3 Effects of competing anions

The presence of anions in solution can affect the efficiency of metal adsorption, with the effects depending on the anion present and the metal ion being adsorbed. Some anions increase the ionic strength of the solution which generally affects metal adsorption while some anions compete with the metal for available adsorption sites (Han *et al.*, 2008; Cheng *et al.*, 2009; Yoon *et al.*, 2017). As(III) removal efficiency was lowered by the presence of anions in the order  $\text{PO}_4^{3-} > \text{SO}_4^{2-} > \text{CO}_3^{2-} > \text{NO}_3^- > \text{Cl}^-$  (Fig. 7.21).  $\text{PO}_4^{3-}$  had the most effect on As(III) adsorption efficiency due to the similar atomic structures and chemical properties between arsenic and phosphate (Li *et al.*, 2012). Both adsorb strongly on iron oxide materials and can form inner-sphere complexes on the adsorbent surface (Yoon *et al.*, 2017). The other anions ( $\text{SO}_4^{2-}$ ,  $\text{CO}_3^{2-}$ ,  $\text{NO}_3^-$ ,  $\text{Cl}^-$ ) affected As(III) adsorption due to competition for adsorption sites but their different adsorption mechanisms resulted in less reduction in adsorption efficiency (Cheng *et al.*, 2009; Yoon *et al.*, 2017; Wu *et al.*, 2018).

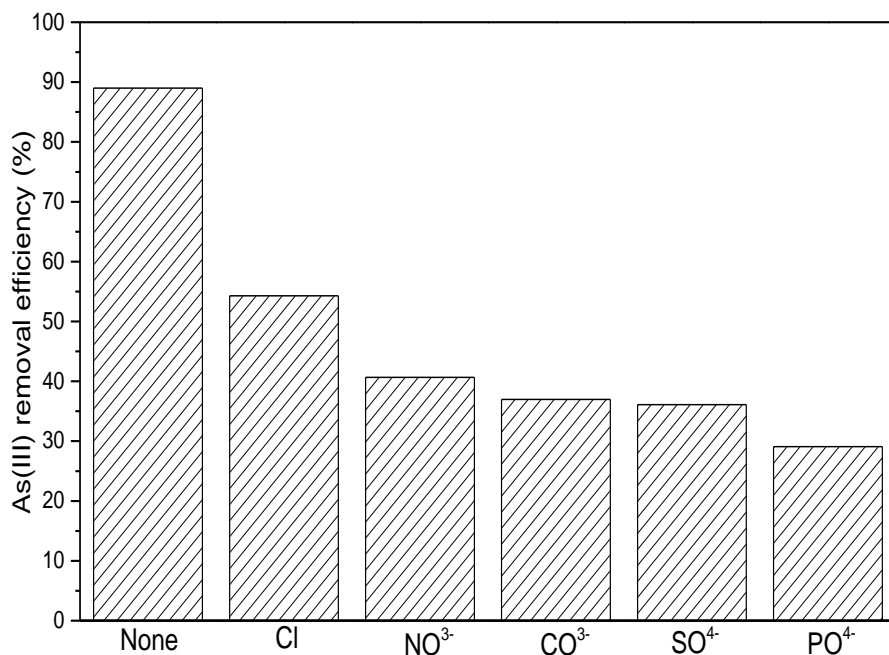


Fig. 7.21: Effect of competing anions on As(III) adsorption onto FTP-MNP

Cr(VI) removal was hindered by the presence of anions in the order  $\text{CO}_3^{2-} > \text{PO}_4^{3-} > \text{SO}_4^{2-} > \text{NO}_3^- > \text{Cl}^-$  (Fig. 7.22). The presence of anions in solution lead to a competition for adsorption sites with Cr(VI) indication that there were no specific adsorption sites for chromium adsorption on the adsorbent surface (Namasivayam & Sureshkumar, 2008). In the adsorption of Cr(VI) by microalgae, Han *et al.*, reported that Cr(VI) was more affected by the presence of the anions than the solution's ionic strength (Han *et al.*, 2008). Carbonate ions have been reported to offer the highest hinderance by binding chromium ions and making them more mobile at low solution pH (Cheng *et al.*, 2011).



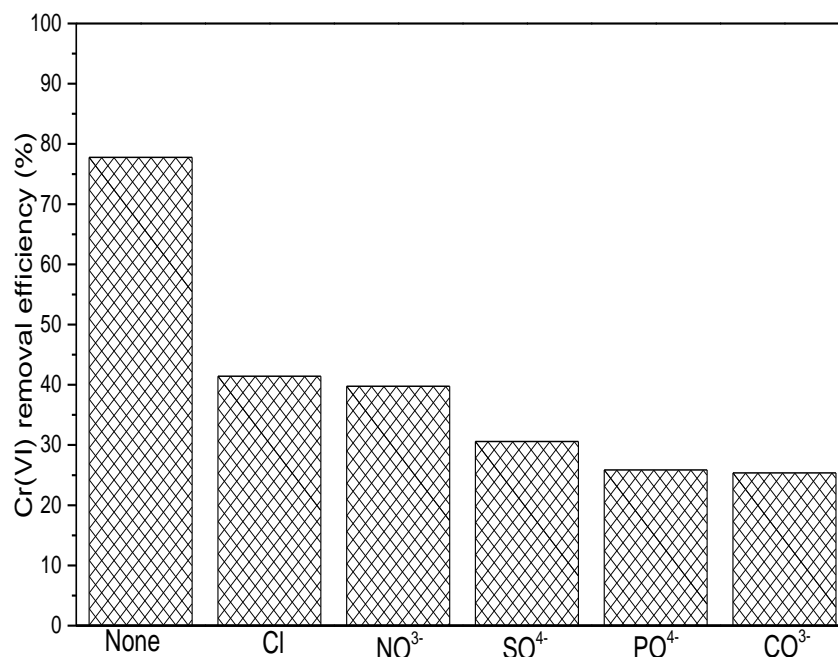


Fig. 7.22: Effect of competing anions on Cr(VI) adsorption onto FTP-MNP

#### 7.4 Conclusion

Desorption studies revealed that the type of binding between the adsorbates and the adsorbent was chemical in nature with NaOH being the best eluent for both adsorbates. All the adsorbents were successfully reused up to three times without significant loss in adsorption capacity.

As(III) adsorption was determined to involve the formation of inner-sphere complexes with ion exchange being responsible for the formation of complexes. As(III) was oxidised to As(V) on the adsorbent surface with simultaneous oxidation of Fe(II) to Fe(III). At low solution pH, electrostatic interaction was responsible for the binding of anionic chromium species to the adsorbent surface. Hydrogen ions took part in both electrostatic binding of Cr(VI) and reduction to Cr(III) resulting in an increase in solution pH after adsorption. The presence of Cr(III) ions in solution and on the adsorbent surface confirmed that Cr(VI) was reduced to Cr(III) during the adsorption process. The mechanism of Cr(VI) adsorption onto FTP-MNP was determined to involve electrostatic attraction, surface complexation, reduction and ion exchange. The presence of anions in solution affected the adsorption of both As(III) and Cr(VI) resulting in decreased adsorption efficiency. The results indicated that there were no specific adsorption sites on the adsorbent surface for either arsenic or chromium adsorption.

## 7.5 References

- ALBADARIN, A.B., AL-MUHTASEB, A.H., AL-LAQTAH, N.A., WALKER, G.M., ALLEN, S.J., & AHMAD, M.N.M. (2011). Biosorption of toxic chromium from aqueous phase by lignin: mechanism, effect of other metal ions and salts. *Chem. Eng. J.* 169. p.20–30.
- ARGUN, M.E., & DURSUN, S. (2008). A new approach to modification of natural adsorbent for heavy metal adsorption. *Bioresour. Technol.* 99. p.2516–2527.
- ARYAL, M., & LIAKOPOULOU-KYRIAKIDES, M. (2011). Equilibrium, kinetics and thermodynamic studies on phosphate biosorption from aqueous solutions by Fe(III)-treated *Staphylococcus xylosus* biomass: Common ion effect. *Colloids Surfaces A Physicochem. Eng. Asp.* 387. p.43–49.
- BAGBI, Y., SARSWAT, A., MOHAN, D., PANDEY, A., & SOLANKI, P.R. (2016). Lead (Pb<sup>2+</sup>) adsorption by monodispersed magnetite nanoparticles: Surface analysis and effects of solution chemistry. *J. Environ. Chem. Eng.* 4. p.4237–4247.
- BHOWMICK, S., CHAKRABORTY, S., MONDAL, P., VAN RENTERGHEM, W., VAN DEN BERGHE, S., ROMAN-ROSS, G., CHATTERJEE, D., & IGLESIAS, M. (2014). Montmorillonite-supported nanoscale zero-valent iron for removal of arsenic from aqueous solution: Kinetics and mechanism. *Chem. Eng. J.* 243.
- BRECHBÜHL, Y., CHRISTL, I., ELZINGA, E.J., & KRETZSCHMAR, R. (2012). Competitive sorption of carbonate and arsenic to hematite: Combined ATR-FTIR and batch experiments. *J. Colloid Interface Sci.* 377. p.313–321.
- BURKS, T., UHEIDA, A., SALEEMI, M., EITA, M., TOPRAK, M.S., & MUHAMMED, M. (2013). Removal of Chromium(VI) Using Surface Modified Superparamagnetic Iron Oxide Nanoparticles. *Sep. Sci. Technol.* 48. p.1243–1251.
- CHENG, H., HU, Y., LUO, J., XU, B., & ZHAO, J. (2009). Geochemical processes controlling fate and transport of arsenic in acid mine drainage (AMD) and natural systems. *J. Hazard. Mater.* 165. p.13–26.
- CHENG, S.F., HUANG, C.Y., & TU, Y.T. (2011). Remediation of soils contaminated with chromium using citric and hydrochloric acids: the role of chromium fractionation in chromium

leaching. *Environ. Technol.* 32. p.879–889.

DU, Q., ZHANG, S., PAN, B., LV, L., ZHANG, W., & ZHANG, Q. (2013). Bifunctional resin-ZVI composites for effective removal of arsenite through simultaneous adsorption and oxidation. *Water Res.* 47. p.6064–6074.

FOMINA, M., & GADD, G.M. (2014). Biosorption: current perspectives on concept, definition and application. *Bioresour. Technol.* 160. p.3–14.

GAUTAM, R.K., MUDHOO, A., LOFRANO, G., & CHATTOPADHYAYA, M.C. (2014). Biomass-derived biosorbents for metal ions sequestration: Adsorbent modification and activation methods and adsorbent regeneration. *J. Environ. Chem. Eng.* 2. p.239–259.

GHOSH, A., PAL, M., BISWAS, K., GHOSH, U.C., & MANNA, B. (2015). Manganese oxide incorporated ferric oxide nanocomposites (MIFN): A novel adsorbent for effective removal of Cr(VI) from contaminated water. *J. Water Process Eng.* 7. p.176–186.

GOLDBERG, S., & JOHNSTON, C.T. (2001). Mechanisms of Arsenic Adsorption on Amorphous Oxides Evaluated Using Macroscopic Measurements, Vibrational Spectroscopy, and Surface Complexation Modeling. *J. Colloid Interface Sci.* 234. p.204–216.

HAN, X., WONG, Y.S., WONG, M.H., & TAM, N.F.Y. (2008). Effects of anion species and concentration on the removal of Cr(VI) by a microalgal isolate, *Chlorella miniata*. *J. Hazard. Mater.* 158. p.615–620.

HE, Y.T., & TRAINA, S.J. (2005). Cr(VI) reduction and immobilization by magnetite under alkaline pH conditions: The role of passivation. *Environ. Sci. Technol.* 39. p.4499–4504.

HU, J., LO, I.M.C., & CHEN, G. (2004). Removal of Cr(VI) by magnetite. *Water Sci. Technol.* 50. p.139–146.

HU, J., LO, I.M.C., & CHEN, G. (2007). Comparative study of various magnetic nanoparticles for Cr(VI) removal. *Sep. Purif. Technol.* 56. p.249–256.

JAAFARZADEH, N., AHMADI, M., AMIRI, H., YASSIN, M.H., & MARTINEZ, S.S. (2012). Predicting Fenton modification of solid waste vegetable oil industry for arsenic removal using artificial neural networks. *J. Taiwan Inst. Chem. Eng.* 43. p.873–878.

JOUTEY, N.T., SAYEL, H., BAHAFID, W., & EL GHACHTOULI, N. Reviews of Environmental Contamination and Toxicology Volume 211. New York, NY: Springer New York, 2011. v. 211

KAPOOR, A., & VIRARAGHAVAN, T. (1995). Fungal biosorption — an alternative treatment option for heavy metal bearing wastewaters: a review. *Bioresour. Technol.* 53. p.195–206.

KENDELEWICZ, T., LIU, P., DOYLE, C., & BROWN, G.. (2000). Spectroscopic study of the reaction of aqueous Cr(VI) with Fe<sub>3</sub>O<sub>4</sub> (111) surfaces. *Surf. Sci.* 469. p.144–163.

KUMARI, M., PITTMAN, C.U., & MOHAN, D. (2015). Heavy metals [chromium (VI) and lead (II)] removal from water using mesoporous magnetite (Fe<sub>3</sub>O<sub>4</sub>) nanospheres. *J. Colloid Interface Sci.* 442. p.120–32.

LI, X., HE, K., PAN, B., ZHANG, S., LU, L., & ZHANG, W. (2012). Efficient As(III) removal by macroporous anion exchanger-supported Fe–Mn binary oxide: Behavior and mechanism. *Chem. Eng. J.* 193–194. p.131–138.

LIU, C.H., CHUANG, Y.H., CHEN, T.Y., TIAN, Y., LI, H., WANG, M.K., & ZHANG, W. (2015). Mechanism of Arsenic Adsorption on Magnetite Nanoparticles from Water: Thermodynamic and Spectroscopic Studies. *Environ. Sci. Technol.* 49. p.7726–7734.

LIU, Y., CHEN, M., & YONGMEI, H. (2013). Study on the adsorption of Cu(II) by EDTA functionalized Fe<sub>3</sub>O<sub>4</sub> magnetic nano-particles. *Chem. Eng. J.* 218. p.46–54.

MAKRESKI, P., STEFOV, S., PEJOV, L., & JOVANOVSKEI, G. (2015). Theoretical and experimental study of the vibrational spectra of (para)symplesite and hörnesite. *Spectrochim. Acta - Part A Mol. Biomol. Spectrosc.* 144. p.155–162.

MIRETZKY, P., & CIRELLI, A.F. (2010). Cr(VI) and Cr(III) removal from aqueous solution by raw and modified lignocellulosic materials: a review. *J. Hazard. Mater.* 180. p.1–19.

NAMASIVAYAM, C., & SURESHKUMAR, M.V. (2008). Removal of chromium(VI) from water and wastewater using surfactant modified coconut coir pith as a biosorbent. *Bioresour. Technol.* 99. p.2218–2225.

OUMA, I.L.A., NAIDOO, E.B., & OFOMAJA, A.E. (2017). Iron oxide nanoparticles stabilized

by lignocellulosic waste as green adsorbent for Cr(VI) removal from wastewater. *Eur. Phys. J. Appl. Phys.* 79. p.30401.

PARK, D., YUN, Y.-S., LEE, H.W., & PARK, J.M. (2008). Advanced kinetic model of the Cr(VI) removal by biomaterials at various pHs and temperatures. *Bioresour. Technol.* 99. p.1141–7.

POULIN, S., FRANÇA, R., MOREAU-BÉLANGER, L., & SACHER, E. (2010). Confirmation of X-ray photoelectron spectroscopy peak attributions of nanoparticulate iron oxides, using symmetric peak component line shapes. *J. Phys. Chem. C.* 114. p.10711–10718.

RAMRAKHIANI, L., MAJUMDER, R., & KHOWALA, S. (2011). Removal of hexavalent chromium by heat inactivated fungal biomass of *Termitomyces clypeatus*: Surface characterization and mechanism of biosorption. *Chem. Eng. J.* 171. p.1060–1068.

SANGHI, R., SANKARARAMAKRISHNAN, N., & DAVE, B.C. (2009). Fungal bioremediation of chromates: Conformational changes of biomass during sequestration, binding, and reduction of hexavalent chromium ions. *J. Hazard. Mater.* 169. p.1074–1080.

SETYONO, D., & VALIYAVEETIL, S. (2014). Chemically Modified Sawdust as Renewable Adsorbent for Arsenic Removal from Water. *ACS Sustain. Chem. Eng.* 2. p.2722–2729.

TANG, W., SU, Y., LI, Q., GAO, S., & SHANG, J.K. (2013). Superparamagnetic magnesium ferrite nanoadsorbent for effective arsenic (III, V) removal and easy magnetic separation. *Water Res.* 47. p.3624–3634.

VILLACÍS-GARCÍA, M., VILLALOBOS, M., & GUTIÉRREZ-RUIZ, M. (2015). Optimizing the use of natural and synthetic magnetites with very small amounts of coarse Fe(0) particles for reduction of aqueous Cr(VI). *J. Hazard. Mater.* 281. p.77–86.

WU, K., LIU, R., LI, T., LIU, H., PENG, J., & QU, J. (2013). Removal of arsenic(III) from aqueous solution using a low-cost by-product in Fe-removal plants-Fe-based backwashing sludge. *Chem. Eng. J.* 226. p.393–401.

WU, L.-K., WU, H., ZHANG, H., CAO, H., HOU, G., TANG, Y., & ZHENG, G.-Q. (2018). Graphene oxide/CuFe<sub>2</sub>O<sub>4</sub> foam as an efficient absorbent for arsenic removal from water. *Chem. Eng. J.* 334. p.1808–1819.

- YOON, Y., ZHENG, M., AHN, Y., KYU, W., SEOK, W., & KANG, J. (2017). Synthesis of magnetite / non-oxidative graphene composites and their application for arsenic removal. *Sep. Purif. Technol.* 178. p.40–48.
- YU, R.-F.F., CHI, F.-H.H., CHENG, W.-P.P., & CHANG, J.-C.C. (2014). Application of pH, ORP, and DO monitoring to evaluate chromium(VI) removal from wastewater by the nanoscale zero-valent iron (nZVI) process. *Chem. Eng. J.* 255. p.568–576.
- YUAN, P., FAN, M., YANG, D., HE, H., LIU, D., YUAN, A., ZHU, J., & CHEN, T. (2009). Montmorillonite-supported magnetite nanoparticles for the removal of hexavalent chromium [Cr(VI)] from aqueous solutions. *J. Hazard. Mater.* 166. p.821–829.
- ZHANG, S., LI, X. YAN, & CHEN, J.P. (2010). An XPS study for mechanisms of arsenate adsorption onto a magnetite-doped activated carbon fiber. *J. Colloid Interface Sci.* 343. p.232–238.
- ZHAO, Z., WEI, J., LI, F., QU, X., SHI, L., ZHANG, H., & YU, Q. (2017). Synthesis, Characterization and Hexavalent Chromium Adsorption Characteristics of Aluminum- and Sucrose-Incorporated Tobermorite. *Materials (Basel)*. 10. p.597.

### 8 Conclusions and Recommendations

#### 8.1 Conclusions

Wastewater treatment continues to attract a lot of attention due to the scarcity of potable water in most countries. Several techniques have been reported in the literature for wastewater treatment and adsorption was identified as the most cost-effective method. Adsorption makes use of adsorbents which can be sourced from different materials to ensure efficiency and reduce treatment costs. Agricultural waste materials, commonly referred to as biosorbents have been used for adsorption but face challenges in porosity and adsorption efficiency. To address these challenges, several modifications on the biosorbents have been proposed.

This study focussed on the improvement of the adsorbent properties of pine cone powder by pre-treatment with Fenton's reagent resulting in Fenton's treated pine cone powder (FTP). Fenton's treatment increased oxygenated functional groups which were responsible for both arsenic and chromium adsorption. To further improve the adsorption properties of FTP, magnetite nanoparticles (MNP) were incorporated into the material to form a magnetic composite (FTP-MNP). The introduction of magnetite resulted in the formation of a composite with increased surface area, saturation magnetization and adsorption capacities as compared to FTP. Manganese doping of bare magnetite nanoparticles and nanoparticles on the composite further enhanced their properties with increased adsorption capacities.

Adsorption of As(III) and Cr(VI) at temperatures between 298 K and 319 K showed that adsorption was favourable on all adsorbents. The adsorption resulted in monolayer coverage of the adsorbent surface with chemisorption via ion-exchange being the predominant mechanism of sorption. Thermodynamic data indicated that the process was endothermic and spontaneous for both adsorbates. As(III) adsorption presented higher maximum adsorption capacities than Cr(VI) owing to the higher affinity of iron and manganese for arsenic. Kinetic studies indicated that the adsorption of As(III) and Cr(VI) followed pseudo-second order kinetics. The kinetic mechanism confirmed that the adsorption process was via chemisorption.

Desorption studies further confirmed chemical adsorption of both adsorbates on the adsorbent surface with hydroxyl ions replacing the adsorbed ions on the surface resulting in desorption. All

adsorbents were reused three times with less than 50 % reduction in adsorption capacity after the cycles. The mechanism of As(III) adsorption on FTP-MNP revealed that the adsorption proceeded through the oxidation of As(III) to As(V), exchange with surface hydroxyl groups and the formation of inner-sphere complexes. Cr(VI) adsorption proceeded through the adsorption and reduction of Cr(VI) to Cr(III) with some of the formed Cr(III) being adsorbed while some was released into solution. Ion-exchange on the adsorbent surface also contributed to chromium adsorption. The presence of competing anions in solution resulted in decreased adsorption efficiency for both arsenic and chromium adsorption mainly because of competition for adsorption sites.



## 8.2 Recommendations

Based on the findings of this research, further work may be carried out to continue the scientific development and generation of knowledge about environmental remediation. The adsorbents used were successful in the remediation of arsenite and hexavalent chromium from water and may be efficient in the remediation of other pollutants including heavy metals and organic pollutants. The adsorption of arsenite and hexavalent chromium were carried out separately and both showed significant redox processes in their removal mechanisms. A co-adsorption could therefore be investigated to determine if redox reactions between the adsorbates could potentially improve the adsorption of each pollutant. Adsorption of real waste water from industries should be evaluated on the adsorbent materials in order to evaluate their adsorption properties in the presence of multiple pollutants. Column adsorption studies may also be carried out to improve the adsorption process and better utilize the adsorbent materials. The adsorption mechanism was studied on one of the prepared adsorbents as results had indicated similar adsorption trends in all the adsorbents. A further investigation may however be conducted to determine the individual binding mechanisms on all the adsorbent materials to determine the effects of biosorbent- nanoparticle interactions and manganese doping on the adsorption mechanism. Modelling studies may also be conducted to allow for better insights into the design and modification of adsorbents for arsenic and chromium adsorption.

## **Appendices**

## Appendix A: Isotherm modelling data

Table A-1: Isotherm modelling parameters for the adsorption of As(III) onto FTP

Isotherm Model	298 K	304 K	309 K	314 K	319 K
<b>Langmuir</b>					
$q_m$ (mg g <sup>-1</sup> )	15.846	16.221	16.773	17.435	18.295
$K_L$ (L mg <sup>-1</sup> )	0.177	0.218	0.277	0.370	0.474
$R^2$	1.000	1.000	0.999	0.998	0.995
<b>Freundlich</b>					
$n$ (L g <sup>-1</sup> )	4.961	5.502	6.188	6.968	7.713
$K_F$	3.725	3.919	4.144	4.362	4.468
$R^2$	0.983	0.979	0.975	0.972	0.969
<b>Redlich-Peterson</b>					
$K_R$ (L g <sup>-1</sup> )	3.058	3.673	4.751	6.618	9.319
$\alpha_R$ (L mg <sup>-1</sup> )	0.219	0.239	0.292	0.393	0.553
$\beta$	0.970	0.987	0.992	0.991	0.977
$R^2$	1.000	1.000	0.999	0.998	0.995
<b>Sips</b>					
$q_{\max}$ (mg g <sup>-1</sup> )	16.359	16.242	16.736	17.161	18.164
$K_S$ ((L mg <sup>-1</sup> ) <sup>-1/n</sup> )	0.192	0.219	0.276	0.360	0.473
$1/n$	0.914	0.996	1.008	1.066	1.030
$R^2$	1.000	1.000	0.999	0.998	0.995
<b>Dubinin-Radushkevich</b>					
$q_m$ (mol g <sup>-1</sup> )	5.58E-04	5.69E-04	5.95E-04	5.95E-04	6.20E-04
$E$ (kJ/mol)	12.595	13.101	13.677	14.315	14.884
$R^2$	0.955	0.931	0.919	0.889	0.863

Table A-2: Isotherm modelling parameters for the adsorption of As(III) onto MNP

Isotherm Model	298 K	304 K	309 K	314 K	319 K
<b>Langmuir</b>					
$q_m$ (mg g <sup>-1</sup> )	16.905	16.925	17.300	17.561	18.793
$K_L$ (L mg <sup>-1</sup> )	0.210	0.266	0.364	0.441	0.468
$R^2$	0.999	0.999	0.999	0.998	0.994
<b>Freundlich</b>					
$n$ (L g <sup>-1</sup> )	5.715	6.287	7.057	7.542	8.107
$K_F$	3.925	4.211	4.485	4.650	4.555
$R^2$	0.974	0.971	0.971	0.970	0.971
<b>Redlich-Peterson</b>					
$K_R$ (L g <sup>-1</sup> )	3.323	4.295	17.749	8.475	11.258
$\alpha_R$ (L mg <sup>-1</sup> )	0.178	0.239	0.380	0.526	0.730
$\beta$	1.024	1.015	0.909	0.977	0.948
$R^2$	0.999	0.999	0.999	0.998	0.995
<b>Sips</b>					
$q_{\max}$ (mg g <sup>-1</sup> )	16.887	17.022	17.749	18.216	20.244
$K_S$ ((L mg <sup>-1</sup> ) <sup>-1/n</sup> )	0.209	0.270	0.380	0.455	0.485
$1/n$	1.004	0.980	0.909	0.872	0.777
$R^2$	0.999	0.999	0.999	0.999	0.997
<b>Dubinin-Radushkevich</b>					
$q_m$ (mol g <sup>-1</sup> )	6.07E-04	5.82E-04	5.73E-04	5.73E-04	6.20E-04
$E$ (kJ/mol)	12.723	13.469	14.286	14.841	15.176
$R^2$	0.937	0.932	0.935	0.935	0.953

Table A-3: Isotherm modelling parameters for the adsorption of As(III) onto FTP-MNP

Isotherm Model	298 K	304 K	309 K	314 K	319 K
<b>Langmuir</b>					
$q_m$ (mg g <sup>-1</sup> )	16.942	17.286	17.555	17.867	18.849
$K_L$ (L mg <sup>-1</sup> )	0.282	0.313	0.358	0.489	0.595
$R^2$	1.000	0.998	0.999	0.999	0.996
<b>Freundlich</b>					
$n$ (L g <sup>-1</sup> )	6.307	6.678	7.034	7.843	8.533
$K_F$	4.181	4.280	4.370	4.718	4.689
$R^2$	0.974	0.974	0.975	0.969	0.972
<b>Redlich-Peterson</b>					
$K_R$ (L g <sup>-1</sup> )	4.739	5.822	7.066	9.380	14.250
$\alpha_R$ (L mg <sup>-1</sup> )	0.277	0.365	0.454	0.563	0.916
$\beta$	1.002	0.980	0.969	0.981	0.947
$R^2$	1.000	0.998	0.999	0.999	0.998
<b>Sips</b>					
$q_{\max}$ (mg g <sup>-1</sup> )	16.828	17.770	18.273	18.370	20.218
$K_S$ ((L mg <sup>-1</sup> ) <sup>-1/n</sup> )	0.277	0.331	0.378	0.496	0.576
$1/n$	1.025	0.906	0.870	0.898	0.785
$R^2$	1.000	0.998	1.000	0.999	0.999
<b>Dubinin-Radushkevich</b>					
$q_m$ (mol g <sup>-1</sup> )	5.88E-04	5.82E-04	5.86E-04	5.86E-04	6.23E-04
$E$ (kJ/mol)	13.204	13.788	14.231	14.940	15.430
$R^2$	0.920	0.939	0.945	0.927	0.945

Table A-4: Isotherm modelling parameters for the adsorption of As(III) onto Mn MNP

Isotherm Model	298 K	304 K	309 K	314 K	319 K
<b>Langmuir</b>					
$q_m$ (mg g <sup>-1</sup> )	19.046	23.767	24.057	24.848	25.798
$K_L$ (L mg <sup>-1</sup> )	0.306	0.241	0.358	0.528	0.637
$R^2$	1.000	0.999	0.999	0.992	0.997
<b>Freundlich</b>					
$n$ (L g <sup>-1</sup> )	7.031	7.175	8.356	9.783	10.642
$K_F$	4.022	3.201	3.430	3.719	3.753
$R^2$	0.972	0.982	0.978	0.961	0.964
<b>Redlich-Peterson</b>					
$K_R$ (L g <sup>-1</sup> )	5.806	6.536	9.535	12.848	16.062
$\alpha_R$ (L mg <sup>-1</sup> )	0.303	0.333	0.454	0.502	0.606
$\beta$	1.001	0.949	0.962	1.009	1.009
$R^2$	1.000	0.999	1.000	0.992	0.997
<b>Sips</b>					
$q_{\max}$ (mg g <sup>-1</sup> )	19.064	25.004	24.567	23.750	25.158
$K_S$ ((L mg <sup>-1</sup> ) <sup>-1/n</sup> )	0.306	0.253	0.360	0.538	0.655
$1/n$	0.997	0.887	0.944	1.184	1.096
$R^2$	1.000	1.000	0.999	0.993	0.998
<b>Dubinin-Radushkevich</b>					
$q_m$ (mol g <sup>-1</sup> )	7.13E-04	1.09E-03	1.13E-03	1.19E-03	1.26E-03
$E$ (kJ/mol)	12.986	12.265	12.808	13.377	13.759
$R^2$	0.927	0.966	0.934	0.860	0.884

Table A-5: Isotherm modelling parameters for the adsorption of As(III) onto Mn FTP-MNP

Isotherm Model	298 K	304 K	309 K	314 K	319 K
<b>Langmuir</b>					
$q_m$ (mg g <sup>-1</sup> )	23.019	24.665	26.154	27.420	28.637
$K_L$ (L mg <sup>-1</sup> )	0.264	0.279	0.336	0.397	0.524
$R^2$	1.000	0.999	0.999	1.000	0.998
<b>Freundlich</b>					
$n$ (L g <sup>-1</sup> )	7.267	7.606	8.608	9.468	10.513
$K_F$	3.316	3.120	3.192	3.204	3.028
$R^2$	0.981	0.985	0.977	0.974	0.985
<b>Redlich-Peterson</b>					
$K_R$ (L g <sup>-1</sup> )	6.790	8.571	8.974	10.074	19.094
$\alpha_R$ (L mg <sup>-1</sup> )	0.346	0.468	0.354	0.325	0.874
$\beta$	0.957	0.917	0.991	1.037	0.908
$R^2$	1.000	1.000	0.999	1.000	1.000
<b>Sips</b>					
$q_{\max}$ (mg g <sup>-1</sup> )	23.791	26.548	26.271	27.029	30.947
$K_S$ ((L mg <sup>-1</sup> ) <sup>-1/n</sup> )	0.271	0.284	0.337	0.396	0.481
$1/n$	0.921	0.853	0.988	1.043	0.848
$R^2$	1.000	1.000	0.999	1.000	1.000
<b>Dubinin-Radushkevich</b>					
$q_m$ (mol g <sup>-1</sup> )	1.06E-03	1.55E-03	1.38E-03	1.53E-03	1.69E-03
$E$ (kJ/mol)	12.105	12.230	12.417	12.639	13.050
$R^2$	0.950	0.959	0.944	0.938	0.955

Table A-6: Isotherm modelling parameters for the adsorption of Cr(VI) onto FTP

Isotherm Model	298 K	304 K	309 K	314 K	319 K
<b>Langmuir</b>					
$q_m$ (mg g <sup>-1</sup> )	13.788	14.095	15.347	16.290	16.716
$K_L$ (L mg <sup>-1</sup> )	0.031	0.058	0.044	0.053	0.063
$R^2$	0.997	0.996	0.987	0.999	0.998
<b>Freundlich</b>					
$n$ (L g <sup>-1</sup> )	1.342	2.470	2.103	2.428	2.711
$K_F$	2.194	2.808	2.497	2.531	2.583
$R^2$	0.993	0.977	0.981	0.992	0.996
<b>Redlich-Peterson</b>					
$K_R$ (L g <sup>-1</sup> )	0.524	0.595	0.766	0.997	1.647
$\alpha_R$ (L mg <sup>-1</sup> )	0.071	0.013	0.069	0.087	0.228
$\beta$	0.872	1.247	0.932	0.925	0.818
$R^2$	0.997	0.999	0.987	0.999	1.000
<b>Sips</b>					
$q_{\max}$ (mg g <sup>-1</sup> )	15.481	12.741	17.550	17.782	21.323
$K_s$ ((L mg <sup>-1</sup> ) <sup>-1/n</sup> )	0.037	0.034	0.057	0.063	0.081
$1/n$	0.880	1.269	0.829	0.878	0.734
$R^2$	0.997	0.998	0.987	0.999	1.000
<b>Dubinin-Radushkevich</b>					
$q_m$ (mol g <sup>-1</sup> )	8.43E-04	8.27E-04	7.78E-04	9.16E-04	9.12E-04
$E$ (kJ/mol)	9.382	10.394	10.753	10.825	11.323
$R^2$	0.970	0.946	0.947	0.987	0.992



Table A-7: Isotherm modelling parameters for the adsorption of Cr(VI) onto MNP

Isotherm Model	298 K	304 K	309 K	314 K	319 K
<b>Langmuir</b>					
$q_m$ (mg g <sup>-1</sup> )	14.267	14.841	15.546	16.604	17.182
$K_L$ (L mg <sup>-1</sup> )	0.039	0.073	0.122	0.174	0.333
$R^2$	0.997	0.999	0.999	0.997	0.996
<b>Freundlich</b>					
$n$ (L g <sup>-1</sup> )	1.773	2.870	4.011	4.974	6.461
$K_F$	2.413	2.863	3.295	3.534	4.050
$R^2$	0.988	0.993	0.990	0.990	0.988
<b>Redlich-Peterson</b>					
$K_R$ (L g <sup>-1</sup> )	0.487	1.391	2.429	4.432	8.707
$\alpha_R$ (L mg <sup>-1</sup> )	0.021	0.150	0.229	0.435	0.751
$\beta$	1.106	0.898	0.913	0.883	0.898
$R^2$	0.997	1.000	1.000	1.000	1.000
<b>Sips</b>					
$q_{\max}$ (mg g <sup>-1</sup> )	14.128	16.694	17.197	19.261	19.548
$K_S$ ((L mg <sup>-1</sup> ) <sup>-1/n</sup> )	0.038	0.092	0.148	0.210	0.351
$1/n$	1.015	0.820	0.809	0.725	0.710
$R^2$	0.997	1.000	1.000	1.000	0.999
<b>Dubinin-Radushkevich</b>					
$q_m$ (mol g <sup>-1</sup> )	8.21E-04	7.67E-04	7.62E-04	7.82E-04	7.79E-04
$E$ (kJ/mol)	9.816	11.162	12.211	13.088	14.318
$R^2$	0.979	0.984	0.977	0.982	0.965

Table A-8: Isotherm modelling parameters for the adsorption of Cr(VI) onto FTP-MNP

Isotherm Model	298 K	304 K	309 K	314 K	319 K
<b>Langmuir</b>					
$q_m$ (mg g <sup>-1</sup> )	14.826	15.410	16.025	17.324	18.091
$K_L$ (L mg <sup>-1</sup> )	0.046	0.078	0.126	0.134	0.204
$R^2$	0.994	0.997	0.993	0.999	0.999
<b>Freundlich</b>					
$n$ (L g <sup>-1</sup> )	2.073	3.142	4.234	4.603	5.779
$K_F$	2.519	2.951	3.353	3.318	3.691
$R^2$	0.980	0.980	0.977	0.980	0.973
<b>Redlich-Peterson</b>					
$K_R$ (L g <sup>-1</sup> )	0.532	1.048	1.951	2.230	3.420
$\alpha_R$ (L mg <sup>-1</sup> )	0.014	0.046	0.114	0.120	0.166
$\beta$	1.205	1.089	1.016	1.016	1.032
$R^2$	0.995	0.997	0.994	0.999	0.999
<b>Sips</b>					
$q_{\max}$ (mg g <sup>-1</sup> )	13.631	14.093	15.438	17.091	17.287
$K_S$ ((L mg <sup>-1</sup> ) <sup>-1/n</sup> )	0.032	0.051	0.108	0.128	0.175
$1/n$	1.175	1.258	1.115	1.037	1.167
$R^2$	0.994	0.998	0.994	0.999	0.999
<b>Dubinin-Radushkevich</b>					
$q_m$ (mol g <sup>-1</sup> )	8.63E-04	5.45E-04	5.53E-04	4.46E-04	4.62E-04
$E$ (kJ/mol)	9.924	12.895	14.580	18.602	19.455
$R^2$	0.944	0.976	0.977	0.943	0.956

Table A-9: Isotherm modelling parameters for the adsorption of Cr(VI) onto Mn MNP

Isotherm Model	298 K	304 K	309 K	314 K	319 K
<b>Langmuir</b>					
$q_m$ (mg g <sup>-1</sup> )	16.328	16.382	16.959	17.342	18.461
$K_L$ (L mg <sup>-1</sup> )	0.050	0.072	0.130	0.224	0.286
$R^2$	0.997	0.991	0.997	0.989	0.990
<b>Freundlich</b>					
$n$ (L g <sup>-1</sup> )	2.342	3.196	4.616	6.135	6.896
$K_F$	2.509	2.904	3.429	4.091	4.137
$R^2$	0.982	0.968	0.973	0.960	0.967
<b>Redlich-Peterson</b>					
$K_R$ (L g <sup>-1</sup> )	0.648	0.794	1.796	3.191	5.602
$\alpha_R$ (L mg <sup>-1</sup> )	0.016	0.011	0.070	0.139	0.323
$\beta$	1.193	1.321	1.097	1.068	0.984
$R^2$	0.998	0.995	0.998	0.990	0.990
<b>Sips</b>					
$q_{\max}$ (mg g <sup>-1</sup> )	14.893	14.791	16.454	17.351	19.190
$K_S$ ((L mg <sup>-1</sup> ) <sup>-1/n</sup> )	0.035	0.040	0.114	0.224	0.313
$1/n$	1.196	1.312	1.093	0.998	0.875
$R^2$	0.998	0.993	0.998	0.989	0.991
<b>Dubinin-Radushkevich</b>					
$q_m$ (mol g <sup>-1</sup> )	1.04E-03	1.00E-03	9.05E-04	8.37E-04	8.76E-04
$E$ (kJ/mol)	9.797	10.527	11.920	13.271	13.929
$R^2$	0.960	0.925	0.941	0.910	0.930

Table A-10: Isotherm modelling parameters for the adsorption of Cr(VI) onto Mn FTP-MNP

Isotherm Model	298 K	304 K	309 K	314 K	319 K
<b>Langmuir</b>					
$q_m$ (mg g <sup>-1</sup> )	16.682	16.807	17.500	18.273	19.133
$K_L$ (L mg <sup>-1</sup> )	0.068	0.131	0.144	0.141	0.158
$R^2$	0.996	0.991	0.995	0.996	0.993
<b>Freundlich</b>					
$n$ (L g <sup>-1</sup> )	2.991	4.590	4.954	4.986	5.374
$K_F$	2.745	3.432	3.483	3.353	3.355
$R^2$	0.982	0.969	0.971	0.976	0.976
<b>Redlich-Peterson</b>					
$K_R$ (L g <sup>-1</sup> )	1.015	1.885	2.110	2.412	3.099
$\alpha_R$ (L mg <sup>-1</sup> )	0.045	0.083	0.085	0.117	0.168
$\beta$	1.065	1.071	1.082	1.029	0.991
$R^2$	0.996	0.991	0.996	0.996	0.993
<b>Sips</b>					
$q_{\max}$ (mg g <sup>-1</sup> )	16.299	16.351	17.047	18.395	19.607
$K_S$ ((L mg <sup>-1</sup> ) <sup>-1/n</sup> )	0.063	0.117	0.130	0.144	0.169
$1/n$	1.048	1.085	1.083	0.982	0.938
$R^2$	0.996	0.991	0.996	0.996	0.993
<b>Dubinin-Radushkevich</b>					
$q_m$ (mol g <sup>-1</sup> )	9.71E-04	8.90E-04	9.35E-04	9.80E-04	1.03E-03
$E$ (kJ/mol)	10.433	11.764	12.049	12.230	12.557
$R^2$	0.960	0.921	0.934	0.951	0.946

## Appendix B: Kinetics modelling data

Table B-11: Kinetic modelling parameters for the adsorption of As(III) onto FTP

Kinetic model	25 mg L <sup>-1</sup>	50 mg L <sup>-1</sup>	75 mg L <sup>-1</sup>	100 mg L <sup>-1</sup>	150 mg L <sup>-1</sup>
<b>PFOM</b>					
$q_e$ (mg g <sup>-1</sup> ) (exp)	4.376	7.621	9.746	12.596	14.168
$q_e$ (mg g <sup>-1</sup> ) (model)	4.150	7.282	9.257	11.910	13.311
$k_1$ (min <sup>-1</sup> )	0.469	0.493	0.480	0.295	0.439
$R^2$	0.992	0.990	0.992	0.992	0.984
<b>PSOM</b>					
$q_e$ (mg g <sup>-1</sup> ) (model)	4.439	7.763	9.888	12.935	14.293
$k_2$ (g mg <sup>-1</sup> min <sup>-1</sup> )	0.153	0.094	0.071	0.031	0.044
$h$ (mg g <sup>-1</sup> min <sup>-1</sup> )	3.012	5.690	6.932	5.120	8.915
$R^2$	1.000	1.000	1.000	0.997	0.998
<b>Elovich</b>					
$\alpha$ (mg g <sup>-1</sup> )	18.008	40.438	44.062	16.753	47.608
$\beta$ (model)	1.656	0.982	0.753	0.484	0.500
$R^2$	0.938	0.970	0.968	0.973	0.975
<b>Intraparticle diffusion</b>					
$k_{id}$ (mg g <sup>-1</sup> min <sup>-0.5</sup> )	0.035	0.047	0.076	0.162	0.122
$C$	4.011	7.155	8.964	10.920	12.939
$R^2$	0.941	0.899	0.951	0.945	0.897

Table B-12: Kinetic modelling parameters for the adsorption of As(III) onto MNP

Kinetic model	25 mg L <sup>-1</sup>	50 mg L <sup>-1</sup>	75 mg L <sup>-1</sup>	100 mg L <sup>-1</sup>	150 mg L <sup>-1</sup>
<b>PFOM</b>					
$q_e$ (mg g <sup>-1</sup> ) (exp)	4.718	8.414	11.546	13.176	14.352
$q_e$ (mg g <sup>-1</sup> ) (model)	4.538	8.071	11.051	12.513	13.605
$k_1$ (min <sup>-1</sup> )	0.609	0.539	0.428	0.392	0.477
$R^2$	0.994	0.990	0.992	0.993	0.992
<b>PSOM</b>					
$q_e$ (mg g <sup>-1</sup> ) (model)	4.821	8.587	11.832	13.449	14.534
$k_2$ (g mg <sup>-1</sup> min <sup>-1</sup> )	0.190	0.094	0.052	0.041	0.048
$h$ (mg g <sup>-1</sup> min <sup>-1</sup> )	4.425	6.953	7.304	7.425	10.119
$R^2$	0.999	1.000	1.000	1.000	1.000
<b>Elovich</b>					
$\alpha$ (mg g <sup>-1</sup> )	47.861	59.362	39.106	33.776	64.111
$\beta$ (model)	1.719	0.921	0.605	0.512	0.512
$R^2$	0.922	0.968	0.969	0.970	0.969
<b>Intraparticle diffusion</b>					
$k_{id}$ (mg g <sup>-1</sup> min <sup>-0.5</sup> )	0.019	0.034	0.072	0.117	0.114
$C$	4.528	8.074	10.811	11.967	13.163
$R^2$	0.894	0.840	0.886	0.947	0.972

Table B-13: Kinetic modelling parameters for the adsorption of As(III) onto FTP-MNP

Kinetic model	25 mg L <sup>-1</sup>	50 mg L <sup>-1</sup>	75 mg L <sup>-1</sup>	100 mg L <sup>-1</sup>	150 mg L <sup>-1</sup>
<b>PFOM</b>					
$q_e$ (mg g <sup>-1</sup> ) (exp)	4.993	8.936	12.144	15.180	16.284
$q_e$ (mg g <sup>-1</sup> ) (model)	4.788	8.477	11.579	14.439	15.519
$k_1$ (min <sup>-1</sup> )	0.819	0.728	0.756	0.796	0.508
$R^2$	0.990	0.987	0.989	0.988	0.992
<b>PSOM</b>					
$q_e$ (mg g <sup>-1</sup> ) (model)	5.059	8.984	12.251	15.268	16.541
$k_2$ (g mg <sup>-1</sup> min <sup>-1</sup> )	0.256	0.125	0.097	0.082	0.046
$h$ (mg g <sup>-1</sup> min <sup>-1</sup> )	6.550	10.103	14.497	19.110	12.456
$R^2$	1.000	1.000	1.000	1.000	1.000
<b>Elovich</b>					
$\alpha$ (mg g <sup>-1</sup> )	192.318	182.622	309.342	485.638	91.440
$\beta$ (model)	1.917	1.004	0.756	0.622	0.464
$R^2$	0.932	0.969	0.968	0.969	0.968
<b>Intraparticle diffusion</b>					
$k_{id}$ (mg g <sup>-1</sup> min <sup>-0.5</sup> )	0.017	0.038	0.059	0.074	0.113
$C$	4.818	8.529	11.548	14.411	15.134
$R^2$	0.916	0.962	0.919	0.952	0.934

Table B-14: Kinetic modelling parameters for the adsorption of As(III) onto Mn MNP

Kinetic model	25 mg L <sup>-1</sup>	50 mg L <sup>-1</sup>	75 mg L <sup>-1</sup>	100 mg L <sup>-1</sup>	150 mg L <sup>-1</sup>
<b>PFOM</b>					
$q_e$ (mg g <sup>-1</sup> ) (exp)	4.998	9.076	13.440	16.240	18.040
$q_e$ (mg g <sup>-1</sup> ) (model)	4.767	8.605	12.669	15.325	17.039
$k_1$ (min <sup>-1</sup> )	0.934	0.917	0.680	0.865	0.472
$R^2$	0.985	0.987	0.988	0.989	0.989
<b>PSOM</b>					
$q_e$ (mg g <sup>-1</sup> ) (model)	5.024	9.088	13.442	16.195	18.204
$k_2$ (g mg <sup>-1</sup> min <sup>-1</sup> )	0.301	0.160	0.077	0.084	0.038
$h$ (mg g <sup>-1</sup> min <sup>-1</sup> )	7.601	13.199	13.988	22.088	12.599
$R^2$	0.999	0.999	0.999	1.000	1.000
<b>Elovich</b>					
$\alpha$ (mg g <sup>-1</sup> )	399.979	546.309	201.797	725.634	79.765
$\beta$ (model)	2.085	1.118	0.647	0.608	0.408
$R^2$	0.944	0.970	0.969	0.969	0.973
<b>Intraparticle diffusion</b>					
$k_{id}$ (mg g <sup>-1</sup> min <sup>-0.5</sup> )	0.019	0.053	0.098	0.118	0.156
$C$	4.808	8.555	12.413	15.023	16.428
$R^2$	0.933	0.772	0.931	0.949	0.954



Table B-15: Kinetic modelling parameters for the adsorption of As(III) onto Mn FTP-MNP

Kinetic model	25 mg L <sup>-1</sup>	50 mg L <sup>-1</sup>	75 mg L <sup>-1</sup>	100 mg L <sup>-1</sup>	150 mg L <sup>-1</sup>
<b>PFOM</b>					
$q_e$ (mg g <sup>-1</sup> ) (exp)	4.998	9.484	13.840	17.204	21.200
$q_e$ (mg g <sup>-1</sup> ) (model)	4.768	8.999	13.332	16.334	20.168
$k_1$ (min <sup>-1</sup> )	1.043	0.923	0.744	0.858	0.601
$R^2$	0.986	0.988	0.990	0.987	0.990
<b>PSOM</b>					
$q_e$ (mg g <sup>-1</sup> ) (model)	5.018	9.499	14.096	17.268	21.452
$k_2$ (g mg <sup>-1</sup> min <sup>-1</sup> )	0.340	0.155	0.083	0.078	0.042
$h$ (mg g <sup>-1</sup> min <sup>-1</sup> )	8.550	13.955	16.486	23.311	19.368
$R^2$	0.999	1.000	1.000	1.000	1.000
<b>Elovich</b>					
$\alpha$ (mg g <sup>-1</sup> )	751.612	619.155	354.572	754.840	197.113
$\beta$ (model)	2.221	1.079	0.658	0.569	0.382
$R^2$	0.945	0.970	0.964	0.970	0.967
<b>Intraparticle diffusion</b>					
$k_{id}$ (mg g <sup>-1</sup> min <sup>-0.5</sup> )	0.016	0.052	0.030	0.081	0.141
$C$	4.834	8.951	13.526	16.370	19.813
$R^2$	0.961	0.932	0.936	0.904	0.873

Table B-16: Kinetic modelling parameters for the adsorption of Cr(VI) onto FTP

Kinetic model	25 mg L <sup>-1</sup>	50 mg L <sup>-1</sup>	75 mg L <sup>-1</sup>	100 mg L <sup>-1</sup>	150 mg L <sup>-1</sup>
<b>PFOM</b>					
$q_e$ (mg g <sup>-1</sup> ) (exp)	3.096	5.784	7.222	8.768	10.796
$q_e$ (mg g <sup>-1</sup> ) (model)	2.904	5.562	6.824	8.019	10.099
$k_1$ (min <sup>-1</sup> )	0.225	1.936	0.306	0.175	0.228
$R^2$	0.994	0.992	0.992	0.992	0.993
<b>PSOM</b>					
$q_e$ (mg g <sup>-1</sup> ) (model)	3.195	5.777	7.402	8.968	11.112
$k_2$ (g mg <sup>-1</sup> min <sup>-1</sup> )	0.091	0.625	0.056	0.024	0.026
$h$ (mg g <sup>-1</sup> min <sup>-1</sup> )	0.925	20.852	3.062	1.916	3.253
$R^2$	1.000	1.000	1.000	1.000	1.000
<b>Elovich</b>					
$\alpha$ (mg g <sup>-1</sup> )	2.409	47.643	10.416	4.174	8.510
$\beta$ (model)	1.805	3.083	0.855	0.595	0.520
$R^2$	0.963	0.983	0.977	0.988	0.981
<b>Intraparticle diffusion</b>					
$k_{id}$ (mg g <sup>-1</sup> min <sup>-0.5</sup> )	0.053	0.010	0.088	0.233	0.190
$C$	2.545	5.671	6.327	6.306	8.833
$R^2$	0.945	0.999	0.925	0.979	0.948

Table B-17: Kinetic modelling parameters for the adsorption of Cr(VI) onto MNP

Kinetic model	25 mg L <sup>-1</sup>	50 mg L <sup>-1</sup>	75 mg L <sup>-1</sup>	100 mg L <sup>-1</sup>	150 mg L <sup>-1</sup>
<b>PFOM</b>					
$q_e$ (mg g <sup>-1</sup> ) (exp)	3.478	5.888	6.791	8.216	11.024
$q_e$ (mg g <sup>-1</sup> ) (model)	3.293	5.563	6.493	7.816	10.513
$k_1$ (min <sup>-1</sup> )	0.203	0.314	0.356	0.250	0.453
$R^2$	0.995	0.994	0.995	0.994	0.992
<b>PSOM</b>					
$q_e$ (mg g <sup>-1</sup> ) (model)	3.641	6.027	6.991	8.538	11.238
$k_2$ (g mg <sup>-1</sup> min <sup>-1</sup> )	0.071	0.071	0.071	0.039	0.059
$h$ (mg g <sup>-1</sup> min <sup>-1</sup> )	0.935	2.568	3.471	2.821	7.400
$R^2$	1.000	1.000	0.999	0.999	1.000
<b>Elovich</b>					
$\alpha$ (mg g <sup>-1</sup> )	2.265	8.909	14.143	8.073	43.399
$\beta$ (model)	1.539	1.058	0.956	0.700	0.651
$R^2$	0.962	0.975	0.969	0.977	0.969
<b>Intraparticle diffusion</b>					
$k_{id}$ (mg g <sup>-1</sup> min <sup>-0.5</sup> )	0.057	0.069	0.057	0.101	0.086
$C$	2.895	5.174	6.199	7.185	10.158
$R^2$	0.917	0.962	0.927	0.912	0.880

Table B-18: Kinetic modelling parameters for the adsorption of Cr(VI) onto FTP-MNP

Kinetic model	25 mg L <sup>-1</sup>	50 mg L <sup>-1</sup>	75 mg L <sup>-1</sup>	100 mg L <sup>-1</sup>	150 mg L <sup>-1</sup>
<b>PFOM</b>					
$q_e$ (mg g <sup>-1</sup> ) (exp)	3.576	6.180	9.246	10.264	11.424
$q_e$ (mg g <sup>-1</sup> ) (model)	3.422	5.888	8.846	9.678	10.826
$k_1$ (min <sup>-1</sup> )	0.536	0.448	0.470	0.227	0.324
$R^2$	0.991	0.993	0.991	0.993	0.992
<b>PSOM</b>					
$q_e$ (mg g <sup>-1</sup> ) (model)	3.643	6.295	9.448	10.642	11.711
$k_2$ (g mg <sup>-1</sup> min <sup>-1</sup> )	0.220	0.103	0.073	0.027	0.038
$h$ (mg g <sup>-1</sup> min <sup>-1</sup> )	2.920	4.097	6.496	3.113	5.204
$R^2$	1.000	1.000	1.000	1.000	1.000
<b>Elovich</b>					
$\alpha$ (mg g <sup>-1</sup> )	24.100	3.643	41.149	8.136	18.869
$\beta$ (model)	2.159	0.220	0.787	0.543	0.551
$R^2$	0.935	1.000	0.969	0.981	0.975
<b>Intraparticle diffusion</b>					
$k_{id}$ (mg g <sup>-1</sup> min <sup>-0.5</sup> )	0.019	0.052	0.053	0.164	0.114
$C$	3.387	5.647	8.709	8.595	10.245
$R^2$	0.933	0.932	0.849	0.926	0.932

Table B-19: Kinetic modelling parameters for the adsorption of Cr(VI) onto Mn MNP

Kinetic model	25 mg L <sup>-1</sup>	50 mg L <sup>-1</sup>	75 mg L <sup>-1</sup>	100 mg L <sup>-1</sup>	150 mg L <sup>-1</sup>
<b>PFOM</b>					
$q_e$ (mg g <sup>-1</sup> ) (exp)	3.742	6.770	9.844	11.266	12.978
$q_e$ (mg g <sup>-1</sup> ) (model)	3.553	6.456	9.262	10.683	12.100
$k_1$ (min <sup>-1</sup> )	0.356	0.443	0.588	0.319	0.350
$R^2$	0.993	0.992	0.987	0.993	0.990
<b>PSOM</b>					
$q_e$ (mg g <sup>-1</sup> ) (model)	3.832	6.904	9.855	11.552	13.071
$k_2$ (g mg <sup>-1</sup> min <sup>-1</sup> )	0.129	0.093	0.090	0.038	0.037
$h$ (mg g <sup>-1</sup> min <sup>-1</sup> )	1.888	329.096	8.723	5.068	6.304
$R^2$	1.000	1.000	1.000	1.000	1.000
<b>Elovich</b>					
$\alpha$ (mg g <sup>-1</sup> )	7.549	25.195	85.656	18.346	24.666
$\beta$ (model)	1.735	1.052	0.824	0.558	0.505
$R^2$	0.944	0.938	0.973	0.975	0.978
<b>Intraparticle diffusion</b>					
$k_{id}$ (mg g <sup>-1</sup> min <sup>-0.5</sup> )	3.377	6.314	8.991	10.057	11.095
$C$	0.035	0.043	0.084	0.117	0.181
$R^2$	0.941	0.930	0.935	0.947	0.957

Table B-20: Kinetic modelling parameters for the adsorption of Cr(VI) onto Mn FTP-MNP

Kinetic model	25 mg L <sup>-1</sup>	50 mg L <sup>-1</sup>	75 mg L <sup>-1</sup>	100 mg L <sup>-1</sup>	150 mg L <sup>-1</sup>
<b>PFOM</b>					
$q_e$ (mg g <sup>-1</sup> ) (exp)	4.082	7.270	10.684	12.074	13.978
$q_e$ (mg g <sup>-1</sup> ) (model)	3.799	6.938	10.121	11.448	13.301
$k_1$ (min <sup>-1</sup> )	0.432	0.619	0.571	0.513	0.387
$R^2$	0.988	0.989	0.989	0.991	0.992
<b>PSOM</b>					
$q_e$ (mg g <sup>-1</sup> ) (model)	4.076	7.367	10.767	12.205	14.292
$k_2$ (g mg <sup>-1</sup> min <sup>-1</sup> )	0.151	0.128	0.080	0.062	0.038
$h$ (mg g <sup>-1</sup> min <sup>-1</sup> )	2.513	6.944	9.244	9.266	7.814
$R^2$	1.000	1.000	1.000	1.000	1.000
<b>Elovich</b>					
$\alpha$ (mg g <sup>-1</sup> )	13.134	80.484	86.132	68.335	35.594
$\beta$ (model)	1.745	1.137	0.747	0.630	0.481
$R^2$	0.954	0.968	0.970	0.969	0.972
<b>Intraparticle diffusion</b>					
$k_{id}$ (mg g <sup>-1</sup> min <sup>-0.5</sup> )	0.053	0.037	0.076	0.091	0.121
$C$	3.531	6.899	9.902	11.126	12.748
$R^2$	0.945	0.843	0.951	0.959	0.918

---